

# Isoporous Block Copolymer Membranes with Charged Nanochannels



Universität Hamburg

DER FORSCHUNG | DER LEHRE | DER BILDUNG

Dissertation with the aim of achieving a doctoral degree (Dr. rer. nat.)

Institute of Physical Chemistry, Department of Chemistry, MIN Faculty

University of Hamburg

Submitted by

**Zhenzhen Zhang**

Hamburg, 2020



Reviewer 1: Prof. Dr. Volker Abetz

Reviewer 2: Prof. Dr. Horst Weller

Date of Oral Defense: 18.09.2020

Examiner 1: Prof. Dr. Volker Abetz

Examiner 2: Prof. Dr. Michael Fröba

Examiner 3: Priv. Doz. Dr. Christoph Wutz

Date of Print Release: 22.09.2020



This study was conducted between October 2015 and May 2020 at the Institute of Polymer Research, Helmholtz-Zentrum Geesthacht under the supervision of Prof. Dr. Volker Abetz.



---

---

## List of Publications

- 1) Quaternization of a Polystyrene-*block*-poly(4-vinylpyridine) Isoporous Membrane: An Approach to Tune the Pore Size and the Charge Density.  
Zhenzhen Zhang, Md. Mushfequr Rahman, Clarissa Abetz, Barbara Bajer, Jiali Wang, Volker Abetz, *Macromolecular Rapid Communications*, 2019, 40, 1800729, DOI: 10.1002/marc.201800729.
  
- 2) Chemically-Tailored Multifunctional Asymmetric Isoporous Triblock Terpolymer Membranes for Selective Transport.  
Zhenzhen Zhang, Md. Mushfequr Rahman, Clarissa Abetz, Anke-Lisa Höhme, Evgeni Sperling, Volker Abetz, *Advanced Materials*, 2020, 32, 1907014, DOI: 10.1002/adma.201907014.
  
- 3) High-performance asymmetric isoporous nanocomposite membranes with chemically-tailored amphiphilic nanochannels.  
Zhenzhen Zhang, Md. Mushfequr Rahman, Clarissa Abetz, Volker Abetz, *Journal of Materials Chemistry A*, 2020, 8, 9554-9566, DOI: 10.1039/d0ta01023e.
  
- 4) Novel Posttreatment Approaches to Tailor the Pore Size of PS-*b*-PHEMA Isoporous Membranes.  
Jiali Wang, Md. Mushfequr Rahman, Clarissa Abetz, Sofia Rangou, Zhenzhen Zhang, Volker Abetz, *Macromolecular Rapid Communications*, 2018, 39, 1800435, DOI: 10.1002/marc.201800435.



---



---

## Table of Content

<b>List of Publications .....</b>	<b>i</b>
<b>List of Figures.....</b>	<b>ix</b>
<b>List of Tables .....</b>	<b>xxi</b>
<b>List of Schemes.....</b>	<b>xxiii</b>
<b>List of Symbols .....</b>	<b>xxv</b>
<b>List of Abbreviations .....</b>	<b>xxvii</b>
<b>Chapter 1 Introduction.....</b>	<b>- 1 -</b>
1.1 Objective.....	- 2 -
1.2 Isoporous Block Copolymer Membrane with Charged Nanochannels .....	- 4 -
1.3 Strategy of the Research and Outline of the Thesis.....	- 6 -
<b>Chapter 2 Theoretical Background.....</b>	<b>- 11 -</b>
2.1 Microphase Separation of Block Copolymers .....	- 12 -
2.2 Membrane and Membrane Preparation .....	- 19 -
2.2.1 Types of Membranes .....	- 19 -
2.2.2 Membrane Preparation .....	- 20 -
2.2.3 Integral Asymmetric Membrane by Nonsolvent Induced Phase Separation (NIPS)- 21 -	
2.3 Integral Asymmetric Isoporous Block Copolymer Membrane .....	- 26 -
2.4 Membrane Separation Process.....	- 31 -
<b>Chapter 3 Materials and Methods.....</b>	<b>- 37 -</b>
3.1 Materials .....	- 38 -
3.2 Synthesis of Block Copolymers.....	- 39 -
3.2.1 Synthesis of PS- <i>b</i> -P4VP Diblock Copolymer .....	- 39 -
3.2.2 Synthesis of PS- <i>b</i> -P(HTMB- <i>r</i> -I) Diblock Terpolymers .....	- 39 -
3.2.3 Synthesis of PI- <i>b</i> -PS- <i>b</i> -P4VP Triblock Terpolymer and P(HTMB- <i>r</i> -I)- <i>b</i> -PS- <i>b</i> - P4VP Triblock Quaterpolymers .....	- 40 -

---

---

3.3	Preparation of Block Copolymer Membranes via SNIPS .....	- 42 -
3.4	Post-functionalization of Block Copolymers.....	- 43 -
3.4.1	Quaternization of P4VP Blocks with MeI.....	- 43 -
3.4.2	Sulfonation of P(HTMB- <i>r</i> -I) Blocks with 1,3-Propane Sultone .....	- 43 -
3.5	Characterization.....	- 44 -
3.5.1	Nuclear Magnetic Resonance Spectroscopy (NMR).....	- 44 -
3.5.2	Gel Permeation Chromatography (GPC).....	- 44 -
3.5.3	Transmission Electron Microscopy (TEM).....	- 44 -
3.5.4	Atomic Force Microscopy (AFM).....	- 45 -
3.5.5	Scanning Electron Microscopy (SEM).....	- 45 -
3.5.6	Energy Dispersive X-rays Analysis (EDX).....	- 46 -
3.5.7	Fourier Transform Infrared Spectroscopy (FTIR).....	- 46 -
3.5.8	Surface Zeta Potential.....	- 46 -
3.5.9	Dynamic Water Contact Angle.....	- 47 -
3.5.10	Thermogravimetric Analysis (TGA).....	- 47 -
3.5.11	Differential Scanning Calorimetry (DSC) .....	- 47 -
3.5.12	Membrane Performance Tests .....	- 48 -
3.5.12.1	Water Permeance Measurements .....	- 48 -
3.5.12.2	Retention Measurements.....	- 49 -
3.5.12.3	Adsorption Measurements .....	- 51 -
3.5.12.4	Dynamic Filtration Measurements for Antifouling Property.....	- 51 -
 <b>Chapter 4 PS-<i>b</i>-P4VP Isoporous Membranes with Tunable Positively Charged Nanochannels - 53 -</b>		
4.1	Introduction.....	- 55 -
4.2	Quaternization of PS- <i>b</i> -P4VP Membranes .....	- 56 -
4.3	Quaternized PS- <i>b</i> -P4VP Membranes with Tailored Pore Size in Hydrated State -	61 -
4.4	Influence of the Size of Alkyl Groups on the Membrane Morphology and Performance .....	- 61 -
4.4.1	Influence of the Degree of Quaternization on the Membrane Morphology and Performance .....	- 68 -
4.4.2	Limitations of Determination of the Effective Pore Size of the Membranes from Water Flux Measurements .....	- 72 -
4.5	Conclusion .....	- 74 -

<b>Chapter 5</b>	<b>High-Performance Asymmetric Isoporous Nanocomposite Membranes with Chemically-Tailored Amphiphilic Negatively Charged Nanochannels .....</b>	<b>- 77 -</b>
5.1	Introduction.....	- 79 -
5.2	Synthesis of PS- <i>b</i> -P(HTMB- <i>r</i> -I) Diblock Terpolymers .....	- 80 -
5.3	Microphase Separation of PS- <i>b</i> -PI/PS- <i>b</i> -P(HTMB- <i>r</i> -I) Diblock Terpolymers in Bulk	- 83 -
5.4	Solvent Evaporation Induced Self-assembly of Block Copolymers During Spin-coating and SNIPS .....	- 86 -
5.5	Organic-inorganic Hybrid Nanocomposite PS- <i>b</i> -P(HTMB- <i>r</i> -I) Isoporous Membrane with TiO <sub>2</sub> Nanoparticles .....	- 90 -
5.6	Sulfonation of Organic-inorganic Hybrid Nanocomposite Isoporous Membranes .....	- 102 -
5.7	Membrane Performance.....	- 105 -
5.7.1	Membrane Permeability and Selectivity.....	- 105 -
5.7.2	Fouling Resistance of Organic Solutes.....	- 108 -
5.8	Conclusion .....	- 110 -
<b>Chapter 6</b>	<b>Chemically-Tailored Multifunctional Asymmetric Isoporous Triblock Quaterpolymer Membranes for Selective Transport .....</b>	<b>- 113 -</b>
6.1	Introduction.....	- 115 -
6.2	Synthesis of P(HTMB- <i>r</i> -I)- <i>b</i> -PS- <i>b</i> -P4VP Triblock Quaterpolymers .....	- 116 -
6.3	Microphase Separation of PI- <i>b</i> -PS- <i>b</i> -P4VP Triblock Terpolymer and P(HTMB- <i>r</i> -I)- <i>b</i> -PS- <i>b</i> -P4VP Triblock Quaterpolymers .....	- 118 -
6.3.1	Microphase Separation of PI- <i>b</i> -PS- <i>b</i> -P4VP and P(HTMB- <i>r</i> -I)- <i>b</i> -PS- <i>b</i> -P4VP with Different Compositions using Different Solvent Systems .....	- 118 -
6.3.2	Influence of Evaporation Speed on the Miscibility of P(HTMB- <i>r</i> -I) and P4VP Blocks	- 122 -
6.4	Fabrication of Isoporous Membrane via SNIPS .....	- 127 -
6.5	Post-functionalization of Isoporous Membrane toward Negatively or Positively Charged Membrane.....	- 132 -
6.6	Performance of Multifunctional Isoporous Membranes.....	- 135 -
6.6.1	pH Responsive Behavior and Water Permeance .....	- 135 -
6.6.2	Charge-based Selective Transport of Small Molecules through Positively Charged Membrane .....	- 136 -
6.6.3	Charge/Size-based Selective Transport of Small Molecules through Negatively Charged Membrane .....	- 142 -
6.7	Conclusion .....	- 145 -

---

---

<b>Chapter 7</b>	<b>Potential of Integral Aysmmetric Isoporous Membrane towards Enzymatic Membrane Reactors.....</b>	<b>147 -</b>
7.1	Introduction.....	149 -
7.2	Preliminary Study of Anchor Peptides Binding on Homo-PS and Homo-P4VP Dense Films -	151 -
7.3	Preparation of PS- <i>b</i> -P4VP Membranes with Different Pore Sizes and Degrees of Quaternization.....	151 -
7.4	Immobilization of YmPh-AP Fusion Proteins on Various PS- <i>b</i> -P4VP Membranes... -	153 -
7.5	Conclusion .....	156 -
<b>Chapter 8</b>	<b>Summary.....</b>	<b>157 -</b>
8.1	Summary.....	158 -
8.2	Zusammenfassung .....	162 -
<b>Chapter 9</b>	<b>References.....</b>	<b>167 -</b>
<b>Chapter 10</b>	<b>Appendix.....</b>	<b>175 -</b>
10.1	Exploratory Investigation Aiming for Charge-mosaic Isoporous Membranes... -	176 -
10.1.1	Synthesis of PS- <i>b</i> -PtBMA Diblock Copolymers .....	176 -
10.1.2	Synthesis of PtBMA- <i>b</i> -PS- <i>b</i> -P4VP Triblock Terpolymers .....	177 -
10.1.3	Fabrication of Isoporous Membrane via SNIPS from PS- <i>b</i> -PtBMA Diblock Copolymers .....	179 -
10.1.4	Hydrolysis of the PS- <i>b</i> -PtBMA Diblock Copolymer Membrane .....	181 -
10.1.5	Synthesis of PDMAi- <i>b</i> -PS- <i>b</i> -PtBMA Triblock Terpolymer .....	183 -
10.1.6	Membrane Fabrication of PDMAi- <i>b</i> -PS- <i>b</i> -PtBMA Triblock Terpolymer . -	184 -
10.1.7	Post-functionalization of PDMAi- <i>b</i> -PS- <i>b</i> -PtBMA Triblock Terpolymer .. -	185 -
10.2	PS- <i>b</i> -P4VP Isoporous Membranes with Tunable Positively Charged Nanochannels. -	187 -
10.3	High-Performance Asymmetric Isoporous Nanocomposite Membranes with Chemically-Tailored Amphiphilic Negatively Charged Nanochannels .....	190 -
10.4	Chemically-Tailored Multifunctional Asymmetric Isoporous Triblock Quaterpolymer Membranes for Selective Transport.....	193 -
10.5	Potential of Integral Aysmmetric Isoporous Membrane towards Enzymatic Membrane Reactors .....	200 -
10.6	Toxicity of Chemicals.....	205 -

<b>Chapter 11 Acknowledgement .....</b>	<b>- 209 -</b>
<b>Curriculum Vitae .....</b>	<b>- 213 -</b>
<b>Declaration of Oath.....</b>	<b>- 215 -</b>



## List of Figures

- Figure 1.1. The schematic representation of the approach to achieve the charge-mosaic isoporous membrane derived from triblock copolymers. .... - 7 -
- Figure 1.2. Schematic outline of the thesis. .... - 9 -
- Figure 2.1. (a) Theoretical phase diagram of a linear diblock copolymer composed of components with similar statistic segment lengths and flexibility from SCFT ( $S_{cp}$ : close packed spheres, S: spheres, C: cylinders, L: lamellae, G: gyroid). (b) Equilibrium morphologies of a diblock copolymer. From left to right the volume fraction of the dark-colored component increases: spheres, cylinders, double gyroid, and lamellae. Adapted from the references.<sup>72, 73</sup> ..... - 15 -
- Figure 2.2. Microphase separation structures of linear ABC terpolymer copolymers with  $\chi_{AB} \approx \chi_{BC} > \chi_{AC}$ :  $\phi_A \approx \phi_C$  with increasing  $\phi_B$  (a-c), increasing ratio  $\phi_B/\phi_C$  (e-g), and increasing ratio  $\phi_B/\phi_A$  (h-j). The blocks A, B and C are coloured grey, dark and white, respectively. The figure is adapted from reference.<sup>73</sup> ..... - 17 -
- Figure 2.3. Microphase separation structures of linear ABC terpolymer copolymers with with  $\chi_{AB} \approx \chi_{BC} < \chi_{AC}$  and  $\phi_A \approx \phi_C$ . The blocks A, B and C are colored black, white and grey, respectively. The figure is adapted from reference.<sup>79, 80</sup> ..... - 18 -
- Figure 2.4. Schematic representation of different types of membranes: (a) symmetric membranes, (b) Asymmetric membranes. The figure is adapter from reference<sup>83</sup> ..... - 19 -
- Figure 2.5. Schematic illustration of a three-component phase diagram typically used to rationalize the membrane formation via NIPS (water precipitation). A path from initial polymer casting solution A to the final membrane D can explain the membrane formation process. The figure is adapted from reference<sup>31, 87</sup> ..... - 23 -
- Figure 2.6. Different layers of a phase inversion precipitation membrane follow different precipitation pathways through ternary phase diagram. The figure is adapted from reference<sup>31, 87</sup> ..... - 25 -
- Figure 2.7. (a) Schematic representation of the SNIPS process: casting of the BCP solution on the substrates (e.g. glass plate or non-woven support), evaporation of volatile solvent from the cast film surface within a certain time, immersing the cast film in the nonsolvent bath (e.g. water), drying of the membrane. (b) Top and cross-section view of a representative integral asymmetric isoporous BCP membrane prepared via SNIPS process. The figure is adapted from references<sup>37, 44, 93</sup> ..... - 28 -

---

---

Figure 2.8. Schematic representation of isoporous structure formation on the top of SNIPS membrane from the casting solution. (a) disordered or weakly segregated diblock copolymer in a mixed selective solvent (red: polystyrene rich domains, blue: poly(4-vinylpyridine) rich domains), (b) microphase separation with polystyrene rich matrix after film casting, (c) solidification of the matrix due to solvent evaporation, (d) open pores in the poly(4-vinylpyridine) rich domains after non-solvent induced phase separation, (e) isoporous structure of the dried membrane. This figure is adapted from reference <sup>19</sup> .....	- 30 -
Figure 2.9. Membrane processes that are driven by pressure typically can be classified into microfiltration (MF), ultrafiltration (UF), nanofiltration (NF), reverse osmosis (RO) and forward osmosis (FO) based on the size of the retained solutes. The figure is adapted from the reference <sup>107</sup> .....	- 32 -
Figure 3.1. Schematic representation of membrane casting via SNIPS. ....	- 43 -
Figure 3.2. (a) Schematic representation of the home-made automatic testing device. (b) Measurement cell. ....	- 48 -
Figure 3.3. (a)A photo of the employed EMD Millipore XFUF04701 cell, (b) Photos of the in-house prepared reduction ring to reduce the effective membrane size. ....	- 50 -
Figure 4.1. Secondary electron (SE) images of SEM of the pristine membrane: (a) top surface and (b) cross section. ....	- 56 -
Figure 4.2. (a) Reaction scheme of quaternization of the PS- <i>b</i> -P4VP membrane. (b) ATR-FTIR spectra of the pristine membrane and the quaternized membranes with MeI, EtI and 1-PrI. The relative intensities were normalized using the characteristic CH <sub>2</sub> stretching vibrations (*) of the unreactive backbone around 2924 cm <sup>-1</sup> . (c) <sup>1</sup> H NMR spectra of the pristine membrane and the representative quaternized membrane with 3 days MeI. ....	- 57 -
Figure 4.3. Secondary electron (SE) images of SEM of the representative quaternized membrane after 3 days exposure to MeI: (a) top surface and (b) the cross section. Back scattered electron (BSE) images of SEM: (c) top surface of the pristine membrane, (d, e) top surface and cross section of the representative quaternized membrane after 3 days exposure to MeI.....	- 58 -
Figure 4.4. <sup>1</sup> H NMR spectra of (a) the membranes quaternized with MeI as a function of time, (b) the membranes quaternized with EtI as a function of time, (c) the membranes quaternized with 1-PrI as a function of time. (d) Degree of quaternization of P4VP via MeI, EtI, and 1-PrI as a function of time based on the calculation from <sup>1</sup> H NMR spectra.....	- 59 -
Figure 4.5. Snapshots of dynamic contact angle of a water droplet onto (a) I0 surface (b) M52 surface, (c) E52 surface, (d) P52 surface. ....	- 61 -

- Figure 4.6. (a) The change of contact angles onto I0, M52, E52 and P52 surface with time. (b) Water flux of I0, M52, E52 and P52 at a transmembrane pressure up to 1 bar at room temperature. Secondary electron (SE) images of SEM: top surface of (c) M52, (d) E52, (e) P52. (f) Schematic representation of I0, M52, E52 and P52 in the hydrated state. .... - 63 -
- Figure 4.7. (a) Molecular structure and space-filling model of methylene blue (MB<sup>+</sup>). (b) The photography of the feed and permeate solutions of I0, M52, E52, and P52, and the prepared membranes after MB<sup>+</sup> rejection measurements using a 10 mg L<sup>-1</sup> feed solution. (c) UV-vis absorbance of the feed and the permeate solutions of I0, M52, E52, and P52 with feed solution of concentration 10 mg L<sup>-1</sup>. (d) MB<sup>+</sup> retention of I0, M52, E52, and P52 with feed solution of concentration 10 mg L<sup>-1</sup>. .... - 65 -
- Figure 4.8. (a) The photographs of permeate solutions of I0, M52, E52, and P52, and the prepared membranes before and after MB<sup>+</sup> rejection measurements using a 100 mg L<sup>-1</sup> feed solution. (b) UV-vis absorbance of the permeate solutions of I0, M52, E52, and P52 using a 100 mg L<sup>-1</sup> feed solution. (c) MB<sup>+</sup> rejection of I0, M52, E52, and P52 using a 100 mg L<sup>-1</sup> feed solution. .... - 68 -
- Figure 4.9. Secondary electron (SE) images of SEM: top surface and cross section of (a, d) M12, (b, e) M25, (c, f) M42, (g, i) M52, (h, j) M100. .... - 69 -
- Figure 4.10. Secondary electron (SE) images of SEM: top surface and cross section of (a, d) P12, (b, e) P25, (c, f) P42, (g, i) P52, (h, j) P55. .... - 70 -
- Figure 4.11. (a) Water flux (average value of 0-2 h measurement) of I0 and the membranes having the series of different degrees of quaternization with MeI and 1-PrI, respectively. (b) MB<sup>+</sup> retention of I0 and the membranes having the series of different degrees of quaternization with MeI and 1-PrI, respectively, with feed solution of concentration 10 mg L<sup>-1</sup>. .... - 71 -
- Figure 4.12. Effective pore size with the degree of quaternization calculated by the Hagen-Poiseuille equation based on water flux measurements: (a) 0-2 h measurement, (b) 22-24 h measurement. .... - 73 -
- Figure 5.1. Schematic representation of the integral asymmetric isoporous membrane with amphiphilic pores and the in situ integration of sulfonic acid moieties along the pore walls. .... - 79 -
- Figure 5.2. <sup>1</sup>HNMR spectra of (a) PS precursor, (b) diblock copolymer PS-*b*-PI and (c) PS-*b*-P(HTBM-*r*-I). .... - 81 -
- Figure 5.3. Molar mass distribution determined by GPC for the PS precursor (Pre-PS), PS-*b*-PI in THF, and P1, P2, P3 and P4 in DMAC/LiCl. .... - 81 -
- Figure 5.4. TEM images of block copolymer films prepared from different solvent systems – (a) PS-*b*-PI, (b) P1, (c) P2, (d) P3 and (e) P4 films prepared from pure CHCl<sub>3</sub>. (f) PS-*b*-PI, (g) P1, (h) P2, (i) P3 and (g) P4 films prepared from CHCl<sub>3</sub>/DMF (95/5 v/v) solvent mixture. All the films were

- stained by OsO<sub>4</sub> vapour for 1 h, where the PI or P(HTMB-*r*-I) domains appear dark in the bright PS matrix. .... - 84 -
- Figure 5.5. TEM images of block copolymer films prepared from pure CHCl<sub>3</sub>– (a) PS-*b*-PI, (b) P1, (c) P2, (d) P3 and (e) P4. All the films were stained by RuO<sub>4</sub> vapor for 20 min, where the edge of PI or P(HTMB-*r*-I) domains appear dark in the bright PS matrix. .... - 84 -
- Figure 5.6. (a) Schematic representation of the spin-coating process. Atomic force microscopy (AFM) phase maps of the spin-coated dense films prepared from CHCl<sub>3</sub>: (b) P1, (c) P2, (d) P3, (e) P4. .... - 86 -
- Figure 5.7. Secondary electron (SE) images of SEM of representative membranes cast from: (a) 16 wt% P2 solution in THF/DMF/DOX 2/1/1, the evaporation time  $t = 30$  s, (b) 20 wt% P3 solution in THF/DMF 2/3, the evaporation time  $t = 20$  s, (c) 18 wt% P3 solution in THF/DMF/DOX 2/2/1, the evaporation time  $t = 20$  s, (d) 18 wt% P3 solution in THF/DMF/DOX 1/1/1, the evaporation time  $t = 20$  s. .... - 87 -
- Figure 5.8. Secondary electron (SE) images of SEM of representative P4 membranes cast from (a) 18 wt% solution in THF/DMF 1/1, the evaporation time  $t = 10$  s, (b) 20 wt% solution in THF/DMF 2/3, the evaporation time  $t = 5$  s, (c, d) 24 wt% solution in THF/DMF/DOX 1/1/1, the evaporation time  $t = 20$  s: (c) overview, (d) higher magnification. .... - 87 -
- Figure 5.9. Secondary electron (SE) images of SEM of the most representative membranes cast from: (a) 28 wt% P1 solution in THF/DMF 1/1, the evaporation time  $t = 2$  s, (b) 20 wt% P2 solution in THF/DMF 3/2, the evaporation time  $t = 25$  s, (c) 20 wt% P3 solution in THF/DMF 3/2, the evaporation time  $t = 20$  s, (d) 24 wt% P4 solution in THF/DMF/DOX 2/1/1, the evaporation time  $t = 10$  s. .... - 88 -
- Figure 5.10. Secondary electron (SE) images of SEM of P4 membranes cast from 24 wt% solution in THF/DMF/DOX 2/1/1 using different evaporation time: (a)  $t = 5$  s, (b)  $t = 10$  s, (c)  $t = 20$  s, (d)  $t = 30$  s. .... - 90 -
- Figure 5.11. Secondary electron (SE) images of SEM of P4 membranes cast from different concentration solutions in THF/DMF/DOX 2/1/1 with the evaporation time  $t = 10$  s: (a) 22 wt%, (b) 25 wt%, (c) 28 wt%, (d) 30 wt%. .... - 90 -
- Figure 5.12. Secondary electron (SE) images of SEM: (a) cross section near the top surface, (b) overview of cross section, (c) bottom surface of P4 membrane cast from 24 wt% solution in THF/DMF/DOX 2/1/1, the evaporation time  $t = 10$  s. .... - 90 -
- Figure 5.13. Secondary electron (SE) images of SEM: top surface and bottom interface of the representative P4 membranes cast by using THF/DMF/DOX (2/1/1): (a, e) in the 4 °C H<sub>2</sub>O bath, 28 wt% polymer concentration; (b, f) in the 15 °C H<sub>2</sub>O bath, 28 wt% polymer concentration; (c, g) in the 32 °C H<sub>2</sub>O bath, 25 wt% polymer concentration; (d, h) in the

50 °C H <sub>2</sub> O bath, 25 wt% polymer concentration. Evaporation time is t = 5 s in all cases.....	- 91 -
Figure 5.14. Secondary electron (SE) images of SEM: top surface and bottom interface of the representative P4 membranes cast from 25 wt% solution in THF/DMF/DOX 2/1/1: (a, c) in the non-solvent bath of methanol/H <sub>2</sub> O (20/80 v/v); (b, d) in the non-solvent bath of methanol/H <sub>2</sub> O (10/90 v/v). Evaporation time is t = 5 s in both cases.....	- 92 -
Figure 5.15. Secondary electron (SE) images of SEM: top surface and bottom interface of the representative P4 membranes cast from: (a, c) 25 wt% solution in THF/DMF/DOX 4/3/3; (b, d) 25 wt% solution in THF/DMF/DOX 1/1/1. Evaporation time is t = 5 s in both cases. ....	- 93 -
Figure 5.16. Secondary electron (SE) images of SEM: top surface and bottom interface of the representative P4 membranes cast from 25 wt% solution in THF/DMF/DOX 2/1/1: (a, c) with 6 wt% (as P4) PEG400 as the porogen; (b, d) with 20 wt% (as P4) PEG400 as the porogen. Evaporation time is t = 5 s in both cases. ....	- 94 -
Figure 5.17. Secondary electron (SE) images of SEM: top surface and bottom interface of P4 membranes from 16 wt% solution in THF/DMF/DOX 2:1:1 wt% with different amount of TiO <sub>2</sub> NPs as the additives: (a, f) without TiO <sub>2</sub> NPs, the evaporation time t = 15 s, (b, g) 6 wt% TiO <sub>2</sub> NPs, the evaporation time t = 15 s, (c, h) 8 wt% TiO <sub>2</sub> NPs, the evaporation time t = 15 s, (d, i) 10 wt% TiO <sub>2</sub> NPs, the evaporation time t = 10 s, (e, j) 20 wt% TiO <sub>2</sub> NPs, the evaporation time t = 5 s. ....	- 95 -
Figure 5.18. Secondary electron (SE) images of SEM: top surface and bottom interface of P4 membranes from different concentration of casting solutions in THF/DMF/DOX (2:1:1 wt%) with 6 - 8 wt% of TiO <sub>2</sub> NPs as the additives: (a, e) 14 wt%, the evaporation time t = 15 s, (b, f) 15 wt%, the evaporation time t = 15 s, (c, g) 16 wt%, the evaporation time t = 15 s, (d, h) 18 wt%, the evaporation time t = 15 s, (i, m) 19 wt%, the evaporation time t = 10 s, (j, n) 20 wt%, the evaporation time t = 10 s, (k, o) 22 wt%, the evaporation time t = 10 s, (l, p) 25 wt%, the evaporation time t = 15 s. The insert images are the overview of the cross section of the membranes. ....	- 96 -
Figure 5.19. Back-scattered electron (BSE) images of SEM of (a) the purely organic P4 membrane without TiO <sub>2</sub> NPs, (b) the hybrid membrane with TiO <sub>2</sub> NPs. ....	- 97 -
Figure 5.20. (a) TGA curves of the dried purely organic membrane cast from 25 wt% P4 without TiO <sub>2</sub> NPs and hybrid nanocomposite membrane cast from 18 wt% P4 with 8 wt% TiO <sub>2</sub> NPs. (b) DSC curves of PS- <i>b</i> -PI diblock copolymer, purely organic membrane and hybrid nanocomposite membrane with 8 wt% TiO <sub>2</sub> NPs.....	- 98 -

- Figure 5.21. (a) SEM image of an overview of the cross section of a hybrid nanocomposite membrane. TEM images of (b, c) overview of ultrathin sections of the membrane cross section by combining the images from different positions, (d) top layer, (e) middle porous structure, (f) bottom porous structure..... - 100 -
- Figure 5.22. Water fluxes of a representative P4/TiO<sub>2</sub> NPs hybrid isoporous membrane at various transmembrane pressures from 0.25 to 2.9 bar..... - 102 -
- Figure 5.23. Schematic representation, chemical structure and SEM images of (a) the pristine membrane I0, (b) the sulfonated membrane (SM). (c) FTIR spectra of I0 and SM. The relative intensities were normalized using the characteristic aromatic C-H stretches (\*) of the unreactive polystyrene segment between 3100 and 3000 cm<sup>-1</sup>. (d) Comparison of EDX spectra of I0 and SM. (e) Dynamic water contact angle of I0 and SM as a function of time. (f) The surface zeta potential of I0 and SM as a function of pH (2.5 - 10). Experiments were performed with a background electrolyte of 1 mM NaCl..... - 104 -
- Figure 5.24. (a) Comparison of water permeance of the pristine membrane I0 and the sulfonated membrane SM under trans-membrane pressure of 1 bar. (b) The separation behavior of small organic molecules (*i.e.* orange II (OR<sup>-</sup>) and reactive green 19 (RG6<sup>-</sup>)) using I0 and SM. (c-d) Molecular structure and space-filling model of the small molecules, and the corresponding UV-vis spectra and a color change of the solution: (c) OR<sup>-</sup> and (d) RG6<sup>-</sup>. ..... - 106 -
- Figure 5.25. The photographs of the membranes after adsorption measurements using 0.1 mM solute aqueous solutions. (a) I0 after OR<sup>-</sup> adsorption test, (b) I0 after RG6<sup>-</sup> adsorption test, (c) SM after OR<sup>-</sup> adsorption test, (d) SM after RG6<sup>-</sup> adsorption test. .... - 108 -
- Figure 5.26. (a) Time-dependent normalized permeance variations of the pristine membrane I0 and the sulfonated membrane SM during the filtration process using OR<sup>-</sup> and RG6<sup>-</sup> as the permeate solutes, respectively. The operation process included four steps: (1) 30 min pure water filtration, (2) 3 h filtration of small molecules aqueous solution, (3) 20 min water washing, (4) 30 min pure water filtration after washing. (b) A summary of the corresponding *FRR*, *FDR<sub>t</sub>*, *FDR<sub>r</sub>*, *FDR<sub>ir</sub>* values of I0 and SM. .... - 108 -
- Figure 5.27. The photographs of the membranes after antifouling filtration measurements using 0.1 mM solute aqueous solutions. (a) Blank I0 without antifouling test, (b) I0 after OR<sup>-</sup> antifouling test, (c) I0 after RG6<sup>-</sup> antifouling test, (d) Blank SM without antifouling test, (e) SM after OR<sup>-</sup> antifouling test, (f) SM after RG6<sup>-</sup> antifouling test. .... - 110 -
- Figure 6.1. Schematic illustration of the formation mechanism of the SNIPS membranes featuring positively or negatively charged nanochannels..... - 115 -

- Figure 6.2. Synthesis route of PI-*b*-PS-*b*-P4VP triblock terpolymers by living anionic polymerization and thiol-ene click chemistry of PI-*b*-PS-*b*-P4VP to obtain P(HTMB-*r*-I)-*b*-PS-*b*-P4VP copolymers. .... - 116 -
- Figure 6.3. <sup>1</sup>HNMR spectra of (a) the precursor PI, (b) the precursor PI-*b*-PS, (c) PI-*b*-PS-*b*-P4VP, (d) P(HTMB-*r*-I)-*b*-PS-*b*-P4VP. .... - 117 -
- Figure 6.4. TEM images and schematic representation – (a) PI-*b*-PS-*b*-P4VP, (b) P1, (c) P2, (d) P3 films prepared from CHCl<sub>3</sub>/DMF 95/5 (v/v). (e) PI-*b*-PS-*b*-P4VP, (f) P1, (g) P2, (h) P3 films prepared from CHCl<sub>3</sub>/methanol 95/5 (v/v). In the I<sub>2</sub> stained films, the P4VP domains appear dark in the bright PS matrix while the PI and P(HTMB-*r*-I) domains are not distinguishable from PS. In the double-stained films with I<sub>2</sub> and OsO<sub>4</sub>, the P4VP, PI and P(HTMB-*r*-I) domains are darker than the PS matrix. All the images have the same magnification. .... - 120 -
- Figure 6.5. AFM height, modulus, adhesion and deformation images of (a-d) blank PI-*b*-PS-*b*-P4VP thin film, (e-h) PI-*b*-PS-*b*-P4VP thin film with 3 days methyl iodide (MeI) post-modification, (i-l) PI-*b*-PS-*b*-P4VP thin film with 2 days trimethylchlorosilane (TMCS) post-modification. .... - 122 -
- Figure 6.6. AFM height, modulus, adhesion and deformation images of (a-d) blank thin film of hydroxylated diblock terpolymer PS-*b*-P(HTMB-*r*-I), (e-h) PS-*b*-P(HTMB-*r*-I) thin film with 3 days methyl iodide (MeI) post-modification, (i-l) PS-*b*-P(HTMB-*r*-I) thin film with 2 days trimethylchlorosilane (TMCS) post-modification. .... - 123 -
- Figure 6.7. AFM height, modulus, adhesion and deformation images of (a, d, g, j) blank thin film of copolymer P3, (b, e, h, k) P3 thin film with 3 days methyl iodide (MeI) post-modification, (c, f, i, l) P3 thin film with 3 days MeI post-modification and subsequent 2 days trimethylchlorosilane (TMCS) post-modification. All the post-modifications were employed on the same piece of the blank thin film. .... - 125 -
- Figure 6.8. SEM images of the top surface of representative P3 membranes cast from different solvent systems using different polymer concentrations (indicated in the images) and evaporation times (indicated in the images): (a-c) THF/DMF 40/60, (d-f) THF/DMF 50/50, (g-i) THF/DMF/DOX 50/25/25. .... - 127 -
- Figure 6.9. SEM images of the top surface of representative P3 membranes cast from (a) 23 wt% solution in a THF/DMF/DOX 50/37.5/12.5 solvent mixture, the evaporation time  $t = 5$  s, (b) 22 wt% solution in a THF/DMF/DOX 40/30/30 solvent mixture, the evaporation time  $t = 4$  s, (c) 24 wt% solution in a THF/DMF/DOX 50/25/25 solvent mixture, the evaporation time  $t = 10$  s, (d) 22 wt% solution in a THF/DMF/DOX 55/22.5/22.5 solvent mixture, the evaporation time  $t = 6$  s. .... - 128 -

- Figure 6.10. SEM images of the top surface of representative P3 membranes cast from 24 wt% solution in THF/DMF/DOX 2/1/1 with different evaporation time (a)  $t = 2$  s, (b)  $t = 4$  s, (c)  $t = 6$  s, (d)  $t = 8$  s..... - 129 -
- Figure 6.11. SEM images of the top surface of representative P3 membranes cast from ternary solvent system THF/DMF/DOX 2/1/1 (a) 22 wt% polymer concentration, the evaporation time  $t = 10$  s, (b) 23 wt% polymer concentration, the evaporation time  $t = 10$  s, (c) 25 wt% polymer concentration, the evaporation time  $t = 8$  s. .... - 130 -
- Figure 6.12. SEM images of top surface of representative P3 membranes cast from (a) 22 wt% solution with 0.75 wt%  $\text{Mg}(\text{acetate})_2$  ( $\text{MgAc}_2$ ) as BCP, the evaporation time  $t = 10$  s, (b) 22 wt% solution with 1.5 wt%  $\text{Mg}(\text{acetate})_2$  ( $\text{MgAc}_2$ ) as BCP, the evaporation time  $t = 8$  s (c) 21 wt% solution with 2.25 wt%  $\text{MgAc}_2$  as BCP, the evaporation time  $t = 4$  s, (d) 20 wt% solution with 3 wt%  $\text{MgAc}_2$  as BCP, the evaporation time  $t = 6$  s, (e) 21 wt% solution with 4.75 wt%  $\text{MgAc}_2$  as BCP, the evaporation time  $t = 5$  s. .... - 131 -
- Figure 6.13. SEM images of P3 SNIPS membrane: (a) cross-section near the top surface, (b) bottom interface contacting with glass substrates..... - 131 -
- Figure 6.14. Schematic representation, chemical structure and SEM images of top surface and cross section of (a) methyl iodide treated membrane MM, (b) 1,3-propane sultone treated membrane PM. .... - 132 -
- Figure 6.15. FTIR spectra of the pristine membrane I0, MM and PM. The relative intensities were normalized using the characteristic  $\text{CH}_2$  stretching vibrations (\*) of the unreactive backbone around  $2924 \text{ cm}^{-1}$ ..... - 133 -
- Figure 6.16. Comparison of the surface zeta potential as a function of pH of (a) P(HTMB-*r*-I)-*b*-PS-*b*-P4VP (I0) and PS-*b*-P4VP membrane, (b) methyl iodide treated P(HTMB-*r*-I)-*b*-PS-*b*-P4VP (MM) and PS-*b*-P4VP membrane, (c) 1,3-propane sultone treated P(HTMB-*r*-I)-*b*-PS-*b*-P4VP (SM) and PS-*b*-P4VP membrane. Experiments were carried out with a background electrolyte of 1 mM NaCl. .... - 134 -
- Figure 6.17. (a) pH responsive behaviour of I0. (b) Water permeance of I0, MM and PM..... - 136 -
- Figure 6.18. Charge-based selectivity between similarly sized organic solutes ( $\sim 1$  nm) in single and mixed solute systems based on the positively charged membrane MM. Molecular structure and space-filling model of three model organic molecules with distinct charges while similar size of ca. 1 nm, and the corresponding separation behaviour of the pristine membrane I0 and the positively charged membrane MM determined by UV-vis spectra and a colour change of the solution in single solute retention measurement: (a) cationic methylene blue ( $\text{MB}^+$ ), (b) neutral riboflavin ( $\text{RB}^0$ ), (c) anionic orange II ( $\text{OR}^-$ ), measured with MM close to saturated adsorption by immersing in a 0.1 mM  $\text{OR}^-$  solution for 30 days. (d) The competitive separation behavior of I0 and MM in the mixed-solute

- retention of MB<sup>+</sup> and RB0 (50/50, molar ratio) confirmed by UV-vis spectra and the colour change of the solution. .... - 137 -
- Figure 6.19. The separation behaviour of OR<sup>-</sup> of a freshly prepared positively charged membrane MM determined by UV-vis spectra and a colour change of the solution. .... - 139 -
- Figure 6.20. Size- and charge-based selectivity between the organic solutes (1–2 nm) in single and mixed solute systems based on the negatively charged membrane PM. Molecular structure and space-filling model of three model organic molecules with distinct size and the number of negative charges, and the corresponding separation behaviour of the pristine membrane IO and the negatively charged membrane PM determined by UV-vis spectra and a colour change of the solution in single solute retention measurement: (a) monovalent orange II (OR<sup>-</sup>, 350.32 g mol<sup>-1</sup>, 1.3 nm), (b) trivalent naphthol green B (NG3<sup>-</sup>, 878.45 g mol<sup>-1</sup>, 1.8 nm), (c) hexavalent reactive green 19 (RG6<sup>-</sup>, 1418.93 g mol<sup>-1</sup>, 1.9 nm). (d) The competitive separation behaviour of IO and PM in the mixed-solute retention of OR<sup>-</sup> and NG3<sup>-</sup> (50/50, molar ratio) confirmed by UV-vis spectra and a colour change of the solution. .... - 142 -
- Figure 7.1. ATR-FTIR spectra of two series of membranes with different degrees of quaternization modified by MeI: (a) the series of the membranes with bigger pore size. (b) the series of the membranes with smaller pore size. The relative intensities were normalized using the characteristic CH<sub>2</sub> stretching vibrations (\*) of the unreactive backbone around 2924 cm<sup>-1</sup>..... - 152 -
- Figure 7.2. SEM images of the top surfaces of two series of membranes with different degrees of quaternization: (a-d) M0B, M22B, M40B and M76B, (e-h) M0S, M16S, M39S and M69S..... - 152 -
- Figure 7.3. Comparison of relative improvement of YmPh-AP binding calculated relative to wild type YmPh (YmPh WT). (a) the series of membranes with bigger pore size. (b) the series of the membrane with smaller pore size. Note: The fusion proteins of enzyme-AP are prepared and the corresponding characterizations are performed by the group of Prof. Ulrich Schwaneberg. .... - 153 -
- Figure 7.4. SEM images of the top surfaces of the representative membranes with the immobilization of YmPh-AP fusion constructs: (a) M0B\_TA2-YmPh, (b) M40B\_TA2-YmPh, (c) M0B\_Cec-YmPh, (d) M40B\_Cec-YmPh, (e) M0S\_TA2-YmPh, (f) M39S\_TA2-YmPh, (g) M0S\_Cec-YmPh, (h) M39S\_Cec-YmPh. .... - 155 -
- Figure 10.1. (a) Synthesis of PS-*b*-P*t*BMA diblock copolymer by living anionic polymerization. (b) <sup>1</sup>HNMR spectrum of the prepared PS-*b*-P*t*BMA. .... - 176 -
- Figure 10.2. <sup>1</sup>HNMR spectrum of macroinitiator P*t*BMA prepared by ATRP. .... - 179 -
- Figure 10.3. SEM images of representative membranes cast from (a) PS<sub>85</sub>-*b*-P*t*BMA<sub>15</sub><sup>100</sup> with 39 wt%, THF/DMF 1/1, the evaporation time is 5 s. (b)

- PS<sub>80</sub>-*b*-PtBMA<sub>20</sub><sup>154</sup> with 33 wt%, THF/DMF 1/1, the evaporation time is 3 s. (c) PS<sub>80</sub>-*b*-PtBMA<sub>20</sub><sup>154</sup> with 33 wt%, THF/DMF 1/1 with 0.05 wt% CuCl<sub>2</sub> as the casting solution, the evaporation time is 5 s. .... - 180 -
- Figure 10.4. (a) Acid-catalyzed hydrolysis of PS-*b*-PtBMA membrane to PS-*b*-PMAA membrane. (b) FTIR spectra of the pristine membrane and modified membranes using different hydrolysis conditions. The relative intensities were normalized using the characteristic CH<sub>2</sub> stretching vibrations (\*) of the unreactive backbone around 2924 cm<sup>-1</sup>. All the reactions were performed for 7 days. .... - 181 -
- Figure 10.5. SEM images of the membranes: Exemplary PS<sub>85</sub>-*b*-PtBMA<sub>15</sub><sup>100k</sup> membrane (a) before and (b) after hydrolysis. Exemplary PS<sub>80</sub>-*b*-PtBMA<sub>20</sub><sup>150k</sup> membrane (c) before and (d) after hydrolysis. .... - 183 -
- Figure 10.6. Scheme of synthesis route of the triblock terpolymer PDMAi-*b*-PS-*b*-PtBMA by living anionic polymerization. .... - 183 -
- Figure 10.7. (a) Schematic representation of the desired membrane derived from PDMAi<sub>17</sub>-*b*-PS<sub>57</sub>-*b*-PtBMA<sub>26</sub><sup>40</sup>. (b) SEM images of a representative membrane cast from PDMAi<sub>17</sub>-*b*-PS<sub>57</sub>-*b*-PtBMA<sub>26</sub><sup>40k</sup> with 26 wt% polymer in THF/DMF 1/1, the evaporation time is 5 s. .... - 184 -
- Figure 10.8. (a) Post-functionalization of PDMAi-*b*-PS-*b*-PtBMA by trimethyloxonium tetrafluoroborate ((CH<sub>3</sub>)<sub>3</sub>O(BF<sub>4</sub>)). (b) FTIR spectra of the pristine polymer and the modified polymers in the homogeneous or heterogeneous conditions. The relative intensities were normalized using the characteristic CH<sub>2</sub> stretches (\*) of the unreactive backbone around 2926 cm<sup>-1</sup>. .... - 185 -
- Figure 10.9. ATR-FTIR spectra: (a) the membranes quaternized with MeI as a function of time, (b) the membranes quaternized with EtI as a function of time, (c) the membranes quaternized with 1-PrI as a function of time. The relative intensities were normalized using the characteristic CH<sub>2</sub> stretching vibrations (\*) of the unreactive backbone around 2924 cm<sup>-1</sup>. .... - 187 -
- Figure 10.10. Back scattered electron (BSE) images of the top surface of membrane: (a) I0, (b) M52, (c) E52, (d) P52. .... - 188 -
- Figure 10.11. Water flux (average values of 22~24 h measurement) of the membranes having the series of different degrees of quaternization with MeI and 1-PrI, respectively. .... - 188 -
- Figure 10.12. (a, b) The photography of the permeate solutions of the membranes having the series of different degrees of quaternization with MeI and 1-PrI, respectively, and the corresponding prepared membranes after MB rejection measurements with feed solution of 10 mg L<sup>-1</sup>. (c, d) UV-vis absorbance of the corresponding permeate solutions. .... - 190 -

- Figure 10.13. AFM height maps of the thin films of the polymers prepared by spin-coating procedure from  $\text{CHCl}_3$  solutions: (a) P1, (b) P2, (c) P3 and (d) P4. .... - 190 -
- Figure 10.14. AFM maps of the thin films of PS-*b*-PI prepared by spin-coating procedure from  $\text{CHCl}_3$  solutions: (a) height, (b) phase. .... - 191 -
- Figure 10.15. AFM height and phase maps with lower magnification (scale 1  $\mu\text{m}$ ) of the thin films of the polymers prepared by spin-coating procedure from  $\text{CHCl}_3$  solutions: (a, f) PS-*b*-PI, (b, g) P1, (c, h) P2, (d, i) P3 and (e, j) P4. .... - 191 -
- Figure 10.16. Comparison of membrane morphology determined by SEM of (a-c) the pristine membrane I0 and (d-f) the sulfonated membrane SM. Both were cast from 18 wt% solution with 8 wt%  $\text{TiO}_2$  in THF/DMF/DOX 2/1/1, the evaporation time  $t = 15$  s. .... - 192 -
- Figure 10.17. Molar mass distribution obtained by GPC for the precursor PI, the precursor PI-*b*-PS in THF, and triblock terpolymers P1, P2, P3 in DMAC/LiCl. .... - 193 -
- Figure 10.18. TEM images of PI-*b*-PS-*b*-P4VP films double stained with  $\text{I}_2$  and  $\text{OsO}_4$ . Films were cast from polymer solution in  $\text{CHCl}_3/\text{DMF}$  (95/5 v/v). All the images demonstrate the cylinder-sphere three-phase morphology of P4VP cylinder and PI sphere in the PS matrix. .... - 194 -
- Figure 10.19. TEM images of PI-*b*-PS-*b*-P4VP films: (a) stained with  $\text{I}_2$  (only selective for P4VP (dark domain)), (b) stained with  $\text{OsO}_4$  (strong selective for PI (dark domain) and weak selective P4VP (gray domain)). Films were cast from polymer solutions in  $\text{CHCl}_3/\text{DMF}$  (95/5 v/v). All the images also demonstrate the cylinder-sphere three-phase morphology of P4VP cylinder and PI sphere in the PS matrix. .... - 195 -
- Figure 10.20. TEM images of (a, e) PI-*b*-PS-*b*-P4VP, (b, f) P1, (c, g) P2, (d, h) P3 films stained with  $\text{OsO}_4$ , which is selective for both P4VP and P(HTMB-*r*-I). Films were cast from polymer solutions in  $\text{CHCl}_3/\text{methanol}$  (95/5 v/v) and  $\text{CHCl}_3/\text{DMF}$  (95/5 v/v), respectively. .... - 196 -
- Figure 10.21. TEM images of films cast from PI-*b*-PS-*b*-P4VP and P3 solutions in pure  $\text{CHCl}_3$ : (a) PI-*b*-PS-*b*-P4VP film stained with  $\text{OsO}_4$  (strong selective for PI (dark domain) and weak selective P4VP (gray domain)), (b) PI-*b*-PS-*b*-P4VP film stained with  $\text{I}_2$  (only selective for P4VP (dark domain)), (c) P3 film stained with  $\text{OsO}_4$  (strong selective for PI (dark domain) and weak selective P4VP (gray domain)), (d) P3 film stained with  $\text{I}_2$  (only selective for P4VP (dark domain)). .... - 196 -
- Figure 10.22. (a) Comparison of the fluorescence intensity of the product 4-MU from enzymatic reaction with different immobilized YmPh-AP fusion constructs on the dense films of homo-PS and homo-QP4VP with 14 h MeI quaternization. (b) Relative improvement of YmPh-AP binding calculated relative to the wild type YmPh (YmPh WT). .... - 201 -

Figure 10.23. SEM images of the cross sections of two series of membranes with different degree of quaternization: (a-d) M0B, M22B, M40B and M76B, (e-h) M0S, M16S, M39S and M69S. .... - 202 -

Figure 10.24. Comparison of the fluorescence intensity of the product 4-MU from enzymatic reaction with different immobilized YmPh-AP fusion constructs on two series of PS-*b*-P4VP derived membranes: (a) bigger pore size, (b) smaller pore size..... - 203 -

Figure 10.25. SEM images of the top surfaces of the representative membranes with the immobilized YmPh-AP fusion proteins: (a) M0B\_TA2-YmPh, (b) M40B\_TA2-YmPh, (c) M0B\_Cec-YmPh, (d) M40B\_Cec-YmPh, (e) M0S\_TA2-YmPh, (f) M39S\_TA2-YmPh, (g) M0S\_Cec-YmPh, (h) M39S\_Cec-YmPh. .... - 204 -

Figure 10.26. Stability of the immobilized TA2-YmPh and Cec-YmPh on the representative membranes was roughly evaluated by comparison of the conversion of substrates 4-MUP before and after storage at 4 °C or 25 °C for 3 days, respectively: (a) M0B, (b) M40B, (c) M0S and (d) M39S. .... - 205 -

## List of Tables

Table 4.1 Preparation of a series of the membranes quaternized with MeI and 1-PrI.....	- 68 -
Table 5.1. Molecular characterization of the parent PS- <i>b</i> -PI diblock copolymer and thiol-ene click reaction modified diblock terpolymers PS- <i>b</i> -P(HTMB- <i>r</i> -I). .....	- 82 -
Table 6.1. Molecular characterization of the triblock terpolymer PI- <i>b</i> -PS- <i>b</i> -P4VP and hydroxylated triblock quaterpolymers P(HTMB- <i>r</i> -I)- <i>b</i> -PS- <i>b</i> -P4VP with different degrees of hydroxylation (DH). ....	- 118 -
Table 6.2 Retention ( <i>R</i> ) and separation selectivity ( $\psi$ ) for the pristine membrane I0 and the positively charged membrane MM in single- and mixed-solute retention experiments. ....	- 139 -
Table 6.3. Adsorption of five model organic molecules MB <sup>+</sup> , RB0, OR <sup>-</sup> , NG3 <sup>-</sup> and RG6 <sup>-</sup> onto the pristine membrane I0, the positively charged membrane MM and the negatively charged membrane PM. ....	- 140 -
Table 6.4. pH of aqueous solutions with 0.1 mM single or mixed organic small molecules. ....	- 140 -
Table 6.5 Retention ( <i>R</i> ) and separation selectivity ( $\psi$ ) for the pristine membrane I0 and the negatively charged membrane PM in single- and mixed-solute retention experiments. ....	- 144 -
Table 7.1. Molecular characterization of the polymers used for the sample preparation .....	- 150 -
Table 10.1. Molecular characterization of the polymers used for the sample preparation (Synthesis was performed by Brigitte Lademann) .....	- 177 -
Table 10.2. Molecular characteristics of the macroinitiator PtBMA prepared using different initiator and catalyst systems.....	- 179 -
Table 10.3. Comparison of the calculated lateral dimensions of five model organic molecules using MM2 force field energy minimization model and the reported Stokes diameters. ....	- 189 -
Table 10.4. Performance comparison of the pristine membrane I0 and the sulfonated membrane SM, including water permeance, retention and adsorption of OR <sup>-</sup> and RG6 <sup>-</sup> . ....	- 192 -
Table 10.5. The concentrations of feed ( $C_f$ ), permeate ( $C_p$ ), retentate ( $C_r$ ) and the calculated retention ( $R_0$ ) employed in single-solute retention measurements.....	- 197 -
Table 10.6. The concentrations of feed ( $C_f$ ), permeate ( $C_p$ ), retentate ( $C_r$ ) and the calculated retention ( $R_0$ ) employed in mixed-solute retention measurements.....	- 198 -

## List of Tables

---

---

Table 10.7. Performance comparison among various membranes for charge- and charge/size-based separation of small molecules..... - 199 -

Table 10.8. List of chemicals with GHS symbol, H- and P-data..... - 205 -

---

---

## List of Schemes

Scheme 3.1. Synthesis route of PS- <i>b</i> -P4VP diblock copolymers by living anionic polymerization. ....	- 39 -
Scheme 3.2. Synthesis route of PS- <i>b</i> -P(HTMB- <i>r</i> -I) diblock terpolymer by living anionic polymerization and subsequent thiol-ene click chemistry. ....	- 40 -
Scheme 3.3. Synthesis route of PI- <i>b</i> -PS- <i>b</i> -P4VP triblock terpolymers by living anionic polymerization and thiol-ene click chemistry of PI- <i>b</i> -PS- <i>b</i> -P4VP to obtain P(HTMB- <i>r</i> -I)- <i>b</i> -PS- <i>b</i> -P4VP triblock quaterpolymer.....	- 42 -
Scheme 10.1. Synthesis route of PtBMA- <i>b</i> -PS- <i>b</i> -P4VP triblock terpolymers by ATRP. ....	- 177 -
Scheme 10.2. Schematic illustration of the phytase hydrolytic reaction using 4-methylumbelliferyl phosphate (4-MUP) as the substrate. The product methylumbelliferone (4-MU) are fluorescent which can be measured with excitation at 360 nm and emission at 465 nm. ....	- 200 -



## List of Symbols

$\Delta G_{mix}$	Gibbs free energy of mixing
$\Delta H_{mix}$	Enthalpy of mixing
$\Delta S_{mix}$	Entropy of mixing
$T$	Absolute temperature
$N_i$	Degree of polymerization of the component i
$\varphi_i$	Volume fraction of the component i
$R$	Universal gas constant
$N$	Overall degree of polymerization
$\chi_{i,j}$	Flory-Huggins-Staverman segmental interaction parameter of the component i and j.
$z$	Number of nearest neighbours per repeat unit in the polymer
$k_B$	Boltzman constant
$\varepsilon_{i,j}$	Interaction energies per repeat unit of i and j.
$D$	Microdomain period
$a$	Statistic segment length
$n_i$	Number of moles of component i
$\Delta\mu_i$	Chemical potential of the components i
$J_v$	Volumetric water flux
$A$	Water permeability of coefficient
$\Delta P$	Applied hydraulic transmembrane pressure
$\Delta\pi_m$	Osmotic pressure difference across the active layer
$v$	Volume flow
$A_m$	Membrane area
$t$	Time
$J$	Solvent flux
$\eta$	Solution viscosity
$r$	Pore radius
$\varepsilon$	Surface porosity
$\Delta x$	Thickness of the membrane active layer
$\tau$	Pore tortuosity
$\zeta$	Volume fraction of pores
$S$	Internal surface area of pores
$K$	Kozeny-Carman constant
$R_a$	Actual rejection of solute
$a$	Radius of a solute
$R_0$	Observed rejection
$c_p$	Concentration of the permeate solution
$c_f$	Concentration of the feed solution
$c_r$	Concentration of the retentate solutions
$J_i$	Flux of solute i
$c_i$	Concentration of the solute i
$z_i$	Valence of the solute i
$F$	Faraday constant
$\phi$	Membrane potential
$D_{i,p}$	Diffusion coefficient of the solute i inside the confined pores

## List of Symbols

---

$D_{i,\infty}$	Diffusion coefficient of the solute $i$ in water at infinite dilution
$K_{i,c}$	hindrance factors to account for the convection of the solutes in the confined pores
$\zeta$	Zeta potential
$U_{str}$	Streaming potential
$\varepsilon$	Permittivity of the electrolyte solution
$\varepsilon_0$	Vacuum permittivity
$l$	Length of the streaming channel
$A_c$	Cross-section of the streaming channel
$R_e$	Electrical resistance inside the streaming channel
$J_w$	Normalized water permeanc
$\psi$	Membrane selectivity
$m$	Mass of the solute
$J_p$	Permeate permeance
$N_p$	Number of surface pores per unit area
$d$	Effective pore diameter
$L$	Length of the cylindrical pores

---



---

## List of Abbreviations

(CH <sub>3</sub> ) <sub>3</sub> O(BF <sub>4</sub> )	Trimethyloxonium tetrafluoroborate
1-PrI	1-Propyl iodide
4VP	4-Vinyl pyridine
AFM	Atomic force microscopy
Al <sub>2</sub> O <sub>3</sub>	Aluminum oxide
ALD	Atomic layer deposition
AP	Anchor peptide
ATRP	Atom transfer radical polymerization
BCPs	Block copolymers
BCC	Body-centered cubic
C	Cylinders
CaH <sub>2</sub>	Calcium hydride
Cec	Cecropin A
CHCl <sub>3</sub>	Chloroform
CVD	Chemical vapor deposition
DH	Degrees of hydroxylation
DMAc	Dimethylacetamide
DMF	<i>N,N</i> -dimethylformamide
DMPA	2,2-Dimethoxy-2-phenyl acetophenone
DOX	1,4-Dioxane
DSC	Differential scanning calorimetry
DSPM	Donnan steric pore model
DSPM&DE	Donnan steric pore model & dielectric exclusion
EDX	Energy disperse X-rays
EIPS	Evaporation induced phase separation
EtI	Ethyl iodide
<i>FDR<sub>ir</sub></i>	Irreversible flux decline ratio
<i>FDR<sub>r</sub></i>	Reversible flux decline ratio
<i>FDR<sub>t</sub></i>	Flux decline ratio
FO	Forward osmosis
<i>FRR</i>	Flux recovery ratio
FTIR	Fourier transform infrared spectroscopy
G	Gyroid
GPC	Gel permeation chromatography
ISR	Intermediate segregation regime
L	Lamellae
LCI	Liquid chromatography peak I
MB+	Methylene blue
MBrP	Methyl-2-bromopropionate
MeI	Methyl iodide
MeOH	Methanol
MF	Microfiltration
MgAc <sub>2</sub>	Magnesium acetate
MgBu <sub>2</sub>	Di- <i>n</i> -butyl magnesium
<i>n</i> -BuLi	<i>n</i> -Butyl lithium
NF	Nanofiltration
NG	Nucleation and growth

NG3-	Naphthol green B
NIPS	Nonsolvent induced phase separation
NMP	Nitroxide-mediated radical polymerization
ODT	Order-disorder transition
OR-	Orange II
P(HTMB- <i>r</i> -I)	Poly(4-(2-hydroxyethyl-thio)-2-methyl butene- <i>random</i> -4-(2-hydroxyethyl-thio)-3-methyl butene- <i>random</i> -isoprene)
P(HTMB- <i>r</i> -I)- <i>b</i> -PS- <i>b</i> -P4VP	Poly(4-(2-hydroxyethyl-thio)-2-methyl butene- <i>random</i> -4-(2-hydroxyethyl-thio)-3-methyl butene- <i>random</i> -isoprene)- <i>block</i> -polystyrene- <i>block</i> -poly(4-vinylpyridine)
P2VP	Poly(2-vinylpyridine)
PCTE	Polycarbonate track-etched
PDMAi- <i>b</i> -PS- <i>b</i> -PtBMA	Poly[5-( <i>N,N</i> -dimethylamino)isoprene]- <i>block</i> -polystyrene- <i>block</i> -poly( <i>tert</i> -butyl methacrylate)
PEG400	Poly(ethylene glycol) with molecular weight 400 g mol <sup>-1</sup>
PHEMA	Poly(2-hydroxylethyl methacrylate)
PIB-PEG-PIB	Polyisobutylene-polyethylene glycol-polyisobutylene
PI- <i>b</i> -PS- <i>b</i> -P4VP	Polyisoprene- <i>block</i> -polystyrene- <i>block</i> -poly(4-vinylpyridine)
PI- <i>b</i> -PS- <i>b</i> -PAA	Polyisoprene- <i>block</i> -polystyrene- <i>block</i> -poly(acrylic acid)
PI- <i>b</i> -PS- <i>b</i> -PDMA	Polyisoprene- <i>block</i> -polystyrene- <i>block</i> -poly( <i>N,N</i> -dimethylacrylamide)
PMDETA	<i>N,N,N',N'',N'''</i> -pentamethyldiethylenetriamine
PS	Polystyrene
PS- <i>b</i> -P(HTMB- <i>r</i> -I)	Polystyrene- <i>block</i> -poly(4-(2-hydroxyethyl-thio)-2-methyl butene- <i>random</i> -4-(2-hydroxyethyl-thio)-3-methyl butene- <i>random</i> -isoprene)
PS- <i>b</i> -P2VP- <i>b</i> -PEO	Polystyrene- <i>block</i> -poly(2-vinylpyridine)- <i>block</i> -poly(ethylene oxide)
PS- <i>b</i> -P4VP	Polystyrene- <i>block</i> -poly(4-vinylpyridine)
PS- <i>b</i> -P4VP- <i>b</i> -PPS	Poly(styrene)- <i>block</i> -poly(4-vinylpyridine)- <i>block</i> -poly(propylene sulfide)
PS- <i>b</i> -P4VP- <i>b</i> -PSMA	Polystyrene- <i>block</i> -poly(4-vinylpyridine)- <i>block</i> -poly(solketal methacrylate)
PS- <i>b</i> -PHEMA	Polystyrene- <i>block</i> -poly(2-hydroxylethyl methacrylate)
PS- <i>b</i> -PtBMA	Polystyrene- <i>block</i> -poly( <i>tert</i> -butyl methacrylate)
PtBMA- <i>b</i> -PS- <i>b</i> -P4VP	Poly( <i>tert</i> -butyl methacrylate)- <i>block</i> -polystyrene- <i>block</i> -poly(4-vinylpyridine)
<i>p</i> TsCl	<i>p</i> -Toluene sulfonyl chloride
RAFT	Reversible addition-fragmentation chain transfer
RB0	Riboflavin
RG6-	Reactive green 19
RO	Reverse osmosis
S	Spheres
SANS	Small-angle neutron scattering
SAXS	Small-angle X-ray scattering
<i>s</i> -BuLi	<i>sec</i> -Butyl lithium
SC	Simple cubic
SCFT	Self-consistent field theory
S <sub>cp</sub>	Close packed spheres
SD	Spinodal decomposition

---

---

SEDE	Steric Electric and Dielectric
SEM	Scanning electron microscopy
SNIPS	The evaporation induced self-assembly together with the non-solvent induced phase separation
SSL	Strong segregation limit
TA2	Tachystatin A2
<i>t</i> BMA	<i>Tert</i> -butyl methacrylate
TEM	Transmission electron microscopy
TGA	Thermogravimetric analysis
TiO <sub>2</sub> NPs	Titanium dioxide sol nanoparticles
TIPS	Thermally induced phase separation
TMCS	Trimethylchlorosilane
TTIP	Titanium tetraisopropoxide
UF	Ultrafiltration
VIPS	Vapor induced phase separation
WSL	Weak segregation limit
YmPh	<i>Yersinia mollaretii</i> phytase



# **Chapter 1    Introduction**

## 1.1 Objective

Two of the greatest challenges afflicting people throughout the world are to provide sustainable supplies of clean water and energy. The lack of clean water is a well-known problem in several regions of the world. According to a 2017 World Health Organization (WHO) report, 2.2 billion people lack access to safe and reliable drinking water; millions of people are suffering from diseases linked to contaminated water, inadequate sanitation and hygiene. Each year approximately 829000 people die from diarrhoea, including around 300000 children aged under five. Yet waterborne diseases are largely preventable by the improvement of drinking water, sanitation and hygiene. Water scarcity is expected to grow worse in the coming decades with the growth of population, climate changes, demographic changes, industrialization and urbanization. By 2025, half of the world's population will be living in water scarce areas.<sup>1</sup> Therefore, effective, lowcost and robust technologies to decontaminate water are of utmost importance.<sup>2</sup> Membrane technology represents an advanced and sustainable solution, due to its energy efficiency, low carbon foot print, environmental friendliness, compared to other separation technologies, e.g. thermal separations.

The overarching goal of water treatment is to effectively remove the undesirable contaminants and to make it suitable for a variety of applications, e.g., drinking and domestic uses, irrigation, chemical, medical, petroleum, food processing and textile industries, or discharging the water into the environment.<sup>3</sup> A wide range of contaminants is involved in the water purification. For example, macroscopic waterborne pathogens are linked to the transmission of diseases with a devastating effect on public health, e.g., parasites, bacteria, protozoa, fungi, viruses and prions.<sup>2</sup>

<sup>3</sup> Organic micropollutants (e.g., pharmaceuticals, hormones, personal-care products, pesticides, textile dyes, disinfection by-products) are closely associated with potentially negative effects on aquatic ecosystems and human health, including bacterial resistance, the feminization of

fish, endocrine effects.<sup>4-8</sup> Sub-nanometer toxic ions also present acute health risks, such as lead, arsenic, mercury, copper, manganese, nitrites, phosphates, and so on.<sup>9</sup> Besides the water treatment, membranes also play a significant role in many other applications.<sup>10, 11</sup> For example, hemodialysis (artificial kidney) for the treatment of chronic kidney failure in biomedicine, is the single largest market for membranes.<sup>11</sup> Separation of valuable biomolecules, pharmaceutical/chemical molecules are holding a huge potential market for membranes, e.g., in the purification and fractionation of proteins,<sup>12</sup> peptides, amino acids,<sup>13, 14</sup> antibiotics,<sup>15</sup> drugs, and nutraceuticals.<sup>16, 17</sup> Porous membranes can act as the support of catalytic membrane reactors where the catalytic reaction and separation can be integrated in one single unit. Due to these applications dealing with different sized molecules from micro- to sub-nanometers, there is a pressing need to further develop membrane technology by material design and improved fabrication processes.

Although the liquid membranes with high selectivity and inorganic membranes (e.g., ceramics, metal/metal oxide) with high tolerance towards harsh operational conditions play a role in membrane technology, polymer-based membranes have been gaining more importance as they are less expensive and easy to scale up. Notably, polymer membranes possess the wide tunability of the membrane structures and properties, which is attributed to chemical flexibility of polymer materials.<sup>18</sup> However, their separation efficiency is still often limited, e.g., in the separation of sub- to few nanometer molecules or similarly sized molecules, due to less ordered pores with random pore size and orientation on the selective layer, and the lack of tunable pore structure and functionalities. It is clear that membranes with uniform pores and a high pore number density can facilitate the efficient separation with high flux and good selectivity.<sup>19</sup> Furthermore, the isoporous membranes combining pore functionality with controllable pore size are underdeveloped and demand further improvement of their performance and extend different potential applications with lower energy consumption, which can be achieved from

the molecular design of polymer materials. The aim of this PhD work is to contribute to the development of the isoporous membranes with tailored pore size and pore functionalities which are promising candidates as next generation membranes.

## 1.2 Isoporous Block Copolymer Membrane with Charged Nanochannels

The available techniques to fabricate isoporous membranes include track-etching,<sup>20, 21</sup> aperture array lithography,<sup>22</sup> phase separation micro-moulding,<sup>23, 24</sup> pillar template technique,<sup>25</sup> etc. Due to the complexity of the manufacturing processes, these fabrication techniques are limited for scalable production at low cost.

Self-assembled block copolymers (BCPs) offer a very strong platform to fabricate the membranes with high pore number density and pore uniformity.<sup>26-31</sup> Such membranes based on BCP self-assembly have been generated through selective removal of the minority blocks<sup>32-34</sup> or blend partners<sup>35, 36</sup> from bulky BCP thin films with multiple treatment steps. A fascinating straightforward one-step scalable approach to translate the periodically ordered nanostructure of BCPs into high-performance membranes employs the evaporation induced self-assembly together with the non-solvent induced phase separation (SNIPS), which has been received great attention over the past decade.<sup>19, 37-50</sup> Current research efforts have been mainly focusing on the tunability of pore size and the functionalization of the pore structure in order to address different applications. For example, a few relationships have been found to tailor the pore size of SNIPS membranes. One rather straightforward approach is to vary either the molecular weight or the composition of BCPs.<sup>51, 52</sup> Binary blending of polystyrene-*block*-poly(4-vinylpyridine) (PS-*b*-P4VP) with different molecular weights and compositions has also shown to tailor the pore size according to the different ratio of the blend partners.<sup>53</sup> In order to endow the membrane pores with different chemical properties, it is important to synthesize the well-

designed BCPs with new functional groups within the pore-forming blocks, such as polystyrene-*block*-poly(2-vinylpyridine)-*block*-poly(ethylene oxide) (PS-*b*-P2VP-*b*-PEO),<sup>40</sup> polystyrene-*block*-poly(4-vinylpyridine)-*block*-poly(solketal methacrylate) (PS-*b*-P4VP-*b*-PSMA),<sup>50</sup> polyisoprene-*block*-polystyrene-*block*-poly(*N,N*-dimethylacrylamide) (PI-*b*-PS-*b*-PDMA),<sup>42</sup> poly(styrene)-*block*-poly(4-vinylpyridine)-*block*-poly(propylene sulfide) (PS-*b*-P4VP-*b*-PPS).<sup>43</sup> Another strategy is to begin with a given porous membrane and alter its pore properties or pore size by post-treatments, which do not destroy the basic membrane structure, e.g., electroless gold deposition<sup>54</sup> and atomic layer deposition (ALD)<sup>19</sup>. Post-treatment of a PS-*b*-P4VP SNIPS membrane with dopamine and poly(*N*-isopropyl acrylamide) led to a temperature and pH-responsive membrane.<sup>55</sup> Based on a dopamine functionalization also atom transfer radical polymerization (ATRP) of poly(2-hydroxyethyl methacrylate) (PHEMA) was carried out on a PS-*b*-P4VP SNIPS membrane.<sup>56</sup> Physical and chemical routes of post-treatment were also introduced to reduce the pore size of a polystyrene-*block*-poly(2-hydroxyethyl methacrylate) (PS-*b*-PHEMA) SNIPS membrane by thermal treatment or reaction of the hydroxyl groups with an alkyl isocyanate, respectively.<sup>39</sup>

A recent promising trend is to reduce the pore size by taking advantage of the swelling of the charged pore-forming block at the hydrated state that are confined within the mesopores of a SNIPS membrane. As P4VP and poly(2-vinylpyridine) (P2VP) are pH responsive, the nitrogen moieties are protonated at low pH which leads to stretching of the P4VP and P2VP block in corresponding BCPs.<sup>43, 44, 55, 57</sup> Gu *et al.* demonstrated that the pore size of a polyisoprene-*block*-polystyrene-*block*-poly(4-vinylpyridine) (PI-*b*-PS-*b*-P4VP) membrane can be reduced to 5 nm using an additive driven pore expansion together with chain stretching of the P4VP block at pH 3.6.<sup>58</sup> Similarly, Mulvenna *et al.* reported the pore size of a polyisoprene-*block*-polystyrene-*block*-poly(acrylic acid) (PI-*b*-PS-*b*-PAA) membrane can be reduced to 3.4 nm at pH 5.5.<sup>42</sup> Later, Zhang *et al.* attached sulfonic acid moieties to the pore wall of a PI-*b*-PS-*b*-

PAA membrane using carbodiimide coupling. The resulting membrane exhibited a smaller effective pore diameter and lower degree of ionic strength response compared to the PI-*b*-PS-*b*-PAA counterpart.<sup>59</sup> Overall, this intriguing approach can not only tune the pore size but also introduce the charge function for transport nanochannels. It is highly desirable to fabricate the isoporous BCP membranes with controlled pore size and charged pores.

### 1.3 Strategy of the Research and Outline of the Thesis

The prerequisite of fabrication of the isoporous BCP membrane with charged nanochannels and tunable pore size via SNIPS and subsequent post-functionalization is the synthesis of the asymmetric BCPs having high-segregation strength and reactive functional groups. The functional groups should be in the pore-forming blocks (i.e. minor blocks), which provide the capability for further post-functionalization to integrate the charged moiety within the nanochannels. Therefore, the synthesis of BCPs having the desired composition and molecular weight is the first issue to be addressed. The next challenge is to experimentally optimize the casting parameters, e.g., polymer concentration of the casting solution, composition of binary or ternary solvent mixture, solvent evaporation time, content of the additives (if required) in the casting solution, etc. to obtain the desired integral asymmetric isoporous membrane.<sup>19</sup> Another issue is to post-functionalize the pore structure of the prepared SNIPS membranes without damaging the already formed porous structure. Therefore, it is crucial to perform the post-functionalization effectively under mild heterogeneous conditions, for instance, by using a non-solvent of the membrane as the reaction medium or a vapour-phase reaction without any solvent. This requirement also limits the selection of functional groups of the well-designed BCPs.

The membranes with charged nanochannels can be categorized as positively charged membranes, negatively charged membranes, zwitterionic membranes, and charge-mosaic membranes with discrete oppositely charged nanochannels. The aim of this work is assigned to achieve different charged isoporous membranes for different applications. Taking into account the above mentioned concerns, three triblock copolymers were initially designed to prepare the charge-mosaic membranes (Figure 1.1), i.e., poly[5-(*N,N*-dimethylamino)isoprene]-*block*-polystyrene-*block*-poly(*tert*-butyl methacrylate) (PDMAi-*b*-PS-*b*-P*t*BMA), poly(*tert*-butyl methacrylate)-*block*-polystyrene-*block*-poly(4-vinylpyridine) (P*t*BMA-*b*-PS-*b*-P4VP), poly(4-(2-hydroxyethyl-thio)-2-methyl butene-*random*-4-(2-hydroxyethyl-thio)-3-methyl butene-*random*-isoprene)-*block*-polystyrene-*block*-poly(4-vinylpyridine) (P(HTMB-*r*-I)-*b*-PS-*b*-P4VP). They contain the predetermined functional groups in minor blocks, respectively, i.e., tertiary amine groups, *tert*-butyl ester groups, pyridine groups, and hydroxyl groups (-OH), which are highly reactive and accessible to charged groups. Due to the morphological diversity of the triblock copolymers and delicacy of the casting parameters and the subsequent post-functionalization reactions, three diblock copolymers were thoroughly investigated in order to gain the initial knowledge and experience to choose one triblock copolymer for membrane fabrication. These are polystyrene-*block*-poly(*tert*-butyl methacrylate) (PS-*b*-P*t*BMA), PS-*b*-P4VP, polystyrene-*block*-poly(4-(2-hydroxyethyl-thio)-2-methyl butene-*random*-4-(2-hydroxyethyl-thio)-3-methyl butene-*random*-isoprene) (PS-*b*-P(HTMB-*r*-I)) (Figure 1.2).

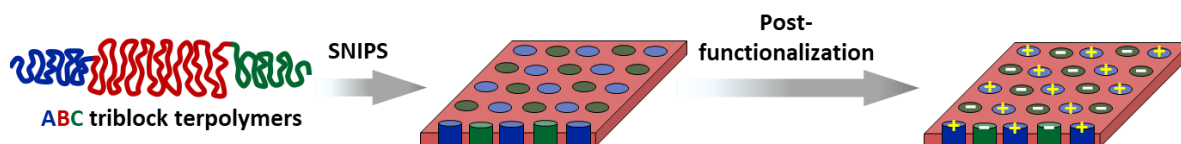


Figure 1.1. The schematic representation of the approach to achieve the charge-mosaic isoporous membrane derived from triblock copolymers.

Initial exploratory investigations (around 1.5 years) were performed on triblock terpolymers *PtBMA-b-PS-b-P4VP* (synthesized by Atom Transfer Radical Polymerization, ATRP) and *PDMAi-b-PS-b-PtBMA* (synthesized by Dr. Ruth Bieringer using living anionic polymerization), and diblock copolymer *PS-b-PtBMA* (prepared by Brigitte Lademann using living anionic polymerization), as *PtBMA-b-PS-b-P4VP* and *PDMAi-b-PS-b-PtBMA* both can microphase separate into three-phase morphologies.<sup>60, 61</sup> The functional groups (i.e. *tert*-butyl ester groups and tertiary amine groups) were transformed into the desired distinct charged moieties by proposed post-functionalization methods successfully. However, the difficulties associated with the synthesis of *PtBMA-b-PS-b-P4VP* by ATRP and the preparation of the desired SNIPS membrane from the small amounts of available *PDMAi-b-PS-b-PtBMA* and *PS-b-PtBMA* was not overcome (the detailed information is supplied in Chapter 10 Appendix). Therefore, the goal of this PhD work was to fabricate integral asymmetric isoporous membranes having positively charged, negatively charged and charge mosaic (having distinctly separate positively and negatively charged pores) moieties using *PS-b-P4VP*, *PS-b-P(HTMB-*r*-I)* and *P(HTMB-*r*-I)-b-PS-b-P4VP*, respectively. However, regarding the triblock quaterpolymer *P(HTMB-*r*-I)-b-PS-b-P4VP*, the two end blocks *P(HTMB-*r*-I)* and *P4VP* formed one mixed domain instead of discrete domains in the PS matrix during membrane fabrication via SNIPS. Therefore, eventually the triblock quaterpolymer *P(HTMB-*r*-I)-b-PS-b-P4VP* was used to prepare an isoporous membrane with two distinct functional groups on the interior of the same pore walls (called as the multifunctional isoporous membrane).

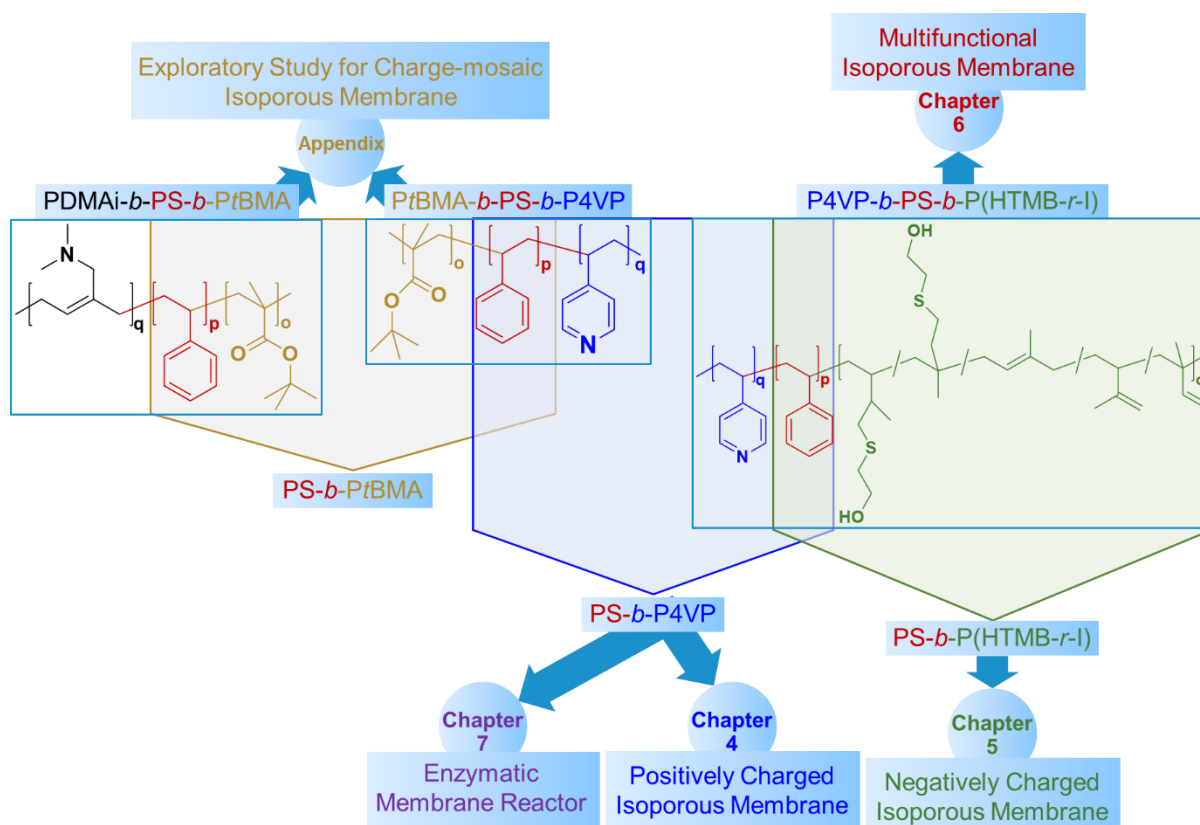


Figure 1.2. Schematic outline of the thesis.

The thesis is organized as follows:

-In **Chapter 2**, a theoretical background is presented in short on microphase separation of block copolymers, membrane and membrane preparation, integral asymmetric isoporous BCP membranes, and membrane separation processes.

-In **Chapter 3**, the materials used in this work are given. The experimental procedures are summarized including synthesis of block copolymers, membrane preparation, post-functionalization of membranes, and specification of the equipment for various characterization.

-**Chapter 4** reports a PS-*b*-P4VP isoporous membrane with tunable positively charged nanochannels. This chapter highlights that the nanochannels can be tailored by using different

reaction agents. The effective pore sizes of the resulting membrane in a hydrated state are gradually tuned in a wide range from ultrafiltration toward nanofiltration.

-**Chapter 5** presents a high-performance isoporous nanocomposite membrane with negatively charged amphiphilic nanochannels, which is prepared from a tailor-made PS-*b*-P(HTMB-*r*-I) diblock terpolymer. The prepared negatively charged membrane displays the potential to separate small molecules with high permeance and excellent antifouling properties.

-It is intriguing to decorate the pore-forming block with different functional groups which can endow more possibilities to functionalize the pore structure, **Chapter 6** reports a novel multifunctional asymmetric isoporous membrane with different functional groups embedded on the interior of the pore wall, which is derived from a well-designed P(HTMB-*r*-I)-*b*-PS-*b*-P4VP triblock quaterpolymers with two miscible functionalized end blocks. We readily post-functionalized the membrane to decorate nanochannels with positively or negatively charged moieties, respectively. The selective transport properties are elaborated in different systems.

-**Chapter 7** portrays some preliminary results obtained on the development way towards an enzymatic membrane reactor based on PS-*b*-P4VP.

-**Chapter 8** depicts the summary of the whole thesis.

-**Chapter 9, 10** and **11** are references, appendix and acknowledgement, respectively.

## **Chapter 2    Theoretical Background**

## 2.1 Microphase Separation of Block Copolymers

BCPs are macromolecules, consisting of two or more chemically distinct polymeric blocks via covalent bonding. The BCP properties depend on chemical composition, sequence and topology of the blocks, the strength of incompatibility between different blocks, and the molecular weights of the blocks.<sup>62</sup> Various synthetic strategies have been built up to prepare a remarkable range of well-defined BCPs with a high degree of molecular, compositional and structural homogeneity, such as living anionic polymerization, nitroxide-mediated radical polymerization (NMP), atom transfer radical polymerization (ATRP), reversible addition-fragmentation chain transfer (RAFT) polymerization, etc.<sup>63</sup> BCPs with different molecular architectures and functionalities have myriad of applications ranging from, for example, thermoplastic elastomers to nanolithography and nanofabrication, controlled delivery of drugs and diagnostic agents, and fuel cell.<sup>64-66</sup> A rich variety of well-defined self-assembled structures of BCPs are the basis for their applications.

To determine the miscibility of a multicomponent system, e.g., two components of homopolymers A and B, the thermodynamic enthalpic and entropic energy contributions must be taken into account, as shown in Equation 2.1. When the Gibbs free energy of mixing  $\Delta G_{mix}$  is negative, two components A and B are miscible.

$$\Delta G_{mix} = \Delta H_{mix} - T\Delta S_{mix} \quad 2.1$$

where  $\Delta H_{mix}$  is the enthalpy of mixing,  $\Delta S_{mix}$  is the entropy of mixing, and  $T$  is the absolute temperature.

Based on the Flory-Huggins-Staverman Theory under assumption of random mixing of polymer chains (e.g., A and B),  $\Delta S_{mix}$  and  $\Delta H_{mix}$  can be expressed as Equation 2.2 and 2.3, respectively.<sup>67, 68</sup>

$$\Delta S_{mix} = -R \left[ \frac{\varphi_A}{N_A} \ln \varphi_A + \frac{\varphi_B}{N_B} \ln \varphi_B \right] \quad 2.2$$

$$\Delta H_{mix} = RT \varphi_A \varphi_B \chi_{A,B} \quad 2.3$$

where  $N_i$ ,  $\varphi_i$ , and  $R$  are the degree of polymerization of the component  $i$ , the volume fraction of the component  $i$ , and the universal gas constant, respectively. The Flory-Huggins-Staverman segmental interaction parameter  $\chi_{AB}$  is determined by the selection of the repeating unit pair (A and B), as shown in Equation 2.4:<sup>67</sup>

$$\chi_{AB} = \left( \frac{z}{k_B T} \right) \left[ \varepsilon_{AB} - \frac{1}{2} (\varepsilon_{AA} + \varepsilon_{BB}) \right] \quad 2.4$$

where  $z$  is the number of nearest neighbours per repeat unit in the polymer,  $k_B$  is the Boltzmann constant,  $k_B T$  is the thermal energy, and  $\varepsilon_{AB}$ ,  $\varepsilon_{AA}$  and  $\varepsilon_{BB}$  are the interaction energies per repeat unit of A-B, A-A, and B-B, respectively. For typical BCPs with dissimilar monomer pairs but no strong specific interactions (e.g. hydrogen bonding, ionic charges),  $\chi_{AB}$  is positive and small, and usually changes inversely with temperature.<sup>69, 70</sup>

In a polymer system, the gain of mixing entropy  $\Delta S_{mix}$  is very small due to the large configurational entropy of long macromolecular chains. Therefore, relatively weak repulsive interactions between segments of different chains are sufficient to yield the phase separation. The macroscopic phase separation occurs in the polymer blends (e.g. the mixture of two homopolymers). A BCP can only undergo the microphase separation due to the connectivity of different blocks. Therefore the entropic contribution to the free energy cannot be described by the Flory-Huggins-Staverman theory. In the case of BCPs with sufficiently strong

incompatible segments, the self-assembled structure can be formed with a characteristic lattices size from approximately 10 to 100 nm.<sup>71</sup>

The simplest and most studied BCPs are the linear diblock copolymers having two dissimilar blocks A and B. The thermodynamic equilibrium phase behaviour of BCPs is the result of a “competition” between the interfacial energy and the entropic penalty owing to the chain stretching . It is well recognized that the phase behaviour of AB diblock copolymers is determined by three experimentally controllable factors: the overall degree of polymerization  $N$ , the volume fraction  $\phi$  of the A and B blocks ( $\phi_A$  and  $\phi_B$ ), and the Flory-Huggins-Staverman segmental interaction parameter  $\chi_{AB}$ . The factors  $N$  and  $\phi$  are regulated through polymerization stoichiometry and affect the translational and configurational entropy.

The phase diagram of a conformationally symmetric diblock copolymer with equal statistical segment length has been obtained by Matsen and Bates using the standard Gaussian chain model and self-consistent field theory(SCFT) (Figure 2.1).<sup>72</sup> The degree of segregation between different blocks is determined by the product of  $\chi N$ . When either  $\chi$  or  $N$  is sufficiently decreased, the entropic contribution to the free energy is predominating, and BCPs chains are in a disordered phase with unperturbed random coil conformations. By increasing  $\chi N$  to a critical point, disordered diblock copolymers show order-disorder transition (ODT), leading to a microphase separation between dissimilar blocks. At a fixed  $\chi N$  above the critical point of ODT, order-order transition (OOT) between different microphase structures undergoes by varying  $\phi$  (Figure 2.1).<sup>69</sup>

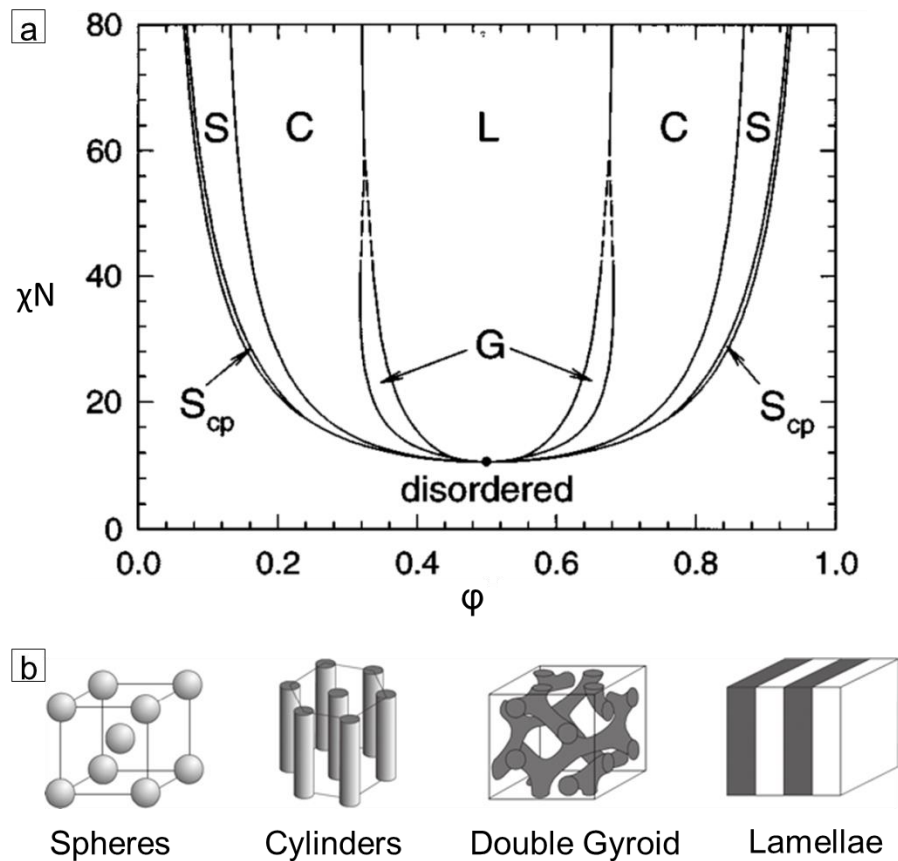


Figure 2.1. (a) Theoretical phase diagram of a linear diblock copolymer composed of components with similar statistic segment lengths and flexibility from SCFT ( $S_{cp}$ : close packed spheres, S: spheres, C: cylinders, L: lamellae, G: gyroid). (b) Equilibrium morphologies of a diblock copolymer. From left to right the volume fraction of the dark-colored component increases: spheres, cylinders, double gyroid, and lamellae. Adapted from the references.<sup>72,73</sup>

According to the degree of segregation  $\chi N$ , the phase behavior of BCPs consists of three distinct regimes: the so-called weak segregation limit (WSL), intermediate segregation regime (ISR) and strong segregation limit (SSL). The WSL approach based on the works of Leibler<sup>74</sup> and Yerukhimovich<sup>75</sup> is used to map out the phase diagram of a diblock copolymer near the ODT. In the WSL regime ( $10 \leq \chi N \leq 15$ ), due to the weak repulsive interaction between different blocks, the connected blocks interdiffuse more with each other, leading to a broad interface between neighbouring microdomains. The local compositional fluctuation changes smoothly

across the domain boundary in a small deviation as a sine function and the macromolecules behave like Gaussian chains. For symmetric diblock copolymers ( $\phi = 1/2$ ), the transition from the disordered to the lamellar phase occurs at the critical point of  $\chi N \cong 10.5$  based on mean-field theory. Due to the Gaussian nature of the block copolymer chains, the microdomain period scales as  $D \sim N^{1/2}$ .<sup>69, 74, 76</sup> With increasing the  $\chi N$ , the conformations of polymer chains become significantly perturbed from the ideal Gaussian distribution, the crossover regime ISR ( $15 \leq \chi N \leq 100$ ) from WSL to SSL was developed by Matsen and Bates based on a SCFT.<sup>72</sup> Within ISR, the phase behaviour is the result of a delicate balance between interfacial area, chain stretching, spontaneous mean curvature, packing frustration, segment distribution. The scaling regime is characterized by  $D \sim N^{0.8}$ .<sup>72, 77</sup> Within the SSL regime ( $\chi N \geq 100$ ), the strong interfacial tension between the incompatible blocks tends to minimize the interface while the conformational entropy favours a larger interface. As a consequence, the minimum free energy configuration is adopted with strongly stretched polymer chains and a well-defined sharp interface. The ordered-state composition profile endows an abrupt change of the composition across the domain boundary. The microdomain period scale as  $D \sim aN^{2/3}\chi^{1/6}$  ( $a$  is the statistic segment length).<sup>69, 78</sup>

Under the assumption of similar segmental lengths of the different components, the parameters  $\chi_{AB}N$  and  $\phi_A$  are sufficient to specify the morphology of AB diblock copolymers, however, at least there are three interaction parameters  $\chi_{AB}$ ,  $\chi_{BC}$ ,  $\chi_{AC}$  and two independent composition variables (e.g.  $\phi_A$ ,  $\phi_B$ ) required to determine the morphology of ABC triblock terpolymers. Therefore, it is clear that triblock terpolymers show a much richer variety of morphologies than diblock copolymers. Additionally, the architectural parameters also play the crucial role in the phase behaviour of ABC systems, e.g. block sequence (A-B-C, B-C-A, or C-A-B), linear or

branched topology, which further increase the complexity and number of their self-assembled microphase structures.<sup>70, 73</sup>

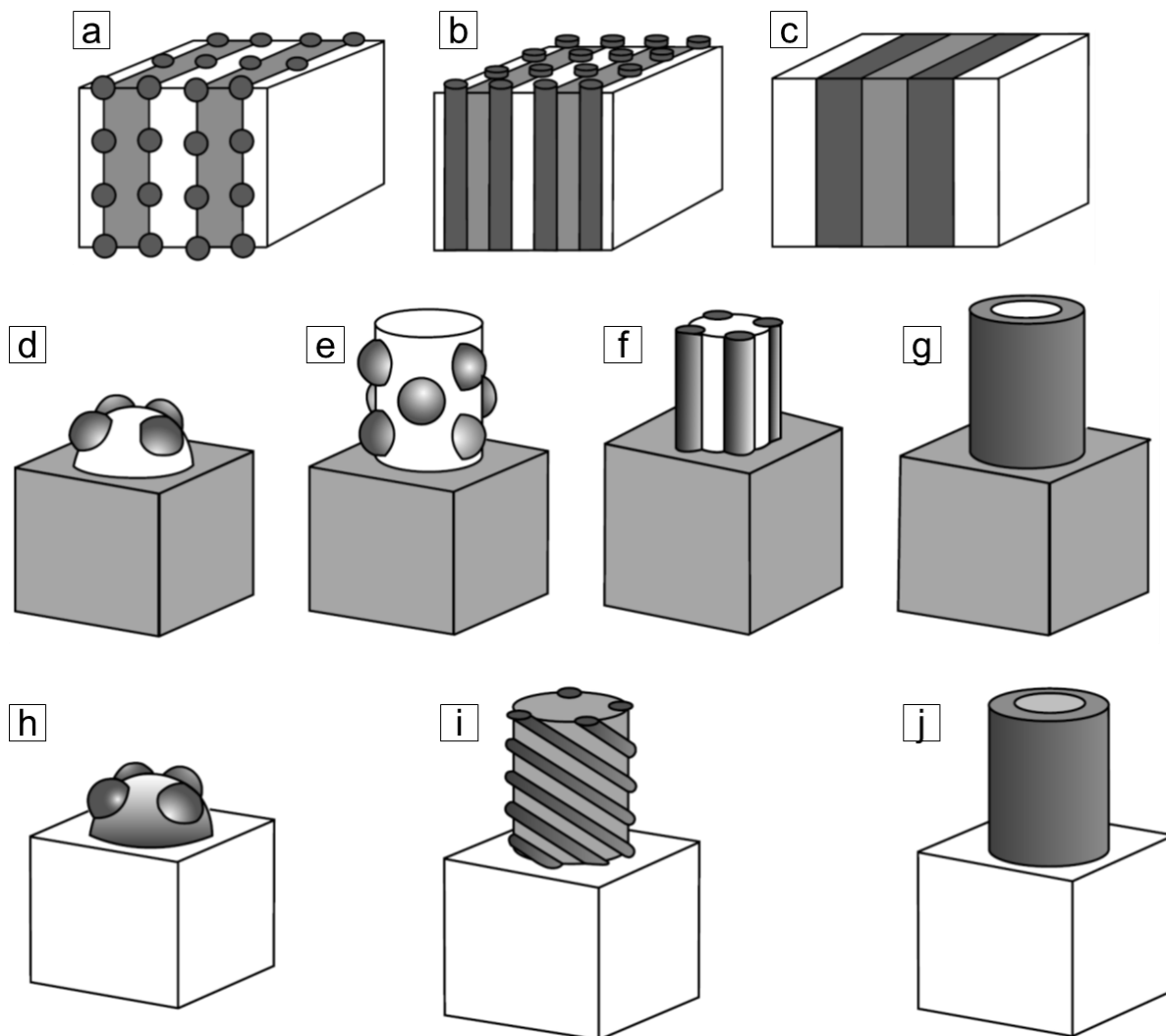


Figure 2.2. Microphase separation structures of linear ABC terpolymer copolymers with  $\chi_{AB} \approx \chi_{BC} > \chi_{AC}$ :  $\varphi_A \approx \varphi_C$  with increasing  $\varphi_B$  (a-c), increasing ratio  $\varphi_B/\varphi_C$  (e-g), and increasing ratio  $\varphi_B/\varphi_A$  (h-j). The blocks A, B and C are coloured grey, dark and white, respectively. The figure is adapted from reference.<sup>73</sup>

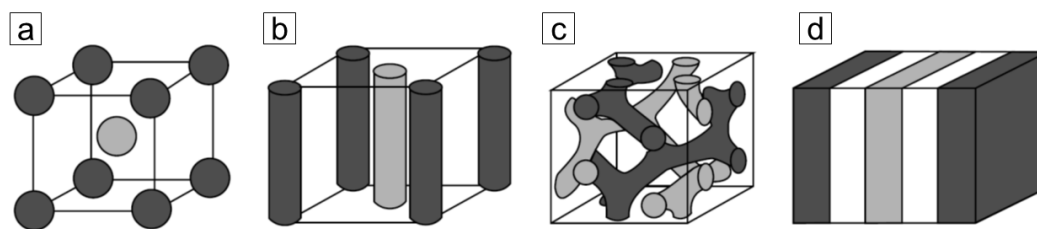


Figure 2.3. Microphase separation structures of linear ABC terpolymer copolymers with  $\chi_{AB} \approx \chi_{BC} < \chi_{AC}$  and  $\phi_A \approx \phi_C$ . The blocks A, B and C are colored black, white and grey, respectively. The figure is adapted from reference.<sup>79, 80</sup>

For example, the simplest system is a linear ABC triblock terpolymer. With the similar compositions ( $\phi_A = \phi_B = \phi_C = 1/3$ ) and also similar interaction parameters ( $\chi_{AB} \approx \chi_{BC} \approx \chi_{AC}$ ), ABC triblock terpolymers self-assemble into lamellar morphology (Figure 2.2c). If  $\phi_A = \phi_B = \phi_C = 1/3$ , but  $\chi_{AB} \ll \chi_{BC}$ , the configuration minimizes the contacts between B and C blocks with a core-shell hexagonal cylindrical structure (Figure 2.2g). A number of spectacular self-assembled morphologies were discovered by Stadler et al. based on the ABC triblock terpolymers with  $\chi_{AB} \approx \chi_{BC} \gg \chi_{AC}$ , e.g., the B blocks were embedded in the AC interfaces in the form of spheres, cylinders, helices, rings, lamellar, etc. (Figure 2.2). The middle B block is strongly segregated by two end blocks A and C and tends to be discontinuous, resulting in more AC contacts.<sup>73, 81, 82</sup> Another series of delicate structures was observed using the systems with  $\chi_{AB} \approx \chi_{BC} < \chi_{AC}$  and  $\phi_A \approx \phi_C$ . By increasing  $\phi_B$ , the lamellae, double gyroids, cylinders, and spheres from A and C blocks are formed separately to avoid AC contacts and reduce the B chain extension (Figure 2.3).<sup>79, 80</sup> Overall, the richness of self-assembly behaviour of ABC triblock terpolymers has been indeed demonstrated, however, the current theoretical and experimental exploitation for such systems is still limited.

## 2.2 Membrane and Membrane Preparation

### 2.2.1 Types of Membranes

A membrane, the permselective barrier or interface between two phases (feed/upstream side and permeate/downstream side), has the ability to transport one component from the feed mixture more readily than other components. According to their morphology or structure, membranes can be classified into symmetric and asymmetric membranes, as shown in Figure 2.4.<sup>83, 84</sup>

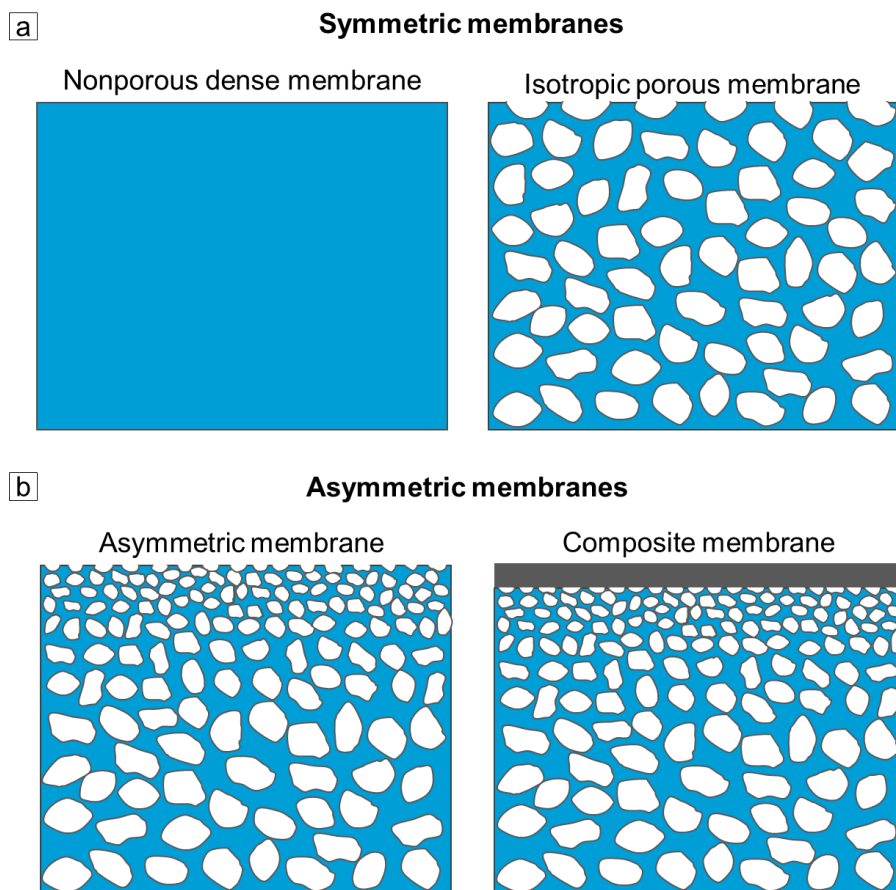


Figure 2.4. Schematic representation of different types of membranes: (a) symmetric membranes, (b) Asymmetric membranes. The figure is adapter from reference<sup>83</sup>.

Symmetric membranes can be subdivided further into isotropic porous membranes and nonporous or dense membranes (Figure 2.4a). The isotropic microporous membranes are similar to the conventional filters in the structure and function. However, the pore sizes in the range of 0.01-10  $\mu\text{m}$  in diameter are much smaller than those of the filters. The components are separated as function of the molecular size of components and the pore size distribution. While in the dense membranes, the separation of components is based on solubility and diffusivity within the membranes. The permeation rate through a symmetric membrane is inversely proportional to the membrane thickness.<sup>83, 84</sup>

The breakthrough of the membrane technology was the development of the asymmetric membranes by Loeb and Sourirajan.<sup>85</sup> Asymmetric membranes consist of a very thin top layer supported by a much thicker porous sublayer (Figure 2.4b). The top layer and its sublayer can be formed in a single step or separately. In composite membranes, the layers are usually fabricated by different materials and optimized independently. The separation properties are determined mainly by the thin top layer while the porous sublayer serves as a mechanical support.<sup>83, 84</sup>

### **2.2.2 Membrane Preparation**

A number of different techniques can be used to prepare the synthetic polymer membranes, for example, sintering, stretching, track-etching, template leaching, phase inversion, dip-coating, plasma polymerization, interfacial polymerization. Among these techniques, the phase inversion process is one of the foremost and versatile approaches to produce large varieties of porous as well as dense integral asymmetric membranes.<sup>86</sup>

Phase separation is a process whereby a one-phase casting solution is precipitated into two separate phases: a polymer-rich phase that forms the solid matrix of the membrane and a

---

---

polymer-poor phase that forms the membrane pores. The phase separation process includes several different techniques. In the nonsolvent induced phase separation (NIPS), which was firstly developed by Loeb and Sourirajan,<sup>85</sup> a cast polymer solution is immersed into a nonsolvent (mostly water) bath, and the exchange of solvent and nonsolvent induces the precipitation and formation of the membrane. If a cast polymer solution is precipitated by adsorption of nonsolvent from a nonsolvent atmosphere (vapour), this is called as vapour induced phase separation (VIPS). A polymer solution can also be phase separated via changing the temperature, normally cooling, which is termed as thermally induced phase separation (TIPS). When the polymer solution is prepared in a mixture of a volatile solvent and less volatile nonsolvent, the evaporation of the volatile solvent leads to a higher content of nonsolvent and polymer leading to phase separation. This process is called evaporation induced phase separation (EIPS). Combinations of different techniques have also been developed to fabricate desired membranes.<sup>86, 87</sup> However, the NIPS process is most widely employed in the fabrication of most commercially available membranes. Also within this study the membrane formation via NIPS is studied and therefore introduced in more detail.

### **2.2.3 Integral Asymmetric Membrane by Nonsolvent Induced Phase Separation (NIPS)**

In the NIPS process, a homogenous (thermodynamically stable) solution with a polymer, a solvent or solvent mixture is cast and then immersed in a coagulation bath with nonsolvent (mostly water). Here solvent and nonsolvent must be miscible with each other. After plunging into the coagulation bath, the system becomes thermodynamically unstable due to the outflow of the solvent from the polymer solution film and the inflow of the nonsolvent into polymer solution film. At this stage, the system phase separates into two coexisting phases to minimize the Gibbs free energy. As a result, the membrane with an integral asymmetric structure is formed with a rather thin selective layer on top of a rather coarse porous sublayer.<sup>86, 88</sup>

In general, for a ternary system, the Gibbs free energy of mixing  $\Delta G_{mix}$  can be given by Equation 2.5 from the Flory-Huggins theory<sup>68</sup>.

$$\Delta G_{mix} = RT(n_1 \ln \varphi_1 + n_2 \ln \varphi_2 + n_3 \ln \varphi_3 + \chi_{12}n_1\varphi_2 + \chi_{13}n_1\varphi_3 + \chi_{23}n_2\varphi_3) \quad 2.5$$

Where  $n_i$  and  $\varphi_i$  are the number of moles and the volume fractions of component  $i$  ( $i = 1, 2, 3$ ). The subscripts refer to nonsolvent (1), solvent (2), and polymer (3).  $\chi_{i,j}$  are the Flory-Huggins interaction parameters of the component  $i$  and  $j$ . When the chemical potentials in each formed phase are equal for all components, a thermodynamical equilibrium state is reached. The chemical potential of the components  $i$  ( $\Delta\mu_i$ ) can be derived using the Equation 2.5 and 2.6.

$$\Delta\mu_i = \left( \frac{\partial \Delta G_{mix}}{\partial n_i} \right)_{P,T,n_j} \quad 2.6$$

The ultimate membrane structure prepared via NIPS process is governed by the interplay between thermodynamics (demixing) and kinetics (diffusion/mass transfer). The formation of NIPS membranes can be rationalized using the three-component phase diagram through which the composition change of the solution-cast film is tracked as a path (Figure 2.5). In this typical triangular phase diagram as shown in Figure 2.5, the corners represent the three pure components, i.e. polymer, solvent, and nonsolvent, while any point represents a mixture of three components. The diagram consists of two main regions: a one-phase region and a two-phase region. In the one-phase region all the components are miscible, whereas in the two phase region the system separates into polymer-rich (solid) phase and polymer-poor (liquid) phase. The one-phase region is homogeneous and thermodynamically stable ( $\Delta G_{mix} < 0$ ), which can be subdivided into different regions based on the polymer concentration, i.e. liquid polymer solution, polymer gel and glassy solid polymer. The boundary between the stable one-phase region and two-phase region is the coexistence curve (so-called binodal curve in binary system) where chemical potentials of component  $i$  are the same in two coexisting equilibrium phases,

i.e.,  $\Delta\mu_i^I = \Delta\mu_i^{II}$  (I: polymer-poor phase; II: polymer-rich phase). Tie lines link a pair of equilibrium compositions in the polymer-rich and polymer-poor phases. Two-phase region can be separated by the spinodal curve ( $\partial^2\Delta G_{mix}/\partial^2\phi_i = 0$ ) into metastable region and unstable region.<sup>86, 87, 89</sup>

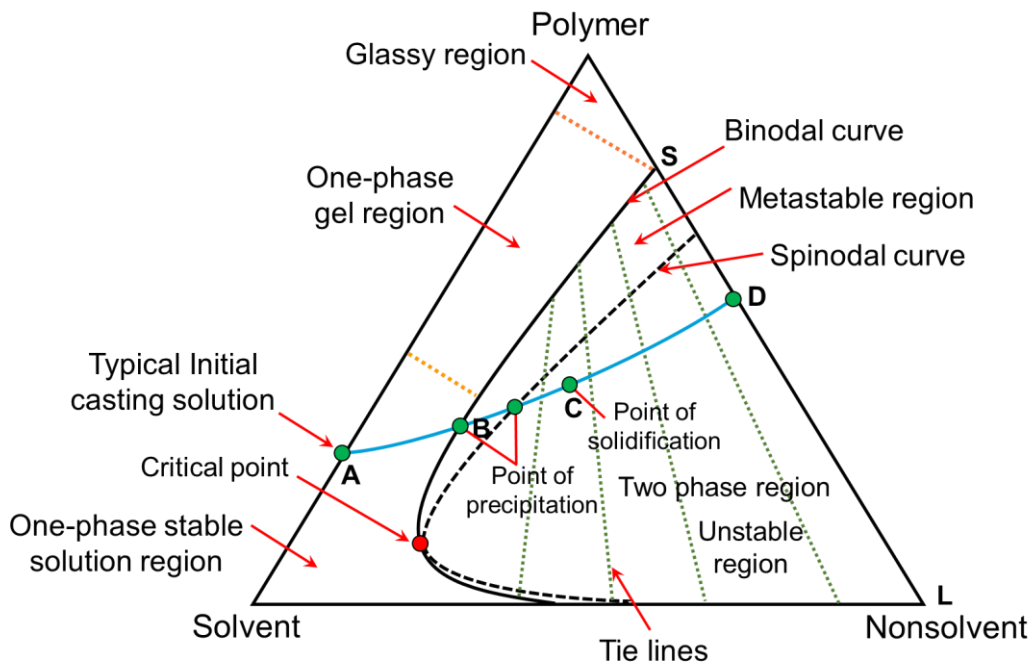


Figure 2.5. Schematic illustration of a three-component phase diagram typically used to rationalize the membrane formation via NIPS (water precipitation). A path from initial polymer casting solution A to the final membrane D can explain the membrane formation process. The figure is adapted from reference<sup>31, 87</sup>.

When the casting solution crosses the coexistence curve (binodal curve) into the metastable region ( $\partial^2\Delta G_m/\partial^2\phi_i > 0$ ), there is no driving force for spontaneous phase separation and demixing can only proceed if the concentration fluctuations generate a stable nucleus. After nucleation, the dispersed nuclei grow further in size while the composition of the continuous phase gradually moves towards that of the other equilibrium phase. By nucleation and growth

(NG), the type of formed structure depends on the initial concentration of the casting solution. In the case of a very diluted casting solution, a latex type of structure is obtained with polymer-rich nuclei dispersed in a continuous polymer-poor phase, which is not suitable for membrane application. Starting with a more concentrated solution, the nucleation of the polymer-poor phase occurs. Consequently, liquid droplets with a mixture of solvent and nonsolvent are dispersed in the continuous polymer phase. If coalescence of the droplets occurs before solidification, an open interconnected porous structure can be formed. In a ternary phase diagram, the entry point from the one-phase region to the metastable region above the critical point (the intersection of coexistence and spinodal curves) brings about the dispersed liquid phase in the continuous solid phase, otherwise, a latex structure is formed. In the unstable region ( $\partial^2 \Delta G_m / \partial^2 \varphi_i < 0$ ), the solution is thermodynamically unstable with respect to even very small concentration fluctuations and demixing occurs spontaneously. The amplitude and wavelength of the local concentration fluctuation increase with time, leading to two interconnected coexisting regions with equilibrium compositions (so-called spinodal decomposition, SD).<sup>86, 88, 90 31</sup>

The membrane formation process is a series of steps, followed by a pathway in the phase diagram, e.g. the path A-D, as shown in Figure 2.5.<sup>86, 87, 89</sup> During the precipitation process, the composition changes from the initial casting solution composition A to the final membrane composition D by losing solvent and gaining nonsolvent. First, just after the initial casting solution (A) contacts with nonsolvent, simultaneously the exchange of solvent and nonsolvent occurs. When nonsolvent inflow and solvent outflow reach to a certain extent, the composition of casting solution reaches the coexistence curve, enters the two-phase region, and initiates the phase separation, i.e., the precipitation point B. At this stage, the polymer-rich phase (the precipitation domain) may still be able to flow or agglomerate. Upon further desolvation and nonsolvent imbibition of the polymer-rich phase, the viscosity of the precipitated polymer

phase is sufficient to be considered as a solid phase. The corresponding composition point is C. The solid polymer phase finally forms the matrix (S) of the final membrane whereas the liquid solvent-nonsolvent phase forms the pores (L) at the composition D. The overall porosity of the membrane is determined by the position of composition D on the S-L line.<sup>86, 87, 89</sup>

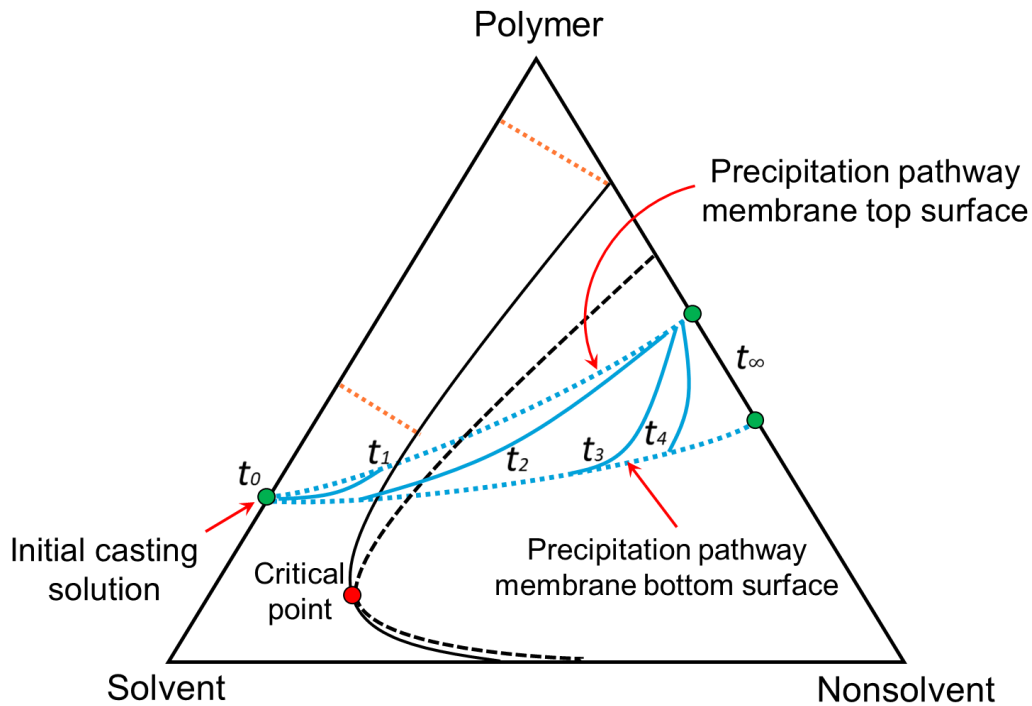


Figure 2.6. Different layers of a phase inversion precipitation membrane follow different precipitation pathways through ternary phase diagram. The figure is adapted from reference<sup>31, 87</sup>.

The precipitation path A-D is a single line representing the average composition of the whole membrane. Different layers in the casting solution follow the different pathways through the phase diagram as shown in Figure 2.6. The precipitation path, the delay time between immersion and the onset of demixing, and precipitation rate have a significant effect on the membrane structure. The top surface layer of the cast film first starts the phase separation due to immediate precipitation upon direct contact with the nonsolvent. This precipitated thin layer

becomes a barrier for further solvent/nonsolvent exchange in the cast film. The phase separation proceeds at a reduced rate across the top surface toward the bottom of the cast film. The precipitation rate is increasingly slower in the deeper layers of the cast films, providing more time for phase separation. As a result, an asymmetric structure with pore gradient along the cross-section of the ultimate membrane is generated.<sup>19,87,91</sup> Additionally, the instantaneous demixing (fast precipitation rate) normally renders an asymmetric structure with a thin skin top layer and finger-like substructure with macrovoids, while the delayed demixing (slow precipitation rate) forms a relatively skinless top layer on the sponge-like sublayer.<sup>86, 89</sup> The ultimate membrane structure can be tuned by changing the parameters of membrane forming system, e.g. composition of nonsolvent and polymer solution, the choice of solvent/nonsolvent, polymer concentration.<sup>86</sup>

### **2.3 Integral Asymmetric Isoporous Block Copolymer Membrane**

A precise control of the pore size during the membrane fabrication process is a prerequisite to achieve a high performance of separation using a porous membrane. The well-known self-assembly of BCPs can endow the uniformly sized microdomains in the microphase separation structure. Therefore, the combination of self-assembly of BCPs with the nonsolvent induced phase separation (SNIPS) is a promising scalable method to fabricate an integral asymmetric membrane with an isoporous surface.<sup>19</sup>

Figure 2.7a depicts a typical SNIPS process.<sup>37</sup> A concentrated polymer solution is typically prepared using a binary or ternary mixture of solvents with different volatility and selectivity towards the blocks. After casting of the solution film, solvent evaporation follows, which is a key step to induce the microphase separation of BCPs at the surface of the film. Thus, the SNIPS process is principally a dry/wet phase inversion. During solvent evaporation, the solvent

---

---

concentration in the top layer decreases to a value below the order-disorder solvent concentration. The directional growth of ordered periodic microdomains is initiated. The orientation of the microphase separation is determined by the rate of variation of the polymer chain relaxation rate and the rate of variation of the effective segregation strength as a function of the solvent concentration. A perpendicularly oriented microphase separation is generated by a sufficiently steep solvent concentration gradient with a solvent concentration at the surface below a critical concentration.<sup>92</sup> The perpendicularly oriented ordered periodic structure can only grow a finite distance into the film, whereas the sublayer is closer to the initial concentration of the casting solution. The formed perpendicularly ordered structure occurs in a highly swollen state due to the different volatility of the different selective solvents in the mixture, and can still rearrange to a thermodynamically more favourable parallel structure. Therefore, at a certain evaporation time, the cast film needs to be plunged into the nonsolvent bath. Upon the exchange of solvent/nonsolvent, the ordered vertically aligned structure in the top layer is quenched while the sublayer is transformed into an unstable state and forms the spongy or finger-like structure by spinodal decomposition similar to the mechanism of the NIPS process. However, the SNIPS process generates an integral asymmetric membrane, which possesses a rather thin selective layer having high number density ( $>10^{14}$  pores  $m^{-2}$ ) of densely packed vertically-aligned cylindrical pores with a very narrow pore size distribution above a macroporous sublayer, as shown in Figure 2.7b.<sup>19</sup>

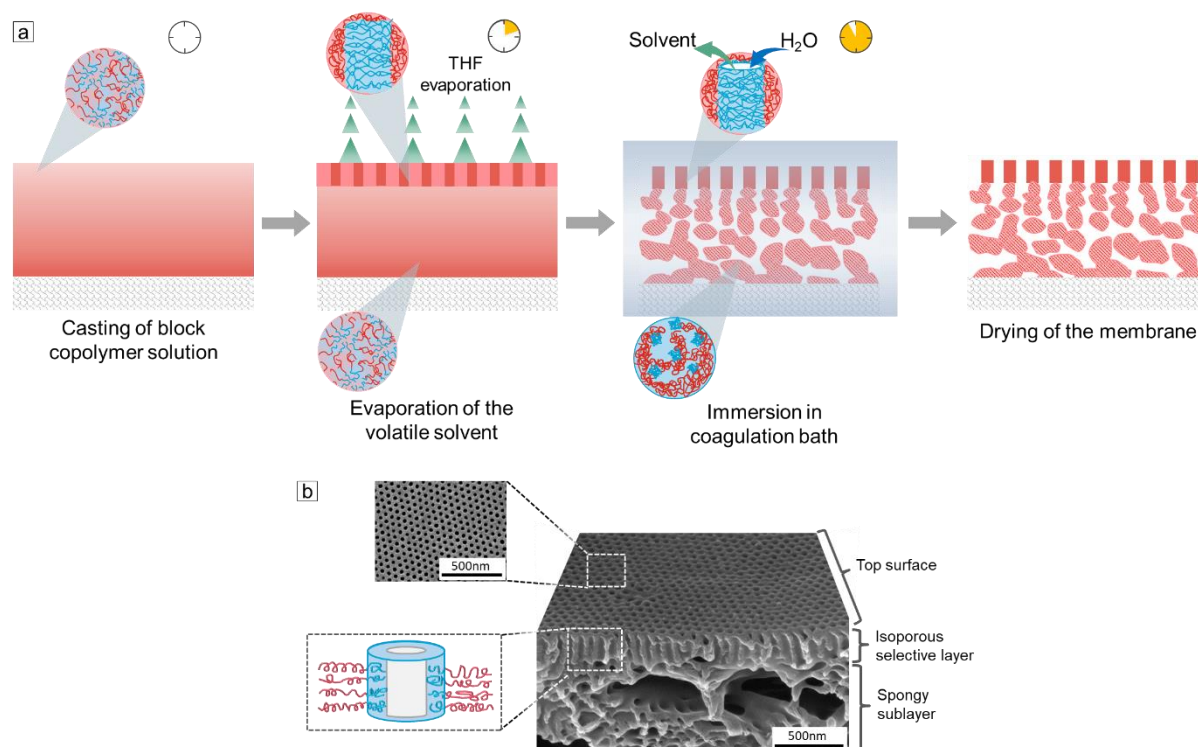


Figure 2.7. (a) Schematic representation of the SNIPS process: casting of the BCP solution on the substrates (e.g. glass plate or non-woven support), evaporation of volatile solvent from the cast film surface within a certain time, immersing the cast film in the nonsolvent bath (e.g. water), drying of the membrane. (b) Top and cross-section view of a representative integral asymmetric isoporous BCP membrane prepared via SNIPS process. The figure is adapted from references <sup>37, 44, 93</sup>.

The first reported and most studied SNIPS membrane system is prepared from PS-*b*-P4VP diblock copolymer.<sup>37</sup> On the basis of PS-*b*-P4VP, to date various diblock copolymers and triblock terpolymers have been exploited for the fabrication of SNIPS membranes, e.g. poly(*tert*-butylstyrene)-*block*-poly(4-vinylpyridine), poly(4-trimethylsilylstyrene)-*block*-poly(4-vinylpyridine),<sup>46</sup> poly( $\alpha$ -methylstyrene)-*block*-poly(4-vinylpyridine) and poly(4-methylstyrene)-*block*-poly(4-vinylpyridine),<sup>48</sup> polystyrene-*block*-poly(2-vinylpyridine) (PS-*b*-P2VP),<sup>44</sup> PS-*b*-PHEMA,<sup>39</sup> polystyrene-*block*-poly(glyceryl methacrylate),<sup>47</sup> polystyrene-*block*-poly(ethylene oxide), polystyrene-*block*-poly(2-hydroxyethyl methacrylate-*ran*-2-

(succinyloxy)ethyl methacrylate,<sup>94</sup> PS-*b*-P2VP-*b*-PEO,<sup>40</sup> PI-*b*-PS-*b*-P4VP,<sup>41</sup> PI-*b*-PS-*b*-PDMA,<sup>42</sup> PS-*b*-P4VP-*b*-PPS,<sup>43</sup> and PS-*b*-P4VP-*b*-PSMA.<sup>50</sup> The most common solvent system used for preparation of some SNIPS membranes is the mixture of tetrahydrofuran (THF) and *N,N*-dimethylformamide (DMF). The more volatile THF has a preferential affinity for matrix-forming blocks (e.g. PS), whereas the less volatile DMF shows selectivity for the hydrophilic-pore forming blocks (e.g. P4VP).<sup>19</sup>

Besides the development of the diversity of BCP materials and functionalities of SNIPS membranes, there have been many efforts for the fundamental understanding of the structure formation of SNIPS membranes. One issue is to determine the BCP phase behavior in the casting solution. The casting solutions for the formation of isoporous membranes are primarily disordered or only weakly segregated or can be sometimes ordered micellar solutions depending on the solvent system, solvent concentration and addition of additives.<sup>51, 95-101</sup> The geometry of the ordered structure in the casting solution can be similar to the pore geometry in the final membrane, e.g. a hexagonal order of PS-*b*-P4VP,<sup>96, 97, 100</sup> while a transition can occur during the solvent evaporation, e.g. a transition from body-centred cubic (BCC) to simple cubic (SC) lattices in the case of PI-*b*-PS-*b*-P4VP.<sup>99</sup> Another issue is to define the micellar structure of BCP in the casting solution, e.g. the widely studied PS-*b*-P4VP. In some studies, the formation of crew-cut micelles with major block PS in the core was presumed.<sup>57, 102-104</sup> On the contrary, the hydrophilic minor block P4VP self-assembled within the core of the highly swollen spherical micelles even in the pure DMF, verified by the investigation of cryo-scanning and cryo-transmission electron microscopy combined with small-angle neutron scattering (SANS).<sup>105</sup> The structure formation pathways and the characteristic transient structures involved in the formation of the SNIPS membrane were investigated using atomic force microscopy (AFM), scanning electron microscopy (SEM) and in situ synchrotron small-angle X-ray scattering (in situ synchrotron SAXS) based on PS-*b*-P2VP and PS-*b*-P4VP system.<sup>95</sup>

Furthermore, the mechanism of the structure formation on the surface of the SNIPS membrane was clarified by V. Abetz, illustrated as shown in Figure 2.8.<sup>19</sup>

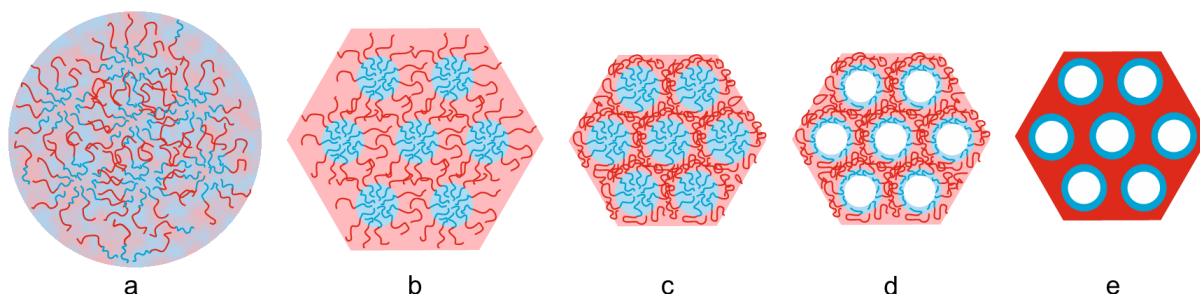


Figure 2.8. Schematic representation of isoporous structure formation on the top of SNIPS membrane from the casting solution. (a) disordered or weakly segregated diblock copolymer in a mixed selective solvent (red: polystyrene rich domains, blue: poly(4-vinylpyridine) rich domains), (b) microphase separation with polystyrene rich matrix after film casting, (c) solidification of the matrix due to solvent evaporation, (d) open pores in the poly(4-vinylpyridine) rich domains after non-solvent induced phase separation, (e) isoporous structure of the dried membrane. This figure is adapted from reference<sup>19</sup>.

The formation of an isoporous top layer in the SNIPS membrane starts with a disordered or weakly segregated initial solution in the mixture of THF and DMF (Figure 2.8a). After casting the liquid film, the more volatile THF evaporates, leading to the formation of spherical micelles with a swollen PS corona and highly swollen P4VP cores (Figure 2.8b). Upon the fast evaporation of THF, the P4VP spheres grow into cylinders perpendicular to the film surface, due to shrinkage of the swollen PS matrix and the simultaneous connection of the highly swollen P4VP spheres (Figure 2.8c). By quenching into the nonsolvent bath, the solvent and nonsolvent exchanges with each other, consequently the highly swollen P4VP chains within cylinders collapse to form the open pores while the major PS block collapses around the cylinders and forms the matrix (Figure 2.8d).<sup>19</sup>

---

---

The formation of SNIPS membranes requires the right choice of a considerable number of parameters, *e.g.*, block structure and architecture, composition and molecular weight of the BCP, polymer concentration of the casting solution, solvent system and its composition, nonsolvent system and its composition, solvent evaporation time and the additives, etc.<sup>19</sup> Significant advances have been made during SNIPS membrane studies for more than one decade, which can guide the fabrication of SNIPS membrane in a more qualitative rather than quantitative way. Therefore, in practice these corresponding parameters have to be optimized for a new BCP system empirically.

## 2.4 Membrane Separation Process

The most important property of membranes is their ability to selectively transport/reject specific components from a multi-component system. Transport through the membranes occurs as a result of a driving force, which can be a gradient in pressure, concentration, electrical potential or temperature between the feed and permeate side.<sup>106</sup> In this study, all the membrane separations are pressure-driven. According to the size of the retained solutes, the pressure-driven separation process typically can be classified into microfiltration (MF), ultrafiltration (UF), nanofiltration (NF), reverse osmosis (RO) and forward osmosis (FO) as shown in Figure 2.9. Different from other processes driven via hydraulic pressure, the FO is driven by an osmotic pressure difference between the feed phase and the permeate phase with a draw solution of high osmotic pressure.<sup>107</sup>

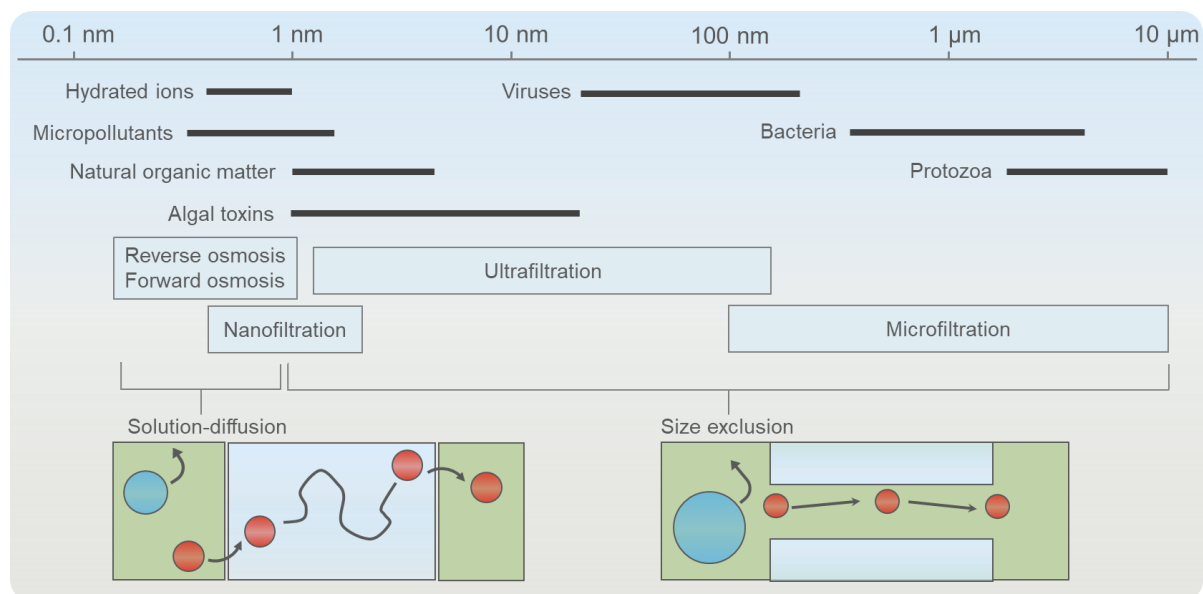


Figure 2.9. Membrane processes that are driven by pressure typically can be classified into microfiltration (MF), ultrafiltration (UF), nanofiltration (NF), reverse osmosis (RO) and forward osmosis (FO) based on the size of the retained solutes. The figure is adapted from the reference<sup>107</sup>.

Two fundamentally different models are used to describe the transport mechanisms for above membranes process: solution-diffusion model and pore-flow model as depicted schematically in Figure 2.9.<sup>108</sup>

In the solution-diffusion model, the permeants traverse the membrane through the free-volume elements (pores) which are tiny spaces between polymer chains caused by the thermal motion of the polymer segments. The free-volume elements appear and disappear on the almost same time scale as permeants motions, which are not fixed. Briefly the transport behaviour involves three steps: adsorption or dissolving of a penetrant molecule at the feed side of a membrane, diffusion through the membrane down a concentration gradient, and ultimately desorption or release from the permeate side of the membrane. The transport of uncharged small solutes and ions through nonporous RO and FO membranes is described by the solution-diffusion model.

Current RO and FO membranes for water purification and desalination can remove almost all the ions and uncharged solutes of molecular weights larger than ~100 Da. The separations are governed by the differences in the solubility and diffusivity of the solutes in the membrane selective layer.<sup>107-109</sup>

In the pore-flow model, the free-volume elements (i.e. fixed pores) do not fluctuate in position or volume on the time scale of the permeant motions. The free-volume elements are the connected relatively large pores. The separation is predominantly accomplished based on the molecular size exclusion mechanism. Transport through porous MF and UF membranes is primarily described by the pore-flow mode. MF membranes are proposed to remove the suspended particles and microbial pathogens while UF membranes are designed to retain the macromolecules and small pathogens with a molecular weight cut-off in the range of 5-500 kDa. While NF membranes are intermediate between UF and RO membranes with effective pore sizes of 0.5-2 nm. Separation of uncharged molecules through NF membranes is mainly based on a size exclusion mechanism, while for charged molecules, both steric (size-sieving) effect and electrical (e.g. Donnan equilibrium) effect have an influence on the separation behaviour.<sup>87, 110, 111</sup> NF membranes are mainly used for water softening and removal/separation of natural/synthetic organic matter(e.g. textile dyes).<sup>107, 112</sup>

Two important parameters for membrane performance are the permeability and selectivity . Flux of water through porous and non-porous membranes can be often described by the following phenomenological equation<sup>87</sup>:

$$J_v = A(\Delta P - \Delta\pi_m) \quad 2.7$$

where  $J_v$  is the volumetric water flux,  $A$  is the water permeability coefficient,  $\Delta P$  is the applied hydraulic transmembrane pressure,  $\Delta\pi_m$  is the osmotic pressure difference across the active

layer, which is negligible for MF and UF membranes. The water flux can be experimentally determined by measuring the volume flow ( $v$ ) through the membrane per unit area ( $A_m$ ) and time ( $t$ ) as Equation 2.8:

$$J_v = \frac{dv}{dt \cdot A_m} \quad 2.8$$

Therefore the water permeability coefficient (or water permeance) can be determined from the slope of the flux-pressure curve.<sup>106</sup>

As in this work, all the studies are based on the porous membranes, the transport phenomena through the porous membranes are given in more detail. The water flux and solute rejection in porous membranes are primarily governed by the pore size and its distribution, porosity and pore tortuosity of membranes.

The simplest and ideal representation of a porous membrane is the one with uniformly sized cylindrical pores perpendicular or oblique to the membrane surface in the active layer. The volume flow through cylindrical channels can be modelled as laminar flow derived by the Hagen-Poiseuille law, as shown in Equation 2.9:

$$J = \frac{\varepsilon_m r^2 \Delta P}{8\eta\tau \Delta x} \quad 2.9$$

where  $J$  is the solvent flux,  $\eta$  is the solution viscosity,  $r$  is the pore radius,  $\varepsilon_m$  is the surface porosity (the fractional pore area),  $\Delta x$  is the thickness of the membrane active layer,  $\tau$  is the pore tortuosity (for the cylindrical perpendicular pores,  $\tau=1$ ).<sup>106</sup>

The Hagen-Poiseuille Equation can best describe the transport through the active layer of membranes with perfectly aligned uniform pores (e.g. an isoporous membrane). However, only few membranes possess such a structure, following Hagen-Poiseuille Equation. Current membranes prepared by the most common technique (e.g. phase inversion or sintering)

normally are characterized by an irregular pore geometry and tortuosity. Such membranes can be described by the Kozeny-Carman relationship:

$$J = \frac{\xi^3}{K\eta S^2(1-\xi)^2} \frac{\Delta P}{\Delta x} \quad 2.10$$

where  $\xi$  is the volume fraction of pores,  $S$  is the internal surface area of pores, and  $K$  is the Kozeny-Carman constant which depends on the shape of the pores and the tortuosity.<sup>106, 113</sup>

The pore size distribution largely governs the rejection of solutes  $R_a$  in the feed solution. The rejection  $R_a$  for a solute with radius  $a$  by a membrane pore of radius  $r$  ( $r > a$ ) was evaluated as a function of  $\lambda = a/r$ , based on a mechanical exclusion model, as shown in Equation 2.11:

$$R_a = 1 - [2(1 - \lambda)^2 - (1 - \lambda)^4] \exp[-0.7146\lambda^2] \quad 2.11$$

This relation is obtained based on some assumptions. For example, the solute transport is dominated by the convection whereas diffusional contribution is negligible. The concentration polarization and membrane-solute interaction are not present.<sup>114</sup> The rejection  $R_a$  is generally called as the actual rejection. In practice, the rejection experimentally measured is considered as the observed rejection  $R_0$ , which is defined as  $R_0 = 1 - 2c_p / (c_f + c_r)$  ( $c_p$ ,  $c_f$  and  $c_r$  are the concentrations of the permeate, feed, retentate solutions, respectively). The actual rejection  $R_a$  can be determined from the observed rejection  $R_0$  by including the influence of concentration polarization on the local feed concentration of rejected solutes.<sup>115</sup> In general, the concentration polarization can be minimized by the optimization of the measurement procedure, e.g. vigorous stirring in dead-end filtration (the feed flow perpendicularly passes through the membranes), or cross-flow filtration (the feed flow travels tangentially across the surface of membranes).

When the charged solutes pass through a charged porous membrane, the separation mechanism is remarkably related to the steric and electrostatic partitioning effects (e.g. Donnan equilibrium)

between the membrane and external solution.<sup>110</sup> Mass transfer of the electrolytes and neutral solutes through charged membranes can be described via different models, e.g. Donnan steric pore model (DSPM), Donnan steric pore model & dielectric exclusion (DSPM&DE), and Steric Electric and Dielectric (SEDE) model. Basically, each model can well describe the separation behaviour of charged membranes in some certain cases, but a generalized model is not yet well developed.<sup>110, 111, 116</sup> However, in essence all the variations of the models are related to the extended Nernst-Planck equation, which defines the mass transport of charged solutes through the membrane by three different contributions: diffusion, convection, and electromigration (down the potential gradient arising from unequal diffusion rates).<sup>110</sup> The transport equation for a solute *i* can be written as

$$J_i = -D_{i,p} \frac{dc_i}{dx} - z_i c_i D_{i,p} \frac{F}{RT} \frac{d\phi}{dx} + K_{i,c} c_i J_v \quad 2.12$$

where  $J_i$  is the flux of solute *i*,  $c_i$  and  $z_i$  is the concentration and the valence of the solute *i*, respectively,  $F$  is the Faraday constant,  $\phi$  is the membrane potential,  $D_{i,p}$  denotes the diffusion coefficient inside the confined pores,  $D_{i,p} = K_{i,d} D_{i,\infty}$  ( $D_{i,\infty}$  is the diffusion coefficient of the solute *i* in water at infinite dilution),  $K_{i,d}$  and  $K_{i,c}$  are hindrance factors to account for the diffusion and convection of the solutes in the confined pores,  $J_v$  is the water flux.<sup>110, 116, 117</sup>

## **Chapter 3    Materials and Methods**

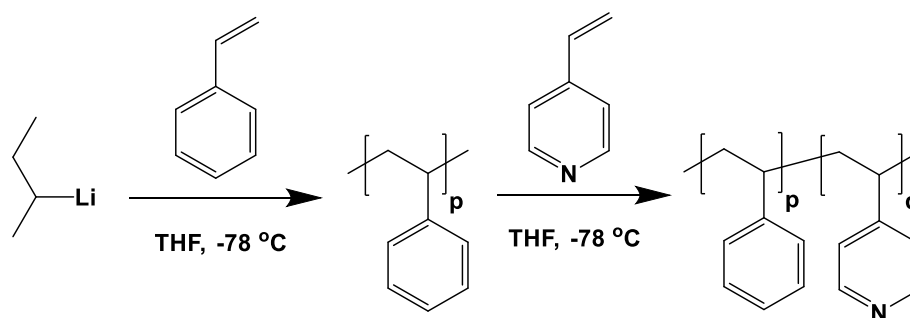
### 3.1 Materials

Styrene, 4-vinyl pyridine (4VP), isoprene, *tert*-butyl methacrylate (*t*BMA), di-*n*-butyl magnesium ( $\text{MgBu}_2$ , 1.0 M solution in heptane), ethylaluminium dichloride (1M in hexane), calcium hydride ( $\text{CaH}_2$ ), *n*-butyl lithium (*n*-BuLi, 1.6 M solution in hexane), *sec*-butyl lithium (*s*-BuLi, 1.4 M solution in cyclohexane), *p*-toluene sulfonyl chloride (*p*TsCl), methyl-2-bromopropionate (MBrP), *N,N,N',N'',N'''*-pentamethyldiethylenetriamine (PMDETA), CuCl, CuBr, aluminium oxide ( $\text{Al}_2\text{O}_3$ ) were purchased from Sigma-Aldrich. Tetrahydrofuran (THF), toluene, *N,N*-dimethylformamide (DMF), chloroform ( $\text{CHCl}_3$ ), 1,4-dioxane (anhydrous 99.8%, DOX), dimethylacetamide (DMAc), methanol (MeOH), dichloromethane, diethyl ether and *n*-pentane were purchased from Merck KGaA (Germany), Sigma-Aldrich or Th. Geyer. 2-mercaptoethanol, 2,2-dimethoxy-2-phenyl acetophenone (DMPA), methyl iodide (MeI), ethyl iodide (EtI), 1-propyl iodide (1-PrI), 1,3-propane sultone, trimethylchlorosilane (TMCS), trimethyloxonium tetrafluoroborate ( $(\text{CH}_3)_3\text{O}(\text{BF}_4)$ ), methylene blue (MB+), riboflavin (RB0), Orange II (OR-), naphthol green B (NG3-) and reactive green 19 (RG6-) were obtained from Sigma-Aldrich. Titanium tetraisopropoxide (TTIP), poly(ethylene glycol) with molecular weight  $400 \text{ g mol}^{-1}$  (PEG400) and magnesium acetate ( $\text{MgAc}_2$ ) were purchased from Sigma-Aldrich. Sodium hydroxide and hydrochloric acid (37 %) were obtained from Merck KGaA (Germany). All materials were used as received without further purification unless described specifically. Isoprene was distilled twice from  $\text{CaH}_2$  and twice from *n*-BuLi. Styrene was purified from a basic  $\text{Al}_2\text{O}_3$  column and subsequently distilled from  $\text{MgBu}_2$ . 4-vinylpyridine (4VP) was distilled under reduced pressure after being treated twice with ethylaluminium dichloride. *t*BMA was purified by passing through a basic  $\text{Al}_2\text{O}_3$  column. The solvent used for polymerization was THF, purified from sodium metal, titrated with *s*-BuLi.

## 3.2 Synthesis of Block Copolymers

### 3.2.1 Synthesis of PS-*b*-P4VP Diblock Copolymer

PS-*b*-P4VP diblock copolymer was synthesized by sequential living anionic polymerization following a previously published procedure,<sup>52</sup> as shown in Scheme 3.1. The polymerization of styrene was initiated by *s*-BuLi in THF at  $-78\text{ }^{\circ}\text{C}$  for approximately 2 h. Afterwards, the purified 4VP was added to the reactor via a syringe and polymerized onto the living polystyrene for approx. 14 h. The polymerization was terminated with methanol/acetic acid (90/10 by volume, v/v). After removal of THF under reduced pressure and precipitation in water, the PS-*b*-P4VP diblock copolymer was obtained.

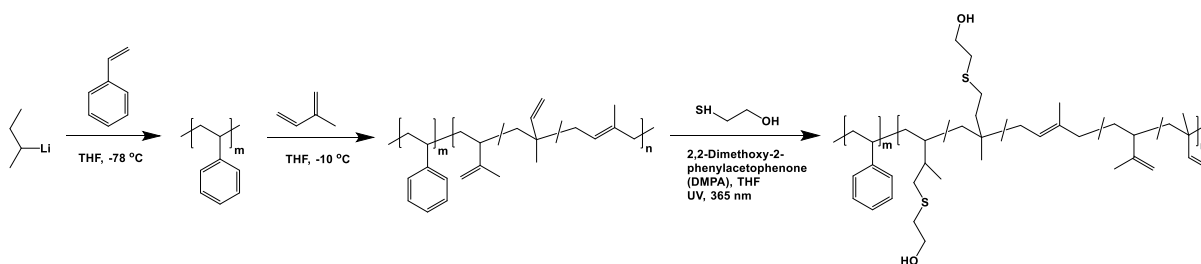


Scheme 3.1. Synthesis route of PS-*b*-P4VP diblock copolymers by living anionic polymerization.

### 3.2.2 Synthesis of PS-*b*-P(HTMB-*r*-I) Diblock Terpolymers

PS-*b*-P(HTMB-*r*-I) diblock terpolymers were prepared by living anionic polymerization with subsequent thiol-ene click chemistry, as shown in Scheme 3.2. First, a PS-*b*-PI diblock copolymer was synthesized by sequential living anionic polymerization following a previously published procedure.<sup>118, 119</sup> The synthesis started with the polymerization of styrene using *s*-BuLi as the initiator in THF at  $-78\text{ }^{\circ}\text{C}$  for approximately 2 h. Afterwards, the purified isoprene

was added to the reactor and subsequently the reaction temperature was increased up to  $-10\text{ }^{\circ}\text{C}$  for further 4–5 h. After termination with methanol/acetic acid (90/10 v/v) and precipitation in methanol, the PS-*b*-PI diblock copolymer was obtained. The polyisoprene (PI) block of PS-*b*-PI was subsequently hydroxylated by a thiol-ene click reaction to obtain the poly(4-(2-hydroxyethyl-thio)-2-methyl butene-*random*-4-(2-hydroxyethyl-thio)-3-methyl butene-*random*-isoprene) (P(HTMB-*r*-I)) with various degrees of hydroxylation (DH). Specifically, 2-mercaptoethanol and the photoinitiator DMPA (molar ratio  $[\text{RSH}]_0/[\text{C}=\text{C}]_0/[\text{DMPA}]_0 = 30:1:1$ ) was added to a ~6% by weight (wt%) solution of PS-*b*-PI in anhydrous THF (Sigma-Aldrich). The mixture was degassed by three freeze-pump-thaw cycles, put under an argon (Ar) atmosphere, and irradiated by ultraviolet (UV) light at room temperature for 2 h (light source: 200W DC super pressure short-arc mercury lamp, LUMATEC, Superlite SUV-DC, Germany, wavelength  $\lambda = 365\text{ nm}$ ). Afterwards, the polymer solution was concentrated, precipitated into methanol, and dried under vacuum. The polymer was redissolved into THF and the precipitation was repeated several times, in order to remove the excess reagents completely. The thiol-ene click reaction was repeated to obtain the different desired DH of polymers.



Scheme 3.2. Synthesis route of PS-*b*-P(HTMB-*r*-I) diblock terpolymer by living anionic polymerization and subsequent thiol-ene click chemistry.

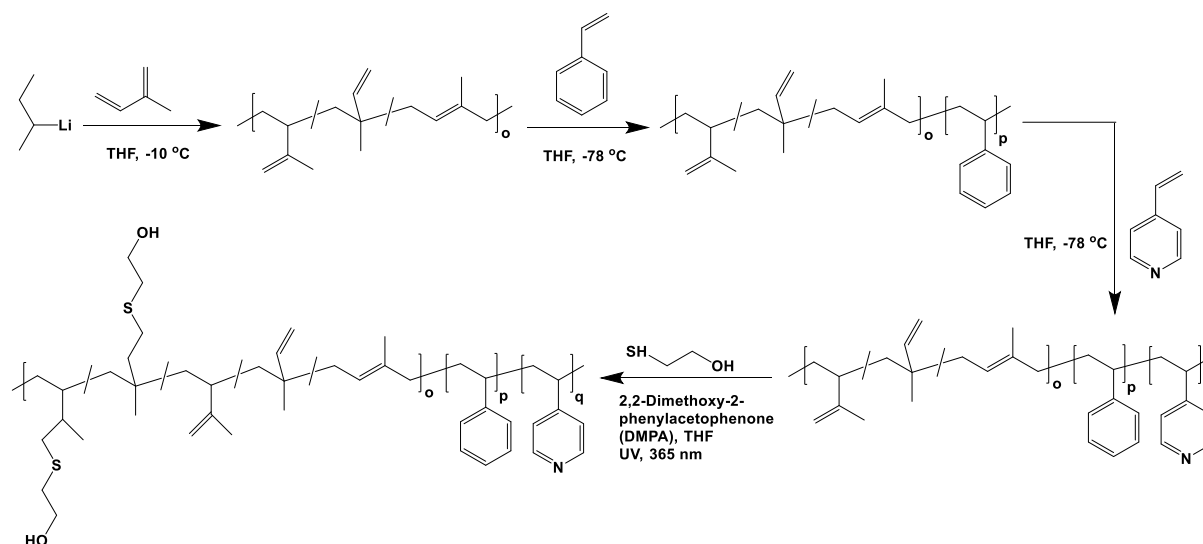
### 3.2.3 Synthesis of PI-*b*-PS-*b*-P4VP Triblock Terpolymer and P(HTMB-*r*-I)-*b*-PS-*b*-P4VP Triblock Quaterpolymers

---

---

A PI-*b*-PS-*b*-P4VP triblock terpolymer was synthesized by sequential living anionic polymerization (Scheme 3.3). The synthesis started with the polymerization of isoprene using *s*-BuLi as the initiator in THF at -10 °C for a minimum of 4 h. A 5 ml aliquot was collected from the reactor and terminated with degassed methanol for <sup>1</sup>H NMR and GPC analysis of the PI. The temperature of the reactor was then decreased to -78 °C and the purified styrene was added to the reactor for approximately 2 h polymerization. Once more a small aliquot was collected from the reactor and terminated with degassed methanol for <sup>1</sup>H NMR and GPC analysis of the PI-*b*-PS. The distilled 4VP was subsequently added to the reactor and polymerized onto the PI-*b*-PS for approx. 14 h. After the termination with degassed methanol/acetic acid (90/10 v/v) and precipitation in water, PI-*b*-PS-*b*-P4VP triblock terpolymer was obtained.

The PI block of PI-*b*-PS-*b*-P4VP was subsequently hydroxylated by thiol-ene click reaction with mercaptoethanol to obtain P(HTMB-*r*-I)-*b*-PS-*b*-P4VP with various DH (Scheme 3.3). 2-mercaptoethanol and the photoinitiator DMPA (molar ratio [RSH]<sub>0</sub>/[C=C]<sub>0</sub>/[DMPA]<sub>0</sub> = 30:1:1) was subsequently added to a ~6 wt% solution of PI-*b*-PS-*b*-P4VP in anhydrous THF. The mixture was degassed by three freeze-pump-thaw cycles, put under an Ar atmosphere, and irradiated by UV light at room temperature for 2 h (light source: 200W DC super pressure short-arc mercury lamp, LUMATEC, Superlite SUV-DC, Germany, wavelength λ = 365 nm). Afterwards, the polymer solution was concentrated, precipitated several times into *n*-pentane/diethyl ether (50/50 v/v) and dried under vacuum. The thiol-ene click reaction was repeated to obtain the different desired DH of polymers.



Scheme 3.3. Synthesis route of PI-*b*-PS-*b*-P4VP triblock terpolymers by living anionic polymerization and thiol-ene click chemistry of PI-*b*-PS-*b*-P4VP to obtain P(HTMB-*r*-I)-*b*-PS-*b*-P4VP triblock quaterpolymer.

### 3.3 Preparation of Block Copolymer Membranes via SNIPS

Membranes were prepared via a SNIPS process. As shown in Figure 3.1, in general, BCP was dissolved in a solvent mixture of THF/DMF or THF/DMF/DOX (The solvent mixtures used for casting solutions are given in relative weight amounts) to prepare the solutions of different concentrations and compositions. After stirring for 24 h at room temperature, the solutions were directly cast on a glass plate or polyester nonwoven support using a doctor blade with a gap height of 200  $\mu\text{m}$ . The cast films were left for a certain time under air before immersing them into a non-solvent bath (water bath). After immersing in the non-solvent bath for several hours, the membranes were dried at  $60\text{ }^\circ\text{C}$  in a vacuum oven for 3 days.

Regarding the inorganic-organic hybrid nanocomposite membrane, the casting procedure is similar to the aforementioned process. Titanium dioxide ( $\text{TiO}_2$ ) sol nanoparticles (NPs) were *in situ* prepared by hydrolysis of  $\text{TiO}_2$  precursor (titanium(IV) isopropoxide, TTIP) in an

aqueous environment, following a reported procedure.<sup>120, 121</sup> After the polymer solution was kept stirring for 24 h, different amounts of TiO<sub>2</sub> sol solution were added into the polymer solution to form the final casting solution.

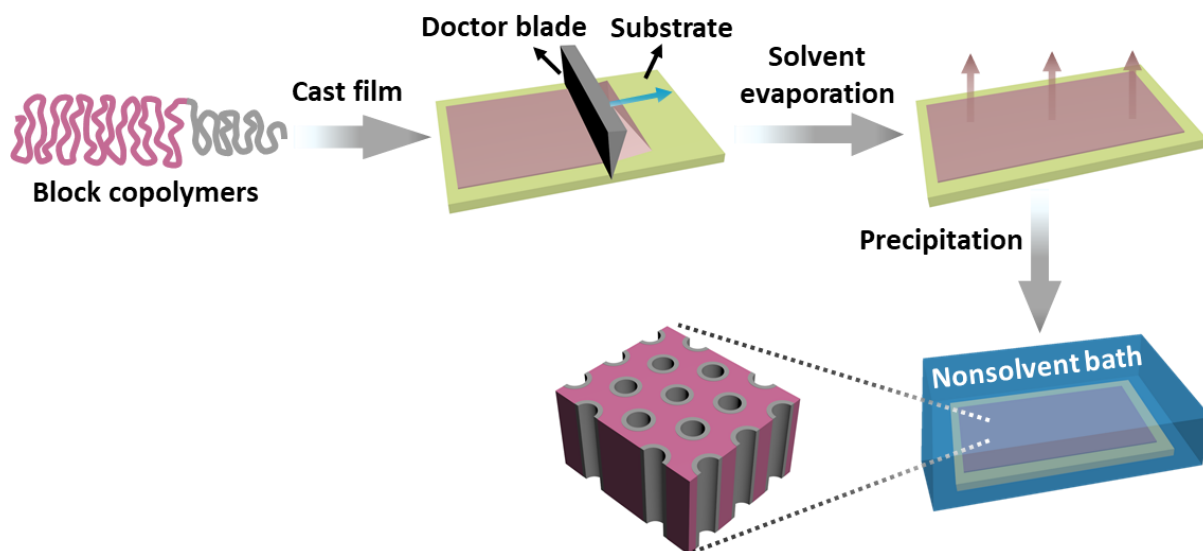


Figure 3.1. Schematic representation of membrane casting via SNIPS.

### 3.4 Post-functionalization of Block Copolymers

#### 3.4.1 Quaternization of P4VP Blocks with MeI

The MeI treatment was accomplished by placing the membranes into MeI vapour (*e.g.*, ca. 60  $\mu$ l MeI (l)/500 ml vessel) at room temperature for 2 days. The resulting membranes were dried at 60 °C under vacuum for several days to remove any unreacted MeI.

#### 3.4.2 Sulfonation of P(HTMB-*r*-I) Blocks with 1,3-Propane Sultone

The 1,3-propane sultone treatment was performed by placing the membranes into a desiccator with a predetermined amount of 1,3-propane sultone. The desiccator was evacuated by a diaphragm vacuum pump (Vacuubrand, Wertheim, Germany) and then placed in an oven

maintained at 50 °C for a certain time (14-18 h). The resulting membranes were immersed into the non-solvent bath of methanol/water (50/50 v/v) under shaking at 90 rpm for 10-14 h at 25 °C, in order to remove the unreacted 1,3-propane sultone, and then dried at 60 °C in a vacuum oven for several days.

### **3.5 Characterization**

#### **3.5.1 Nuclear Magnetic Resonance Spectroscopy (NMR)**

The synthesized block copolymers were characterized by using  $^1\text{H}$  NMR spectroscopy in pure deuterated chloroform ( $\text{CDCl}_3$ ) or deuterated *N,N*-dimethylformamide ( $\text{DMF-}d_7$ ) or in a mixture of  $\text{CDCl}_3$  and deuterated dimethyl sulfoxide ( $\text{DMSO-}d_6$ ) (92/8 v/v) on a Bruker Avance 300 NMR spectrometer at 300 MHz.

#### **3.5.2 Gel Permeation Chromatography (GPC)**

Molecular weights and dispersity indices of the polymers were determined by gel permeation chromatography (GPC). The measurements were performed at 50 °C in THF or DMAc with LiCl using 3  $\mu\text{m}$  PSS SDV gel columns at a flow rate of  $1.0 \text{ mL}\cdot\text{min}^{-1}$  (VWR-Hitachi 2130 pump, Hitachi, Darmstadt, Germany). A Waters 2410 refractive-index detector ( $\lambda = 930 \text{ nm}$ ) with a polystyrene (PS) calibration was used.

#### **3.5.3 Transmission Electron Microscopy (TEM)**

The morphology of the bulk samples and porous membranes was characterized by transmission electron microscopy (TEM). A Tecnai G<sup>2</sup> F20 transmission electron microscope (FEI, Eindhoven, The Netherlands) was operated at an acceleration voltage of 120 kV in bright-field mode. The bulk samples were cast from the solution (around 5 wt%) of the respective block

---

---

copolymers in pure  $\text{CHCl}_3$ , a mixture of  $\text{CHCl}_3$  and DMF (95/5 v/v) or a mixture of  $\text{CHCl}_3$  and methanol (95/5 v/v). The solvents were slowly evaporated in a desiccator over a period of 2 weeks followed by thermal annealing in a vacuum oven to obtain morphologies as close as possible to equilibrium. The porous membranes were embedded in epoxy resin (Epo-Tek 301, two components, curing at room temperature for 3 days) before cutting into ultrathin sections. The samples of dense films and the embedded porous membranes were cut at room temperature to approx. 50 nm thin sections using a Leica EM UCT ultra-microtome (Leica Microsystems, Wetzlar, Germany) equipped with a diamond knife (Diatome AG, Biel, Switzerland). The ultrathin sections of embedded porous membranes were tested without further staining. The staining of the ultrathin sections of dense films was achieved by their exposure to iodine ( $\text{I}_2$ ) vapour for 30 min or 1 h and/or to osmium tetroxide ( $\text{OsO}_4$ ) vapour for 30 min or 1 h or to ruthenium tetroxide ( $\text{RuO}_4$ ) vapour for 20 min.

#### **3.5.4 Atomic Force Microscopy (AFM)**

Polymer thin films were prepared via spin-coating of a 2 wt% polymer solution in  $\text{CHCl}_3$  or  $\text{CHCl}_3$ /methanol (98/2 v/v) on a silicon wafer at 3000 rpm for 1 min. The prepared films were used for further analysis without thermal- or solvent-annealing. The topography of the polymer thin films was monitored by atomic force microscopy (AFM). The images were captured by a Bruker MultiMode 8 AFM (NanoScope V controller) operated in PeakForce QNM mode or tapping mode at ambient conditions, using commercial silicon ScanAsyst-Air or RTESPA 150 tips (Bruker, Karlsruhe, Deutschland).

#### **3.5.5 Scanning Electron Microscopy (SEM)**

The membrane morphology was investigated by scanning electron microscopy (SEM). Secondary electron (SE) images of SEM were taken on a LEO Gemini 1550 VP or a Merlin

(both ZEISS, Oberkochen, Germany) at a voltage of 3 kV or 5 kV. Cross sections of the membranes were prepared while dipping the membrane in isopropanol, freezing in liquid nitrogen and cracked. The samples were coated with ca. 1.0 or 2.0 nm platinum using a coating device Bal-Tec (Capital T) MED 020 (Bal-tec/Leica Microsystems GmbH, Wetzlar, Germany). Backscattered electron (BSE) images were accomplished on the Merlin (ZEISS) at a voltage of 3 kV. In this case the samples were coated with 6.0 nm carbon (EM ACE600, Leica Microsystems GmbH, Wetzlar Germany or a PECSII, Gatan, Inc., Pleasanton, CA, USA). Average pore size values were determined using the software analySIS (Olympus) or IMS (Imagic Bildverarbeitung AG, Opfikon, Switzerland) on the basis of the SEM results.

### **3.5.6 Energy Dispersive X-rays Analysis (EDX)**

Elemental analysis of the membranes was performed by energy disperse X-rays (EDX) with the Merlin (ZEISS) scanning electron microscope.

### **3.5.7 Fourier Transform Infrared Spectroscopy (FTIR)**

Fourier transform infrared spectroscopy (FTIR) was conducted in an attenuated total reflectance (ATR-diamond crystal) mode with a Bruker ALPHA FT-IR spectrometer (Bruker, Karlsruhe, Germany) in a spectral range of 400 - 4000  $\text{cm}^{-1}$  with a resolution of 2  $\text{cm}^{-1}$  and average of 32 scans.

### **3.5.8 Surface Zeta Potential**

Membrane surface zeta potential was determined using a SurPASS 3 electrokinetic analyzer (Anton Paar, Graz, Austria) with a background of 1 mM NaCl solution. The streaming channel gap height was adjusted at 100  $\mu\text{m}$ . The pH values were adjusted using 50 mM HCl and 50

mM NaOH solutions in a range of 2.5 – 10. Each data point was measured 4 times. The zeta potential ( $\zeta$ ) was calculated from the streaming potential ( $U_{str}$ ) using the Helmholtz-Smoluchowski equation:

$$\zeta = \frac{dU_{str}}{d\Delta p} \frac{\eta}{\varepsilon\varepsilon_0} \frac{l}{A_c} \frac{1}{R_e} \quad 3.1$$

where  $U_{str}$  is the streaming potential,  $\Delta p$  is the hydrodynamic pressure difference across the streaming channel,  $\eta$  is the viscosity of the electrolyte solution,  $\varepsilon$  is the permittivity of the electrolyte solution,  $\varepsilon_0$  is the vacuum permittivity,  $l$  is the length of the streaming channel,  $A_c$  is the cross-section of the streaming channel and  $R_e$  is the electrical resistance inside the streaming channel.

### 3.5.9 Dynamic Water Contact Angle

Dynamic contact angles were measured with 1  $\mu$ L water droplets on a Krüss Drop Shape Analysis System DSA 100 (Krüss GmbH, Hamburg, Germany). At least 3 samples were measured.

### 3.5.10 Thermogravimetric Analysis (TGA)

Thermogravimetric analysis (TGA) was performed using a TGA-DSC2 Thermogravimetric Analyzer (Mettler-Toledo, Gießen, Germany) over the range of 25 to 1000 °C with a heating rate of 10 K min<sup>-1</sup> in an argon atmosphere.

### 3.5.11 Differential Scanning Calorimetry (DSC)

Differential scanning calorimetry (DSC) was carried out with a differential scanning calorimeter DSC1 (Mettler-Toledo, Gießen, Germany) in a temperature range between  $-50\text{ }^{\circ}\text{C}$  and  $200\text{ }^{\circ}\text{C}$  under a nitrogen atmosphere and at a heating rate of  $20\text{ K min}^{-1}$ .

### 3.5.12 Membrane Performance Tests

#### 3.5.12.1 Water Permeance Measurements

Water permeance measurements were performed in dead-end mode using a home-made automatic testing device (Figure 3.2) at transmembrane pressures ( $\Delta P$ ) up to 1-2 bar at room temperature. The volume change  $\Delta v$  was measured gravimetrically for time slots  $\Delta t$  of 1-3 min for 2-24 h. The effective membrane area  $A_m$  was  $1.77\text{ cm}^2$ . These studies were carried out employing demineralized water with an electrical conductivity of  $\approx 0.055\text{ }\mu\text{S cm}^{-1}$  and a density of  $0.998\text{ g cm}^{-3}$ . A minimum of 3 samples was measured. The water permeance ( $J_w$ ) was calculated by normalizing the flux by the transmembrane pressure.

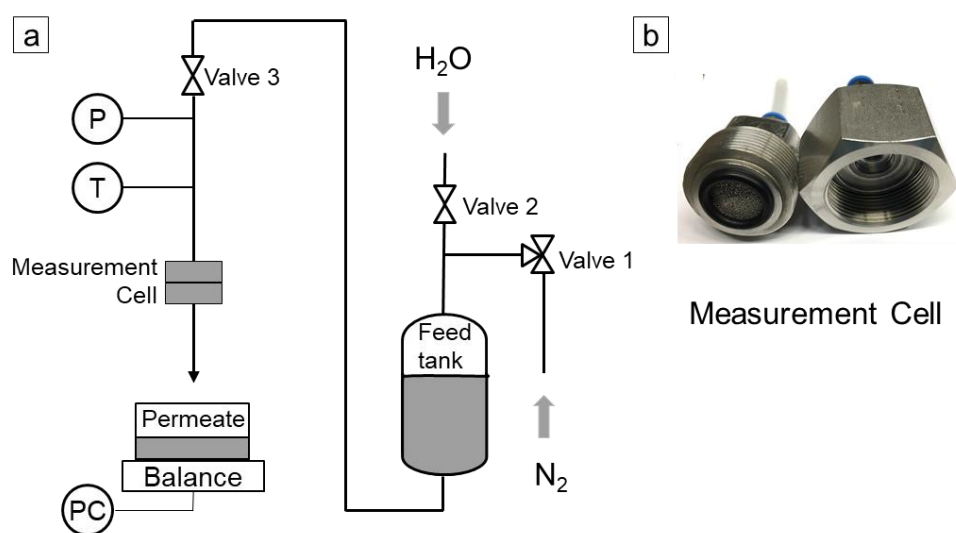


Figure 3.2. (a) Schematic representation of the home-made automatic testing device. (b) Measurement cell.

The water permeance was calculated using the following equation:

$$J_w = \frac{\Delta v}{A_m \Delta t \Delta P} \quad 3.2$$

### 3.5.12.2 Retention Measurements

Retention measurements were carried out using a stirred test cell (EMD Millipore™ XFUF04701, Darmstadt, Germany, Figure 3.3a) at a transmembrane pressure of 2 bar at room temperature. The effective membrane area was reduced to 1.77 cm<sup>2</sup> by using an in-house prepared reduction ring, as shown in Figure 3.3b. Before the membranes were challenged with the solute solutions, ultrapure water was initially passed through the membranes for 0.5 h to stabilize the porous structure of membrane. Afterwards, all water was removed from the test cell and also the membrane was dried completely using a tissue (Kimwipe). A series of aqueous solutions of organic solutes was prepared separately at the concentrations of 0.1 mM, e.g. methylene blue (MB+), riboflavin (RB0), Orange II (OR-), naphthol green B (NG3-) and reactive green 19 (RG6-). Subsequently, a 70 ml aqueous solution was added to the stirred cell. To minimize the effects of concentration polarization, the feed solution was stirred at 500 rpm during measurements. The permeate solution was collected in disposable centrifuge tubes with screw caps. In the case of the pristine membrane I0, which showed the water flux in the ultrafiltration regime, 70 ml aqueous solution ran out within 30 min. Two permeate solutions were collected, e.g., each 10 min one permeate was collected. In the case of post-functionalized membranes, three permeates were collected successively, *i.e.*, each one hour one permeate was collected. Meanwhile, 2 ml of retentate solution was also sampled to determine the retentate concentration for each permeate. All the feed, permeate and retentate samples were sealed properly with screw cap and refrigerated to prevent water evaporation before determination of the concentration. The last permeate solution was used as the final retention performance. The

stirred cell was emptied, and washed with ultrapure water and subsequent acetone between each test. Measurements were made on a minimum of 3 samples.



Figure 3.3. (a) A photo of the employed EMD Millipore XFUF04701 cell, (b) Photos of the in-house prepared reduction ring to reduce the effective membrane size.

The concentration of the solutes in the feed solutions  $C_f$  ( $\text{mg L}^{-1}$ ), permeate solutions  $C_p$  ( $\text{mg L}^{-1}$ ) and retentate solutions  $C_r$  ( $\text{mg L}^{-1}$ ) was determined by a UV-vis spectrophotometer (GENESYS 10S, Thermo Scientific, Dreieich, Germany) and the retention ( $R_0$ , %) of the solutes was calculated using Equation 3.3:

$$R_0 = \left(1 - \frac{C_p}{(C_f + C_r)/2}\right) \times 100 \quad 3.3$$

Two-solute separation measurements were performed using the same procedure as mentioned above. For all the mixtures the molar composition between two solutes is 1:1, but the total solute concentration in the feed was kept at 0.1 mM.

To quantify the figure of merit for molecular separation, we calculated the selectivity  $\psi$ , defined as the ratio of transmission of two species using Equation 3.4:

$$\text{Selectivity } \psi = \frac{1-R_{01}}{1-R_{02}} \quad 3.4$$

where  $R_{01}$  and  $R_{02}$  were observed retention values of the two different solutes.

### 3.5.12.3 Adsorption Measurements

Adsorption measurements were accomplished with different solutes, *e.g.* MB<sup>+</sup>, RB0, OR<sup>-</sup>, NG3<sup>-</sup> and RG6<sup>-</sup>. 2 mL of an aqueous solution of solutes with the concentration of 0.1 mM were placed on a membrane disc of 0.6-2 cm in diameter in a small closed vial. The vials were shaken at 90 rpm for 24 h at 25 °C to reach equilibrium. The membrane was rinsed two times with 2 mL H<sub>2</sub>O for 10 minutes. The solute adsorption on the membrane was calculated as follows:

$$\text{Solute adsorbed} = \frac{m(\text{ads,solute})}{\text{membrane area}} = \frac{m_0 - (m_1 + m_{w1} + m_{w2})}{A_m} \quad 3.5$$

where  $m_0$  is the mass of the solute in the solution before the adsorption experiment,  $m_1$  is the mass of the solute in the solution after the adsorption experiment, and  $m_{w1}$  and  $m_{w2}$  are the masses of solute in the washing solutions and  $A_m$  is the membrane area. The concentration of the solution was determined by a UV-vis spectrophotometer (GENESYS 10S, Thermo Scientific, Dreieich, Germany).

### 3.5.12.4 Dynamic Filtration Measurements for Antifouling Property

The dynamic filtration of 0.1 mM aqueous solutions of individual foulants was performed using the aforementioned dead-end stirred test cell (EMD Millipore™ XFUF04701, Darmstadt,

Germany, Figure 3.3a) at a transmembrane pressure of 1 bar at room temperature. Pure water initially passed through the membrane for 30 min and the average permeance was calculated as  $J_{w0}$ . The feed solution was then changed to the model foulant solution (e.g. 0.1 mM OR- and RG6- aqueous solutions). The filtration of the foulant solution was conducted for 3 h while the corresponding permeate permeance ( $J_p$ ) was recorded every 10 min. After filtration of the foulant solution, the membranes were washed with demineralized water for 20 min, then the pure water permeance of the cleaned membrane ( $J_{w1}$ ) was measured again for 30 min. To evaluate the antifouling property in details, several ratios were defined, *i.e.* the flux recovery ratio ( $FRR$ , %) in Equation 3.6, the total flux decline ratio ( $FDR_t$ , %) in Equation 3.7, the reversible flux decline ratio ( $FDR_r$ , %) in Equation 3.8 and the irreversible flux decline ratio ( $FDR_{ir}$ , %) in Equation 3.9, as shown below:

$$FRR = \frac{J_{w1}}{J_{w0}} \times 100\% \quad 3.6$$

$$FDR_t = \left(1 - \frac{J_p}{J_{w0}}\right) \times 100\% \quad 3.7$$

$$FDR_r = \left(\frac{J_{w1} - J_p}{J_{w0}}\right) \times 100\% \quad 3.8$$

$$FDR_{ir} = \left(\frac{J_{w0} - J_{w1}}{J_{w0}}\right) \times 100\% \quad 3.9$$

# **Chapter 4 PS-*b*-P4VP Isoporous Membranes with Tunable Positively Charged Nanochannels**

Molecular characterization of polymer used in this chapter.

Polymer	PS [wt%]	P4VP [wt%]	M <sub>n</sub> [kg mol <sup>-1</sup> ]	M <sub>w</sub> [kg mol <sup>-1</sup> ]	Dispersity indices
PS <sub>81</sub> - <i>b</i> -P4VP <sub>19</sub> <sup>154K</sup>	82	18	143	154	1.08

## 4.1 Introduction

The introduction of charged functional groups into the pore-forming block can not only tune the pore size by the swelling of the polyelectrolytes along the pore wall in a hydrated state but also endow the nanochannels with a charge function. The resulting charged membrane can separate molecules or particles based on not only their size but also charge features, which may hold much potential for their applications in the removal/recovery of dyes, water purifications and separation of valuable molecules, etc.

In this chapter, positively charged isoporous membranes were prepared based on PS-*b*-P4VP diblock copolymer. The previous studies reported that the tailoring of the pore size is dependent on protonation<sup>43, 44, 55, 57, 58</sup> or deprotonation<sup>42, 59</sup> of functional groups of the pore-forming block. Herein the quaternization of P4VP was employed to bring about positively charged polyelectrolytes along the pore wall. Their swelling behaviour in a hydrated state is not limited to the acid condition. Alkyl iodides with different sizes of alkyl groups (i.e. MeI, EtI and 1-PrI) were used as quaternization agent and the degree of quaternization was varied to construct an adjustable pore size and surface functionality of the positively charged membrane. The resulting positively charged membranes were evaluated by their capability to reject a small cationic dye molecule.

## 4.2 Quaternization of PS-*b*-P4VP Membranes

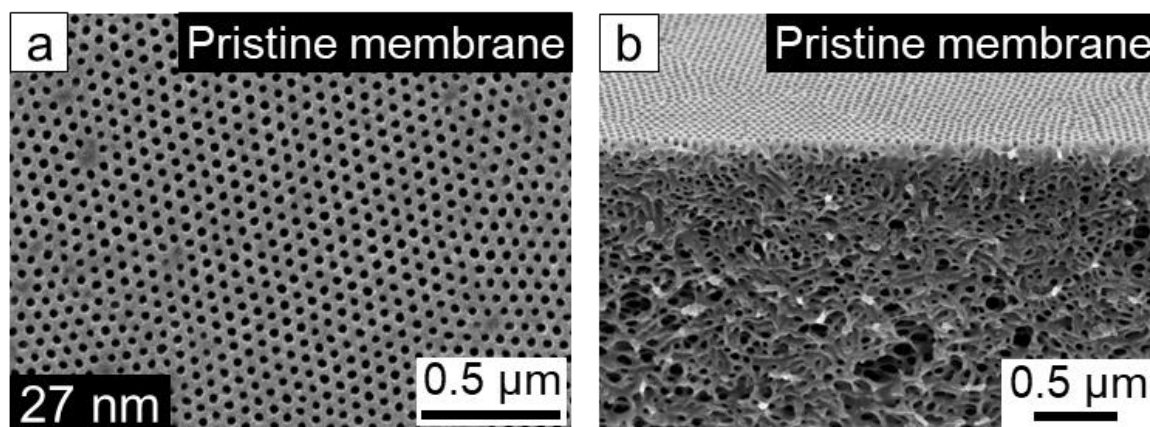


Figure 4.1. Secondary electron (SE) images of SEM of the pristine membrane: (a) top surface and (b) cross section.

A PS-*b*-P4VP diblock copolymer was prepared by living anionic polymerization with a molecular weight of  $154 \text{ kg mol}^{-1}$ , a narrow dispersity index of 1.08, and the composition of 82 wt% PS and 18 wt% P4VP. The integral asymmetric isoporous membranes were prepared using a 26.5 wt% casting solution in THF/DMF 40/60 mixture with a 10 s evaporation time (Figure 4.1a and b). The average pore size at the top surface of the membrane was 27 nm. To retain the original integral asymmetric isoporous structure, the quaternization has to be employed under a mild heterogeneous condition, for instance, by using a non-solvent as the reaction medium<sup>12</sup> or a vapor-phase reaction without any solvent.<sup>122, 123</sup> In this study, a straightforward *in situ* scalable gas-solid interface reaction was selected to carry out the quaternization of a PS-*b*-P4VP membrane (Figure 4.2a). The comparison of FTIR spectra,  $^1\text{H}$  NMR spectra and SEM micrographs of the pristine and the quaternized membrane are depicted in Figure 4.1, Figure 4.2 and Figure 4.3.

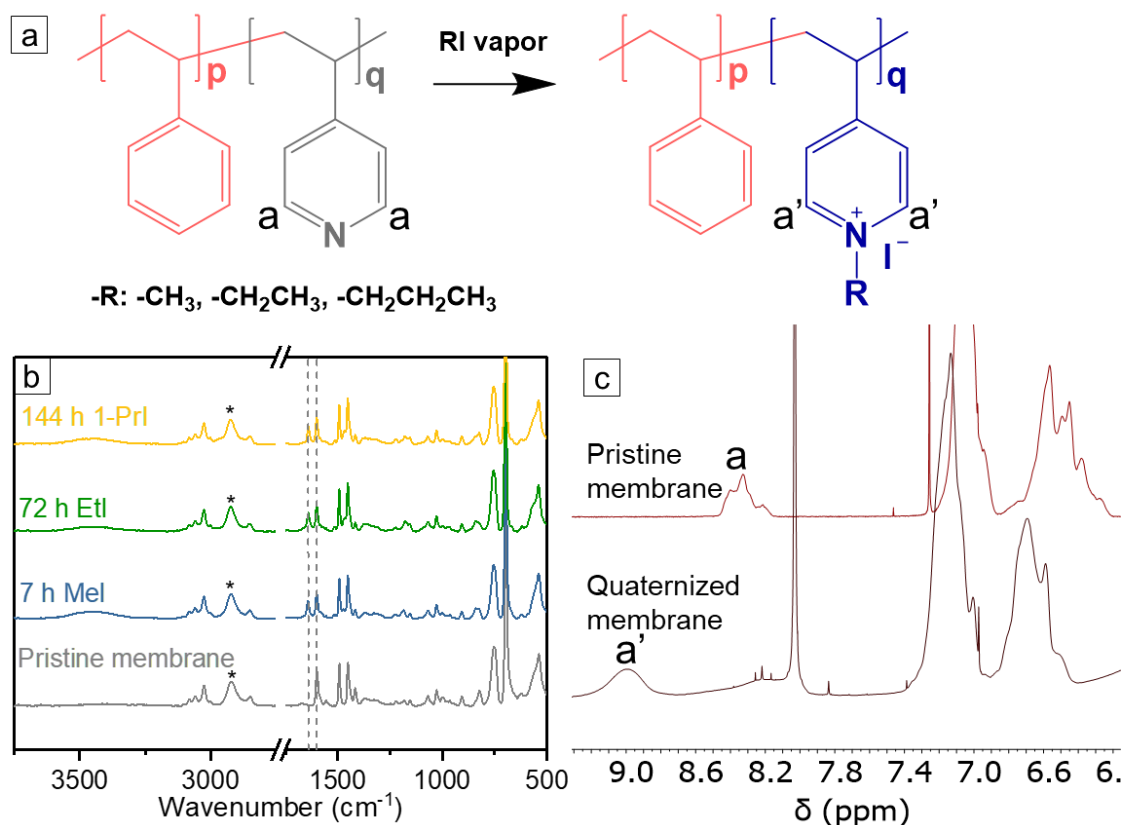


Figure 4.2. (a) Reaction scheme of quaternization of the PS-*b*-P4VP membrane. (b) ATR-FTIR spectra of the pristine membrane and the quaternized membranes with MeI, EtI and 1-PrI. The relative intensities were normalized using the characteristic CH<sub>2</sub> stretching vibrations (\*) of the unreactive backbone around 2924 cm<sup>-1</sup>. (c) <sup>1</sup>H NMR spectra of the pristine membrane and the representative quaternized membrane with 3 days MeI.

In the FTIR spectrum (Figure 4.2b), the pristine membrane shows a characteristic peak at ca. 1600 cm<sup>-1</sup> due to the stretching vibration of C=N and C=C of the aromatic rings. Quaternized membranes with MeI, EtI and 1-PrI show a characteristic peak for the C=N<sup>+</sup> stretching vibration at ca. 1640 cm<sup>-1</sup>.<sup>124</sup> Since after quaternization the stretching vibration of C=N has partially disappeared, the intensity of stretching vibration at ca. 1600 cm<sup>-1</sup> becomes weaker than that of the pristine membrane. Moreover, a broad signal appears at ca. 3400 cm<sup>-1</sup> due to water molecules associated with the quaternized 4VP groups. In the <sup>1</sup>H NMR spectrum of the pristine membrane, the chemical shift at 8.75 ppm (peak a) is ascribed to two protons of

unquaternized pyridine groups. The characteristic chemical shift at 8.95 ppm (peak a') appears from two corresponding protons of quaternized pyridine groups in the  $^1\text{H}$  NMR spectrum of the quaternized membrane (Figure 4.2c). The results confirm that the quaternization successfully occurs with the vapour-phase reaction.

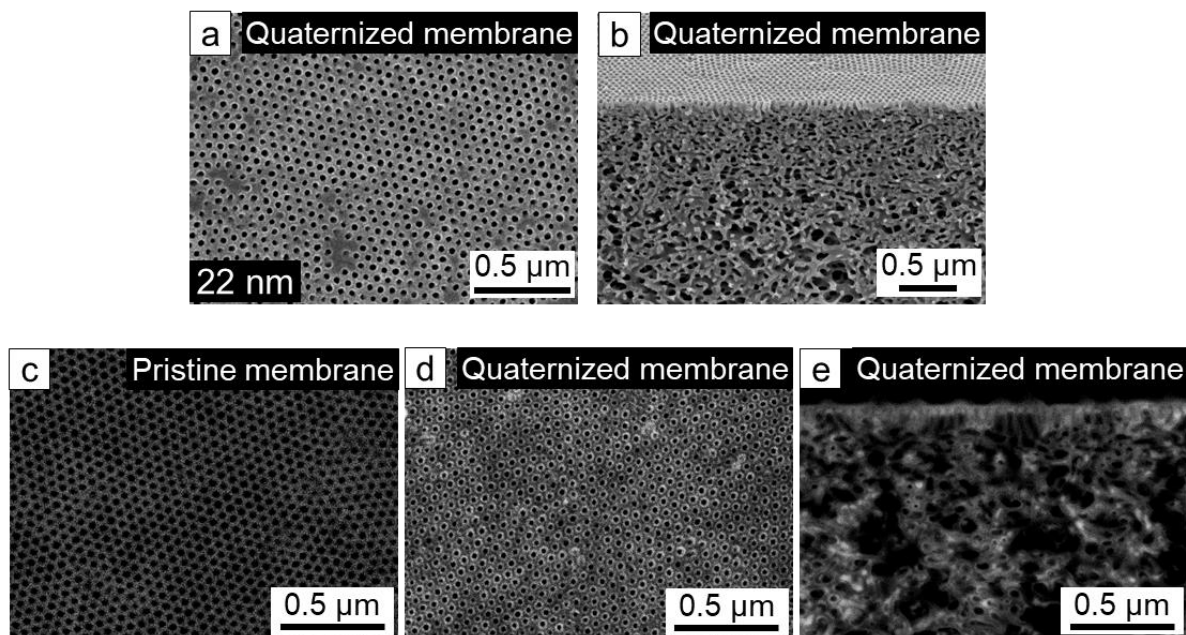


Figure 4.3. Secondary electron (SE) images of SEM of the representative quaternized membrane after 3 days exposure to MeI: (a) top surface and (b) the cross section. Back scattered electron (BSE) images of SEM: (c) top surface of the pristine membrane, (d, e) top surface and cross section of the representative quaternized membrane after 3 days exposure to MeI.

Furthermore, the membrane clearly retains the integral asymmetric isoporous structure after quaternization (Figure 4.3a, b). Owing to the extra attachment of alkyl iodide molecules along the pore walls, the pores on the top surface of the quaternized membrane become 22 nm (Figure 4.3a) while those of the pristine membrane are 27 nm (Figure 4.1a). The back scattered electron (BSE) imaging mode of SEM was used to determine the distribution of the electron rich iodide counterion. The BSE image of the top surface of IO (Figure 4.3c) does not show any contrast between the matrix-forming block PS and the pore-forming block P4VP as the atomic number

of C and N are next to each other. Whereas, there are brighter rings with a uniform thickness along the pore walls of the quaternized membrane, assigned to the electron rich iodide, indicating the homogeneity of quaternization on the top surface (Figure 4.3d). The cross-sectional image also displays the uniform distribution of iodide, which confirms the uniform quaternization of the P4VP block all over the membrane (Figure 4.3e).

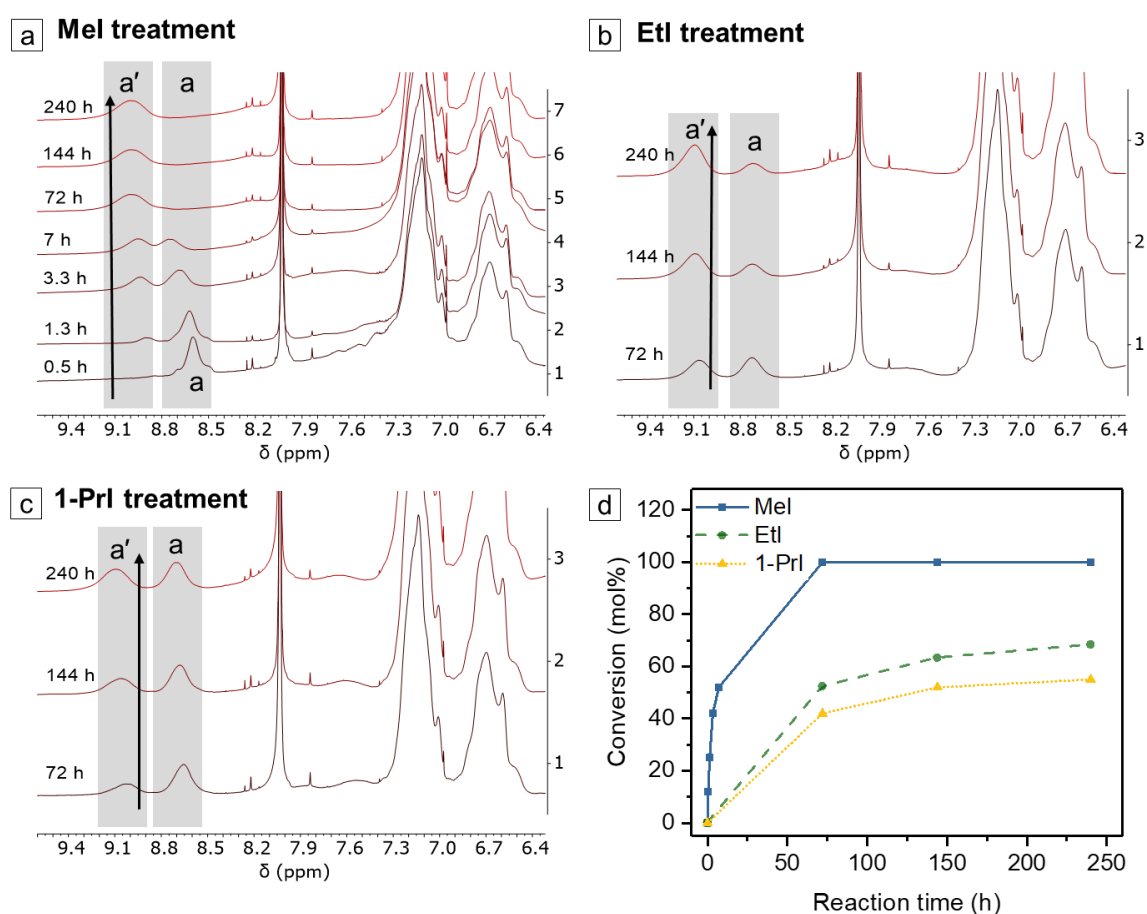


Figure 4.4.  $^1\text{H}$  NMR spectra of (a) the membranes quaternized with MeI as a function of time, (b) the membranes quaternized with EtI as a function of time, (c) the membranes quaternized with 1-PrI as a function of time. (d) Degree of quaternization of P4VP via MeI, EtI, and 1-PrI as a function of time based on the calculation from  $^1\text{H}$  NMR spectra.

In order to control the degree of quaternization with MeI, EtI, and 1-PrI the duration of reaction was varied. As shown in Figure 4.4a-c, the peak originating from the quaternized pyridine

groups increases with the duration of quaternization while that from the unquaternized pyridine groups decreases simultaneously. Therefore, the degree of quaternization for three series of the membranes quaternized with MeI, EtI and 1-PrI can be deduced from  $^1\text{H}$  NMR spectra precisely (Figure 4.4d). Specifically, the degree of quaternization was estimated from the molar ratio of the quaternized 4VP repeating units to the whole 4VP repeating units, including both unquaternized and quaternized 4VP repeating units. In other words, it was calculated from the ratio of the integrated value of the peak from quaternized 4VP (e.g. peak a') to the total integrated value of the peaks from quaternized 4VP and unquaternized 4VP (e.g. peak a and peak a'). The reaction rate gradually decreases with increasing reaction time. In the case of MeI, after 72 h reaction, the pyridine groups were totally quaternized. The reaction rates of the three alkyl iodides follow the sequence  $\text{MeI} > \text{EtI} > 1\text{-PrI}$ , in accordance with their alkylation ability, probably due to the steric hindrance (Figure 4.4d).

### 4.3 Quaternized PS-*b*-P4VP Membranes with Tailored Pore Size in Hydrated State

### 4.4 Influence of the Size of Alkyl Groups on the Membrane Morphology and Performance

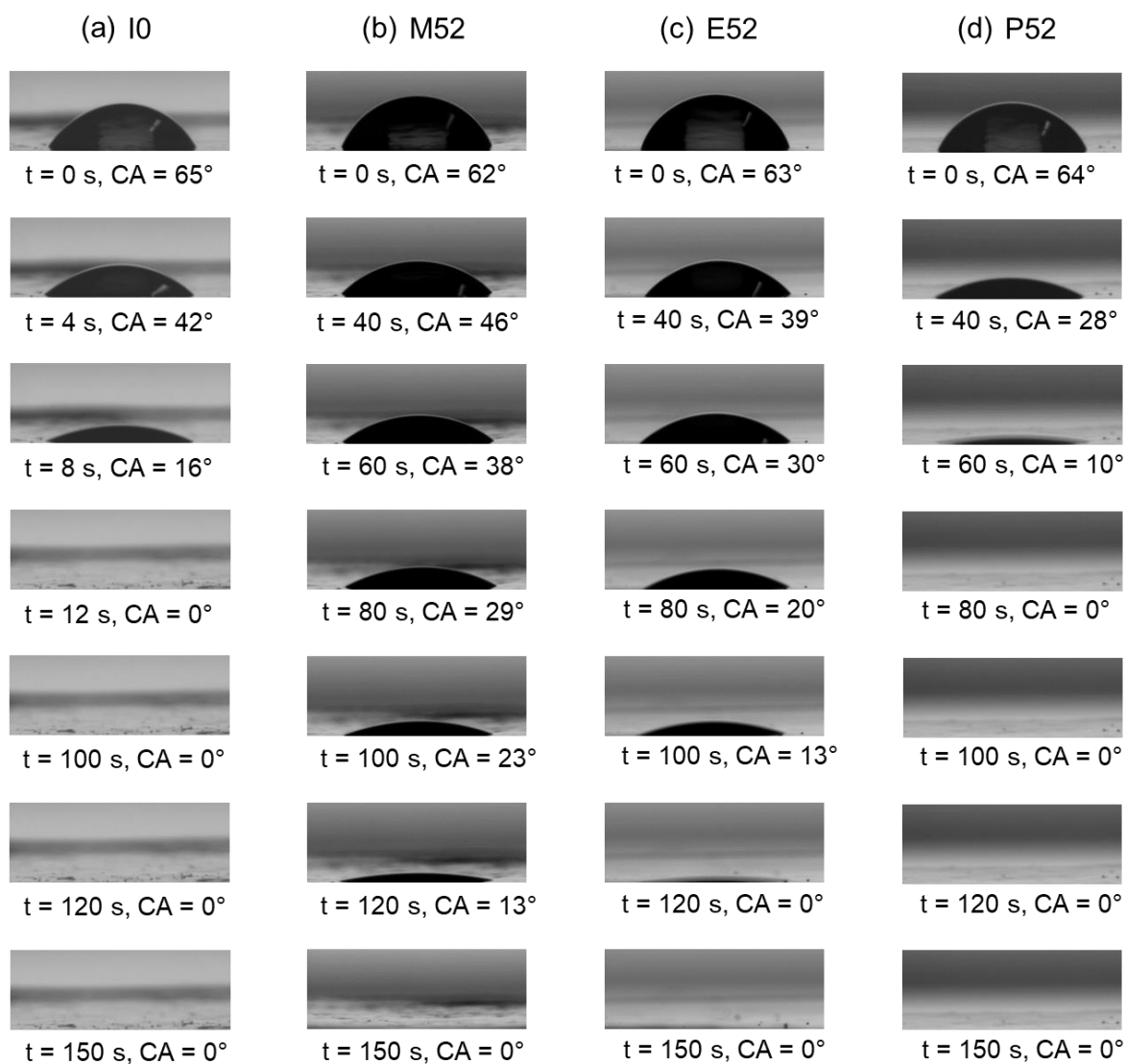


Figure 4.5. Snapshots of dynamic contact angle of a water droplet onto (a) I0 surface (b) M52 surface, (c) E52 surface, (d) P52 surface.

We have compared the membranes with ca. 52% quaternization of 4VP repeating units by MeI (M52), EtI (E52) and 1-PI (P52) to investigate the influence of the size of alkyl groups on the morphology and separation performance of the membranes. The dynamic contact angle of a water droplet was monitored at the surface of the pristine membrane (I0), M52, E52, and P52. Figure 4.5 shows the snapshots of a sinking water droplet at the surface of I0, M52, E52 and P52. In case of I0, the water droplet totally sinks into the membrane after ca. 12 s due to the big open pores. To compare the sinking rate of a water droplet, the contact angle vs time is provided in Figure 4.6a. The sinking rate of a water droplet is much lower in the quaternized membranes compared to I0, which follows the sequence,  $M52 < E52 < P52 < I0$ . The results (Figure 4.5, Figure 4.6a) imply that these membranes have different resistance against the permeation of a water droplet.

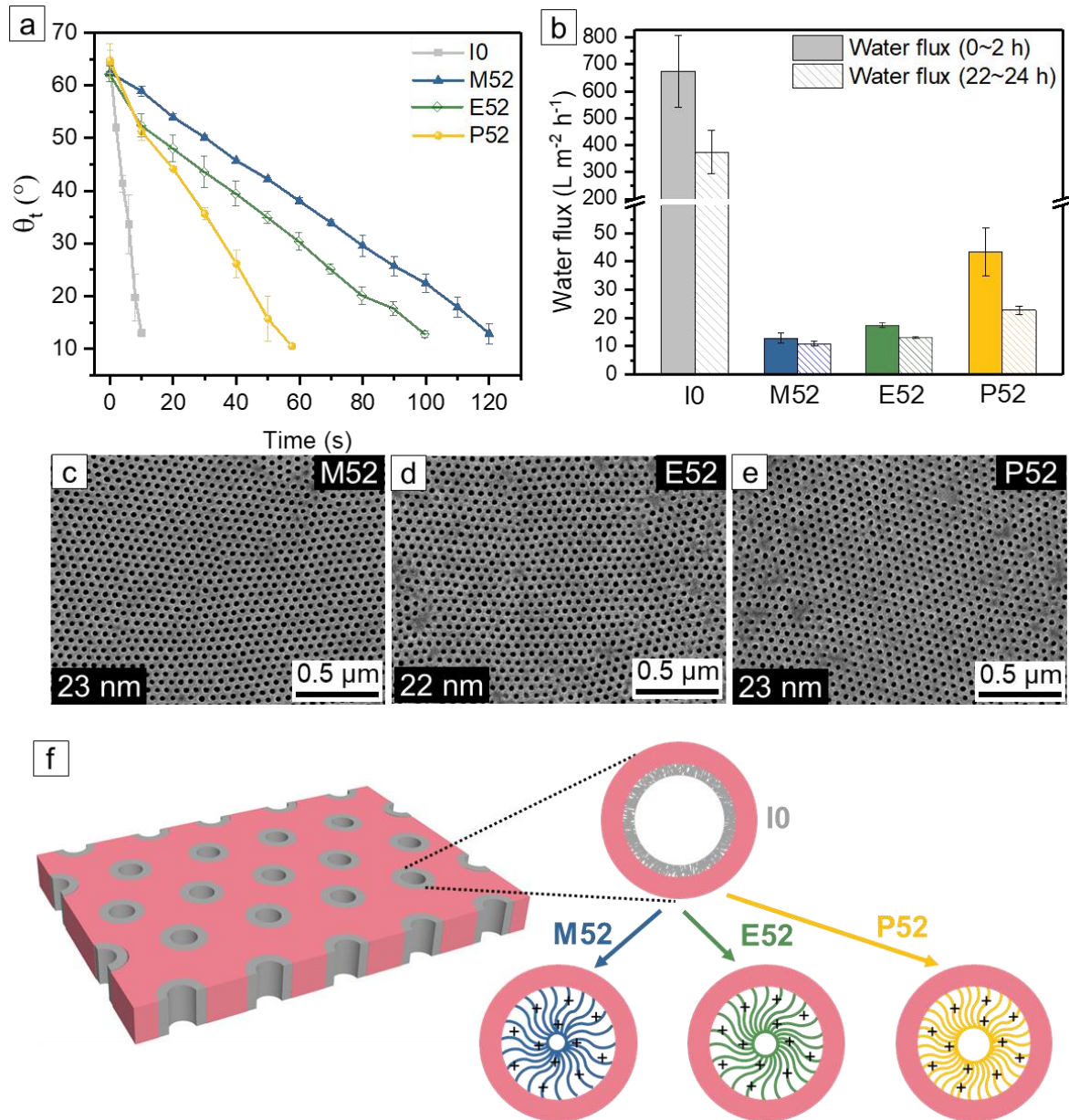


Figure 4.6. (a) The change of contact angles onto I0, M52, E52 and P52 surface with time. (b) Water flux of I0, M52, E52 and P52 at a transmembrane pressure up to 1 bar at room temperature. Secondary electron (SE) images of SEM: top surface of (c) M52, (d) E52, (e) P52. (f) Schematic representation of I0, M52, E52 and P52 in the hydrated state.

To provide further evidence of this phenomenon, the water flux ( $J_w$ ) through I0, M52, E52 and P52 was determined using a dead-end mode filtration device at a trans-membrane pressure of 1 bar. In accordance with the sinking rate of the water droplet, the water fluxes follow the sequence  $J_{wM52} < J_{wE52} < J_{wP52} \ll J_{wI0}$  (Figure 4.6b). The average pore sizes of the isoporous

layer of M52, E52 and P52 are 22 – 23 nm (Figure 4.6c-e) while that of I0 is 27 nm (Figure 4.1a) according to SEM images. In spite of such small difference, for the first 2 hours of water flux measurement,  $J_{wM52}$  is ca. 52 times lower than  $J_{wI0}$  while  $J_{wP52}$  is ca. 15 times lower than  $J_{wI0}$ . During SEM investigation the pore-forming blocks of the membranes were in a collapsed state as the membranes were completely dry. Owing to their polyelectrolyte nature, the quaternized P4VP blocks of M52, E52 and P52 were dissociated in water, making the pore-forming P4VP block partially charged and significantly swelled during the water flux measurement. As the hydrophobic PS matrix was fixed in space, the repulsive electrostatic interaction among the charged 4VP repeating units induced chain stretching toward the centre of the pore, resulting in the smaller effective pore size. The constrained pore size imposed resistance to water penetration through the membrane. Moreover, the water flux through P52 is three times higher compared to that through M52, which proves that the stretching of a P4VP block quaternized by 1-PrI is significantly lower than that quaternized by MeI (Figure 4.6f). The hydrophilicity of the quaternized P4VP decreases with increasing the size of the alkyl group of the quaternization agent.<sup>125</sup> The lower hydrophilicity of the pore-forming block of P52 leads to lower stretching in a hydrated state compared to that of E52 and M52. Consequently, the effective pore size, the rate of sinking of the water droplet (Figure 4.6a), and the water flux (Figure 4.6b) are higher in the case of P52 compared to E52 and M52. The water flux measurements were carried out for 24 h. A gradual decrease of water flux as a function of time is observed. The average water fluxes during the first 2 h measurement ( $(J_{wM52} (13 \text{ L m}^{-2} \text{ h}^{-1}) < J_{wE52} (17 \text{ L m}^{-2} \text{ h}^{-1}) < J_{wP52} (43 \text{ L m}^{-2} \text{ h}^{-1}) \ll J_{wI0} (675 \text{ L m}^{-2} \text{ h}^{-1}))$ ) and during the last 2 h measurement ( $(J_{wM52} (11 \text{ L m}^{-2} \text{ h}^{-1}) < J_{wE52} (13 \text{ L m}^{-2} \text{ h}^{-1}) < J_{wP52} (23 \text{ L m}^{-2} \text{ h}^{-1}) \ll J_{wI0} (375 \text{ L m}^{-2} \text{ h}^{-1}))$ ) show a similar trend, which proves the quaternization is stable during the water flux measurement (Figure 4.6b). In previous studies, it was reported that the hydrophilicity of cross-linked membranes containing amine<sup>126</sup> and 4VP<sup>125</sup> moieties can be tuned by changing the size

of the alkyl group (methyl, ethyl and 1-propyl) of the quaternization agent. Since in a PS-*b*-P4VP SNIPS membrane only one end of the pore-forming block (P4VP) was attached to the matrix-forming block (PS), we utilized this phenomenon to tailor the effective pore size of the membrane in the hydrated state.

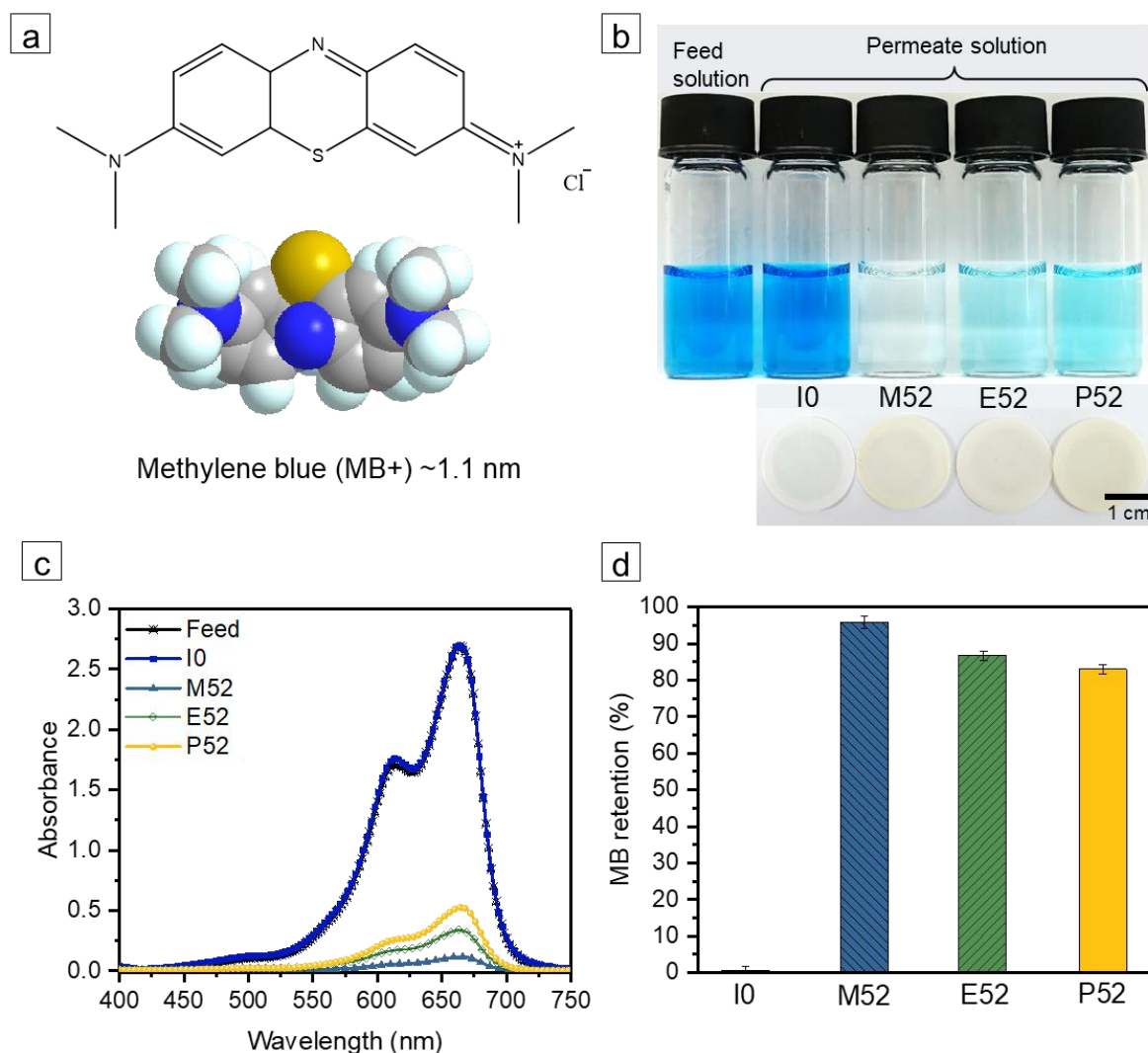


Figure 4.7. (a) Molecular structure and space-filling model of methylene blue (MB<sup>+</sup>). (b) The photography of the feed and permeate solutions of I0, M52, E52, and P52, and the prepared membranes after MB<sup>+</sup> rejection measurements using a 10 mg L<sup>-1</sup> feed solution. (c) UV-vis absorbance of the feed and the permeate solutions of I0, M52, E52, and P52 with feed solution of concentration 10 mg L<sup>-1</sup>. (d) MB<sup>+</sup> retention of I0, M52, E52, and P52 with feed solution of concentration 10 mg L<sup>-1</sup>.

The performance of the membranes was tested by investigation of their separation properties of the model cationic small molecule methylene blue (MB<sup>+</sup>) (MB<sup>+</sup> structure depicted in Figure 4.7a). The permeability and selectivity of membranes can be assessed via two methods: concentration-driven diffusion<sup>126-132</sup> and pressure-driven flow. We determined the separation properties of the model molecules from pressure-driven flow of aqueous solutions as it is more relevant to a realistic application compared to a diffusion cell experiment. Additionally, under applied pressure, some polymers self-regulate to change their conformation, leading to significant changes in the effective pore size and rejection behaviour of the membranes.<sup>133, 134</sup> Figure 4.7b shows that the colour of the permeate solution through I0 is similar to the feed solution. In the permeate solutions through M52, E52 and P52, a substantial reduction of colour is observed. The concentration of MB<sup>+</sup> in the feed solution  $C_f$  (mg L<sup>-1</sup>) and permeate solutions  $C_p$  (mg L<sup>-1</sup>) was determined via UV-vis spectroscopy (Figure 4.7c). Figure 4.7d shows for a 10 mg L<sup>-1</sup> feed solution that the retentions follow the sequence  $R_{M52}$  (96%) >  $R_{E52}$  (87%) >  $R_{P52}$  (83%)  $\gg$   $R_{I0}$  (~0). Similar to the permeation of water, P52 has the lowest resistance against permeation of MB<sup>+</sup> while M52 has the highest resistance. In general, the rejection of a charged solute originates from a combined effect of size exclusion and electrostatic repulsion with a charged porous membrane.<sup>135</sup> As the retention gradually decreases with increasing effective pore size, it is clear that the retention of MB<sup>+</sup> in M52, E52 and P52 is largely dictated by size exclusion. Figure 4.7b displays after the dye retention measurement that I0 becomes bluish in colour, indicating the affinity of the cationic dye MB<sup>+</sup> with the 4VP groups of the membrane. The colour changes of M52, E52 and P52 are significantly lower compared to that of I0. Hence, we assume that the quaternized 4VP groups repel the cationic MB<sup>+</sup> due to electrostatic repulsion, which also contributes to the high retention of MB<sup>+</sup>. The colour difference between I0 and the quaternized membranes M52, E52 and P52 are more obvious when the 100 mg L<sup>-1</sup> aqueous solution of MB is used for the retention measurement (Figure 4.8a). For 100 mg L<sup>-1</sup>

feed solution the MB retentions are  $R_{M52}$  (97%)  $\approx R_{E52}$  (95%)  $\approx R_{P52}$  (96%)  $\gg R_{I0}$  (6%) which are higher than those for 10 mg L<sup>-1</sup> feed solution (Figure 4.8b, c). It is well known that the ionic dyes tend to aggregate in solution which is related to dye concentration.<sup>136</sup> It was reported in the literature that MB<sup>+</sup> exists in a single molecular state in aqueous solution up to 30 mg L<sup>-1</sup>, while at a concentration  $> 60$  mg L<sup>-1</sup> it tends to form aggregates.<sup>137, 138</sup> This probably is the reason behind the similar retention efficiency of M52, E52 and P52 for 100 mg L<sup>-1</sup> feed solution.

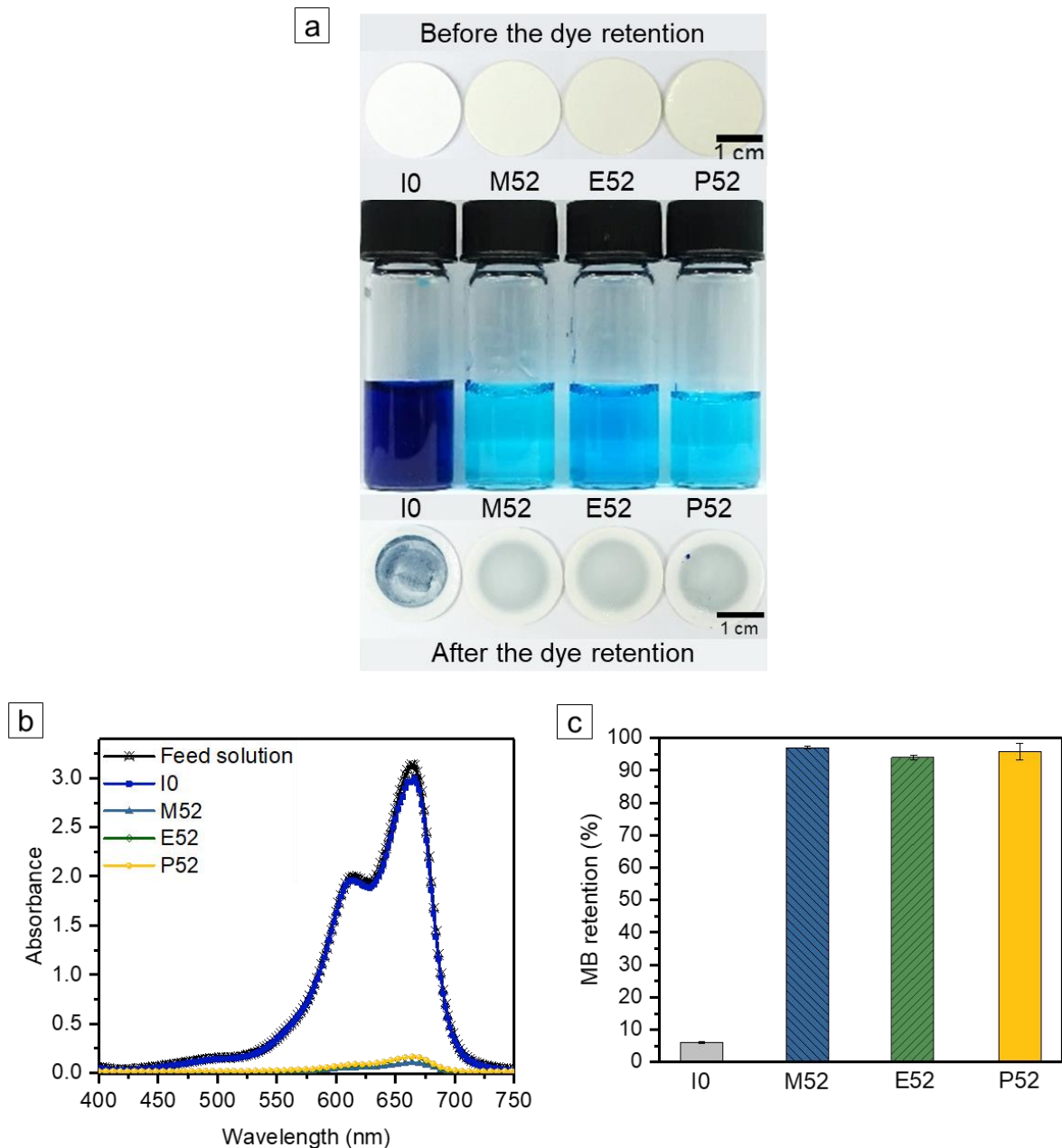


Figure 4.8. (a) The photographs of permeate solutions of I0, M52, E52, and P52, and the prepared membranes before and after MB<sup>+</sup> rejection measurements using a 100 mg L<sup>-1</sup> feed solution. (b) UV-vis absorbance of the permeate solutions of I0, M52, E52, and P52 using a 100 mg L<sup>-1</sup> feed solution. (c) MB<sup>+</sup> rejection of I0, M52, E52, and P52 using a 100 mg L<sup>-1</sup> feed solution.

#### 4.4.1 Influence of the Degree of Quaternization on the Membrane Morphology and Performance

Table 4.1 Preparation of a series of the membranes quaternized with MeI and 1-PrI.

	Conversion <sup>a)</sup> (mol%)	12	25	42	52	55 <sup>b)</sup>	100 <sup>c)</sup>
Reaction time (h)	MeI	0.5	1.3	3.3	7	--	72
	1-PrI	4	13.5	72	144	240	--

<sup>a)</sup> Molar percentage calculated from <sup>1</sup>HNMR; <sup>b)</sup> The maximum degree of quaternization with 1-PrI under the optimal condition of this study; <sup>c)</sup> The maximum degree of quaternization with MeI.

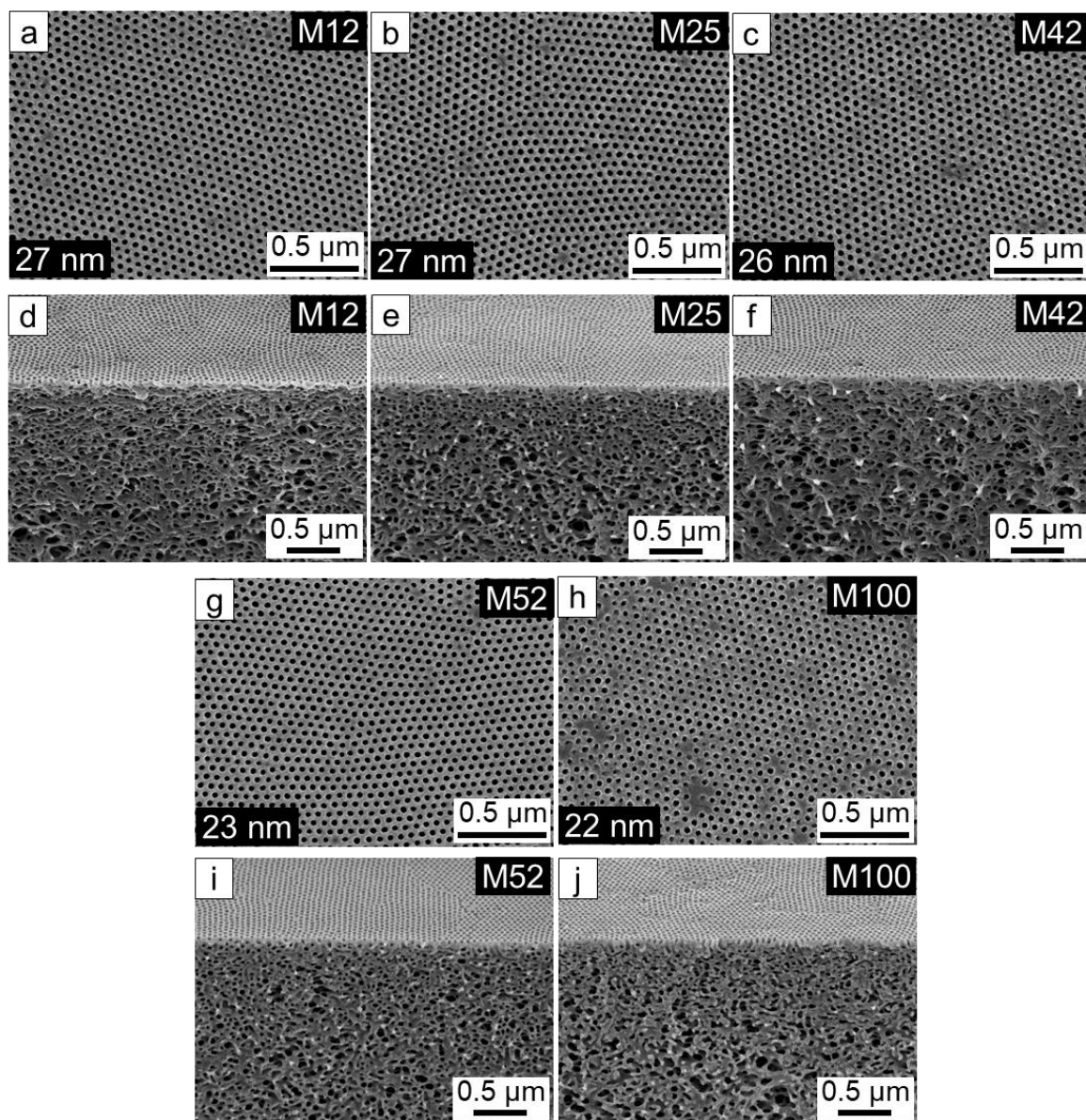


Figure 4.9. Secondary electron (SE) images of SEM: top surface and cross section of (a, d) M12, (b, e) M25, (c, f) M42, (g, i) M52, (h, j) M100.

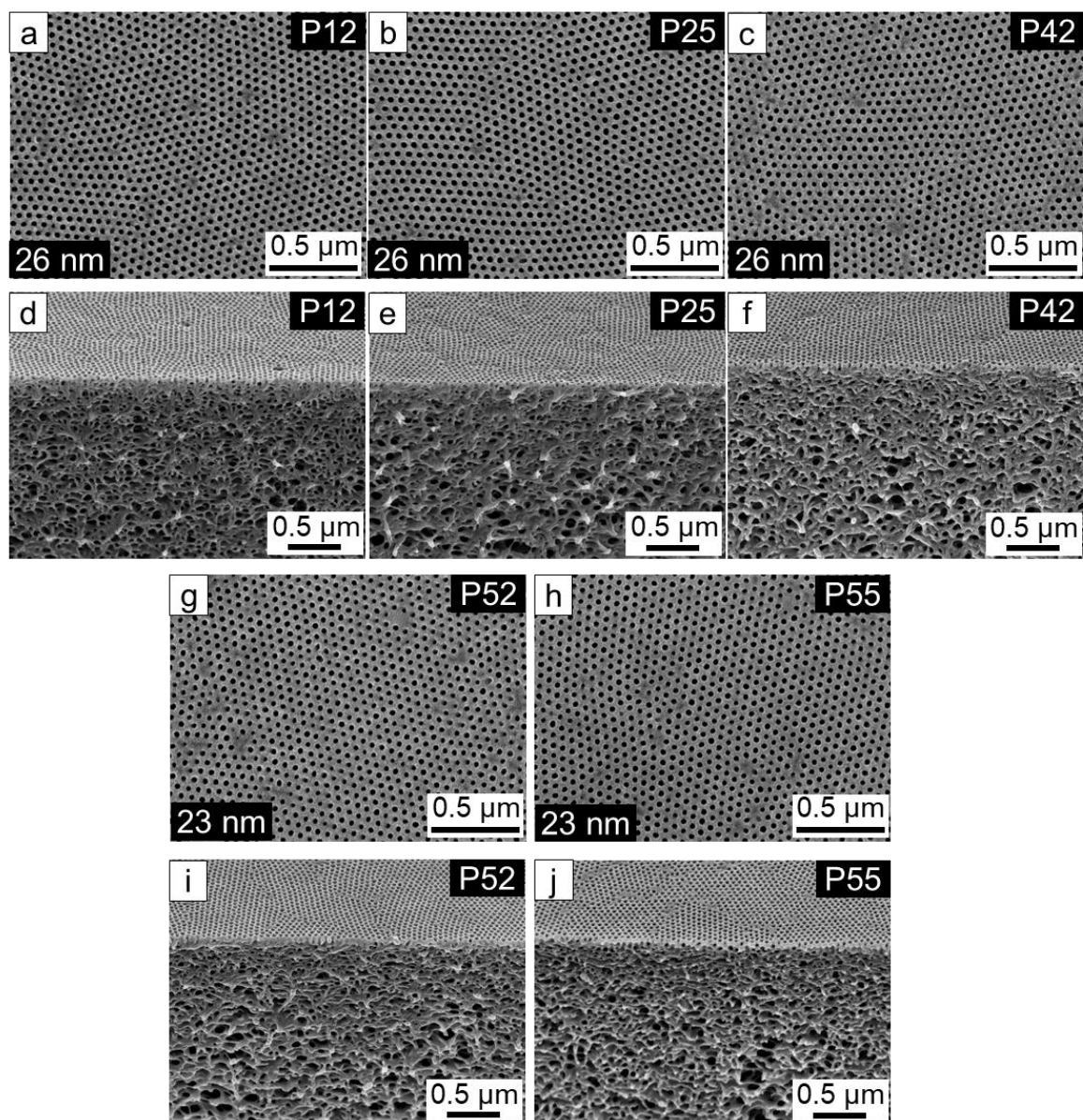


Figure 4.10. Secondary electron (SE) images of SEM: top surface and cross section of (a, d) P12, (b, e) P25, (c, f) P42, (g, i) P52, (h, j) P55.

From Section 4.4, it is evident that M52 and P52 have relatively obvious differences in hydrophilicity. Therefore, we compare the pure water flux (Figure 4.11a) and MB<sup>+</sup> rejection from 10 mg L<sup>-1</sup> aqueous solution (Figure 4.11b) of membranes with a series of different degrees of quaternization with MeI and 1-PrI (Table 4.1, Figure 4.9 and Figure 4.10), namely M12, M25, M42, M52, M100, P12, P25, P42, P52 and P55 (the letters M and P stand for MeI and 1-

PrI while the following number stands for the degree of quaternization, respectively). A decrease of the pure water flux and an increase of MB<sup>+</sup> rejection are observed with the increase of the degree of quaternization. These results demonstrate that the effective pore size of both of the series of quaternized membranes can be successfully tailored by controlling the degree of quaternization in a wide range. For the same degree of conversion (in the range 12 – 52%), the membranes quaternized by 1-PrI has a higher water flux and a lower MB<sup>+</sup> retention compared to MeI, which proves again that the effective pore size can be tuned by controlling the size of alkyl groups. A sharp increase of MB<sup>+</sup> retention is observed for M25 compared to M12. A similar increase of MB<sup>+</sup> retention is also observed for P42 compared to P25. Moreover, it is noteworthy that the MB<sup>+</sup> retention of M25 is dramatically increased compared to P25. These results suggest that the effective pore size of the membranes must cross a minimum limit for high retention of MB<sup>+</sup>. Hence, Figure 4.11b reconfirms that the retention of MB<sup>+</sup> is largely caused by size exclusion.

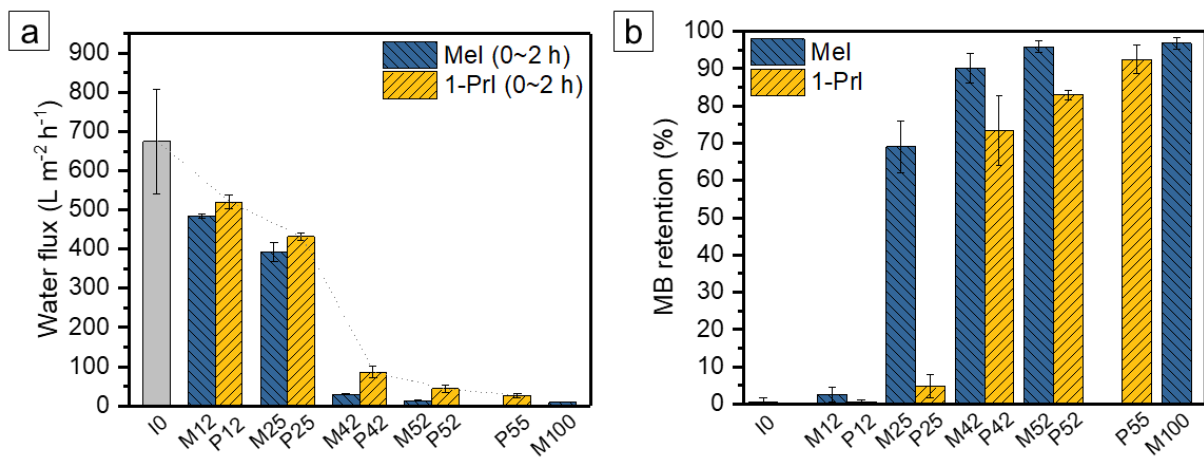


Figure 4.11. (a) Water flux (average value of 0-2 h measurement) of I0 and the membranes having the series of different degrees of quaternization with MeI and 1-PrI, respectively. (b) MB<sup>+</sup> retention of I0 and the membranes having the series of different degrees of quaternization with MeI and 1-PrI, respectively, with feed solution of concentration 10 mg L<sup>-1</sup>.

#### 4.4.2 Limitations of Determination of the Effective Pore Size of the Membranes from Water Flux Measurements

Efforts have been made to predict the pore size at the surface of the SNIPS membrane from the ratio of pure water flux using a relationship derived from the Hagen-Poiseuille equation.<sup>58, 139</sup> Under the assumption that the resistance of the spongy substructure of the membrane is negligible and only the cylindrical ordered top layer of the membrane mainly hinders the permeance, Hagen-Poiseuille equation can be used to predict the water flux ( $J_w$ ) of the membrane as shown in the following Equation 4.1

$$J_w = N_p \frac{\pi d^4 \Delta P}{128 \eta L} \quad 4.1$$

where  $N_p$  is the number of surface pores per unit area,  $d$  is the effective pore diameter,  $\Delta P$  is the transmembrane pressure,  $\eta$  is the water viscosity ( $8.94 \times 10^{-4}$  Pa · s at 24 °C) and  $L$  is the length of the cylindrical pores.

According to the top surface and cross-sectional images of the pristine membrane and quaternized membranes (Figure 4.9, Figure 4.10), all the membranes have the similar number of surface pores ( $N_p$ ) and similar thickness of the top cylindrical layer ( $L$ ). During the whole water flux measurement, the same transmembrane pressure ( $\Delta P$ ) was employed, thus  $J_w$  would scale with  $r^4$ .

Assuming that the swelling of the unquaternized P4VP is negligible, the pore size of the pristine membrane is ca. 27 nm, which was measured based on SEM images in the dry state. The effective pore size was calculated by relating it to the water flux as Equation 4.2

$$\frac{J_{v0}}{J_{vq}} = \frac{27^4}{d^4} \quad 4.2$$

where  $J_{v0}$  is the water flux of the pristine membrane, and  $J_{vq}$  is the water flux of the quaternized membranes. Equation 4.2 is based on the assumption that there is no resistance for the penetration of water from the substructure of the membrane. However, it is a crude approximation as the contribution of the spongy substructure to resist water permeation cannot be completely ignored.<sup>140</sup> We expect the spongy substructure to have much less resistance against the water penetration compared to the isoporous top layer.

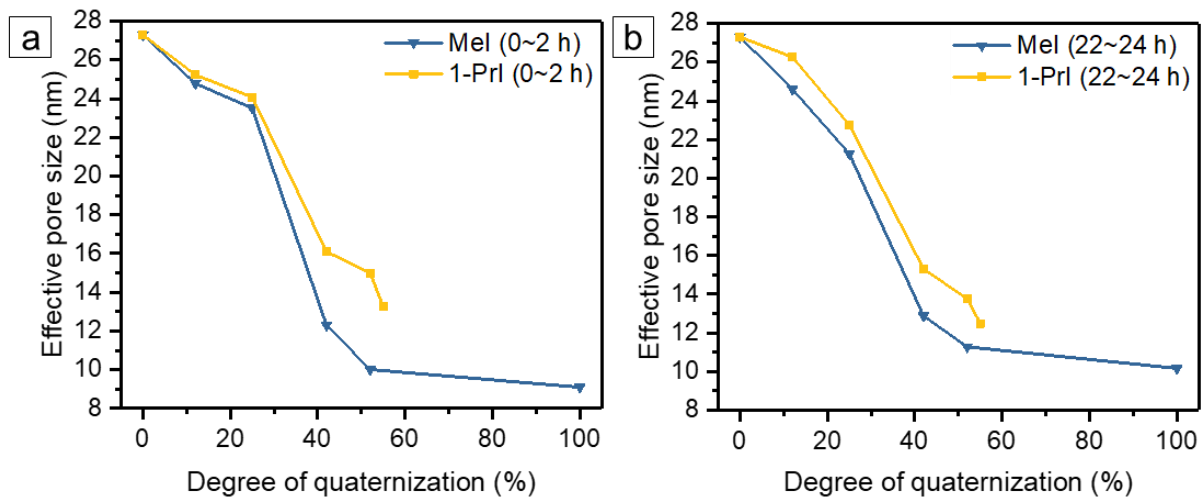


Figure 4.12. Effective pore size with the degree of quaternization calculated by the Hagen-Poiseuille equation based on water flux measurements: (a) 0-2 h measurement, (b) 22-24 h measurement.

Figure 4.12 shows the effective pore size estimated using Equation 4.2 based on the average value of water flux from the 0-2 h measurement and the 22-24 h measurement, respectively. In both cases, the effective pore size in the hydrated state is gradually tailored from ca. 27 nm to ca. 9 nm by adjusting the degree of quaternization. It is worth noting that for the same degree of conversion (in the range 12 – 52%), the effective pore size of the membranes quaternized by 1-PrI is bigger compared to that of MeI, which fits with the trend of water flux and MB+

rejection (Figure 4.11). According to MM2 force field calculation (by chem3D software package in vacuum), the molecular size of MB<sup>+</sup> is 1.1 nm which is consistent with the values reported in the literature.<sup>141, 142</sup> Moreover it has been reported the Stokes-Einstein diameter of MB<sup>+</sup> is 0.886nm.<sup>143</sup> However, the calculated effective pore sizes of M52 and P52 are 10-13 nm, much bigger than the size of single MB<sup>+</sup> molecule (~1.1 nm). As the retention of MB<sup>+</sup> from 10 mg L<sup>-1</sup> aqueous solution is 96% and 83%, respectively, it is clear that the effective pore size of the membranes is much smaller than 10 nm, suggesting the limitations of calculation using Equation 4.2. After the quaternization, there is a significant change of hydrophilicity of the pore-forming block P4VP, which leads to the dramatic increase of affinity of water to the quaternized P4VP block. Equation 4.2 does not take into account the parameter of hydrophilicity which should be one of the biggest limitations to determine the precise effective pore size. Therefore, at this stage it is not possible for us to predict the absolute effective pore size of the quaternized membranes in the hydrated state. In spite of the limitation to determine the absolute value of the pore size in the hydrated state, as we have successfully tuned the retention of MB<sup>+</sup> between 6 – 98% (Figure 4.11), it is evident that the pore size of the PS-*b*-P4VP membrane can be successfully tuned into the nanofiltration regime by the quaternization of pore-forming P4VP blocks.

#### 4.5 Conclusion

The membrane fabrication and post-modification method presented in this chapter is promising for the production of next generation nanofiltration membranes. The PS-*b*-P4VP membrane prepared by SNIPS has an isoporous layer of well-defined cylindrical channels. By using a scalable heterogeneous gas-solid phase reaction the homogeneity of the quaternization of the pore-forming blocks can be successfully controlled. The effective pore size of the membrane in the hydrated state has been successfully tuned in a wide range from ultrafiltration toward

nanofiltration by changing the size of the alkyl groups of the quaternization agent and the degree of quaternization. The excellent performance of the membrane to separate the cationic methylene blue from aqueous solutions demonstrates the potential of these membranes for nanofiltration applications.



**Chapter 5 High-Performance Asymmetric Isoporous  
Nanocomposite Membranes with Chemically-Tailored  
Amphiphilic Negatively Charged Nanochannels**

Molecular characterization of polymers used in this chapter.

Polymer	PS <sup>a)</sup> [wt%]	PI <sup>a)</sup> [wt%]	PHTMB <sup>a)</sup> [wt%]	M <sub>n</sub> <sup>b)</sup> [kg mol <sup>-1</sup> ]	M <sub>w</sub> <sup>b)</sup> [kg mol <sup>-1</sup> ]	Dispersity indices <sup>b)</sup>	DH <sup>c)</sup> (mol%)
PS- <i>b</i> -PI	81	19	0	100	104	1.05	0
P1	76	11	13	113	124	1.06	35
P2	74	10	16	115	125	1.09	44
P3	73	7	20	124	135	1.09	55
P4	71	6	23	132	165	1.25	65

<sup>a)</sup>The composition of polymers calculated from <sup>1</sup>H NMR spectra; <sup>b)</sup>Molecular weight and dispersity index determined by GPC; <sup>c)</sup>Degree of hydroxylation (DH) calculated by <sup>1</sup>HNMR.

## 5.1 Introduction

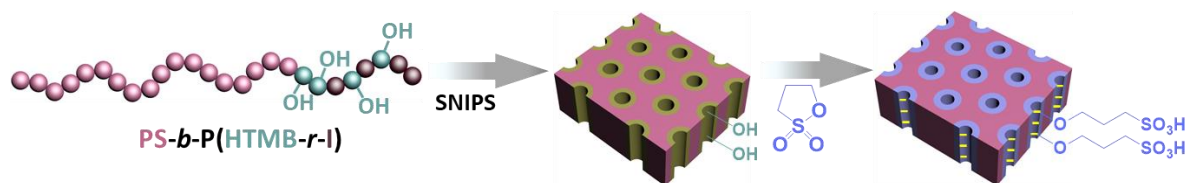


Figure 5.1. Schematic representation of the integral asymmetric isoporous membrane with amphiphilic pores and the in situ integration of sulfonic acid moieties along the pore walls.

To achieve a wide range of the potential applications related to the separation of anionic molecules, it is highly desirable to prepare a negatively charged membrane with a high permeance and good selectivity. For this purpose, a novel tailor-made diblock terpolymer  $PS-b-P(HTMB-r-I)$  was prepared. It consists of a hydrophobic major block PS and a minor block  $P(HTMB-r-I)$  with randomly distributed isoprene (I), 4-(2-hydroxyethyl-thio)-2-methyl butene and 4-(2-hydroxyethyl-thio)-3-methyl butene (HTMB) units. HTMB units are relatively hydrophilic due to hydroxyl groups while I units are hydrophobic. Due to this feature, the minor block  $P(HTMB-r-I)$  itself can be considered an amphiphilic block. A SNIPS membrane was fabricated using the  $PS-b-P(HTMB-r-I)$  which has a hydrophobic major block and an amphiphilic minor block instead of the conventional amphiphilic BCPs used for SNIPS which have a hydrophobic major block and a hydrophilic minor block. In addition, the often encountered problem of a rather dense interface between the bottom of the BCP membrane and the substrate was addressed by introducing a titania sol solution into the BCP solution prior to membrane casting. The  $-OH$  groups of  $P(HTMB-r-I)$  along the pore walls were converted to sulfonic acid moieties using an *in situ* scalable gas-solid interface reaction (Figure 5.1). The negatively charged membrane exhibited a high water permeance and the potential to separate anions having 1-2 nm lateral dimensions from each other. Additionally, antifouling

performance was assessed in static adsorption and dynamic filtration, respectively, demonstrating the excellent fouling resistance of the prepared membranes.

## 5.2 Synthesis of PS-*b*-P(HTMB-*r*-I) Diblock Terpolymers

For the synthesis of PS-*b*-P(HTMB-*r*-I) diblock terpolymers, first a hydrophobic PS-*b*-PI diblock copolymer was prepared by living anionic polymerization in the polar solvent THF rather than non-polar solvent (*i.e.* benzene) used in the previous study.<sup>41</sup> The polar solvent leads to a much higher amount of sterically less hindered pendant double bonds in the polyisoprene (PI) block than a non-polar solvent, which provides more content of accessible double bonds for the introduction of other functional groups via thiol-ene click reaction. The prepared PS-*b*-PI possesses a total molecular weight of 104 kg mol<sup>-1</sup> and a narrow dispersity index of 1.05, confirmed by the <sup>1</sup>H NMR spectra (Figure 5.2a, b) and GPC measurement (Figure 5.3). Subsequently, the hydrophobic polyisoprene (PI) block was partially hydroxylated by mercaptoethanol via thiol-ene click reaction and transformed into the amphiphilic P(HTMB-*r*-I) block successfully. It is confirmed by <sup>1</sup>H NMR spectrum of PS-*b*-P(HTMB-*r*-I) with the characteristic signals of the newly formed thioether linkage (-CH<sub>2</sub>SCH<sub>2</sub>-) at  $\delta = 2.5\sim 2.7$  ppm and methylene groups next to -OH groups (-CH<sub>2</sub>OH) at  $\delta = 3.7$  ppm, and the significant decrease of double bond signals at  $\delta = 4.6\sim 5.8$  ppm (Figure 5.2c).<sup>144, 145</sup> To fabricate the desired SNIPS membrane, four different polymers P1, P2, P3 and P4 were prepared with the degrees of hydroxylation of 35 mol%, 44 mol%, 55 mol% and 65 mol%, respectively (Table 5.1). Notably, the narrow dispersity index of the parent PS-*b*-PI diblock copolymer was always conserved after functionalization, indicating the good control over thiol-ene click reaction (Figure 5.3, Table 5.1).

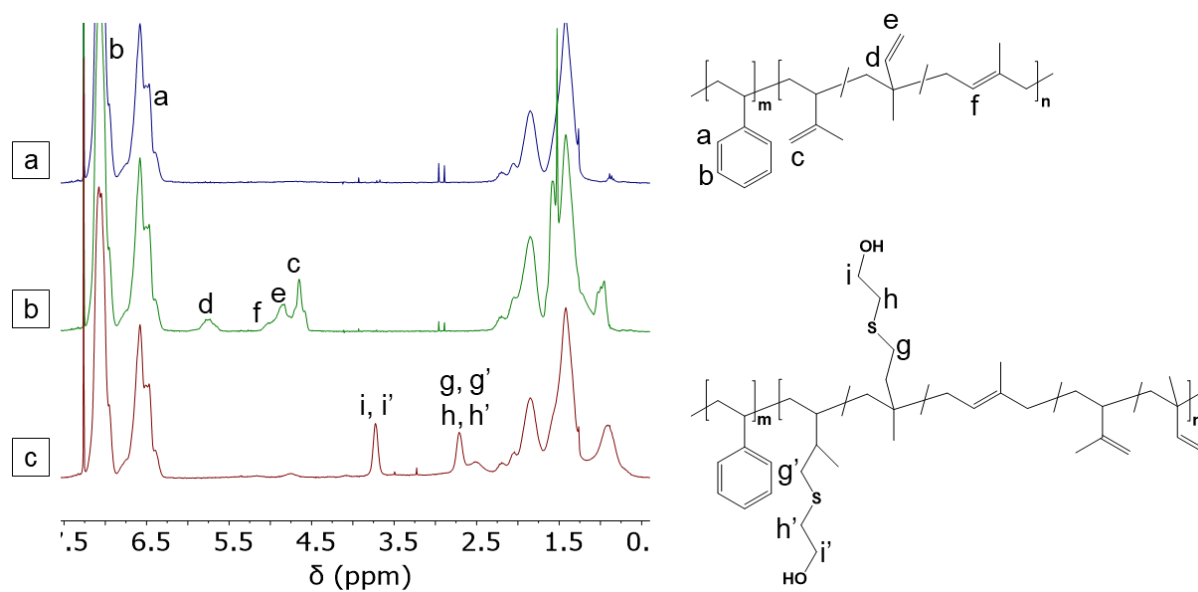


Figure 5.2.  $^1\text{H NMR}$  spectra of (a) PS precursor, (b) diblock copolymer PS-*b*-PI and (c) PS-*b*-P(HTBM-*r*-I).

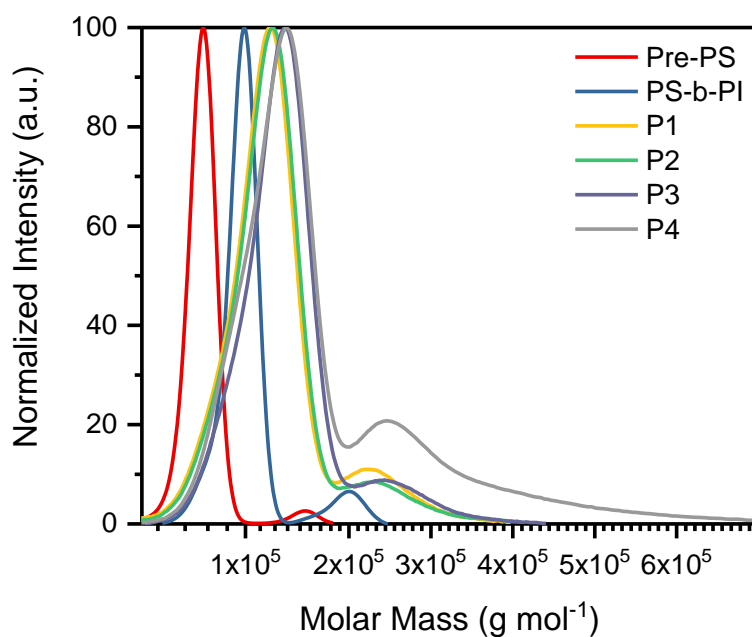


Figure 5.3. Molar mass distribution determined by GPC for the PS precursor (Pre-PS), PS-*b*-PI in THF, and P1, P2, P3 and P4 in DMAC/LiCl.

Table 5.1. Molecular characterization of the parent PS-*b*-PI diblock copolymer and thiol-ene click reaction modified diblock terpolymers PS-*b*-P(HTMB-*r*-I).

Block copolymer	PS <sup>a)</sup> [wt%]	PI <sup>a)</sup> [wt%]	PHTMB <sup>a)</sup> [wt%]	M <sub>n</sub> <sup>b)</sup> [kg mol <sup>-1</sup> ]	M <sub>w</sub> <sup>b)</sup> [kg mol <sup>-1</sup> ]	Dispersity indices <sup>b)</sup>	DH <sup>c)</sup> (mol%)
PS- <i>b</i> -PI	81	19	0	100	104	1.05	0
P1	76	11	13	113	124	1.06	35
P2	74	10	16	115	125	1.09	44
P3	73	7	20	124	135	1.09	55
P4	71	6	23	132	165	1.25	65

<sup>a)</sup>The composition of polymers calculated from <sup>1</sup>H NMR spectra; <sup>b)</sup>Molecular weight and dispersity index determined by GPC; <sup>c)</sup>Degree of hydroxylation (DH) calculated by <sup>1</sup>HNMR.

### 5.3 Microphase Separation of PS-*b*-PI/PS-*b*-P(HTMB-*r*-I) Diblock Terpolymers in Bulk

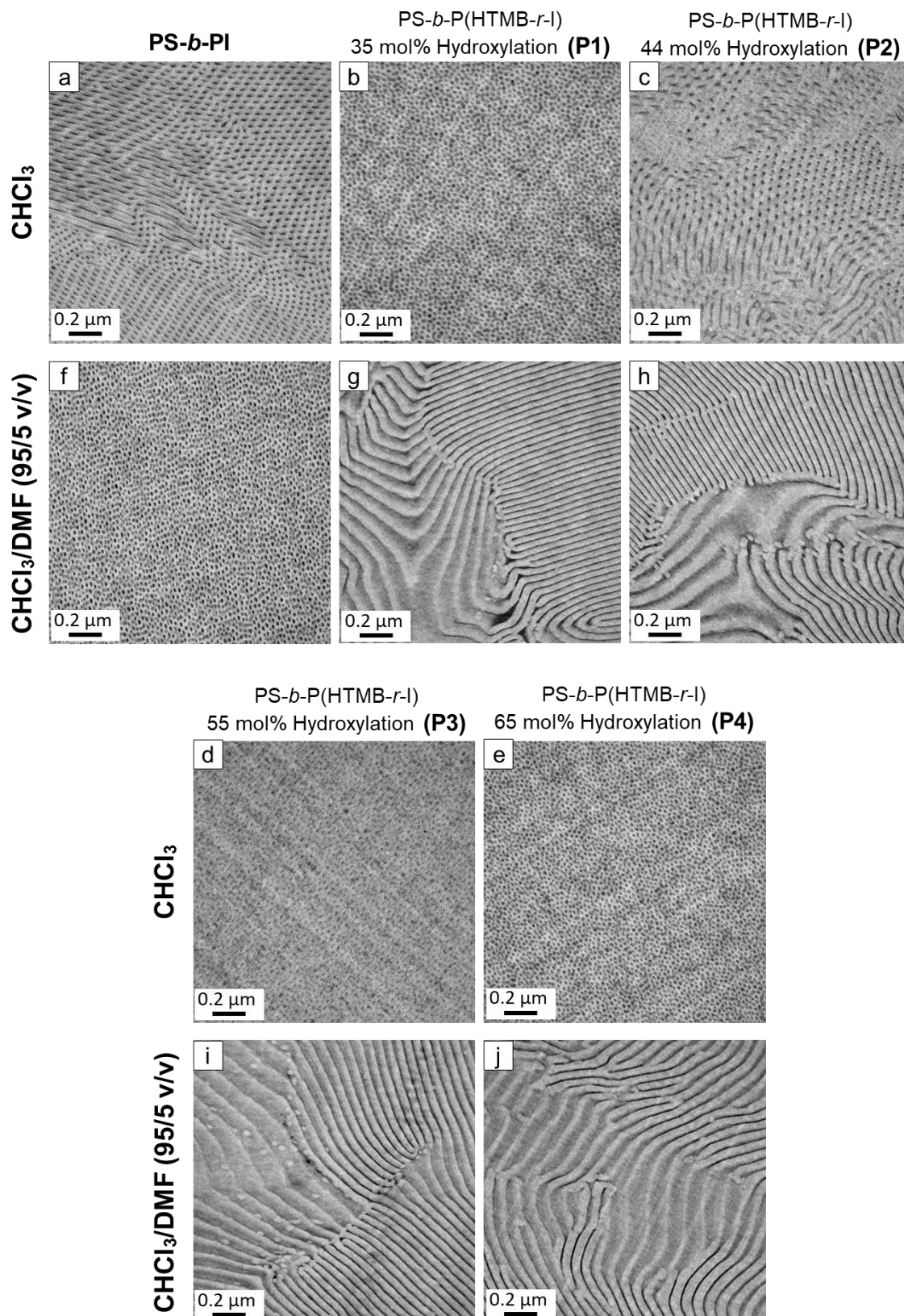


Figure 5.4. TEM images of block copolymer films prepared from different solvent systems – (a) PS-*b*-PI, (b) P1, (c) P2, (d) P3 and (e) P4 films prepared from pure CHCl<sub>3</sub>. (f) PS-*b*-PI, (g) P1, (h) P2, (i) P3 and (g) P4 films prepared from CHCl<sub>3</sub>/DMF (95/5 v/v) solvent mixture. All the films were stained by OsO<sub>4</sub> vapour for 1 h, where the PI or P(HTMB-*r*-I) domains appear dark in the bright PS matrix.

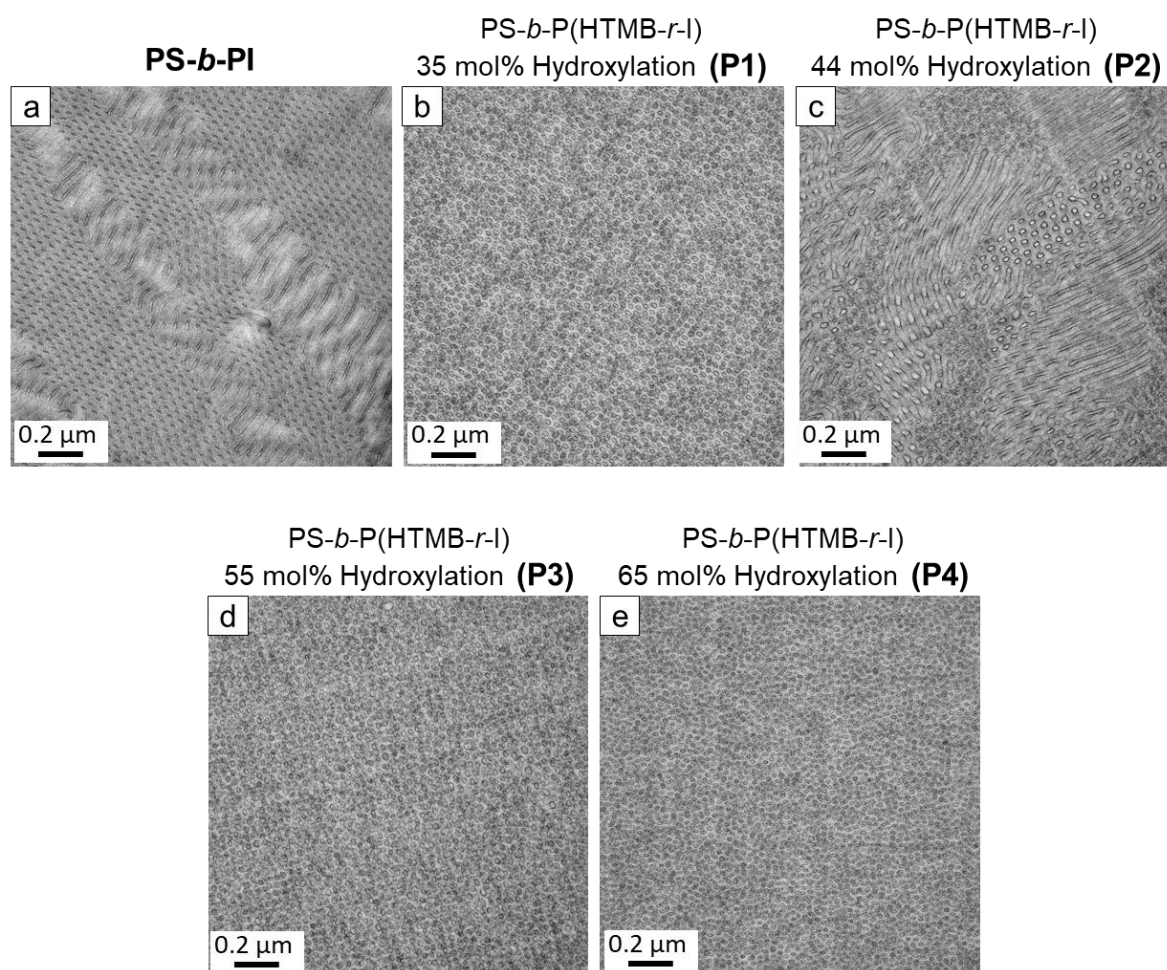


Figure 5.5. TEM images of block copolymer films prepared from pure CHCl<sub>3</sub>– (a) PS-*b*-PI, (b) P1, (c) P2, (d) P3 and (e) P4. All the films were stained by RuO<sub>4</sub> vapor for 20 min, where the edge of PI or P(HTMB-*r*-I) domains appear dark in the bright PS matrix.

We used TEM to investigate the bulk morphology of the PS-*b*-PI, P1, P2, P3 and P4 films prepared from two different solvent systems – CHCl<sub>3</sub> and CHCl<sub>3</sub>/DMF (95/5 v/v). The solvent

was evaporated slowly in a desiccator over a period of two weeks followed by thermal annealing in a vacuum oven at 120 °C to attain morphologies as close as possible to equilibrium. TEM images of Figure 5.4a and Figure 5.5a illustrate a cylindrical two-phase morphology of a PS-*b*-PI film prepared from the CHCl<sub>3</sub>, where the PI blocks form the hexagonally packed cylinders in the PS matrix. Upon the introduction of hydroxyl moieties, the intrinsic incompatibility among the blocks and the volume fraction of the blocks of PS-*b*-P(HTMB-*r*-I) change completely. The P1, P3, P4 films prepared from CHCl<sub>3</sub> show P(HTMB-*r*-I) spherical domains in the PS matrix (Figure 5.4b, d, e and Figure 5.5b, d, e), while the mixture of spherical and cylindrical P(HTMB-*r*-I) domains are formed in the PS matrix of P2 film prepared from CHCl<sub>3</sub> (Figure 5.4c, and Figure 5.5c). When the solvent mixture of CHCl<sub>3</sub>/DMF 95:5 vol% is employed, a cylindrical morphology of PS-*b*-PI is transformed into PI spheres in a PS matrix (Figure 5.4f), and the P1, P2, P3 and P4 films exhibit an alternating lamellae of PS domain and P(HTMB-*r*-I) domain (Figure 5.4g-j). The vapour pressures of CHCl<sub>3</sub> and DMF at 25 °C are 25.9 kPa and 0.49 kPa, respectively. Thus, the composition of the CHCl<sub>3</sub>/DMF solvent mixture is changed gradually to a significantly higher DMF content with the evaporation of the solvents. At a later stage of evaporation of the CHCl<sub>3</sub>/DMF solvent mixture, PS-*b*-PI micelles have a more collapsed PI core in the PS corona compared to those in the pure CHCl<sub>3</sub> system. Upon solidification, the PI segments form the spheres in the PS matrix instead of cylinders. However, in case of P1, P2, P3 and P4, DMF is more selective towards the P(HTMB-*r*-I) compared to PS, resulting in highly swollen P(HTMB-*r*-I) domains. Consequently, the morphology is transformed into a lamellar structure. TEM investigations confirm that despite of the slow solvent evaporation and thermal annealing, the equilibrium morphologies were not obtained. The P(HTMB-*r*-I) blocks swell significantly more in the presence of DMF compared to pure CHCl<sub>3</sub> regardless of the -OH group content.

## 5.4 Solvent Evaporation Induced Self-assembly of Block Copolymers During Spin-coating and SNIPS

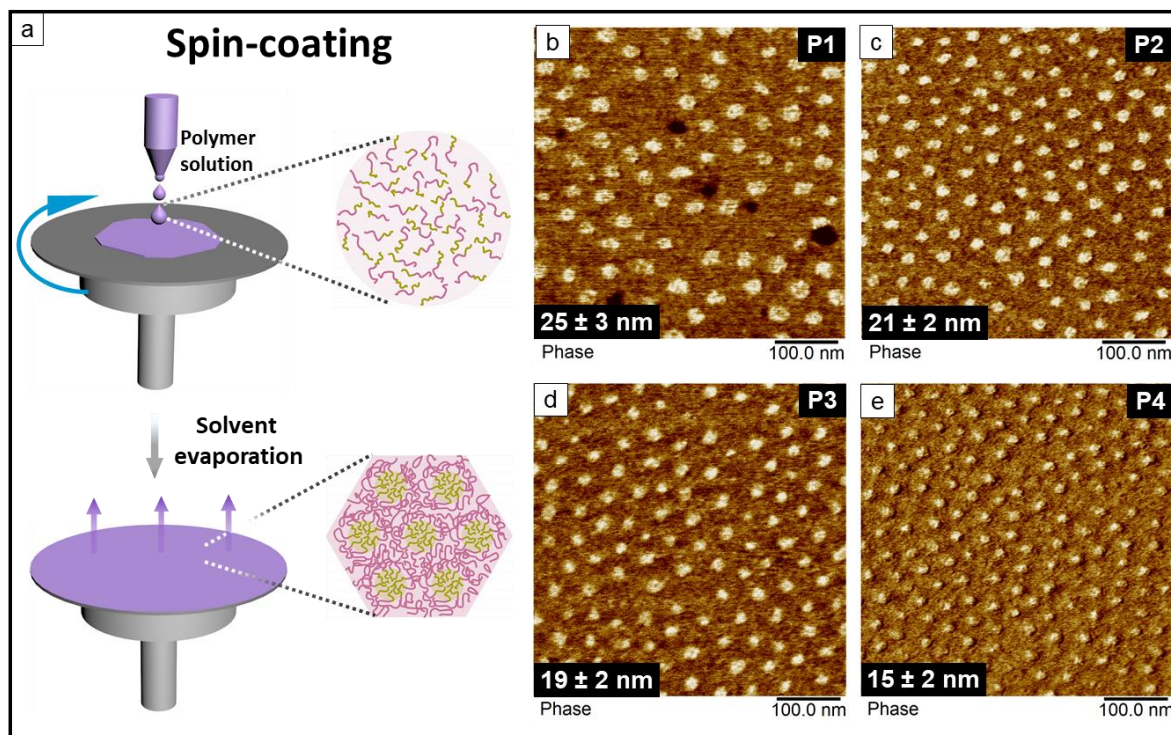


Figure 5.6. (a) Schematic representation of the spin-coating process. Atomic force microscopy (AFM) phase maps of the spin-coated dense films prepared from  $\text{CHCl}_3$ : (b) P1, (c) P2, (d) P3, (e) P4.

Figure 5.6 shows the kinetically trapped surface morphologies of the spin-coated thin films prepared from P1, P2, P3 and P4, respectively. In the AFM phase maps (Figure 5.6b-e) of the spin-coated films, the discrete P(HTMB-*r*-I) domains appear as bright regions on a darker continuous PS matrix. The P(HTMB-*r*-I) domain size is expected to increase with the degree of hydroxylation as the total P(HTMB-*r*-I) content increases (Table 5.1). However, the average sizes of the P(HTMB-*r*-I) domains gradually decrease with increasing the degree of hydroxylation. It implies that  $\text{CHCl}_3$  is not a neutral solvent for these polymers *i.e.*, it does not distribute itself equally between the PS and P(HTMB-*r*-I) microdomains during the drying of

the films. In the 2 wt% spin-coating solutions, the polymer chains are rather isolated. During the evaporation, as the polymer concentration increases, the PS and P(HTMB-*r*-I) blocks start to segregate and CHCl<sub>3</sub> distributes favourably towards the P(HTMB-*r*-I) domains. Upon evaporation of CHCl<sub>3</sub> the PS segments collapse earlier than the swelled P(HTMB-*r*-I) segments and the morphology is trapped. With increasing degree of hydroxylation *i.e.* increasing hydrophilicity, the P(HTMB-*r*-I) blocks adopt a less stretched conformation at the point when PS blocks collapse around them (Figure 5.6a). Consequently, in the completely dried spin-coated films the sizes of the P(HTMB-*r*-I) domains follow the sequence of P1>P2>P3>P4.

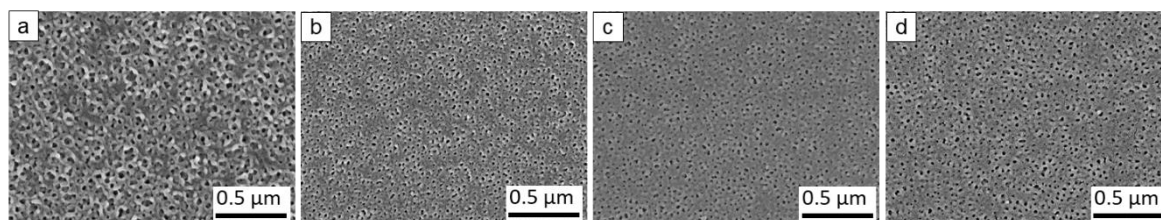


Figure 5.7. Secondary electron (SE) images of SEM of representative membranes cast from: (a) 16 wt% P2 solution in THF/DMF/DOX 2/1/1, the evaporation time  $t = 30$  s, (b) 20 wt% P3 solution in THF/DMF 2/3, the evaporation time  $t = 20$  s, (c) 18 wt% P3 solution in THF/DMF/DOX 2/2/1, the evaporation time  $t = 20$  s, (d) 18 wt% P3 solution in THF/DMF/DOX 1/1/1, the evaporation time  $t = 20$  s.

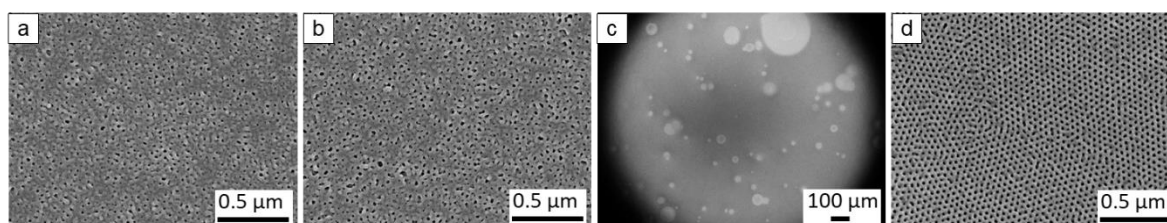


Figure 5.8. Secondary electron (SE) images of SEM of representative P4 membranes cast from (a) 18 wt% solution in THF/DMF 1/1, the evaporation time  $t = 10$  s, (b) 20 wt% solution in THF/DMF 2/3, the evaporation time  $t = 5$  s, (c, d) 24 wt% solution in THF/DMF/DOX 1/1/1, the evaporation time  $t = 20$  s: (c) overview, (d) higher magnification.

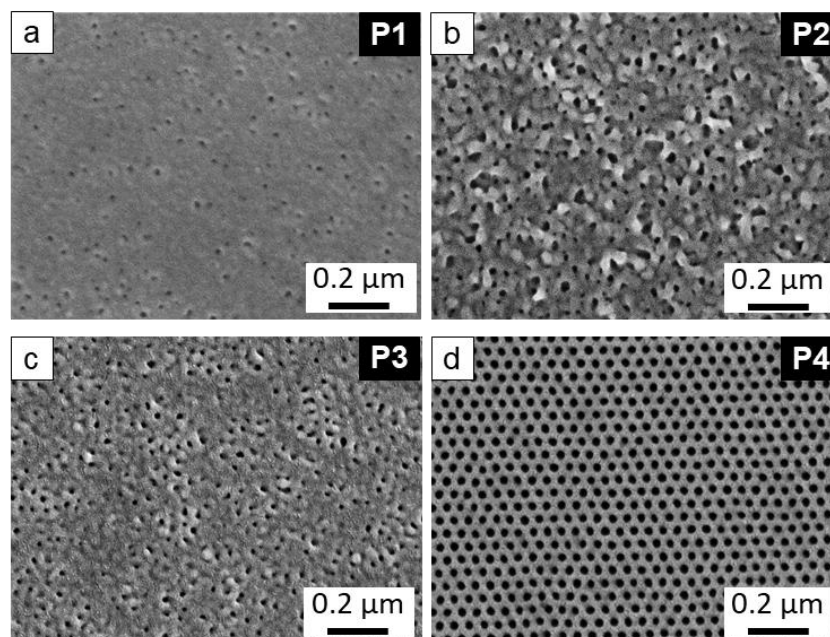


Figure 5.9. Secondary electron (SE) images of SEM of the most representative membranes cast from: (a) 28 wt% P1 solution in THF/DMF 1/1, the evaporation time  $t = 2$  s, (b) 20 wt% P2 solution in THF/DMF 3/2, the evaporation time  $t = 25$  s, (c) 20 wt% P3 solution in THF/DMF 3/2, the evaporation time  $t = 20$  s, (d) 24 wt% P4 solution in THF/DMF/DOX 2/1/1, the evaporation time  $t = 10$  s.

Formation of the isoporous top layer of a SNIPS membrane also requires the selective swelling of the minor block due to unequal distribution of solvents and earlier collapse of the major block of an asymmetric diblock copolymer. Additionally the solvents used for SNIPS must be miscible with the nonsolvent to ensure a fast quenching of the membrane. A series of the casting solutions of P1, P2, P3 and P4 in the binary solvent system THF/DMF or ternary solvent system THF/DMF/DOX were employed to cast the membranes on a neat glass plate or a non-woven (Figure 5.7, Figure 5.8 and Figure 5.9). The concentration of the polymer solution and the evaporation time were varied to find out the optimum condition. Figure 5.9 shows the most representative membrane surface morphology prepared from the four polymers. The membrane prepared from P1 (Figure 5.9a) has very few pores, while the membrane from P2 (Figure 5.9b)

---

---

has irregular pores with a large size distribution. The pores of the membrane from P3 (Figure 5.9c) has higher symmetry and relative narrow size distribution compared to those from P1 and P2. The desired hexagonally packed isoporous morphology is visible for the membrane prepared from a 24 wt% P4 solution in THF/DMF/DOX 2/1/1 (Figure 5.9d). Among the solvents THF and DOX are more selective for the matrix-forming PS block and DMF is more selective for pore-forming P(HTMB-*r*-I) block.<sup>52, 146</sup> After casting the viscous solution the more volatile THF evaporates and directs the self-assembly of BCP domains perpendicular to the surface. Upon evaporation of THF the segregation of the blocks becomes stronger and a preferential swelling of the P(HTMB-*r*-I) domains takes place due to partitioning of the high boiling DMF. Eventually the matrix-forming PS chains acquire a rather collapsed conformation around the highly swollen P(HTMB-*r*-I) chains. While the solvent evaporation induces BCP self-assembly at the surface vicinity a gradient of polymer concentration builds up along the whole thickness of the cast layer. By quenching into a nonsolvent bath, the self-assembled highly swollen P(HTMB-*r*-I) chains collapse to form the open pores on a macroporous sublayerf.

From Figure 5.9 it is clear that the composition of the amphiphilic P(HTMB-*r*-I) block plays a crucial role in partitioning of the solvents. Increasing the degree of hydroxylation leads to a lower partitioning of the hydrophobic CHCl<sub>3</sub> and higher partitioning of the hydrophilic DMF towards the P(HTMB-*r*-I) block. Furthermore, it also demonstrates that the hydroxyl content of P4 is above the threshold to allow a sufficient partitioning of DMF to bring about the formation of an isoporous top layer via SNIPS. Therefore, among the synthesized polymers P4 is selected for the fabrication of the desired membrane. P4 endows a highly ordered isoporous structure in a wide processing window, *i.e.*, the optimum polymer concentration can be tuned from 22 wt% to 30 wt% and the evaporation time is from 5 s up to 20 s (Figure 5.10 and Figure 5.11).

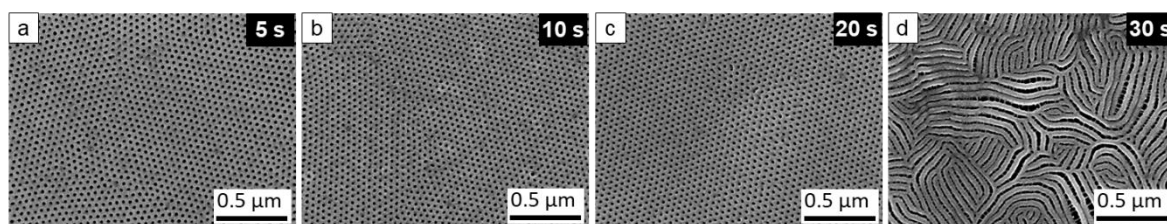


Figure 5.10. Secondary electron (SE) images of SEM of P4 membranes cast from 24 wt% solution in THF/DMF/DOX 2/1/1 using different evaporation time: (a)  $t = 5$  s, (b)  $t = 10$  s, (c)  $t = 20$  s, (d)  $t = 30$  s.

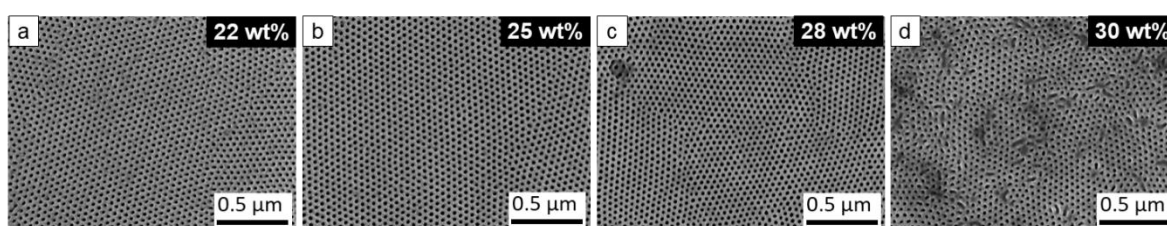


Figure 5.11. Secondary electron (SE) images of SEM of P4 membranes cast from different concentration solutions in THF/DMF/DOX 2/1/1 with the evaporation time  $t = 10$  s: (a) 22 wt%, (b) 25 wt%, (c) 28 wt%, (d) 30 wt%.

### 5.5 Organic-inorganic Hybrid Nanocomposite PS-*b*-P(HTMB-*r*-I) Isoporous Membrane with TiO<sub>2</sub> Nanoparticles

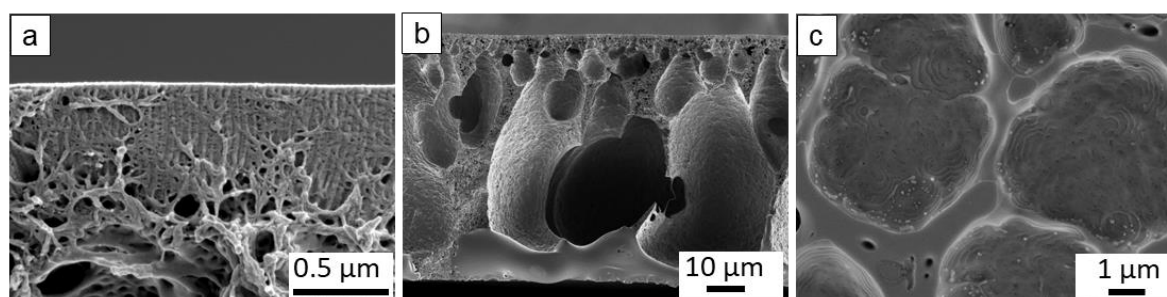


Figure 5.12. Secondary electron (SE) images of SEM: (a) cross section near the top surface, (b) overview of cross section, (c) bottom interface of P4 membrane cast from 24 wt% solution in THF/DMF/DOX 2/1/1, the evaporation time  $t = 10$  s.

The cross section of the membranes prepared from P4 consists of vertically-aligned porous cylinders connected with the disordered macropores and big caverns of the sublayer (Figure 5.12a, b). During the phase inversion process, a typical integral asymmetric structure with a coarse porous network substructure under the denser surface is a result of the spinodal decomposition of the viscous layer having a concentration gradient due to exchange of solvent and nonsolvent.<sup>19, 95</sup> However, the membranes contain a completely dense interface between the bottom of the PS-*b*-P(HTMB-*r*-I) membrane and the substrate (denoted as bottom interface) without any open pores (Figure 5.12c). To our knowledge, there is to date no report to discuss the dense bottom interface structure formed during the SNIPS process.

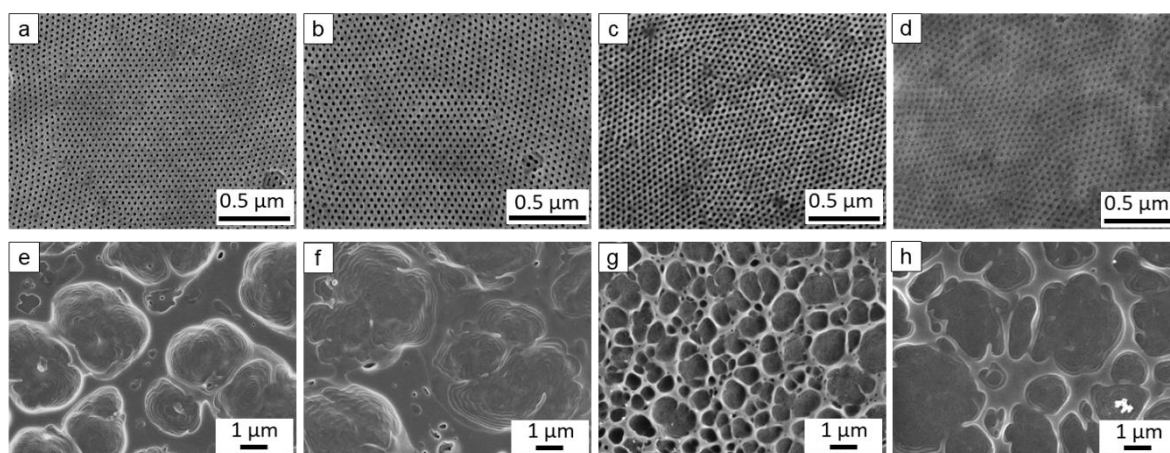


Figure 5.13. Secondary electron (SE) images of SEM: top surface and bottom interface of the representative P4 membranes cast by using THF/DMF/DOX (2/1/1): (a, e) in the 4 °C H<sub>2</sub>O bath, 28 wt% polymer concentration; (b, f) in the 15 °C H<sub>2</sub>O bath, 28 wt% polymer concentration; (c, g) in the 32 °C H<sub>2</sub>O bath, 25 wt% polymer concentration; (d, h) in the 50 °C H<sub>2</sub>O bath, 25 wt% polymer concentration. Evaporation time is  $t = 5$  s in all cases.

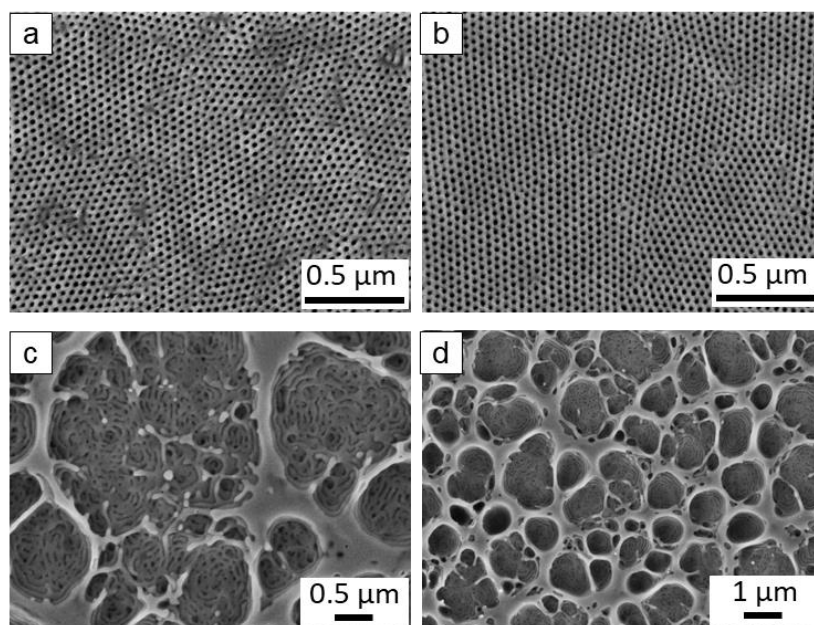


Figure 5.14. Secondary electron (SE) images of SEM: top surface and bottom interface of the representative P4 membranes cast from 25 wt% solution in THF/DMF/DOX 2/1/1: (a, c) in the non-solvent bath of methanol/H<sub>2</sub>O (20/80 v/v); (b, d) in the non-solvent bath of methanol/H<sub>2</sub>O (10/90 v/v). Evaporation time is  $t = 5$  s in both cases.

In order to solve the problem, at first we investigated the influence of the exchange rate of solvent and non-solvent on the bottom interface formation. Therefore, the temperature of the water bath was varied between 4 – 50 °C (Figure 5.13) and the compositions of non-solvent bath and solvent mixture of casting solution were also changed (Figure 5.14 and Figure 5.15).. However, no influence on the bottom interface structure is observed (Figure 5.13, Figure 5.14 and Figure 5.15). Water-soluble polymers are often used as pore-forming agents (porogens) for the fabrication of porous polymeric membranes such as polysulfone (PSF), or polyethersulfone (PES) via non-solvent induced phase separation (NIPS), like poly(ethylene glycol) (PEG)<sup>147, 148</sup>, poly(sodium 4-styrene sulfonate)<sup>149</sup> and poly(vinyl pyrrolidone)<sup>150, 151</sup>. Therefore, PEG of molecular weight 400 g mol<sup>-1</sup> (PEG400) was introduced as a porogen by blending with P4 in

the casting solution. However, in spite of varying the PEG400 content between 6 – 20 wt% with respect to the weight of P4 an open bottom interface was not obtained (Figure 5.16).

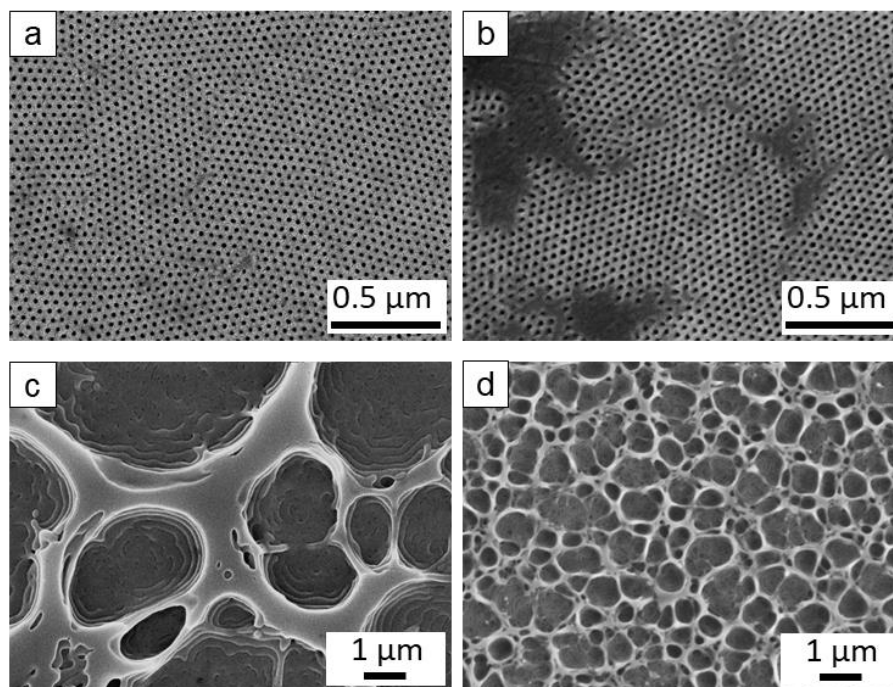


Figure 5.15. Secondary electron (SE) images of SEM: top surface and bottom interface of the representative P4 membranes cast from: (a, c) 25 wt% solution in THF/DMF/DOX 4/3/3; (b, d) 25 wt% solution in THF/DMF/DOX 1/1/1. Evaporation time is  $t = 5$  s in both cases.

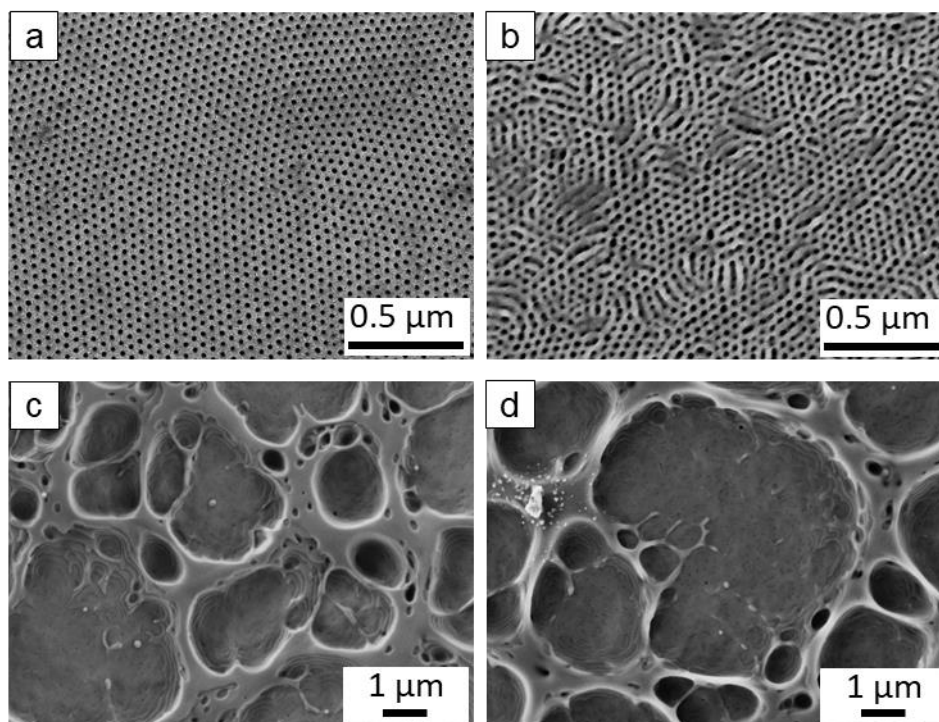


Figure 5.16. Secondary electron (SE) images of SEM: top surface and bottom interface of the representative P4 membranes cast from 25 wt% solution in THF/DMF/DOX 2/1/1: (a, c) with 6 wt% (as P4) PEG400 as the porogen; (b, d) with 20 wt% (as P4) PEG400 as the porogen. Evaporation time is  $t = 5$  s in both cases.

Gu *et al.* reported that due to the introduction of inorganic titanium dioxide ( $\text{TiO}_2$ ) nanoparticles (NPs), the bottom interface of the PI-*b*-PS-*b*-P4VP membranes exhibited big open pores with diameters in the range of 10-30  $\mu\text{m}$ .<sup>120</sup> Therefore, different amounts of a  $\text{TiO}_2$  sol solution prepared by a hydrolytic sol-gel route were added into the P4 casting solutions, *i.e.*, 6 wt%, 8 wt%, 10 wt% and 20 wt% with respect to the weight of P4. Figure 5.17 shows a comparison of the purely organic membrane without  $\text{TiO}_2$  NPs and the membranes with different amounts of  $\text{TiO}_2$  NPs. All the membranes were cast from the same concentration of the polymer solutions, *i.e.* 16 wt%. The purely organic membrane without  $\text{TiO}_2$  NPs displays the completely dense bottom interface and an irregular porous top surface (Figure 5.17a, f), since the polymer solution of 16 wt% is too diluted to microphase separate in a well-ordered

way in the top layer. Notably, the corresponding hybrid nanocomposite membranes possess an open porous bottom interface with macroscale structural features, meanwhile maintaining a highly ordered isoporous top surface except the hybrid nanocomposite membrane with 20 wt%  $\text{TiO}_2$  as P4 (Figure 5.17b-e, g-j). Through the hydrolytic sol-gel process, the resulting  $\text{TiO}_2$  sol NPs have the Ti-OH groups on their surface.<sup>120</sup> Owing to the hydrogen-bonding interactions among -OH groups,  $\text{TiO}_2$  sol NPs are expected to preferentially incorporate into the pore-forming block P(HTMB-*r*-I), increase the volume fraction of P(HTMB-*r*-I), and thus drive BCP- $\text{TiO}_2$  co-assembly<sup>120</sup> and consequently the formation of an isoporous structure at a relatively low polymer concentration. It is remarkable that highly ordered isoporous membranes are achieved by the incorporation of such significant amounts of inorganic  $\text{TiO}_2$  NPs into the casting solution, *i.e.* 6 - 10 wt% with respect to the weight of P4. To our knowledge an isoporous top layer having such hexagonally packed vertically aligned pores has never been reported in a nanocomposite SNIPS membrane.

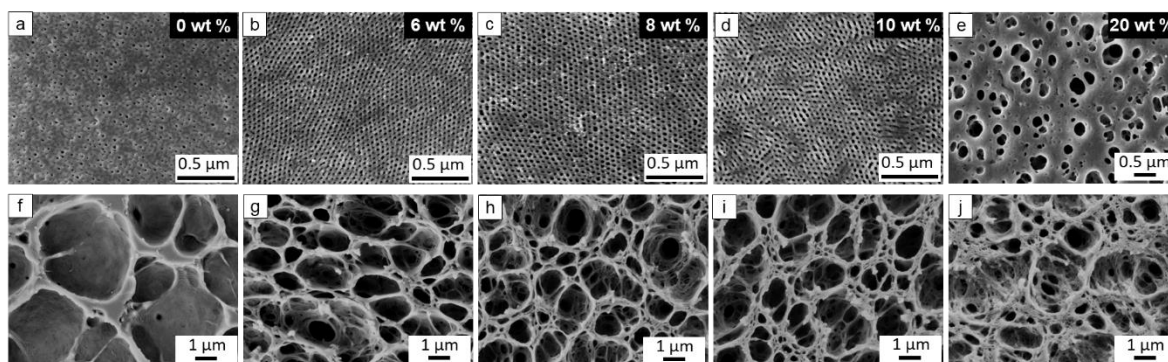


Figure 5.17. Secondary electron (SE) images of SEM: top surface and bottom interface of P4 membranes from 16 wt% solution in THF/DMF/DOX 2:1:1 wt% with different amount of  $\text{TiO}_2$  NPs as the additives: (a, f) without  $\text{TiO}_2$  NPs, the evaporation time  $t = 15$  s, (b, g) 6 wt%  $\text{TiO}_2$  NPs, the evaporation time  $t = 15$  s, (c, h) 8 wt%  $\text{TiO}_2$  NPs, the evaporation time  $t = 15$  s, (d, i) 10 wt%  $\text{TiO}_2$  NPs, the evaporation time  $t = 10$  s, (e, j) 20 wt%  $\text{TiO}_2$  NPs, the evaporation time  $t = 5$  s.

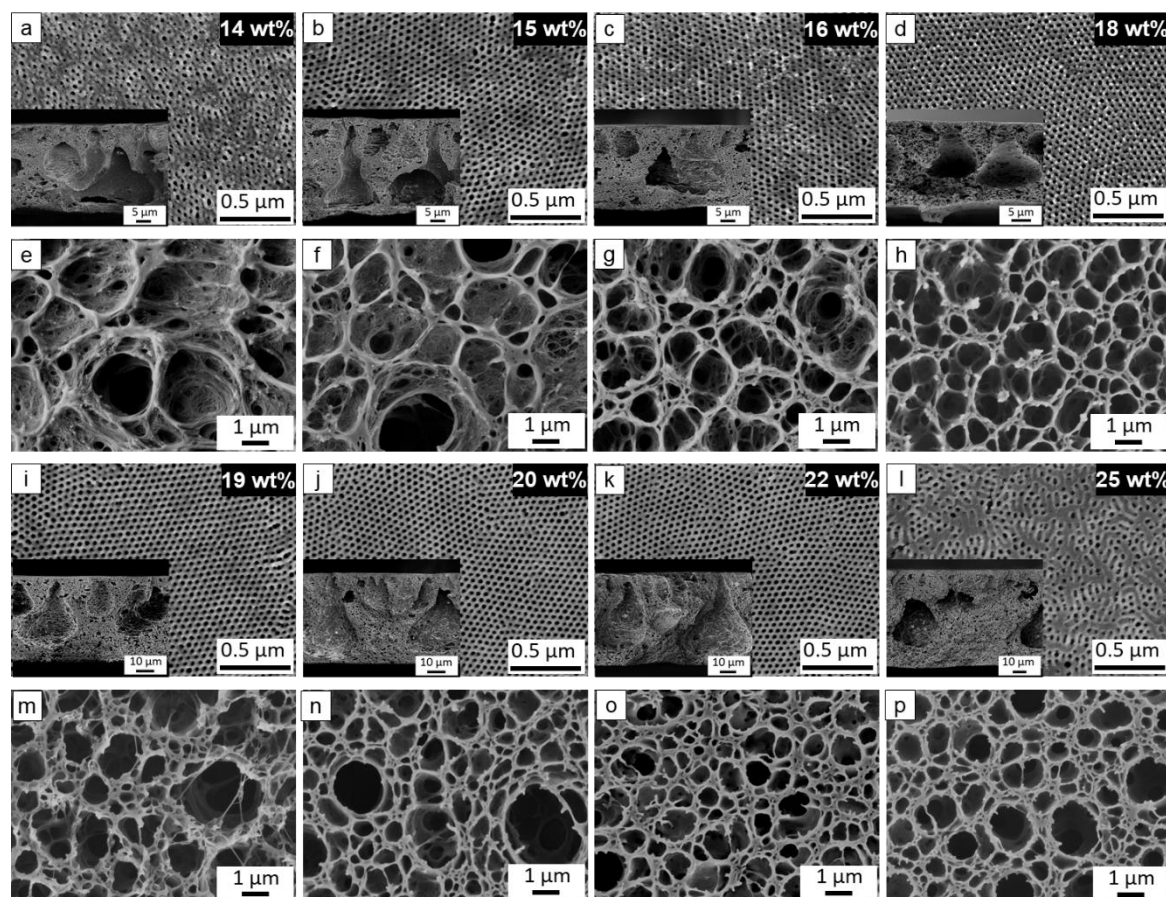


Figure 5.18. Secondary electron (SE) images of SEM: top surface and bottom interface of P4 membranes from different concentration of casting solutions in THF/DMF/DOX (2:1:1 wt%) with 6 - 8 wt% of  $\text{TiO}_2$  NPs as the additives: (a, e) 14 wt%, the evaporation time  $t = 15$  s, (b, f) 15 wt%, the evaporation time  $t = 15$  s, (c, g) 16 wt%, the evaporation time  $t = 15$  s, (d, h) 18 wt%, the evaporation time  $t = 15$  s, (i, m) 19 wt%, the evaporation time  $t = 10$  s, (j, n) 20 wt%, the evaporation time  $t = 10$  s, (k, o) 22 wt%, the evaporation time  $t = 10$  s, (l, p) 25 wt%, the evaporation time  $t = 15$  s. The insert images are the overview of the cross section of the membranes.

To figure out the optimum processing window, different concentrations of polymer solutions were evaluated in the wide range of 14 - 25 wt%. Overall, the desired membrane with a highly ordered isoporous top structure and an open macroporous bottom interface can be successfully obtained in the wide range of 15 - 22 wt% polymer solutions with the content of  $\text{TiO}_2$  NPs of

6 - 8 wt% with respect to the weight of P4 (Figure 5.18). Compared to the 22 - 30 wt% optimum window of the purely organic system, the optimum window of the hybrid nanocomposite system with TiO<sub>2</sub> NPs shifts to a lower polymer concentration range, verifying the hydrogen-bonding interaction between TiO<sub>2</sub> NPs and P(HTMB-*r*-I) and thus BCP-TiO<sub>2</sub> co-assembly. As we know, there is few report to show a BCP SNIPS membrane with such a wide processing window, e.g. PS-*b*-P4VP.<sup>152</sup>

Moreover, the purely organic and hybrid nanocomposite membranes were analyzed by back-scattered electron imaging of SEM (Figure 5.19). The result indicates that TiO<sub>2</sub> sol NPs are present all over the top surface after immersion in the non-solvent bath.

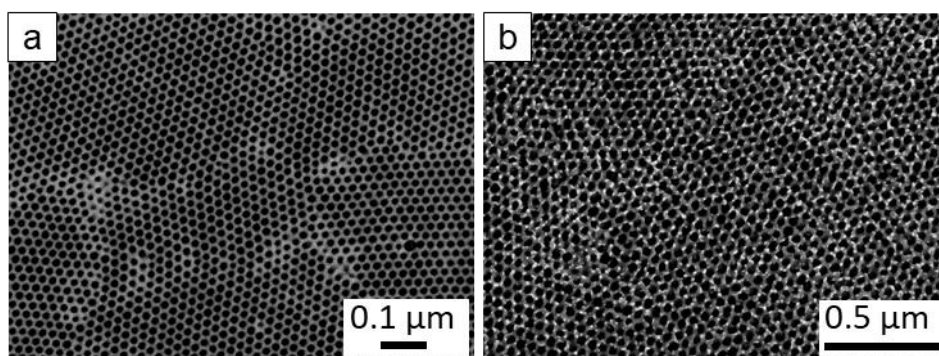


Figure 5.19. Back-scattered electron (BSE) images of SEM of (a) the purely organic P4 membrane without TiO<sub>2</sub> NPs, (b) the hybrid membrane with TiO<sub>2</sub> NPs.

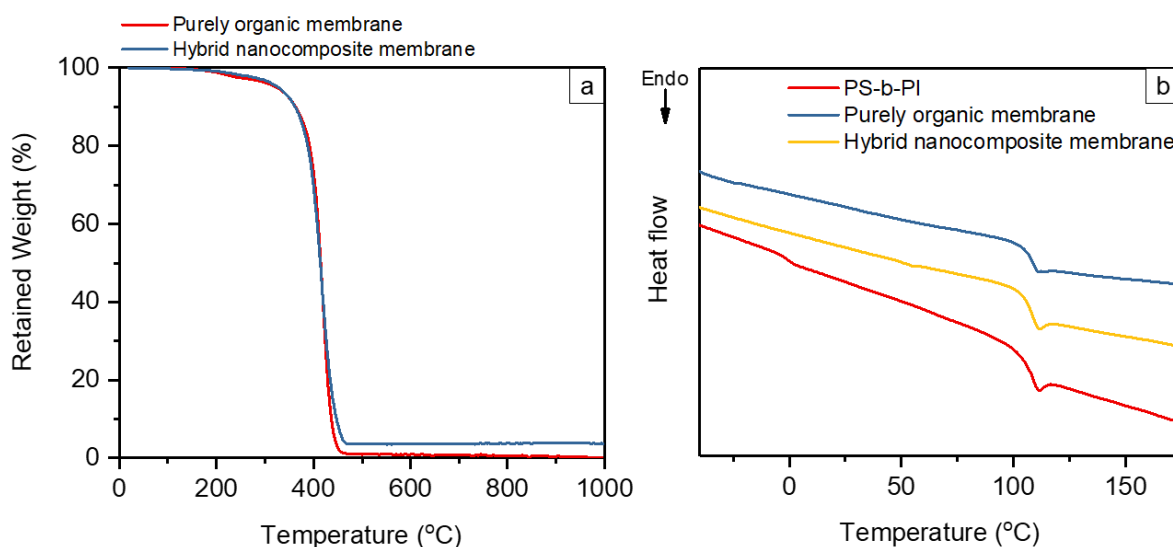


Figure 5.20. (a) TGA curves of the dried purely organic membrane cast from 25 wt% P4 without TiO<sub>2</sub> NPs and hybrid nanocomposite membrane cast from 18 wt% P4 with 8 wt% TiO<sub>2</sub> NPs. (b) DSC curves of PS-*b*-PI diblock copolymer, purely organic membrane and hybrid nanocomposite membrane with 8 wt% TiO<sub>2</sub> NPs.

TGA curves of a purely organic membrane and a hybrid nanocomposite membrane with 8 wt% TiO<sub>2</sub> NPs are depicted in Figure 5.20a. In both cases, no significant weight loss at temperature below 200 °C is observed. The main weight loss steps are similar in both cases, which occur from 200 °C to 450 °C. However, after complete decomposition up to 1000 °C, the retained mass content of hybrid nanocomposite membrane is 3.71 wt%, while that of purely organic membrane is 0.03 wt%. Therefore, it is clear that there is the presence of TiO<sub>2</sub> NPs in the prepared hybrid nanocomposite membrane, which is in agreement with the microscopic investigation. But as the difference in residual mass of the hybrid nanocomposite membrane and pristine polymer membrane is significantly lower than 8 wt%, some of TiO<sub>2</sub> might have been washed out during membrane fabrication.

Figure 5.20b illustrates the DSC thermograms of PS-*b*-PI diblock copolymer, purely organic P4 membrane and hybrid nanocomposite P4 membrane with 8 wt% TiO<sub>2</sub> NPs. The PS block

exhibits a glass transition temperature  $T_g$  of approximately 106 °C in all DSC curves. The  $T_g$  of polyisoprene (PI) block is about -1 °C from the DSC curve of PS-*b*-PI. After partial hydroxylation of PI into P(HTMB-*r*-I), there is no detectable glass transition regarding the purely organic P4 membrane. The DSC thermogram of the hybrid nanocomposite P4 membrane also does not show a glass transition of the P(HTMB-*r*-I) block. Thus, no influence on the thermal transitions is observed by the addition of TiO<sub>2</sub> NPs.

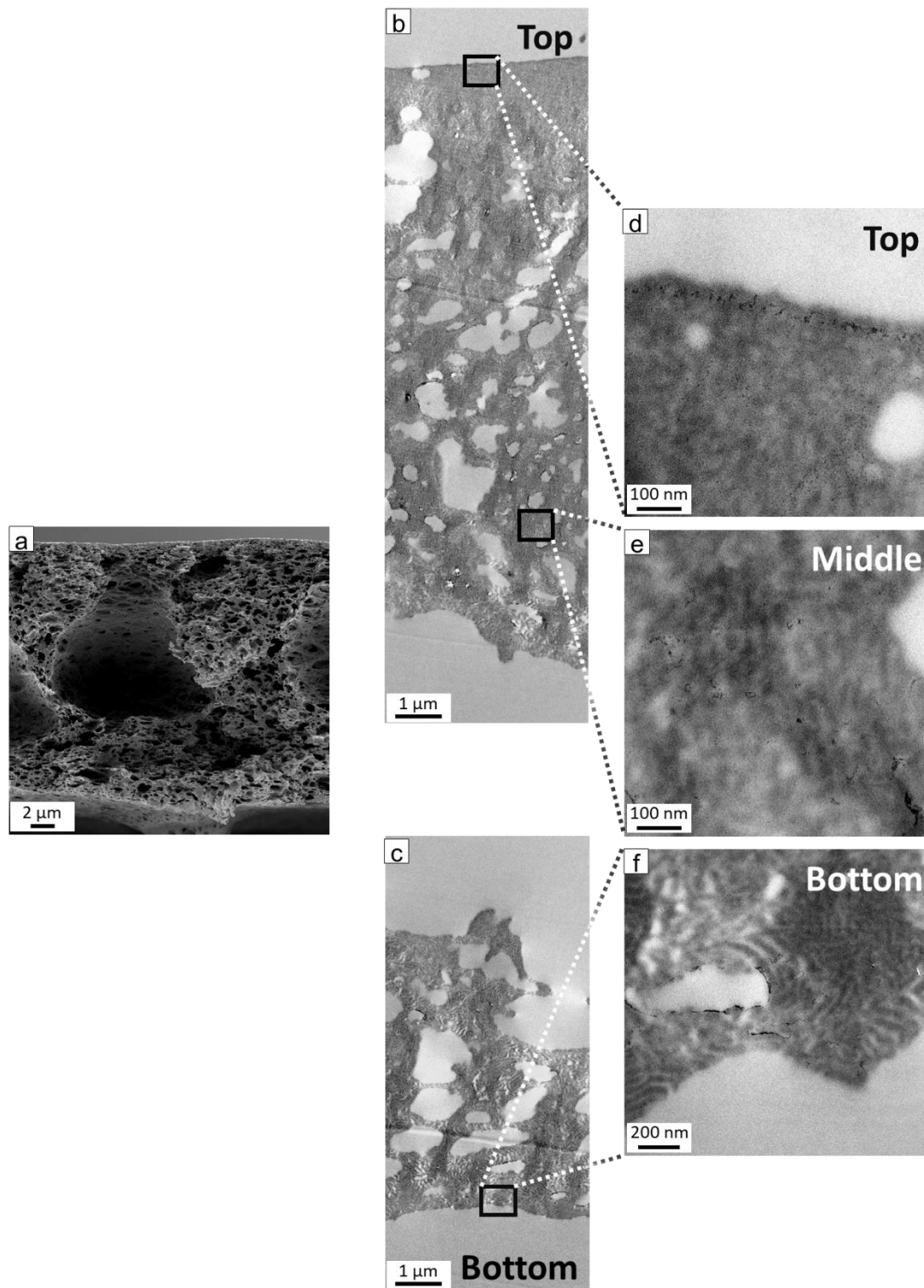


Figure 5.21. (a) SEM image of an overview of the cross section of a hybrid nanocomposite membrane. TEM images of (b, c) overview of ultrathin sections of the membrane cross section by combining the images from different positions, (d) top layer, (e) middle porous structure, (f) bottom porous structure.

The SEM image of Figure 5.21a shows the overview of the cross section of a hybrid nanocomposite membrane. The distribution of TiO<sub>2</sub> in the cross-section of the membrane was investigated by TEM (Figure 5.21b-f). In the TEM images, the TiO<sub>2</sub> NPs appear as black dots due to the electron rich titanium. Finely dispersed TiO<sub>2</sub> NPs are visible at the top (Figure 5.21d), middle (Figure 5.21e) and bottom (Figure 5.21f) part of the membrane. The top selective layer exhibits a higher content of TiO<sub>2</sub> than other areas. It is related to the membrane formation by non-solvent induced phase separation (NIPS) process. During the NIPS process, after casting the polymer solution, the fast evaporation of solvent from the top layer leads to a polymer concentration gradient and subsequent asymmetric porous structure. In the case of the polymer solution with TiO<sub>2</sub> NPs, the solvent evaporation results in a concentration gradient of not only polymer but also TiO<sub>2</sub> NPs along the cross section of the layer, which has a much higher concentration in the top layer than underlying layer. After quenching such casting layer, the formed integral asymmetric membrane displays a top layer with a richer concentration of TiO<sub>2</sub> NPs. In some regions a higher content of the TiO<sub>2</sub> NPs is observed along the pore wall. Thus some of the TiO<sub>2</sub> NPs might have a tendency to accumulate at the polymer-water interface during NIPS. It also implies the possibility of washing out of some TiO<sub>2</sub> during membrane preparation, which could explain the lower amount of TiO<sub>2</sub> found by TGA. Therefore, although the P4 membranes (Figure 5.18) were prepared from casting solutions containing 6 - 8 wt% TiO<sub>2</sub> NPs, the final concentration of TiO<sub>2</sub> NPs in the obtained membranes might be lower.

All the cross sections of the hybrid nanocomposite membranes consist of an isoporous top layer and underneath finger-like macrovoids instead of a spongy porous support structure (Figure 5.18). It is crucial to assess the mechanical stability of the corresponding integral asymmetric structure under pressure driven condition. Therefore, the ultrapure water fluxes of the hybrid membrane were measured at different transmembrane pressures from 0.25-2.9 bar. The ultrapure water fluxes increase linearly with the transmembrane pressure (Figure 5.22). It

reveals that our prepared P4/TiO<sub>2</sub> NPs hybrid nanocomposite isoporous membranes are mechanically stable up to 2.9 bar pressure, whereas in the study by Gu *et al.* it was reported that the PI-*b*-PS-*b*-P4VP/TiO<sub>2</sub> hybrid membranes were stable in a pressure range of 0.01-0.06 bar<sup>120</sup>.

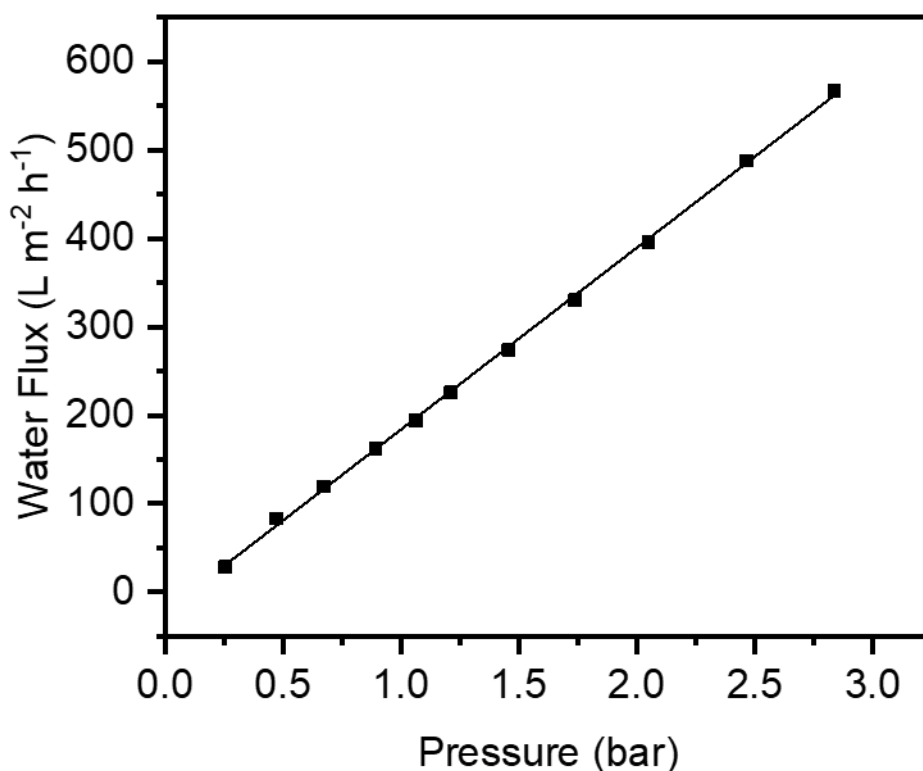


Figure 5.22. Water fluxes of a representative P4/TiO<sub>2</sub> NPs hybrid isoporous membrane at various transmembrane pressures from 0.25 to 2.9 bar.

## 5.6 Sulfonation of Organic-inorganic Hybrid Nanocomposite Isoporous Membranes

The P4/TiO<sub>2</sub> NPs hybrid membranes were post-functionalized with 1,3-propane sultone using a straightforward *in situ* scalable gas-solid interface reaction. The appearance of two new characteristic vibrations at ~1036 cm<sup>-1</sup> and ~1181 cm<sup>-1</sup> in ATR-FTIR spectrum of the

sulfonated membrane (SM) is ascribed to the stretch vibration of the  $\text{-HSO}_3$  groups, indicating the ring opening of 1,3-propane sultone and the successful covalent attachment of the sulfonic acid moieties (Figure 5.23c).<sup>145</sup> Additionally it is clear that compared to the pristine membrane I0, the content of sulfur (S) and oxygen (O) in the EDX spectrum of SM increases (Figure 5.23d), in agreement with the success of the sulfonation reaction. The comparison of SEM images confirms that SM retains the kinetically trapped integral asymmetric isoporous structure of I0 (Figure 5.23a, b). Notably, no big change of the pore size of SM (*i.e.* 22.5 nm) is observed compared to the pore size 22.9 nm of I0. The morphology of their cross sections is also rather similar. Figure 5.23e shows that I0 has a higher initial water contact angle ( $\theta_0 = 94^\circ$ ) than SM ( $\theta_0 = 76^\circ$ ) while the sinking rate of a water droplet through I0 is prominently slower than that of SM. Our previous study showed that after introduction of the hydrophobic moieties (*i.e.*, 2-ethylcarbamoyloxy) within the hydrophilic pore walls of a polystyrene-*block*-poly(2-hydroxyethyl methacrylate) (PS-*b*-PHEMA) membrane, the initial contact angle  $\theta_0$  was changed from  $63.8^\circ$  to  $94.5^\circ$ , and also the changes of contact angles with time showed a very slow decrease, similar to the current trend of membrane I0.<sup>39</sup> Additionally, the reported PS-*b*-P4VP membrane with positively charged nanochannels exhibited a sinking rate of a water droplet similar to that of SM.<sup>153</sup> Therefore, these results reveal that I0 is a strongly hydrophobic membrane, whereas SM turns into a hydrophilic membrane which is ascribed to the introduction of the sulfonate groups along the pore wall. The surface zeta potential ( $\zeta$ ) of I0 is negative in the pH range of 3.9 – 10, likely due to the hydrophobic character and preferred adsorption of hydroxide ions. The isoelectric point (around pH 3.9) and the shape of curve fit with typical hydrophobic polymeric membranes without dissociating groups (Figure 5.23f).<sup>154-</sup>  
<sup>156</sup> Compared to I0, SM displays a much higher negative  $\zeta$  in the whole pH range of 2.5 – 10 without isoelectric point, which demonstrates the presence of acidic groups and their corresponding dissociation (Figure 5.23f).<sup>157</sup>

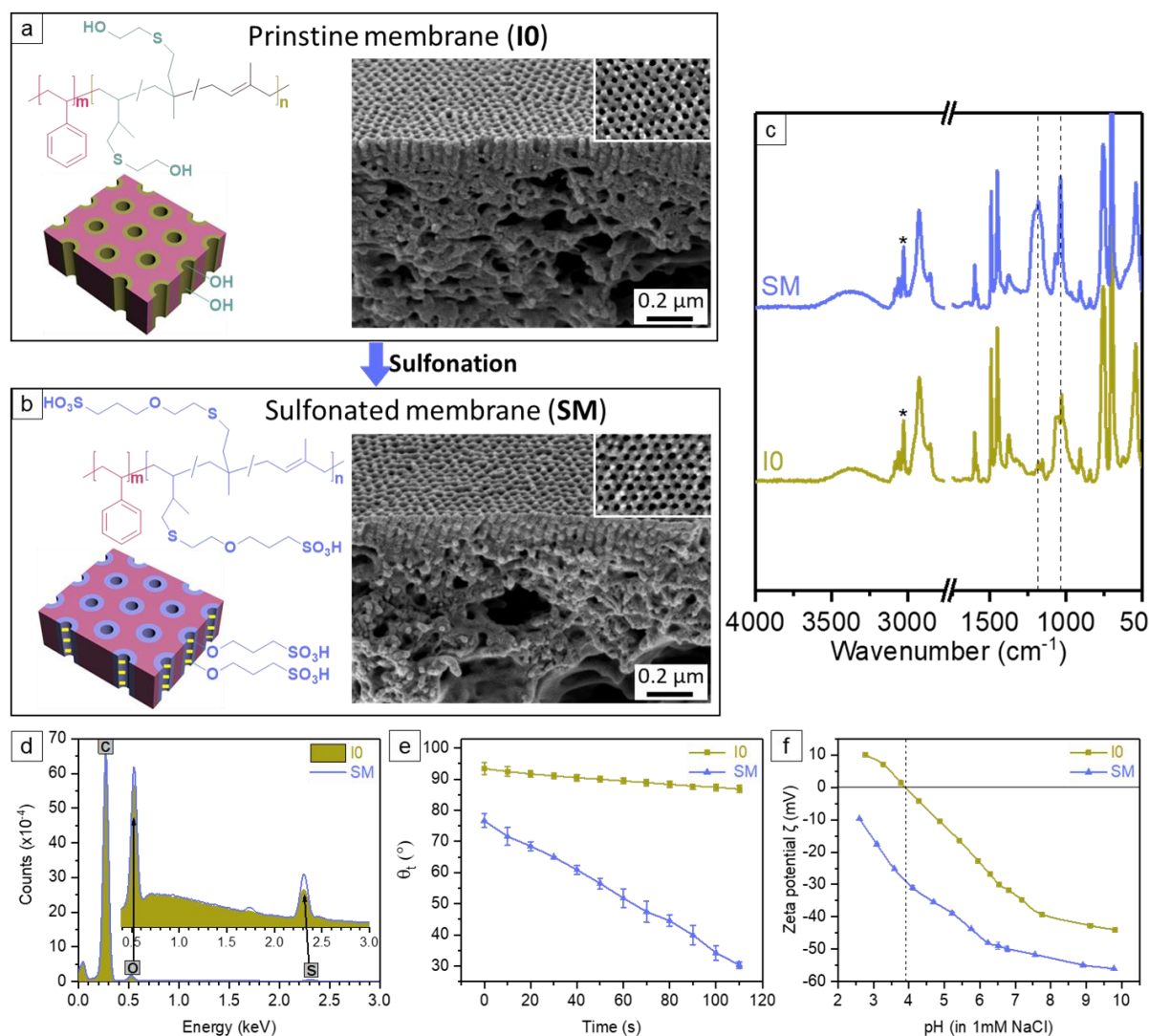


Figure 5.23. Schematic representation, chemical structure and SEM images of (a) the pristine membrane I0, (b) the sulfonated membrane (SM). (c) FTIR spectra of I0 and SM. The relative intensities were normalized using the characteristic aromatic C-H stretches (\*) of the unreactive polystyrene segment between 3100 and 3000 cm<sup>-1</sup>. (d) Comparison of EDX spectra of I0 and SM. (e) Dynamic water contact angle of I0 and SM as a function of time. (f) The surface zeta potential of I0 and SM as a function of pH (2.5 - 10). Experiments were performed with a background electrolyte of 1 mM NaCl.

---

---

## 5.7 Membrane Performance

### 5.7.1 Membrane Permeability and Selectivity

I0 exhibits a constant water permeance of  $159 \text{ L m}^{-2} \text{ h}^{-1} \text{ bar}^{-1}$  (Figure 5.24a) in the pressure range 0.25 – 2.9 bar. Thus the effective pore size of the I0 membrane is big enough to overcome the unfavorable wetting of the hydrophobic surface of I0 to allow fast water transport even at 0.25 bar transmembrane pressure. The negatively charged membrane SM has a water permeance of  $74 \text{ L m}^{-2} \text{ h}^{-1} \text{ bar}^{-1}$  (Figure 5.24a), which is significantly higher than reported SNIPS BCP membranes with swelling polyelectrolyte nanopores ( $0.6 - 15 \text{ L m}^{-2} \text{ h}^{-1} \text{ bar}^{-1}$ ).<sup>42, 55, 58, 59</sup> The amphiphilic pore-forming block P(HTMB-*r*-I) having the randomly distributed hydrophilic HTMB and hydrophobic I repeating units offers compositional heterogeneity on the segmental (molecular) scale<sup>158</sup>. Due to such molecular-level compositional heterogeneity, the negatively charged pore-forming block of SM does not assume a fully stretched conformation but swells to some extent in a hydrated state. Therefore in a hydrated state SM contains charged nanopores which are significantly smaller compared to those of I0. In spite of having higher hydrophilicity (Figure 5.23e) the water permeance of SM is significantly lower than of I0 (Figure 5.24a).

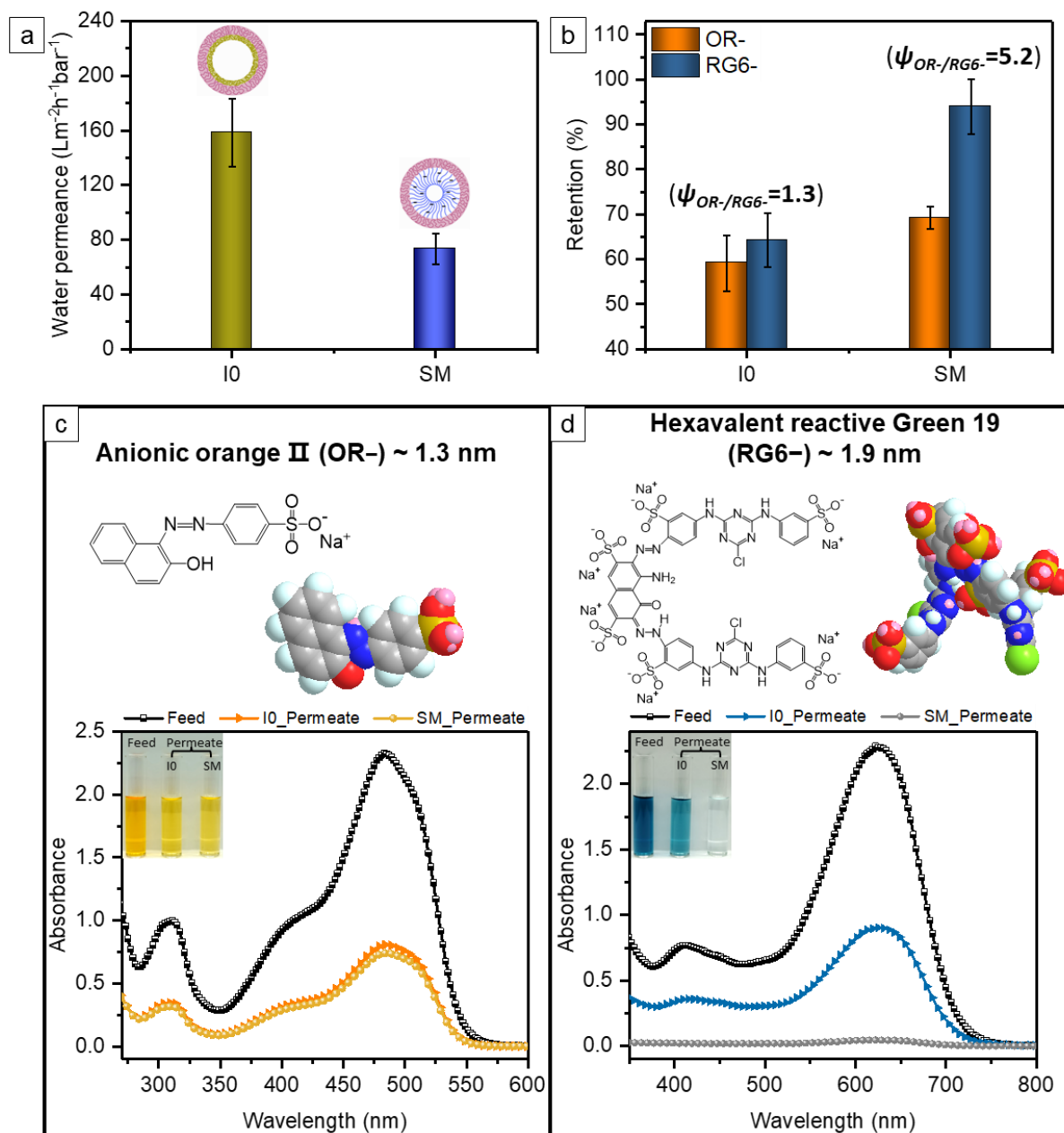


Figure 5.24. (a) Comparison of water permeance of the pristine membrane I0 and the sulfonated membrane SM under trans-membrane pressure of 1 bar. (b) The separation behavior of small organic molecules (*i.e.* orange II (OR<sup>-</sup>) and reactive green 19 (RG6<sup>-</sup>)) using I0 and SM. (c-d) Molecular structure and space-filling model of the small molecules, and the corresponding UV-vis spectra and a color change of the solution: (c) OR<sup>-</sup> and (d) RG6<sup>-</sup>.

To demonstrate the separation efficiency of the membranes, we employed two hydrophilic water-soluble model molecules with negatively charged functional group and different molecular weights (350.32 and 1418.93 g mol<sup>-1</sup>, respectively) - monovalent orange II (OR<sup>-</sup>) and hexavalent reactive green 19 (RG6<sup>-</sup>). According to MM2 force field energy minimization model calculation (in vacuum) the lateral dimensions of OR<sup>-</sup> and RG6<sup>-</sup> are 1.3 nm and 1.9 nm, respectively. The aqueous solutions of OR<sup>-</sup> and RG6<sup>-</sup> permeate through I0 with a similar moderate extent of retention, *i.e.* 59% and 64% (Figure 5.24b-d). It presumably arises from the hydrophilic-hydrophobic repulsive interaction, since hydrophilic molecules (*i.e.* OR<sup>-</sup> and RG6<sup>-</sup>) are unfavourable to be close to the rather hydrophobic surface of I0 (Figure 5.23e) and to reach the entrance of the nanochannels. The pH of OR<sup>-</sup> and RG6<sup>-</sup> aqueous solutions are 6.4 and 4.6, respectively. Although at pH 6.4 I0 has a much stronger negative charge than that at pH 4.6, the pores are still too big to exert the electrostatic repulsion on OR<sup>-</sup> and RG6<sup>-</sup>. The resulting selectivity  $\psi_{OR-/RG6-}$  is thus only 1.3. In the case of SM, 69% of OR<sup>-</sup> is retained from the aqueous solution (Figure 5.24b, c). The negative charge at the surface of SM is very strong at pH 6.4 (Figure 5.23f). Although the hydrophobicity is obviously decreased by sulfonation (Figure 5.23e), the negatively charged nanochannels of SM endow an additional electrostatic repulsion between the like charges to reject OR<sup>-</sup> at a slightly higher extent than I0. At pH 4.6 SM also possesses a strong negative charge and the nanopores of SM are narrow enough to exert a strong electrostatic repulsion on the bigger hexavalent RG6<sup>-</sup> molecules leading to a 94% retention (Figure 5.24b, d). It is clear that RG6<sup>-</sup> is more hindered to enter the charged soft nanochannels of SM due to its higher energy barrier of electrostatic repulsion and bigger molecular dimensions compared to OR<sup>-</sup>. It is remarkable that the selectivity  $\psi_{OR-/RG6-} = 5.2$  of SM is four fold higher than that of I0.

### 5.7.2 Fouling Resistance of Organic Solutes

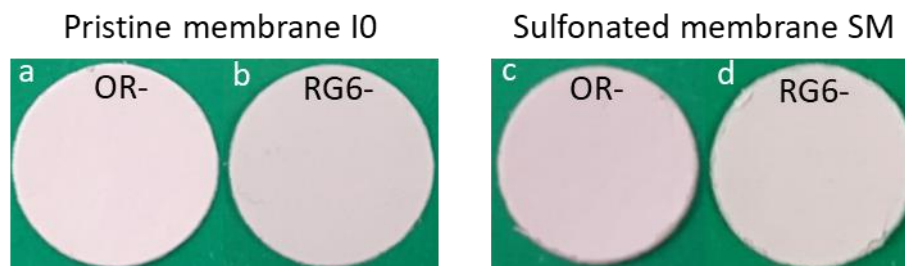


Figure 5.25. The photographs of the membranes after adsorption measurements using 0.1 mM solute aqueous solutions. (a) I0 after OR- adsorption test, (b) I0 after RG6- adsorption test, (c) SM after OR- adsorption test, (d) SM after RG6- adsorption test.

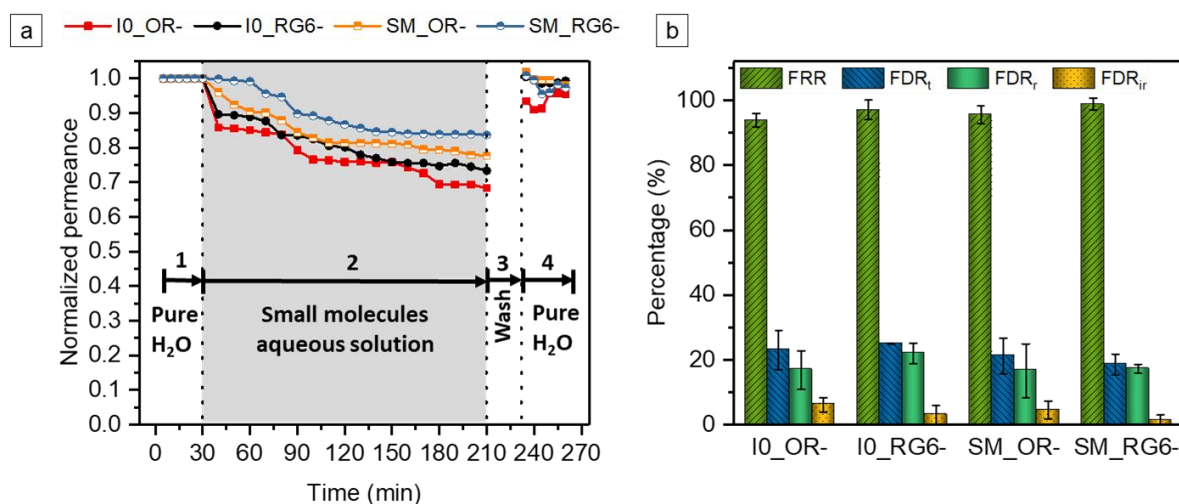


Figure 5.26. (a) Time-dependent normalized permeance variations of the pristine membrane I0 and the sulfonated membrane SM during the filtration process using OR- and RG6- as the permeate solutes, respectively. The operation process included four steps: (1) 30 min pure water filtration, (2) 3 h filtration of small molecules aqueous solution, (3) 20 min water washing, (4) 30 min pure water filtration after washing. (b) A summary of the corresponding  $FRR$ ,  $FDR_t$ ,  $FDR_r$ ,  $FDR_{ir}$  values of I0 and SM.

The model small molecules OR<sup>-</sup> and RG6<sup>-</sup> were employed as foulants to evaluate the antifouling ability of the membranes in static adsorption and dynamic filtration, respectively. There is no static adsorption of OR<sup>-</sup> and RG6<sup>-</sup> onto both I0 and SM. Even after 24 h exposure, the surfaces of the membranes do not show any colour staining (Figure 5.25). Figure 5.26 displays the time-dependent normalized permeance variations during foulant solution filtration and several parameters related to antifouling properties, *i.e.*, flux recovery ratio (*FRR*), total flux-decline ratio (*FDR<sub>t</sub>*), reversible flux-decline ratio (*FDR<sub>r</sub>*), irreversible flux-decline ratio (*FDR<sub>ir</sub>*). A higher value of *FRR* and a lower value of *FDR<sub>t</sub>*, implies a better antifouling property of membrane. For I0, the permeate fluxes of OR<sup>-</sup> and RG6<sup>-</sup> aqueous solutions are decreased compared with the initial pure water flux while *FDR<sub>t</sub>* is around 23.1% and 25.0%, respectively. However, the pure water permeance is recovered to a high extent, *i.e.*,  $FRR^{OR^-} = 93.8\%$ ,  $FRR^{RG6^-} = 97\%$ , indicating a good antifouling property of I0 (Figure 5.26). It was reported that the incorporation of TiO<sub>2</sub> NPs on the membrane surface can mitigate fouling.<sup>159-161</sup> Thus, the addition of TiO<sub>2</sub> NPs not only facilitates the formation of the porous bottom interface to the substrate of the membrane, but it may also impart the fouling resistance. Additionally, the molecular-scale compositional heterogeneity of the amphiphilic random copolymer may discourage thermodynamically favorable interactions between foulant and the surface, leading to a low adsorption of OR<sup>-</sup> and RG6<sup>-</sup> on I0.<sup>158, 162 163</sup> In the case of SM, we observe an enhanced fouling resistance. The corresponding *FRR* values of SM are increased to  $FRR^{OR^-} = 95.5\%$ ,  $FRR^{RG6^-} = 98.7\%$  while *FDR<sub>t</sub>* values are decreased to  $FDR_t^{OR^-} = 21.2\%$ ,  $FDR_t^{RG6^-} = 18.6\%$  (Figure 5.26). Besides the SM possesses a much higher negative charge than I0 at the pH of foulant aqueous solutions (Figure 5.23f), which induces a strong electrostatic repulsive forces preventing the adsorption of anionic foulants. Synergistically, a strong hydration layer forms along the pore walls of SM decorated with sulfonated polyelectrolyte, which acts as a physical and energy barrier to inhibit the adsorption of the foulants on the pore wall<sup>164-166</sup>. The surfaces

of all the membranes display almost no colour staining after fouling filtration measurements (Figure 5.27). It is particularly noteworthy that owing to the excellent antifouling performance, the SM membrane maintains a rather high permeate flux during filtration, around  $60 \text{ L m}^{-2} \text{ h}^{-1} \text{ bar}^{-1}$ , meanwhile ensuring a good selectivity  $\psi_{OR-/RG6-} = 5.2$ . Therefore, it is clear that SM is a very promising membrane for both the high-performance separation of small molecules and the dye wastewater treatment.

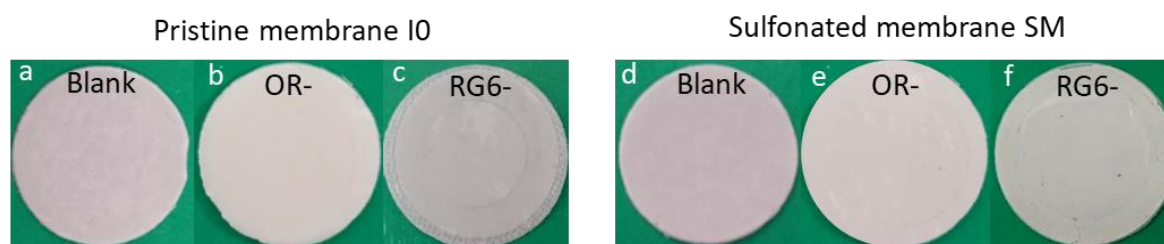


Figure 5.27. The photographs of the membranes after antifouling filtration measurements using 0.1 mM solute aqueous solutions. (a) Blank I0 without antifouling test, (b) I0 after OR- antifouling test, (c) I0 after RG6- antifouling test, (d) Blank SM without antifouling test, (e) SM after OR- antifouling test, (f) SM after RG6- antifouling test.

## 5.8 Conclusion

In this chapter, we presented a novel asymmetric isoporous membrane having embedded hydrophilic hydroxyl groups along the amphiphilic pores, which is derived from a well-designed diblock terpolymer PS-*b*-P(HTMB-*r*-I). For the first time, we have demonstrated that the incorporation of *in situ* formed TiO<sub>2</sub> NPs facilitates the formation of macroporous bottom interface, resulting in an organic-inorganic hybrid nanocomposite integral asymmetric isoporous membrane. The highly accessible hydroxyl groups on the interior of the pore walls allow straightforward scalable gas-solid interface post-functionalization to integrate negatively charged moieties within the pores. The molecular-scale compositional heterogeneity of

amphiphilic pore-forming block P(HTMB-*r*-I) results in a moderate swelling of negatively charged polyelectrolytes along the pore walls. As a result, the membrane with well-defined soft nanochannels in a hydrated state exhibits a significantly high water permeance in the nanofiltration regime and also the potential for a good separation of 1 – 2 nm small anionic molecules (having molecular weights in the range of 300 – 1500 g mol<sup>-1</sup>) from each other. The static absorption and dynamic filtration studies demonstrate the excellent antifouling performance of the prepared membranes. Especially the negatively charged membranes show a rather low permeation flux decline and a high flux recovery, mainly due to the electrostatic repulsion and the physical and energy barrier of the hydration layer.



**Chapter 6 Chemically-Tailored Multifunctional  
Asymmetric Isoporous Triblock Quaterpolymer  
Membranes for Selective Transport**

Molecular characterization of polymers used in this chapter.

Polymer	P <sup>a)</sup> [wt%]	P(HTMB) <sup>a)</sup> [wt%]	PS <sup>a)</sup> [wt%]	P4VP <sup>a)</sup> [wt%]	M <sub>n</sub> <sup>b)</sup> [kg mol <sup>-1</sup> ]	M <sub>w</sub> <sup>b)</sup> [kg mol <sup>-1</sup> ]	Dispersity indices <sup>b)</sup>	DH <sup>c)</sup> (mol%)
PI- <i>b</i> -PS- <i>b</i> -P4VP	15.8	0	65.9	18.3	156 <sup>d)</sup>	--	--	0
P1	7.3	12.7	62.6	17.4	164	202	1.23	46
P2	6.8	15.0	60.6	17.6	164	205	1.25	49
P3	6.5	16.0	59.7	17.8	182	210	1.15	54

<sup>a)</sup>The composition of polymers calculated from <sup>1</sup>H NMR spectra; <sup>b)</sup>Molecular weight and dispersity index determined by GPC; <sup>c)</sup>Degree of hydroxylation (DH) calculated by <sup>1</sup>H NMR measurement. <sup>d)</sup>Molecular weight was calculated based on <sup>1</sup>H NMR spectra and GPC.

## 6.1 Introduction

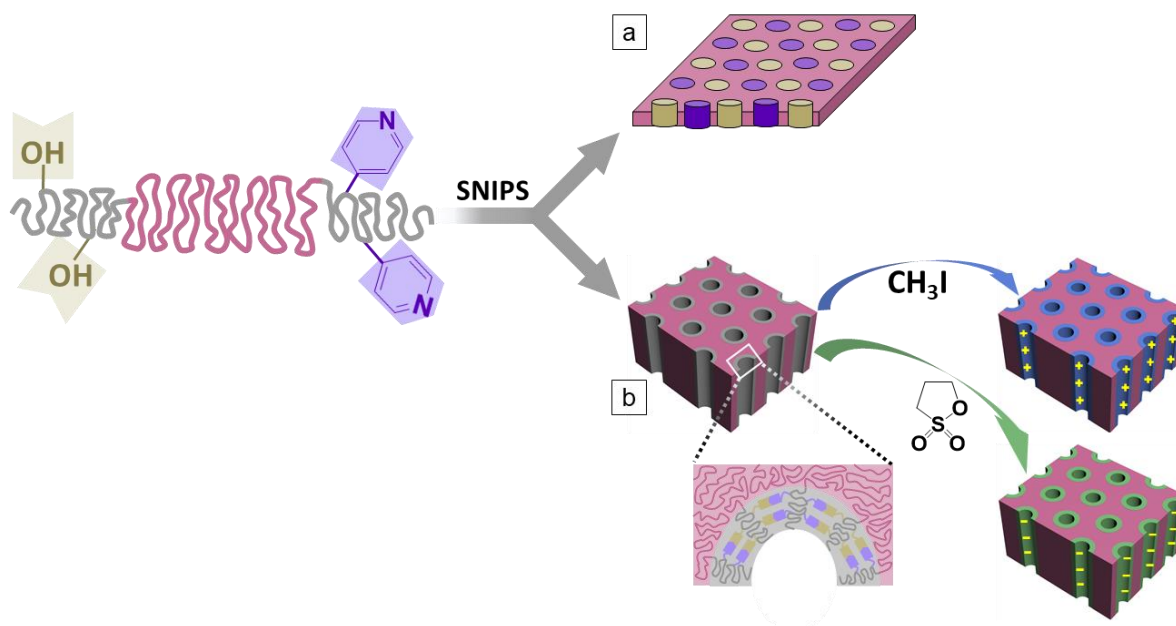


Figure 6.1. Schematic illustration of the formation mechanism of the SNIPS membranes featuring positively or negatively charged nanochannels.

On the basis of the successful fabrication of the charged isoporous membranes derived from PS-*b*-P4VP and PS-*b*-P(HTMB-*r*-I) diblock copolymers, the tailor-made P(HTMB-*r*-I)-*b*-PS-*b*-P4VP triblock quaterpolymer was expected to be a suitable candidate for the preparation of the desired charge-mosaic membrane with two discrete nanochannels formed by P(HTMB-*r*-I) and P4VP, respectively, as shown in Figure 6.1a. However, TEM and AFM studies demonstrated that the two end-blocks P(HTMB-*r*-I) and P4VP in the desired triblock terpolymer formed mixed microdomains instead of the separate ones. Therefore, we did not achieve the initial goal of charge-mosaic membrane. Instead an integral asymmetric isoporous membrane with multifunctional nanopores formed by mixed end blocks was obtained. The functional moieties within the pore walls were readily converted into positively and negatively charged polyelectrolytes via two simple *in situ* one-step functionalization reactions (Figure 6.1b). An unprecedented highly efficient separation of small molecules with lateral dimensions

between 1 – 2 nm was achieved by taking advantage of the well-defined soft polyelectrolyte nanochannels.

## 6.2 Synthesis of P(HTMB-*r*-I)-*b*-PS-*b*-P4VP Triblock Quaterpolymers

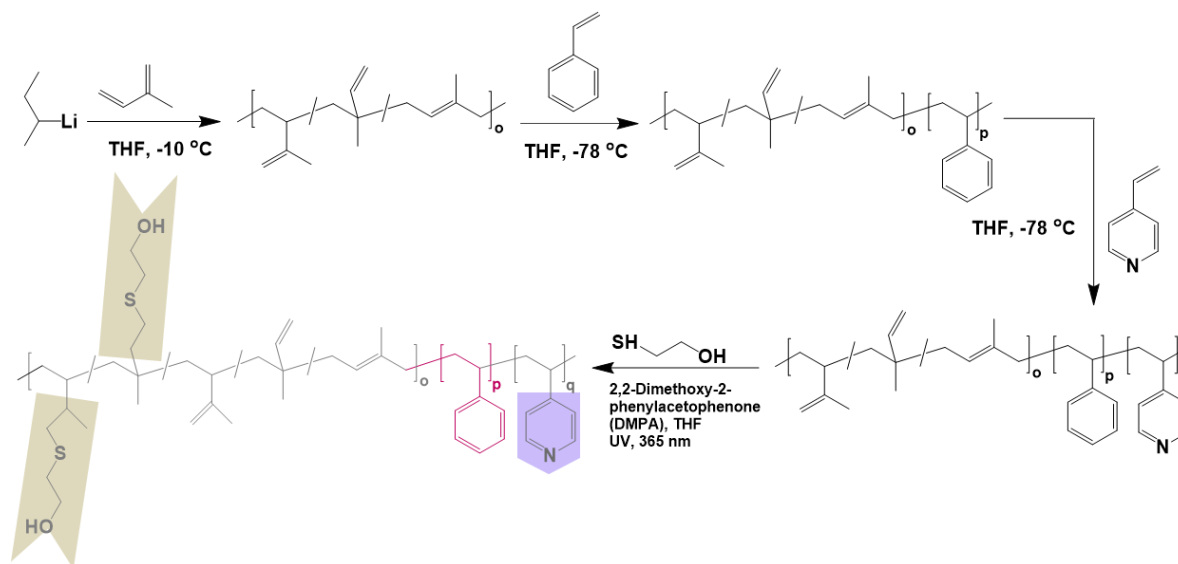


Figure 6.2. Synthesis route of PI-*b*-PS-*b*-P4VP triblock terpolymers by living anionic polymerization and thiol-ene click chemistry of PI-*b*-PS-*b*-P4VP to obtain P(HTMB-*r*-I)-*b*-PS-*b*-P4VP copolymers.

To achieve the multifunctional nanopores, a well-designed triblock copolymer with two miscible functionalized end-blocks is a prerequisite. A polyisoprene-*block*-polystyrene-*block*-poly(4-vinylpyridine) (PI-*b*-PS-*b*-P4VP) triblock terpolymer was prepared by sequential living anionic polymerization in the same polar solvent as Chapter 5 (*i.e.* THF) instead of non-polar solvent (*i.e.* benzene) used in the previous study<sup>41</sup>, confirmed by the <sup>1</sup>H NMR spectra (Figure 6.2, Figure 6.3a-c). The P4VP has the ability to form hydrogen bonding with aliphatic<sup>167-169</sup> and aromatic<sup>170-175</sup> hydroxyl groups. Therefore the polyisoprene (PI) block was subsequently hydroxylated by mercaptoethanol via thiol-ene click chemistry (Figure 6.2) to obtain three triblock terpolymers P1, P2 and P3 having 46 mol%, 49 mol% and 54 mol% degree of

hydroxylation, respectively. The success of thiol-ene click reaction was verified by the corresponding  $^1\text{H}$  NMR spectrum with the characteristic signals of the newly formed methylene groups next to  $-\text{OH}$  groups ( $-\text{CH}_2\text{OH}$ ) at  $\delta = 3.7$  ppm and the significant decrease of double bond signals ( $\delta = 4.6\sim 5.8$  ppm, Figure 6.3d). The compositions of the resulting poly(4-(2-hydroxyethyl-thio)-2-methyl butene-*random*-4-(2-hydroxyethyl-thio)-3-methyl butene-*random*-isoprene)-*block*-polystyrene-*block*-poly(4-vinylpyridine) (P(HTMB-*r*-I)-*b*-PS-*b*-P4VP) are shown in the Table 6.1.

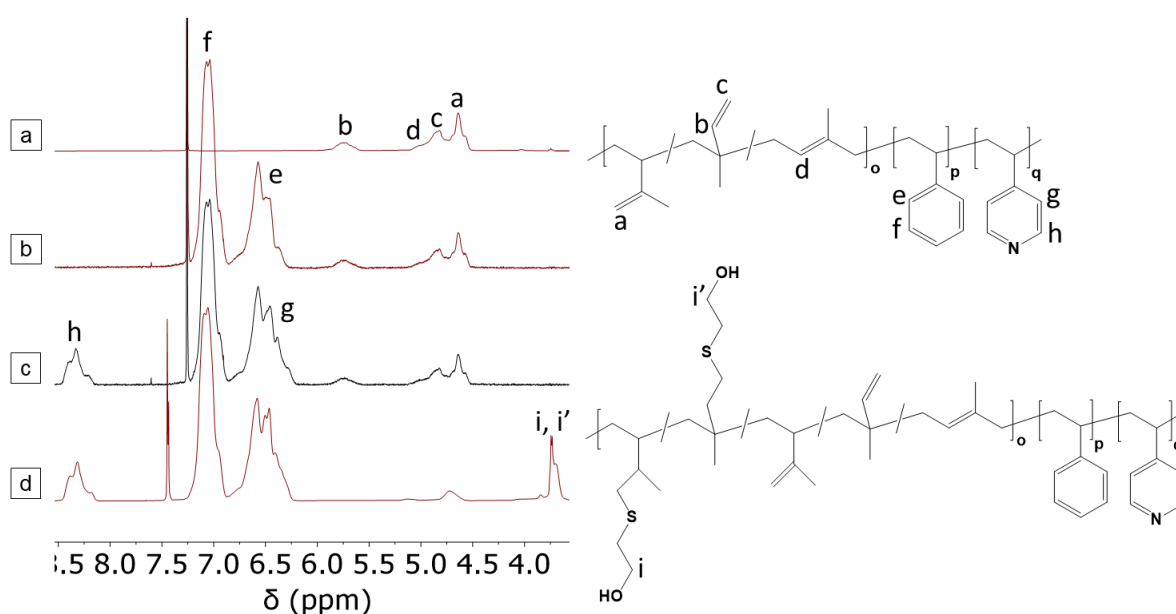


Figure 6.3.  $^1\text{H}$ NMR spectra of (a) the precursor PI, (b) the precursor PI-*b*-PS, (c) PI-*b*-PS-*b*-P4VP, (d) P(HTMB-*r*-I)-*b*-PS-*b*-P4VP.

Table 6.1. Molecular characterization of the triblock terpolymer PI-*b*-PS-*b*-P4VP and hydroxylated triblock quaterpolymers P(HTMB-*r*-I)-*b*-PS-*b*-P4VP with different degrees of hydroxylation (DH).

Block copolymer	PI <sup>a)</sup> [wt%]	P(HTMB) <sup>a)</sup> [wt%]	PS <sup>a)</sup> [wt%]	P4VP <sup>a)</sup> [wt%]	M <sub>n</sub> <sup>b)</sup> [kg mol <sup>-1</sup> ]	M <sub>w</sub> <sup>b)</sup> [kg mol <sup>-1</sup> ]	Dispersity <sup>b)</sup>	DH <sup>c)</sup> (mol%)
PI- <i>b</i> -PS- <i>b</i> -P4VP	15.8	0	65.9	18.3	156 <sup>d)</sup>	--	--	0
P1	7.3	12.7	62.6	17.4	164	202	1.23	46
P2	6.8	15.0	60.6	17.6	164	205	1.25	49
P3	6.5	16.0	59.7	17.8	182	210	1.15	54

<sup>a)</sup>The composition of polymers calculated from <sup>1</sup>H NMR spectra; <sup>b)</sup>Molecular weight and dispersity index determined by GPC; <sup>c)</sup>Degree of hydroxylation (DH) calculated by <sup>1</sup>H NMR measurement. <sup>d)</sup>Molecular weight was calculated based on <sup>1</sup>H NMR spectra and GPC.

### 6.3 Microphase Separation of PI-*b*-PS-*b*-P4VP Triblock Terpolymer and P(HTMB-*r*-I)-*b*-PS-*b*-P4VP Triblock Quaterpolymers

#### 6.3.1 Microphase Separation of PI-*b*-PS-*b*-P4VP and P(HTMB-*r*-I)-*b*-PS-*b*-P4VP with Different Compositions using Different Solvent Systems

To investigate the microphase separation PI-*b*-PS-*b*-P4VP, P1, P2 and P3 films were cast from two different solvent mixtures – CHCl<sub>3</sub>/DMF 95/5 (v/v) and CHCl<sub>3</sub>/methanol 95/5 (v/v). The solvents were evaporated slowly in a desiccator over a period of two weeks followed by thermal annealing in a vacuum oven at 170 °C to attain equilibrium morphologies as close as possible. The transmission electron microscopy (TEM) images of Figure 6.4 illustrate a cylinder-sphere three-phase morphology<sup>176</sup> of a PI-*b*-PS-*b*-P4VP film prepared from the CHCl<sub>3</sub>/DMF solvent mixture. The P4VP blocks form the cylinders and the PI blocks form spheres in the PS matrix. The P4VP cylinders display a hexagonal symmetry with six cylinders at the corners of a hexagon and one cylinder at the centre. The PI spheres are also arranged on a hexagonal lattice but the centre of that hexagon is occupied by a P4VP cylinder (Figure 6.4a). The intrinsic

---

---

incompatibility among the blocks and the volume fraction of the blocks change completely due to hydroxylation of the PI block. PS lamellae are observed in the P1, P2 and P3 films prepared from the  $\text{CHCl}_3/\text{DMF}$  solvent mixture (Figure 6.4b-d). The P1 film has a three-phase morphology as the P(HTMB-*r*-I) and P4VP domains are not miscible (Figure 6.4b). Two distinct phases of bright P(HTMB-*r*-I) and dark P4VP domains are visible between two successive PS lamellae in the  $\text{I}_2$  stained P1 film (Figure 6.4b). However, P2 and P3 films display a two-phase morphology where a PS domain and a mixed P(HTMB-*r*-I) and P4VP domain form alternating lamellae (Figure 6.4c, d). The miscibility is determined by the competing forces of self-association and intermolecular association of the P(HTMB-*r*-I) and P4VP blocks.<sup>169</sup> The self-association of the P(HTMB-*r*-I) block is hindered due to the random distribution of the incompatible HTMB and I repeating units. The intermolecular association of the P(HTMB-*r*-I) and P4VP blocks is favoured by the affinity of the hydroxyl moieties and opposed by the incompatibility of the isoprene moieties with the pyridine rings, respectively. The degree of hydroxylation of P1 is below the threshold to overcome the repulsion between isoprene and pyridine moieties. In P2 and P3 the affinity of the hydroxyl groups and pyridine moiety dominates over the incompatibility of pyridine rings with the isoprene moieties which results in domains of mixed P(HTMB-*r*-I) and P4VP blocks.

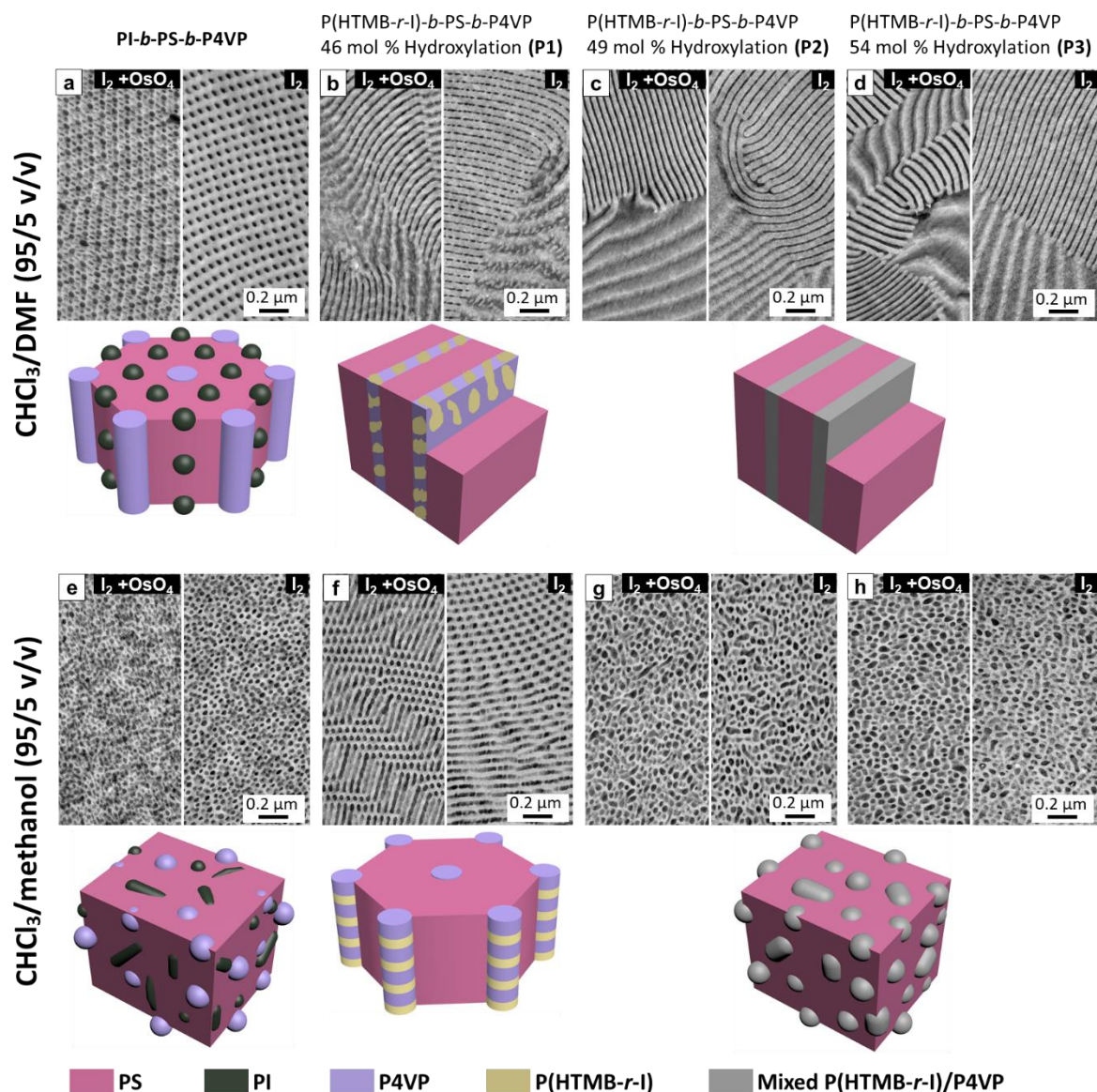


Figure 6.4. TEM images and schematic representation – (a) PI-*b*-PS-*b*-P4VP, (b) P1, (c) P2, (d) P3 films prepared from CHCl<sub>3</sub>/DMF 95/5 (v/v). (e) PI-*b*-PS-*b*-P4VP, (f) P1, (g) P2, (h) P3 films prepared from CHCl<sub>3</sub>/methanol 95/5 (v/v). In the I<sub>2</sub> stained films, the P4VP domains appear dark in the bright PS matrix while the PI and P(HTMB-*r*-I) domains are not distinguishable from PS. In the double-stained films with I<sub>2</sub> and OsO<sub>4</sub>, the P4VP, PI and P(HTMB-*r*-I) domains are darker than the PS matrix. All the images have the same magnification.

A three-phase morphology of PI-*b*-PS-*b*-P4VP is transformed into “banana-like” short PI cylinders and P4VP spheres dispersed in a PS matrix in the film prepared from the CHCl<sub>3</sub>/methanol 95/5 (v/v) solvent mixture (Figure 6.4e). The vapour pressures of CHCl<sub>3</sub>, methanol and DMF at 25 °C are 25.9 kPa, 16.96 kPa and 0.49 kPa, respectively. Hence, the composition of the CHCl<sub>3</sub>/methanol solvent mixture changed less during the drying of the films than in case of the CHCl<sub>3</sub>/DMF solvent mixture. At a later stage of evaporation PI-*b*-PS-*b*-P4VP micelles having a rather collapsed P4VP core and a relatively more swelled PS and PI corona were formed. Upon solidification the P4VP formed spheres and PI formed short range cylinders in the PS matrix. The PI-*b*-PS-*b*-P4VP film could not reach thermodynamic equilibrium as the CHCl<sub>3</sub>/methanol solvent mixture is not a good solvent for the P4VP block. However, for the films prepared from the CHCl<sub>3</sub>/DMF solvent mixture the composition of the solvent changed gradually to a significantly higher DMF content. As a result the P4VP blocks were not kinetically trapped and the morphology reached thermodynamic equilibrium. Similarly, during the preparation of P2 and P3 films from the CHCl<sub>3</sub>/methanol solvent mixture the mixed P(HTMB-*r*-I) and P4VP blocks formed the collapsed core of the micelles and PS formed the swelled corona. Consequently, randomly distributed elongated spherical domains of the mixed P(HTMB-*r*-I) and P4VP blocks are formed in the PS matrix (Figure 6.4g, h). The P1 film shows a hexagonal array of lamellar-within-cylindrical<sup>177</sup> domains of immiscible P(HTMB-*r*-I) and P4VP in the matrix of PS (Figure 6.4f). A possible reason for the formation of symmetrical cylindrical domains with a lamellar substructure could be a gain of conformational entropy of the PS blocks, as they cannot only form bridges between different cylinders, but also fold back and have both PS block ends connected to the same cylinder. This could become possible due to a less repulsive interaction between the two end blocks compared to their repulsive interactions with the central block, in combination with an overall less selective solvent mixture compared to the CHCl<sub>3</sub>/DMF at the moment of freezing in the

morphology. Thus, the composition of the solvent mixture dictates the morphology of the films but has no influence on the miscibility of the end blocks.

### 6.3.2 Influence of Evaporation Speed on the Miscibility of P(HTMB-*r*-I) and P4VP Blocks

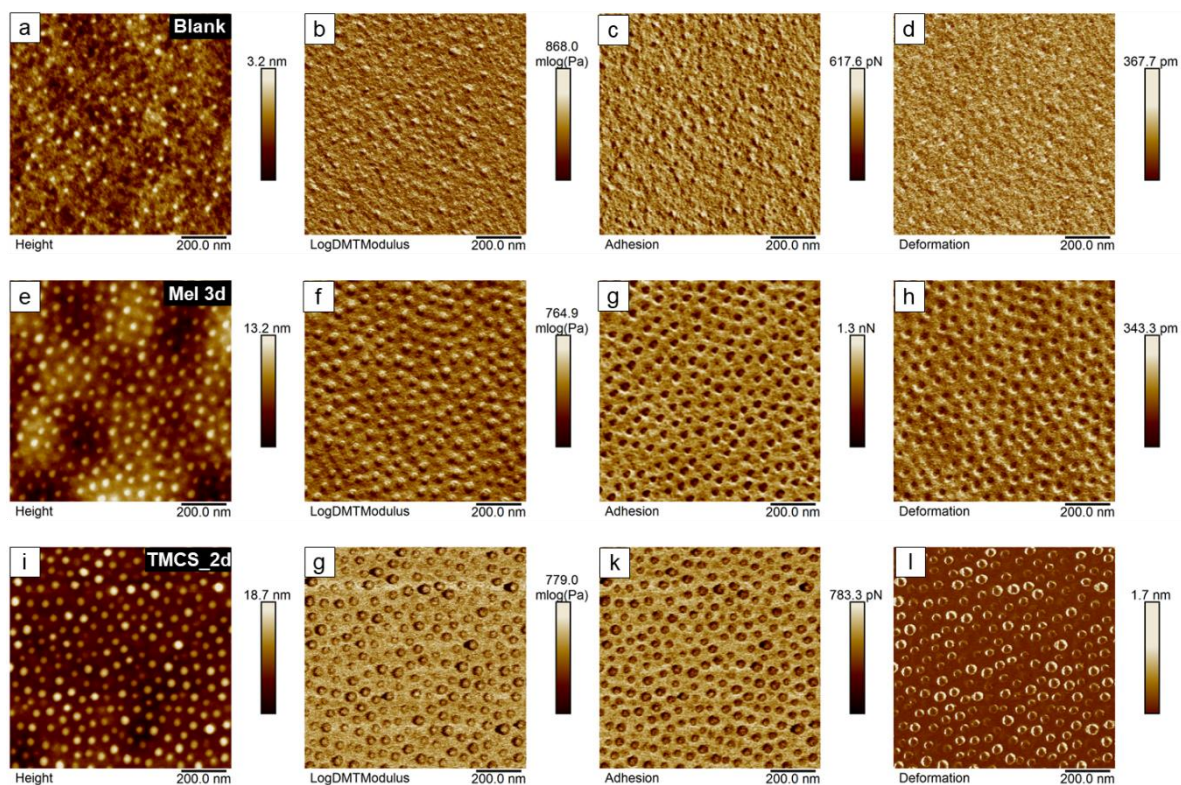


Figure 6.5. AFM height, modulus, adhesion and deformation images of (a-d) blank PI-*b*-PS-*b*-P4VP thin film, (e-h) PI-*b*-PS-*b*-P4VP thin film with 3 days methyl iodide (MeI) post-modification, (i-l) PI-*b*-PS-*b*-P4VP thin film with 2 days trimethylchlorosilane (TMCS) post-modification.

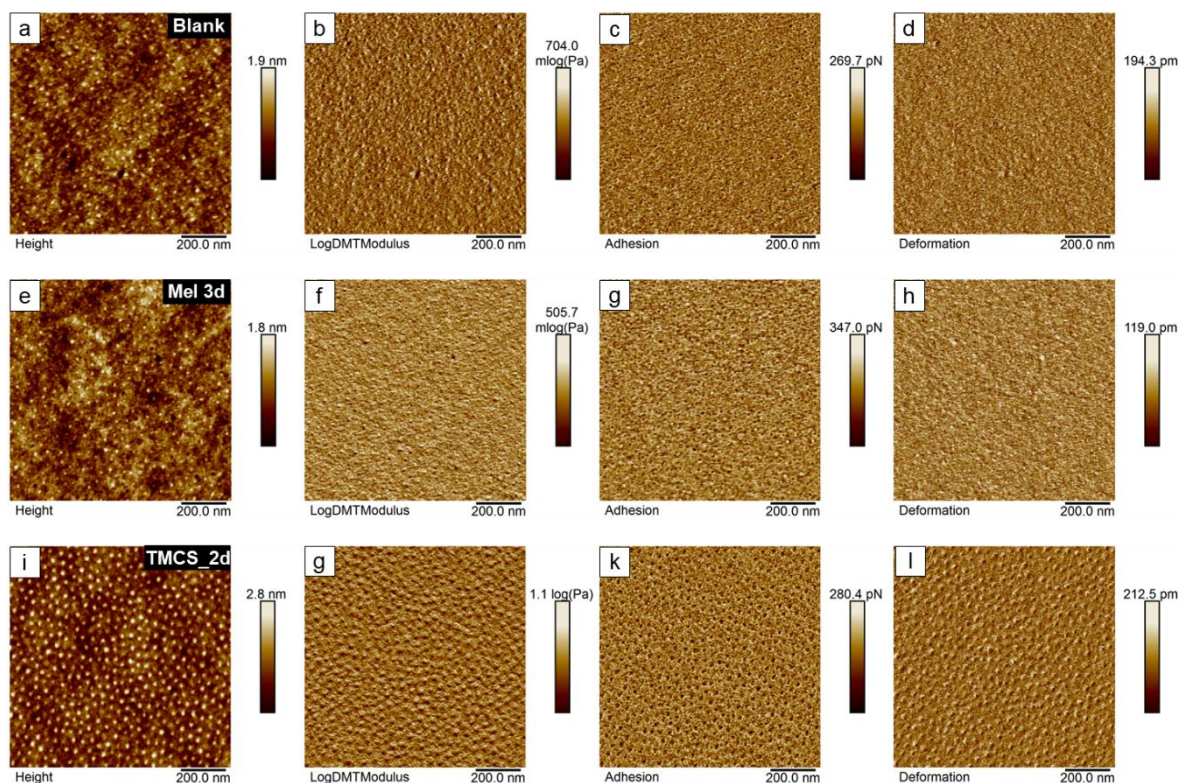


Figure 6.6. AFM height, modulus, adhesion and deformation images of (a-d) blank thin film of hydroxylated diblock terpolymer PS-*b*-P(HTMB-*r*-I), (e-h) PS-*b*-P(HTMB-*r*-I) thin film with 3 days methyl iodide (MeI) post-modification, (i-l) PS-*b*-P(HTMB-*r*-I) thin film with 2 days trimethylchlorosilane (TMCS) post-modification.

In order to investigate the influence of evaporation speed on the miscibility of the P(HTMB-*r*-I) and P4VP blocks nonporous P3 thin films were prepared by spin-coating using a CHCl<sub>3</sub> and methanol 98/2 (v/v) solvent mixture (Figure 6.7). In this case the evaporation was finished within 20 seconds. The morphology of the spin-coated film was investigated by atomic force microscopy in PeakForce QNM (Quantitative Nanomechanical Mapping) mode. Due to the small distinction of nanomechanical properties of different domains, it is difficult to discern the morphology of the spin-coated P3 film (Figure 6.7 a, d, g, j). To improve the contrast between the domains the spin-coated P3 film was post-modified with additional molecules, *i.e.*, methyl iodide (MeI) and trimethylchlorosilane (TMCS). MeI can selectively react with P4VP

segments<sup>153</sup> but not with P(HTMB-*r*-I), which is confirmed by the MeI treatments of PI-*b*-PS-*b*-P4VP (Figure 6.5e-h) and PS-*b*-P(HTMB-*r*-I) (Figure 6.6e-h). TMCS reacts with both P4VP and P(HTMB-*r*-I), as demonstrated by the TMCS treatments of PI-*b*-PS-*b*-P4VP (Figure 6.5i-l) and PS-*b*-P(HTMB-*r*-I) (Figure 6.6i-l). Specifically, after post-modification of the PI-*b*-PS-*b*-P4VP films with MeI vapour (Figure 6.5e-h) and TMCS vapour (Figure 6.5i-l) separately, the height of the discrete domains of P4VP increases. The change of nanomechanical properties of the discrete P4VP domains is also visible in the modulus, adhesion and deformation maps. These changes are attributed to the chemical attachment of MeI and TMCS in the P4VP domains. Regarding the PS-*b*-P(HTMB-*r*-I) films, after MeI vapour post-modification, no obvious change of height difference at the surface and nanomechanical properties is observed, revealing that no reaction occurred between MeI and -OH groups (Figure 6.6e-h). However, after post-modification with TMCS vapour, there is an increased height difference at the surface and also significant changes in the nanomechanical properties, *i.e.* improved contrast in the modulus, adhesion and deformation images (Figure 6.6i-l). These results confirm that TMCS can react with -OH groups of P(HTMB-*r*-I) under a mild heterogeneous condition.

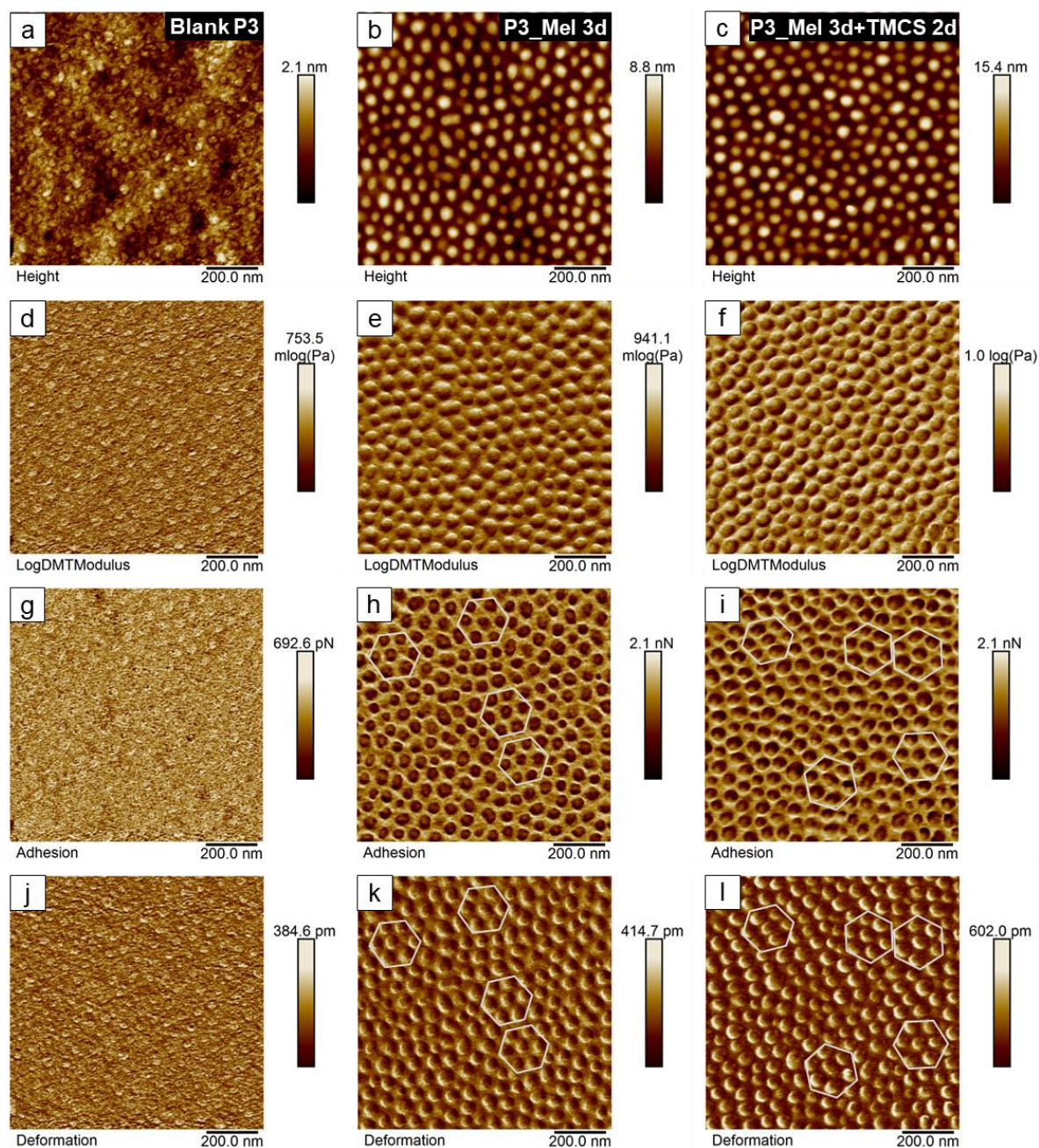


Figure 6.7. AFM height, modulus, adhesion and deformation images of (a, d, g, j) blank thin film of copolymer P3, (b, e, h, k) P3 thin film with 3 days methyl iodide (MeI) post-modification, (c, f, i, l) P3 thin film with 3 days MeI post-modification and subsequent 2 days trimethylchlorosilane (TMCS) post-modification. All the post-modifications were employed on the same piece of the blank thin film.

Unlike the film prepared by slow evaporation of solvents (Figure 6.4d, h), hexagonally packed discrete domains surrounded by a continuous PS matrix are observed in the spin-coated P3 films (Figure 6.7). Although the packing of the domains is mostly hexagonal, some irregularities in the symmetry of the domains (e.g. pentagons, polygons) are also present. The height of the domains increases at the surface of the P3 film after post-modification with 3 days MeI (Figure 6.7b), while in the log DMT Modulus, adhesion and deformation maps the contrast between these domains and the matrix becomes significantly higher (Figure 6.7e, h and k). These results confirm that the discrete hexagonally packed domains contain the P4VP segments. No new (additional) microdomains appear in the AFM images of the film which was post-modified with MeI for 3 days and then with TMCS for 2 days (Figure 6.7c, f, i and l). The P4VP blocks were fully quaternized by MeI within 3 days and the further treatment with TMCS post-modified the –OH groups of the P(HTMB-*r*-I) block. The sizes of the discrete domains in the log DMT Modulus, adhesion and deformation maps (Figure 6.7f, i and l) are bigger and the height of the domains at the surface are more than those in the film modified only with 3 days MeI (Figure 6.7c). It is rather likely that the discrete domains consist of both P(HTMB-*r*-I) and P4VP blocks. Hence, the fast evaporation of the solvent induces a hexagonal symmetry of the microdomains without affecting the miscibility of the end blocks.

TEM and AFM investigations indicate that both the solvent composition and the evaporation rate have no effect on the miscibility of microdomains. Therefore, it is clear that the desired charged mosaic membranes with P3 was not obtained. However, we achieved the fabrication of an isoporous membrane with multifunctional nanochannels, which is thoroughly discussed below.

## 6.4 Fabrication of Isoporous Membrane via SNIPS

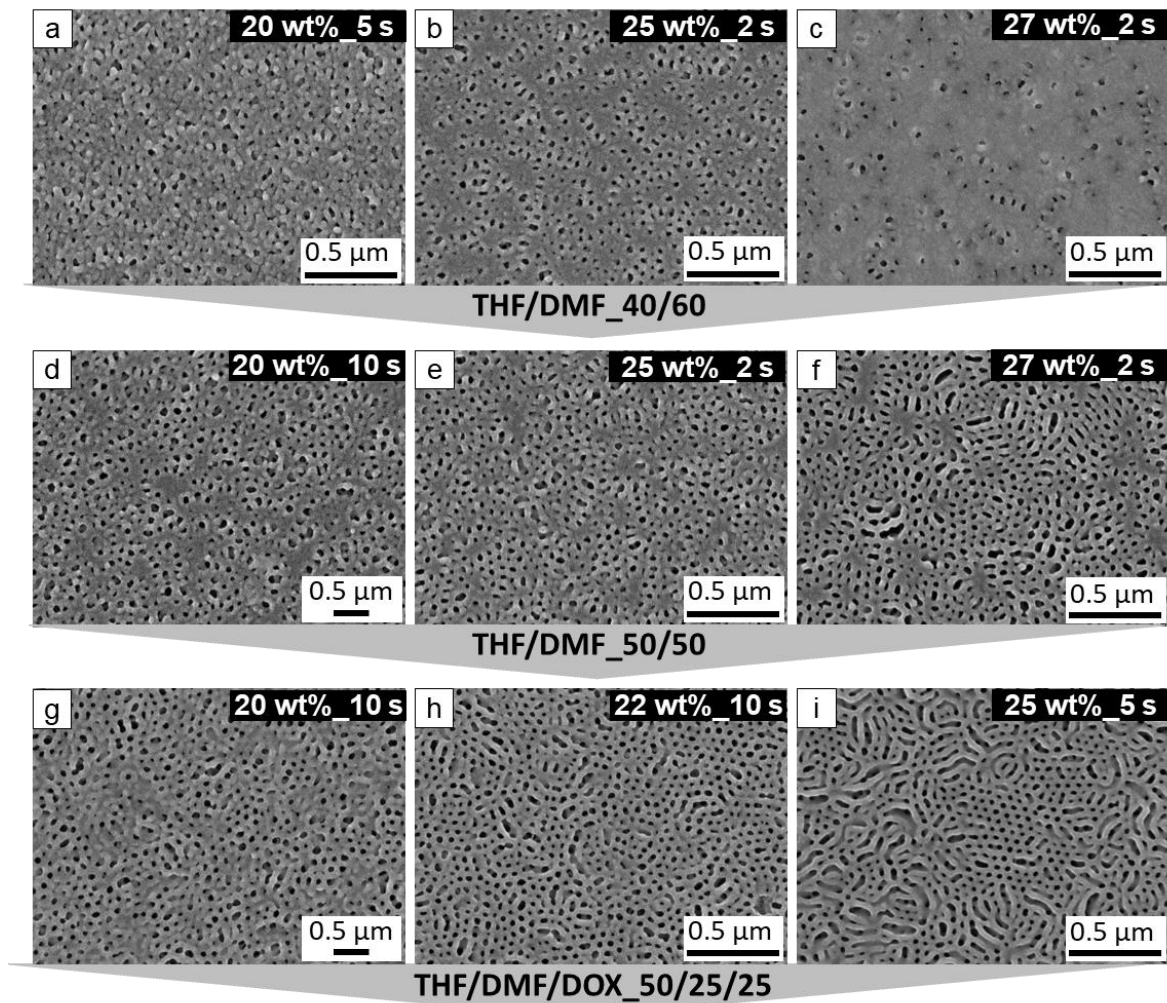


Figure 6.8. SEM images of the top surface of representative P3 membranes cast from different solvent systems using different polymer concentrations (indicated in the images) and evaporation times (indicated in the images): (a-c) THF/DMF 40/60, (d-f) THF/DMF 50/50, (g-i) THF/DMF/DOX 50/25/25.

Based on the work in Chapter 4 and Chapter 5, THF and DOX can be used as selective solvents for the non-polar matrix-forming block PS, while DMF is more selective for the polar pore-forming block P4VP and P(HTMB-*r*-I). A series of the casting solutions of P3 in the binary solvent system THF/DMF or ternary solvent system THF/DMF/DOX was used to cast the

membranes. Compared to binary THF/DMF, ternary THF/DMF/DOX leads to better open porous structure (Figure 6.8).

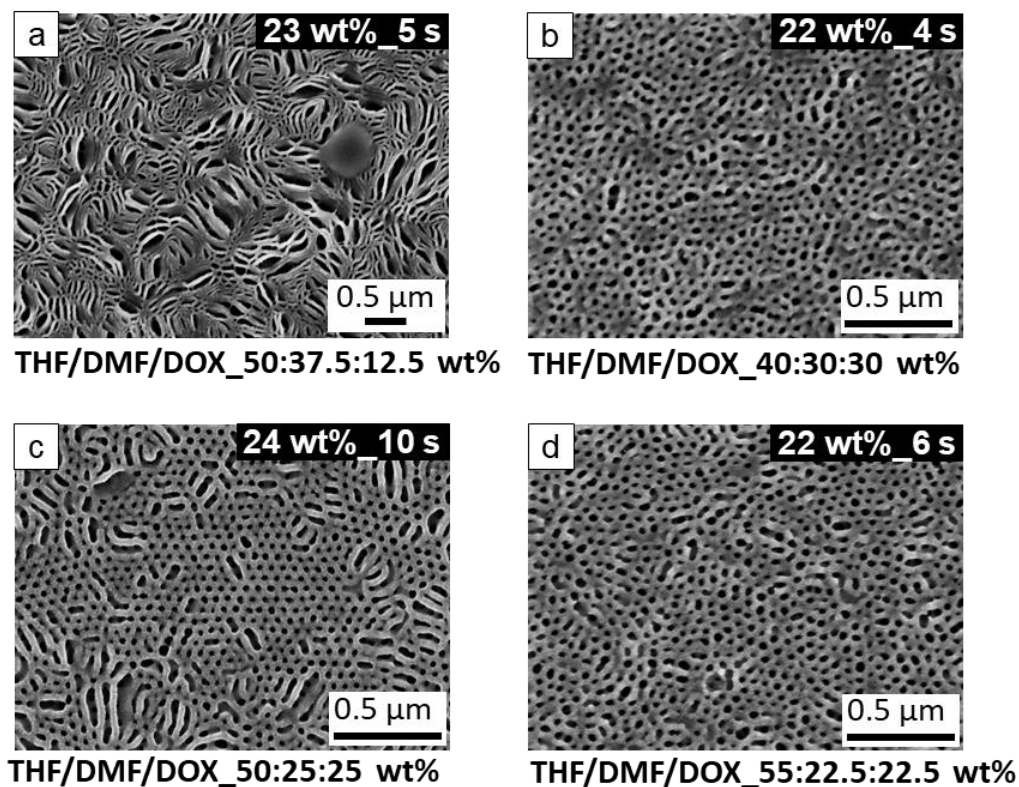


Figure 6.9. SEM images of the top surface of representative P3 membranes cast from (a) 23 wt% solution in a THF/DMF/DOX 50/37.5/12.5 solvent mixture, the evaporation time  $t = 5$  s, (b) 22 wt% solution in a THF/DMF/DOX 40/30/30 solvent mixture, the evaporation time  $t = 4$  s, (c) 24 wt% solution in a THF/DMF/DOX 50/25/25 solvent mixture, the evaporation time  $t = 10$  s, (d) 22 wt% solution in a THF/DMF/DOX 55/22.5/22.5 solvent mixture, the evaporation time  $t = 6$  s.

Furthermore, to ascertain the optimum composition of THF/DMF/DOX, the content of DMF (selective solvent for pore-forming blocks) was relatively changed. Among the investigated solvent systems the best solvent composition is THF/DMF/DOX 50/25/25, as it leads to the best result with vertically-aligned hexagonally packed open pores (Figure 6.9). However, the

isoporous structure is imperfect with an elongated cylindrical structure (Figure 6.9c). According to a previous study based on PS-*b*-P2VP, this phenomenon should be the typical transition state from an ordered spherical pore network (PN) to an ordered cylindrical (OC) structure, attributed to trapping of the ordered micellar array with highly swollen cores in a continuous matrix at a later time.<sup>95</sup> Thus, the fine-tuning of the evaporation time and the concentration of cast solutions might allow us to eliminate these cylindrical defects. However, no obvious improvement is observed by varying the parameters (Figure 6.10, Figure 6.11), implying that the triblock quaterpolymer P3 system possesses a very small stable region of the desired self-assembled structure. In practice, it is almost not possible to identify the exact combination of solution composition and evaporation time to obtain a defect free isoporous top layer.

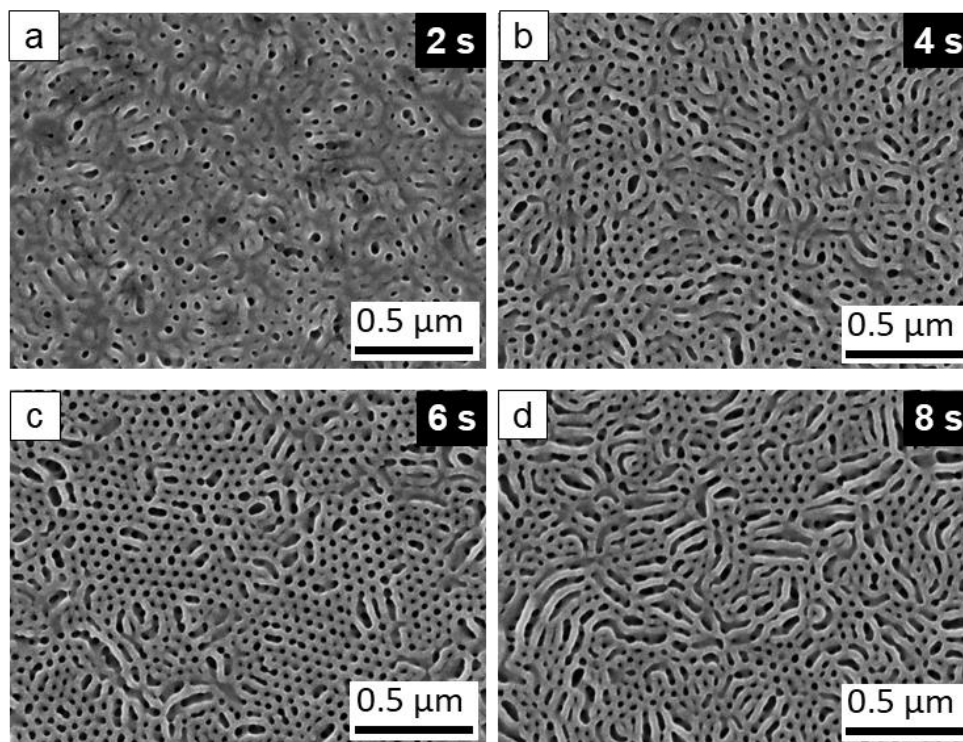


Figure 6.10. SEM images of the top surface of representative P3 membranes cast from 24 wt% solution in THF/DMF/DOX 2/1/1 with different evaporation time (a)  $t = 2$  s, (b)  $t = 4$  s, (c)  $t = 6$  s, (d)  $t = 8$  s.

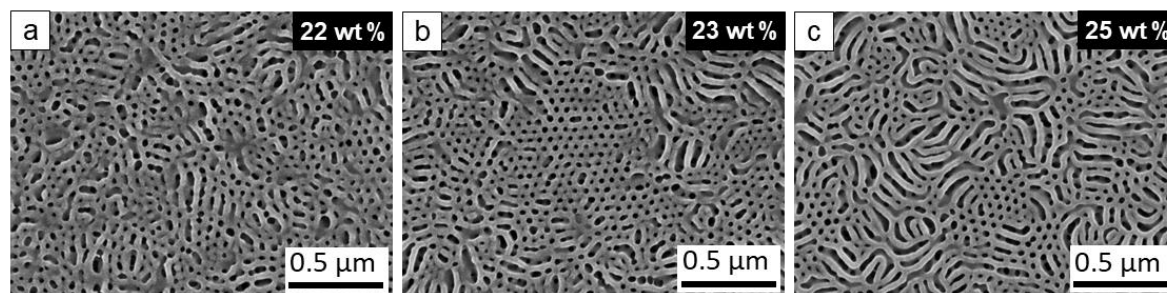


Figure 6.11. SEM images of the top surface of representative P3 membranes cast from ternary solvent system THF/DMF/DOX 2/1/1 (a) 22 wt% polymer concentration, the evaporation time  $t = 10$  s, (b) 23 wt% polymer concentration, the evaporation time  $t = 10$  s, (c) 25 wt% polymer concentration, the evaporation time  $t = 8$  s.

It was proven that the addition of metal salts,<sup>102, 178</sup> carbohydrates,<sup>49</sup> alcohols and organic acid<sup>104</sup> in the casting solution of PS-*b*-P4VP membrane broadens the optimal processing window. These additives generally form the coordination or hydrogen bonding with nitrogen atoms of 4VP groups. Due to the toxicity of most transition metals (e.g. copper (II)) in biotechnological applications, in this study, non-toxic magnesium acetate ( $\text{MgAc}_2$ ) was used as an additive to cast P3 membranes. A series of casting solutions with gradually increasing the amount of  $\text{MgAc}_2$  was employed to define the optimal amount of  $\text{MgAc}_2$ , *i.e.*, from 0.75 to 4.75 wt% with respect to BCP (Figure 6.12). In comparison with the blank membrane without  $\text{MgAc}_2$ , the addition of 0.75 wt%  $\text{MgAc}_2$  (Figure 6.12a) does not show a significant improvement of the membrane morphology, attributed to the weak complexation of magnesium ions with the pyridine moieties. It can be clearly seen that the membrane with 1.5 wt%  $\text{MgAc}_2$  possesses a highly ordered open porous structure without defects, *e.g.* elongated spherical pores (Figure 6.12b). Furthermore, after the amount of  $\text{MgAc}_2$  exceeds 1.5 wt% of BCP, the membrane structure becomes less ordered (Figure 6.12c-e). Therefore the optimum concentration of  $\text{MgAc}_2$  for this system is 1.5 wt% with respect to the BCP, leading to a typical integral asymmetric isoporous membrane (Figure 6.13). Meanwhile, the addition of such

interacting ions, *i.e.*  $\text{MgAc}_2$ , results in the reduction of the required block copolymer concentration from 24 wt % to 22 wt %, which is advantageous for ecologic and economic benefit, consistent with the previous studies based on PS-*b*-P4VP with  $\text{MgAc}_2$ .<sup>101, 178</sup>

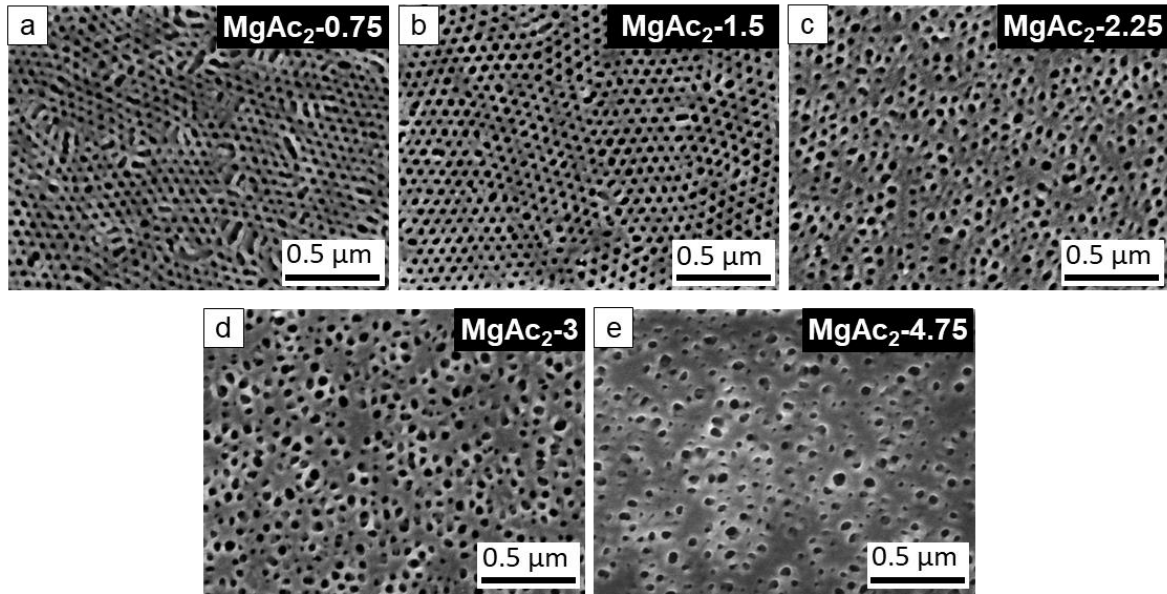


Figure 6.12. SEM images of top surface of representative P3 membranes cast from (a) 22 wt% solution with 0.75 wt%  $\text{Mg}(\text{acetate})_2$  ( $\text{MgAc}_2$ ) as BCP, the evaporation time  $t = 10$  s, (b) 22 wt% solution with 1.5 wt%  $\text{Mg}(\text{acetate})_2$  ( $\text{MgAc}_2$ ) as BCP, the evaporation time  $t = 8$  s (c) 21 wt% solution with 2.25 wt%  $\text{MgAc}_2$  as BCP, the evaporation time  $t = 4$  s, (d) 20 wt% solution with 3 wt%  $\text{MgAc}_2$  as BCP, the evaporation time  $t = 6$  s, (e) 21 wt% solution with 4.75 wt%  $\text{MgAc}_2$  as BCP, the evaporation time  $t = 5$  s.

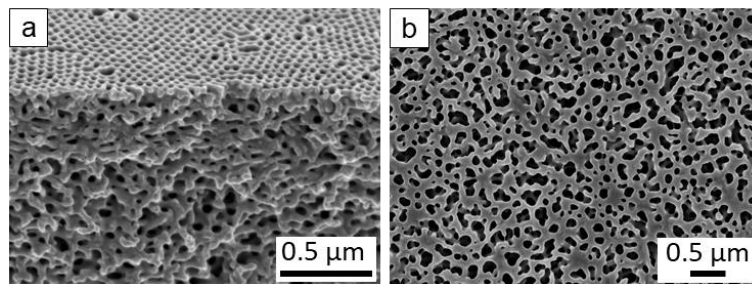


Figure 6.13. SEM images of P3 SNIPS membrane: (a) cross-section near the top surface, (b) bottom interface contacting with glass substrates.

## 6.5 Post-functionalization of Isoporous Membrane toward Negatively or Positively Charged Membrane

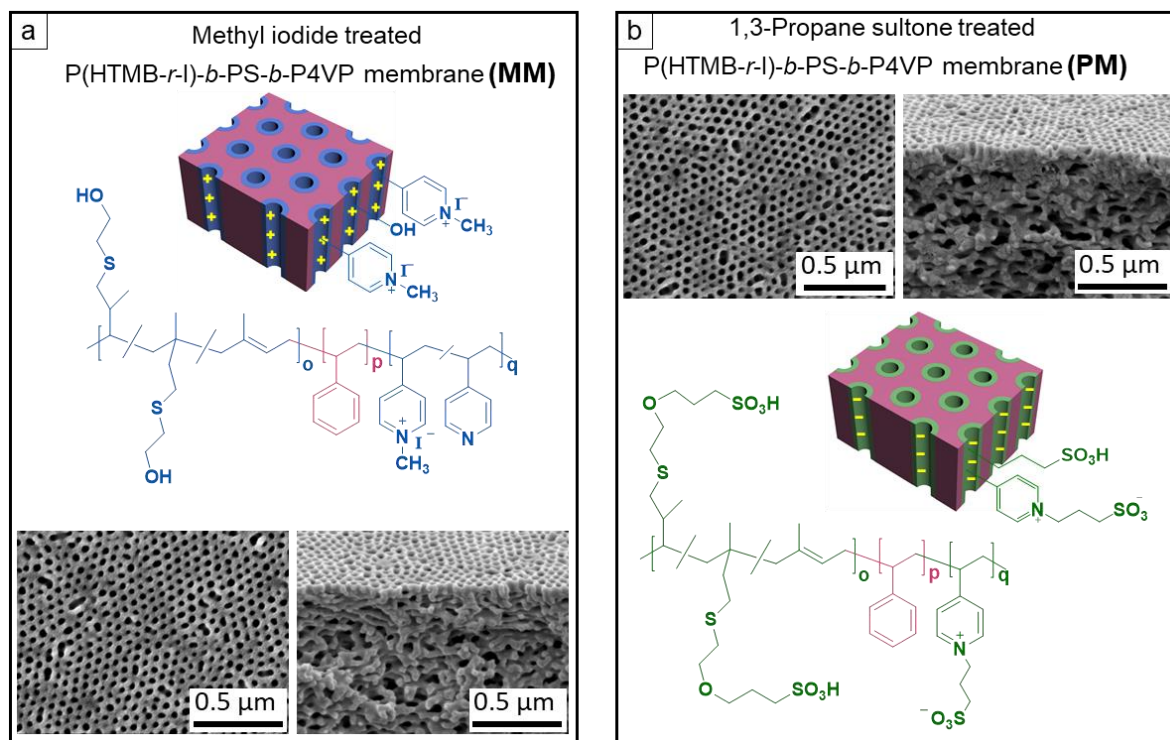


Figure 6.14. Schematic representation, chemical structure and SEM images of top surface and cross section of (a) methyl iodide treated membrane MM, (b) 1,3-propane sultone treated membrane PM.

The P3 membrane was post-functionalized with methyl iodide and 1,3-propane sultone by straightforward *in situ* one step gas-solid interface reaction to obtain positively and negatively charged pores, respectively (Figure 6.14). In the FTIR spectrum of the methyl iodide treated membrane (MM) a new characteristic peak of the  $\text{C} = \text{N}^+$  stretching vibration appears at  $1640 \text{ cm}^{-1}$  due to quaternization of the nitrogen moieties of the pyridine rings, while the intensity of the characteristic stretching vibration of  $\text{C} = \text{N}$  and  $\text{C} = \text{C}$  of the aromatic rings at  $\approx 1600 \text{ cm}^{-1}$  decreases dramatically (Figure 6.15, blue curve). Based on the work of the quaternization of PS-*b*-P4VP membranes in Chapter 4, 2 days exposure to methyl iodide vapour results in a

complete quaternization. As the C = C stretching of aromatic rings of PS block also contributes to the peak at  $\approx 1600 \text{ cm}^{-1}$ , this peak does not disappear even after complete quaternization of the pyridine rings.<sup>153</sup> In case of the 1,3-propane sultone treated membrane (PM) two new characteristic vibrations at  $\approx 1036 \text{ cm}^{-1}$  and  $\approx 1181 \text{ cm}^{-1}$  appear in the FTIR spectrum (Figure 6.15, green curve) owing to the stretching vibration of sulfonate groups. This proves the ring opening of 1,3-propane sultone and the covalent attachment of the sulfonic acid containing moieties on the membrane.<sup>122, 179</sup> From SEM images it is confirmed that MM (Figure 6.14a) and PM (Figure 6.14b) retain the kinetically trapped porous morphology of the pristine membrane (IO) (Figure 6.12b, Figure 6.13a). Due to the covalent attachment of the functional moieties MM and PM show slightly lower surface pore sizes and relatively thicker pore walls along the cross section compared to those of IO. The average surface pore sizes at the dry state (calculated from SEM images) of IO, MM and PM are 32 nm, 30 nm and 30 nm, respectively.

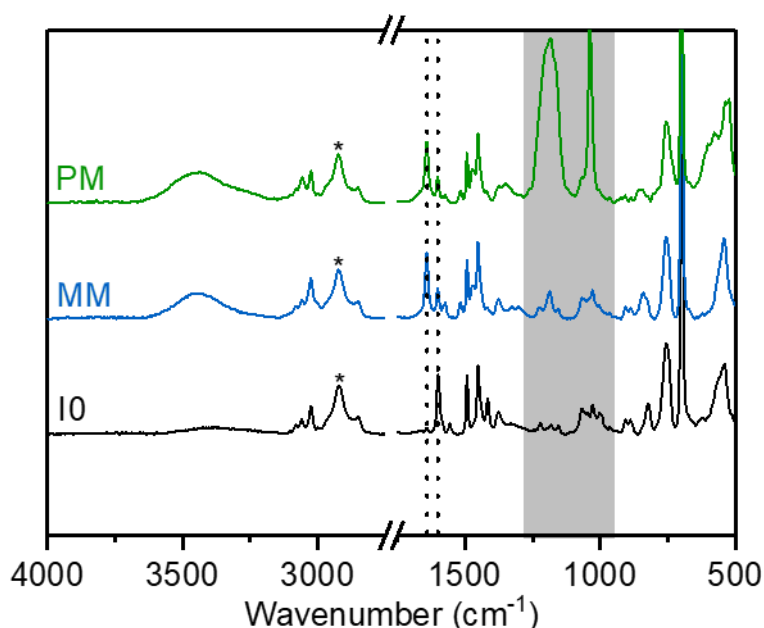


Figure 6.15. FTIR spectra of the pristine membrane IO, MM and PM. The relative intensities were normalized using the characteristic CH<sub>2</sub> stretching vibrations (\*) of the unreactive backbone around 2924 cm<sup>-1</sup>.

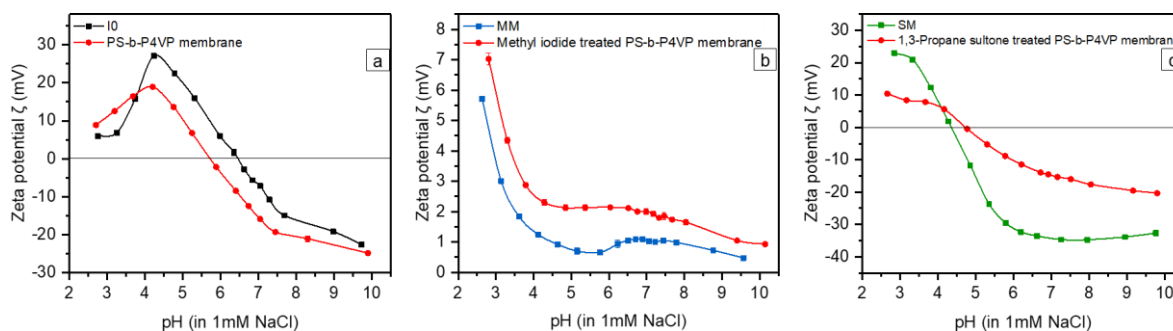


Figure 6.16. Comparison of the surface zeta potential as a function of pH of (a) P(HTMB-*r*-I)-*b*-PS-*b*-P4VP (IO) and PS-*b*-P4VP membrane, (b) methyl iodide treated P(HTMB-*r*-I)-*b*-PS-*b*-P4VP (MM) and PS-*b*-P4VP membrane, (c) 1,3-propane sultone treated P(HTMB-*r*-I)-*b*-PS-*b*-P4VP (SM) and PS-*b*-P4VP membrane. Experiments were carried out with a background electrolyte of 1 mM NaCl.

Surface zeta potential measurements were performed to prove the success of post-functionalization again. Meanwhile in order to corroborate that open isoporous structure of P(HTMB-*r*-I)-*b*-PS-*b*-P4VP membrane are formed by the mixed P(HTMB-*r*-I) and P4VP domains more directly, we also compared the surface zeta potential ( $\zeta$ ) of three pairs of membranes: P(HTMB-*r*-I)-*b*-PS-*b*-P4VP (IO) and PS-*b*-P4VP membrane (Figure 6.16a), methyl iodide treated P(HTMB-*r*-I)-*b*-PS-*b*-P4VP (MM) and PS-*b*-P4VP membrane (Figure 6.16b), 1,3-propane sultone treated P(HTMB-*r*-I)-*b*-PS-*b*-P4VP (SM) and PS-*b*-P4VP membrane (Figure 6.16c). The surface zeta potential ( $\zeta$ ) of IO is negative at a basic pH which becomes positive below pH 6.5 due to protonation of the P4VP block. IO reaches the isoelectric point at a higher pH compared to that of the PS-*b*-P4VP membrane (Figure 6.16a). Owing to quaternization of the nitrogen moieties of the P4VP block, MM and methyl iodide treated PS-*b*-P4VP do not show such pH responsiveness, instead a slightly positive  $\zeta$  is observed in the whole pH range of 2.5 – 10 (Figure 6.16b). But a lower positive  $\zeta$  value of the MM indicates the presence of additional hydroxyl moieties along the pore walls of the isoporous layer. After post-treatment with 1,3-propane sultone the vinyl pyridine moieties were converted into a

zwitterionic structure while the hydroxyl moieties were converted into sulfonic acid groups. Compared to I0, PM displays a remarkable shift of isoelectric point towards a lower pH and a plateau of higher negative  $\zeta$  in the pH range of 6 to 10. Additionally negative  $\zeta$  of PM in the pH range of 6 to 10 is also significantly higher than that of 1,3-propane sultone treated PS-*b*-P4VP membrane (Figure 6.16c). This result is attributed to the presence of acidic groups (sulfonic acid groups) along the pore walls and their corresponding dissociation.<sup>157</sup> These comparisons confirm that miscible P(HTMB-*r*-I) and P4VP are the pore-forming blocks of the P(HTMB-*r*-I)-*b*-PS-*b*-P4VP membrane.

## 6.6 Performance of Multifunctional Isoporous Membranes

### 6.6.1 pH Responsive Behavior and Water Permeance

The pH responsiveness of the P4VP block of I0 has a strong influence on the water permeance. At pH 7 the water permeance through I0 is  $598 \text{ L m}^{-2} \text{ h}^{-1} \text{ bar}^{-1}$  which gradually decreases to  $22 \text{ L m}^{-2} \text{ h}^{-1} \text{ bar}^{-1}$  at pH 3 (Figure 6.17a). It is a distinct signature of swelling of the protonated P4VP blocks in response to pH.<sup>55</sup> At pH 7 the P4VP blocks exist in a collapsed conformation as the nitrogen moieties are in a deprotonated and thus hydrophobic state. The P4VP blocks gradually adopt an extended conformation due to increasing degree of protonation of the nitrogen moieties with the decrease of pH. Consequently the pores of the membranes become narrow and the water permeance drops. As such pH responsive behaviour is not undermined by the mixed P(HTMB-*r*-I) pore-forming block, it is clear that at low pH the nitrogen moieties of the P4VP blocks have a higher tendency to be in the protonated state compared to hydrogen bond formation with the hydroxyl moieties of the P(HTMB-*r*-I) blocks.

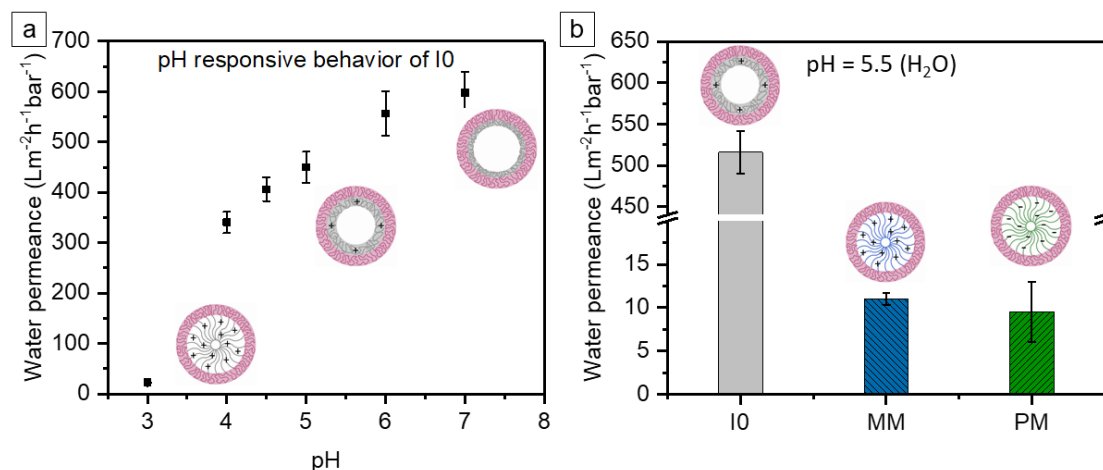


Figure 6.17. (a) pH responsive behaviour of I0. (b) Water permeance of I0, MM and PM.

The permeance of ultrapure water (pH 5.5, conductivity  $0.055 \mu\text{S cm}^{-1}$ ) through I0, MM and PM is  $515 \text{ L m}^{-2} \text{ h}^{-1} \text{ bar}^{-1}$ ,  $11 \text{ L m}^{-2} \text{ h}^{-1} \text{ bar}^{-1}$  and  $9.5 \text{ L m}^{-2} \text{ h}^{-1} \text{ bar}^{-1}$ , respectively (Figure 6.17b). It is worth noting that the water permeance of MM and PM is higher than reported for SNIPS BCP membranes with charged-induced swelling of nanopores ( $0.6\text{--}4 \text{ L m}^{-2} \text{ h}^{-1} \text{ bar}^{-1}$ ),<sup>42, 59</sup> nanofiltration membranes formed by an amphiphilic random copolymer ( $1.4\text{--}7.3 \text{ L m}^{-2} \text{ h}^{-1} \text{ bar}^{-1}$ )<sup>180-182</sup> and comparable to that of commercially available nanofiltration membranes ( $3.7\text{--}11.4 \text{ L m}^{-2} \text{ h}^{-1} \text{ bar}^{-1}$ ).<sup>183, 184</sup> Since at the dry state the pore size of I0, MM and PM are close to each other, it can be seen that during the measurement of ultrapure water permeance (*i.e.* at pH 5.5) the chains of pore-forming block of MM and PM are in a highly swelled state attributed to strong electrostatic repulsion of positive or negative polyelectrolytes while those of I0 are in a rather collapsed state.

## 6.6.2 Charge-based Selective Transport of Small Molecules through Positively Charged Membrane

To demonstrate the charge selective nature of MM we employed aqueous solutions of three model molecules having a comparable molecular weight ( $319 - 377 \text{ g mol}^{-1}$ ) but different

electrostatic charges – a cationic dye methylene blue (MB<sup>+</sup>), an anionic dye orange II (OR<sup>-</sup>) and a neutral vitamin riboflavin (RB0). According to MM2 force field energy minimization model calculation (in vacuum) the lateral dimensions of MB<sup>+</sup>, RB0 and OR<sup>-</sup> are rather similar, *i.e.* 1.1 nm, 1.0 nm and 1.3 nm, respectively.<sup>141</sup> We also compared the calculated lateral dimensions of small molecules with the reported Stokes radius of the molecules in Table 10.3 (Chapter 10 Appendix), the calculated values show a slight deviation compared to reported values. Based on the reported Stokes diameters, MB<sup>+</sup>, RB0 and OR<sup>-</sup> also exhibit a similar size. The aqueous solutions containing single solutes and mixed solutes were employed to determine the retention and selectivity of the model molecules.

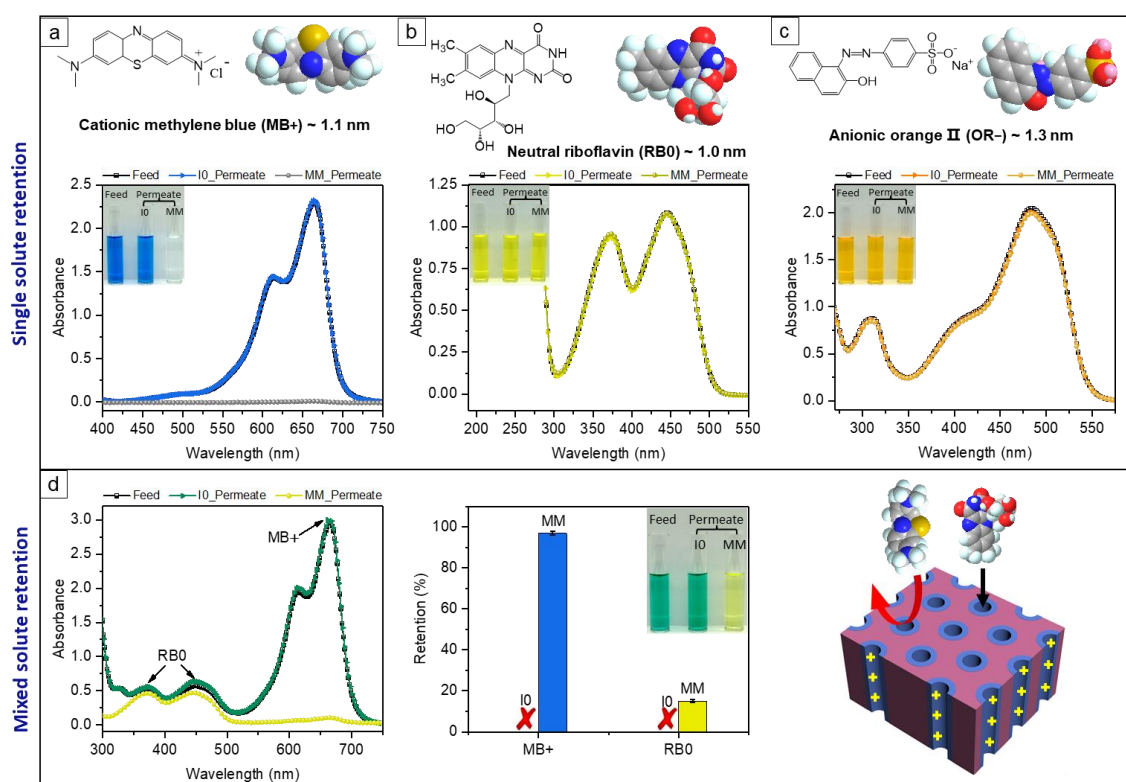


Figure 6.18. Charge-based selectivity between similarly sized organic solutes (~1 nm) in single and mixed solute systems based on the positively charged membrane MM. Molecular structure and space-filling model of three model organic molecules with distinct charges while similar size of ca. 1 nm, and the corresponding separation behaviour of the pristine membrane I0 and

the positively charged membrane MM determined by UV-vis spectra and a colour change of the solution in single solute retention measurement: (a) cationic methylene blue (MB<sup>+</sup>), (b) neutral riboflavin (RB0), (c) anionic orange II (OR<sup>-</sup>), measured with MM close to saturated adsorption by immersing in a 0.1 mM OR<sup>-</sup> solution for 30 days. (d) The competitive separation behavior of IO and MM in the mixed-solute retention of MB<sup>+</sup> and RB0 (50/50, molar ratio) confirmed by UV-vis spectra and the colour change of the solution.

The aqueous solutions of MB<sup>+</sup>, RB0 and OR<sup>-</sup> passed through IO with no rejection of MB<sup>+</sup> and RB0 and only 2% rejection of OR<sup>-</sup> (Figure 6.18a-c). When an aqueous solution of MB<sup>+</sup> was used as a feed solution for MM, a substantial reduction of colour was observed in the permeate solution. 95.3% of MB<sup>+</sup> was retained from the aqueous solution by MM (Figure 6.18a). Remarkably, neutral RB0 permeated through MM completely without any rejection (Figure 6.18b) which proves that MM contains distinct uniform soft nanochannels although the polyelectrolyte pore-forming block swells in the presence of water. According to these results, the ideal selectivity of MB<sup>+</sup> over RB0,  $\psi_{RB0/MB^+}^i$  is 21.3 (Table 6.2). Unlike MB<sup>+</sup> and RB0 the anionic OR<sup>-</sup> showed strong adsorption on the MM membrane (Table 6.3). It is obvious that OR<sup>-</sup> was adsorbed at the positively charged moieties of the MM due to the attraction of two opposite charges. Such adsorption of molecules on the membrane is undesirable as the polyelectrolyte pore-forming block would lose its ability to swell due to neutralization. To confirm this assumption we investigated the retention of OR<sup>-</sup> using a freshly prepared MM (Figure 6.19) and MM close to saturated adsorption by immersing in a 0.1 mM OR<sup>-</sup> solution for 30 days (Figure 6.18c). In the first case the membrane retained 62% of the OR<sup>-</sup> from the feed solution while the latter allowed complete passage of feed solution without any retention of OR<sup>-</sup> (Figure 6.18c). It corroborates that the pore walls of MM are decorated with rather strong positive charges which repel the MB<sup>+</sup> and adsorb the OR<sup>-</sup> from their aqueous solutions. However, the surface zeta potential of MM is only slightly above zero (0.5 – 1.1 mV) in the

pH range 5 – 10 (Figure 6.16b). The discrepancy between the true value of surface zeta potential and the apparent value of the surface zeta potential from streaming current or streaming potential measurement has been pointed out in several studies.<sup>185, 186</sup> Additionally, positive charges at the membrane pore wall can influence the retention of MB<sup>+</sup> only when the nanochannel is narrow enough. The pH of 0.1 mM MB<sup>+</sup> solution is 5.7 (Table 6.4). At pH 5.7 the pores of I0 also carry a positive charge (Figure 6.16a) while the pore-forming block is slightly swelled (Figure 6.17a). However, the pores of I0 are too big to retain MB<sup>+</sup> from aqueous solution.

Table 6.2 Retention ( $R$ ) and separation selectivity ( $\psi$ ) for the pristine membrane I0 and the positively charged membrane MM in single- and mixed-solute retention experiments.

Membrane	Retention ( $R$ , %)				Selectivity ( $\psi$ )	
	Single-solute		Mixture-solute		Single-solute	Mixed-solute
	MB <sup>+</sup>	RB0	MB <sup>+</sup>	RB0	$\psi_{RB0/MB^+}^I$	$\psi_{RB0/MB^+}^{MM}$
I0	0	0	0	0	1.0	1.0
MM	95.3 ± 0.1	0	97.0 ± 0.9	15.0 ± 0.6	21.3	28.3

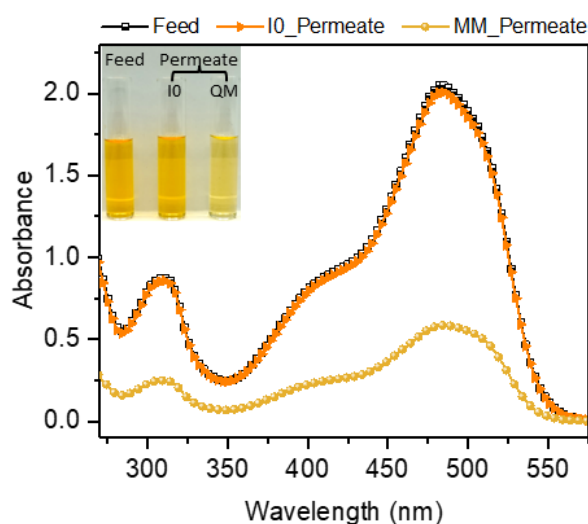


Figure 6.19. The separation behaviour of OR<sup>-</sup> of a freshly prepared positively charged membrane MM determined by UV-vis spectra and a colour change of the solution.

Table 6.3. Adsorption of five model organic molecules MB<sup>+</sup>, RB0, OR<sup>-</sup>, NG3<sup>-</sup> and RG6<sup>-</sup> onto the pristine membrane I0, the positively charged membrane MM and the negatively charged membrane PM.

Organic molecules	Pristine membrane I0 ( $\mu\text{g cm}^{-2}$ )	Positively charged membrane MM ( $\mu\text{g cm}^{-2}$ )	Negatively charged membrane PM ( $\mu\text{g cm}^{-2}$ )
MB <sup>+</sup>	0.34	0	-
RB0	0	0	-
OR <sup>-</sup>	$37.7 \pm 2.5$	$533 \pm 5.0$	$5.4 \pm 1.6$
NG3 <sup>-</sup>	$144.8 \pm 7.8$	-	$24.4 \pm 1.8$
RG6 <sup>-</sup>	$313.0 \pm 26.8$	-	$108.5 \pm 12.0$

Table 6.4. pH of aqueous solutions with 0.1 mM single or mixed organic small molecules.

Organic molecules	Single-solute					Mixed-solute	
	MB <sup>+</sup>	RB0	OR <sup>-</sup>	NG3 <sup>-</sup>	RG6 <sup>-</sup>	MB <sup>+</sup> /RB0	OR <sup>-</sup> / NG3 <sup>-</sup>
pH	5.7	6.7	6.4	6.5	4.6	5.9	6.4

To validate the excellent ideal selectivity  $\psi^i_{RB0/MB^+}$  obtained from single solute retention experiments, the real selectivity  $\psi^r_{RB0/MB^+}$  of the I0 and MM were determined using a 0.1 mM aqueous solution containing a 50:50 (molar ratio) mixture of MB<sup>+</sup> and RB0 ((Figure 6.18d). As expected, the permeation selectivity through I0 does not show any change in the mixed solute retention, that is,  $\psi^r_{RB0/MB^+} = \psi^i_{RB0/MB^+} = 1$ . For MM  $\psi^r_{RB0/MB^+} = 28.3$  is significantly higher than  $\psi^i_{RB0/MB^+} = 21.3$  (Table 6.2).

Such enhancement of the real selectivity compared to the ideal selectivity was reported in a few studies of non-biological systems.<sup>130, 180</sup> In the single solute retention measurement 100% of neutral RB0 permeated through MM while only 4.7% of cationic MB<sup>+</sup> could permeate through the membrane. MB<sup>+</sup> lagged far behind RB0 to enter the positively charged nanochannels of MM as it had to overcome an additional energy barrier (due to electrostatic repulsion) compared to RB0. Therefore, during the mixed solute retention study the nanochannels of MM constantly allowed the favorable entrance of RB0 molecules rather than

---

---

unfavorable MB<sup>+</sup> from the background of a mixture of MB<sup>+</sup> and RB0. However, RB0 still had to compete with MB<sup>+</sup> to reach the entrance of the nanochannels from the bulk of the solution.<sup>187</sup> As a result 85% of RB0 and 3% of MB<sup>+</sup> permeated through MM during the mixed solute retention measurement ( $\psi_{RB0/MB^+}^r = 28.3$ ). A possibility of back diffusion after the entrance of MB<sup>+</sup> and RB0 in the nanochannels of MM could be ruled out due to the applied transmembrane pressure. Overall, these results demonstrate the competition-induced enhancement of selectivity and strong capability of the prepared MM to perform charge based separation of organic molecules having a lateral molecular dimension of ~1 nm.

### 6.6.3 Charge/Size-based Selective Transport of Small Molecules through Negatively Charged Membrane

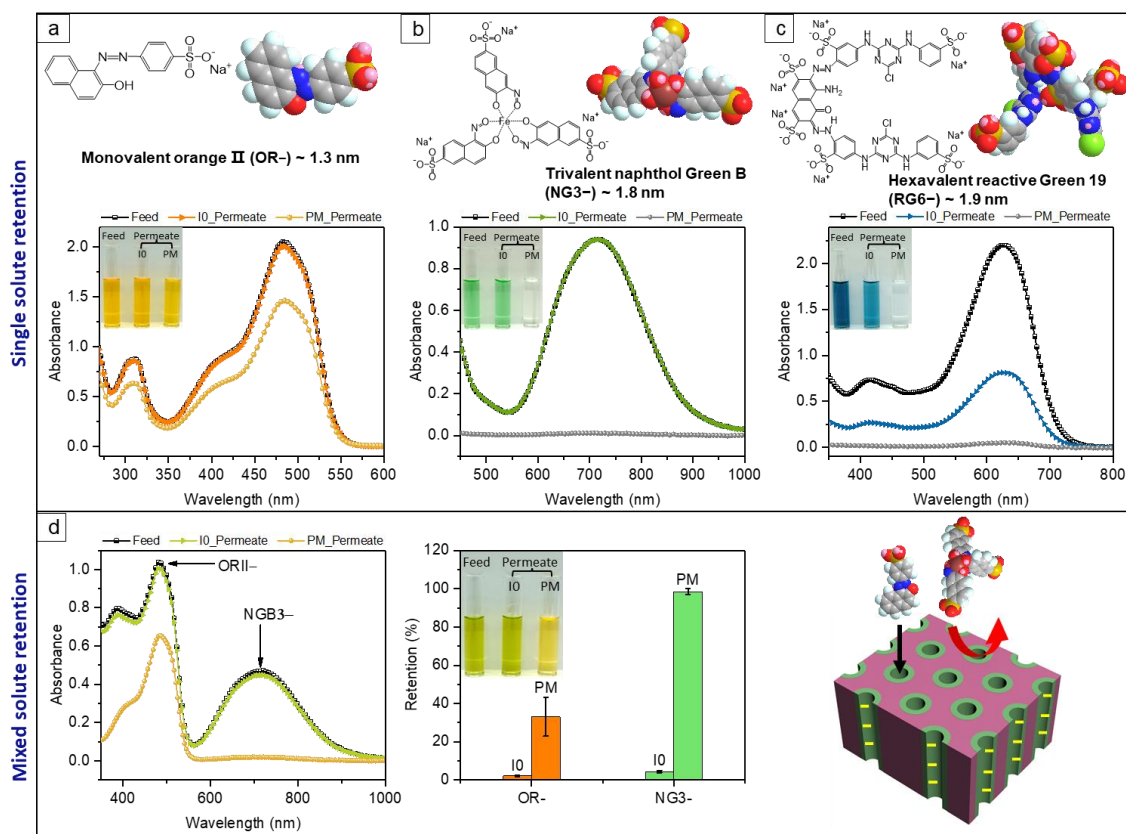


Figure 6.20. Size- and charge-based selectivity between the organic solutes (1–2 nm) in single and mixed solute systems based on the negatively charged membrane PM. Molecular structure and space-filling model of three model organic molecules with distinct size and the number of negative charges, and the corresponding separation behaviour of the pristine membrane I0 and the negatively charged membrane PM determined by UV-vis spectra and a colour change of the solution in single solute retention measurement: (a) monovalent orange II (OR<sup>-</sup>, 350.32 g mol<sup>-1</sup>, 1.3 nm), (b) trivalent naphthol green B (NG3<sup>-</sup>, 878.45 g mol<sup>-1</sup>, 1.8 nm), (c) hexavalent reactive green 19 (RG6<sup>-</sup>, 1418.93 g mol<sup>-1</sup>, 1.9 nm). (d) The competitive separation behaviour of I0 and PM in the mixed-solute retention of OR<sup>-</sup> and NG3<sup>-</sup> (50/50, molar ratio) confirmed by UV-vis spectra and a colour change of the solution.

To investigate separation efficiency of the negatively charged membrane PM three anionic dyes having sulphonate functional groups and different molecular weights (350.32, 878.45, 1418.93 g mol<sup>-1</sup>, respectively) were used as model compounds – monovalent orange II (OR<sup>-</sup>), trivalent naphthol green B (NG3<sup>-</sup>) and hexavalent reactive green 19 (RG6<sup>-</sup>). The pH of 0.01 mM aqueous solutions of OR<sup>-</sup>, NG3<sup>-</sup> and RG6<sup>-</sup> are 6.4, 6.5 and 4.6, respectively (Table 6.4). Single solute aqueous solutions of OR<sup>-</sup> and NG3<sup>-</sup> permeated through I0 with only 1 – 2% rejection of the solutes (Figure 6.20a, b). At pH 4.6 the P4VP blocks of I0 swell (Figure 6.17a) and acquire positive charge due to protonation (Figure 6.16a). 55% of RG6<sup>-</sup> was retained from the aqueous solution presumably due to a strong tendency of adsorption of RG6<sup>-</sup> on I0 (Table 6.3). The pores of PM have strong negative charges in the range of pH 6.4 – 6.5 (Figure 6.16c). In the single solute retention measurement, 29.3% OR<sup>-</sup> was retained from the aqueous solution by PM (Figure 6.20a). In spite of the electrostatic repulsion between the like charges, the nanochannels of PM are big enough to allow 70.7% of OR<sup>-</sup> to permeate through the membrane. But the pores of PM are narrow enough for the bigger NG3<sup>-</sup> molecules to exert strong electrostatic repulsion, rejecting 95.2% NG3<sup>-</sup> (Figure 6.20b). As PM exhibited only a very slight adsorption of OR<sup>-</sup> and NG3<sup>-</sup> after soaking in the aqueous solution even for 24 h (Table 6.3), the solute adsorption might have a very small contribution on the rejection. Although pH 4.6 is pretty close to the isoelectric point of PM, 98.9% of RG6<sup>-</sup> was retained from the aqueous solution by PM (Figure 6.20c). RG6<sup>-</sup> showed a much stronger adsorption on PM compared to OR<sup>-</sup> and NG3<sup>-</sup>, which would form a negatively charged surface from adsorbed RG6<sup>-</sup> molecules and consequently repel the anionic RG6<sup>-</sup>.<sup>165</sup> Such high rejection of RG6<sup>-</sup> is presumably ascribed to the combination of charge/size-based separation and also small portion of the adsorption. Notably the ideal selectivities  $\psi^i_{OR-/NG3-}$  and  $\psi^i_{OR-/RG6-}$  are 14.7 and 64.3, respectively (Table 6.5).

Table 6.5 Retention ( $R$ ) and separation selectivity ( $\psi$ ) for the pristine membrane I0 and the negatively charged membrane PM in single- and mixed-solute retention experiments.

Membrane	Retention ( $R$ , %)					Selectivity ( $\psi$ )		
	Single-solute			Mixed-solute		Single-solute		Mixed-solute
	OR <sup>-</sup>	NG3 <sup>-</sup>	RG6 <sup>-</sup>	OR <sup>-</sup>	NG3 <sup>-</sup>	$\psi^i_{OR-/NG3-}$	$\psi^i_{OR-/RG6-}$	$\psi^r_{OR-/NG3-}$
I0	2.0 ± 0.6	1.4 ± 0.2	55.0 ± 12.8	2.2 ± 0.3	4.5 ± 0.6	1.0	2.2	1.0
PM	29.3 ± 9.1	95.2 ± 1.2	98.9 ± 0.6	33.1 ± 10.1	98.5 ± 1.5	14.7	64.3	44.6

As the pH of NG3<sup>-</sup> and OR<sup>-</sup> aqueous solutions are close to each other, we have used this pair of mixed solutes to investigate the competitive permeation through PM. PM retained 33.1% of OR<sup>-</sup> and 98.5% of NG3<sup>-</sup> from a 0.1 mM aqueous solution of a 50:50 (molar ratio) mixture of OR<sup>-</sup> and NG3<sup>-</sup> which resulted in the real selectivity  $\psi^r_{OR-/NG3-} = 44.6$  (Figure 6.20d, Table 6.5). OR<sup>-</sup> and NG3<sup>-</sup> repelled each other while competing to reach the entrance of the pores from the bulk of the solution. Both OR<sup>-</sup> and NG3<sup>-</sup> solutes had to overcome the energy barrier of electrostatic repulsion to enter the pores of the membrane which was larger for the trivalent NG3<sup>-</sup> compared to the monovalent OR<sup>-</sup>. The entry of NG3<sup>-</sup> was further hindered due to higher molecular dimensions in an aqueous solution compared to OR<sup>-</sup>. The monovalent OR<sup>-</sup> was likely to orient in a way so that the non-charged end enters the pore of the membrane first which was an additional advantage to overcome the energy barrier. Such orientation was not possible for the trivalent NG3<sup>-</sup> as each of three arms had a charged end. More strikingly due to these competing factors the real selectivity  $\psi^r_{OR-/NG3-}$  is three fold higher compared to the ideal selectivity  $\psi^i_{OR-/NG3-}$ . The prepared membrane PM can indeed be used to efficiently separate organic molecules with molecular dimension of 1 – 2 nm by taking advantage of small differences in size and charge number.

## 6.7 Conclusion

In this chapter, we presented a novel multifunctional asymmetric isoporous membrane with different functional groups embedded on the interior of the pore walls, *i.e.*, -OH and 4VP groups, which is derived from a well-designed amphiphilic triblock quaterpolymer, P(HTMB-*r*-I)-*b*-PS-*b*-P4VP, via SNIPS. We have demonstrated that the formation of multifunctional nanochannels arises from the mixed domain consisting of two end blocks via hydrogen bonding. These highly accessible functional groups within the pore walls can readily allow straightforward scalable gas-solid interface post-functionalizations to integrate the positively or negatively charged moieties along the pore walls. The diameter of the well-defined soft nanochannels in a hydrated state is within the nanofiltration regime due to swelling of the polyelectrolyte pore-forming blocks. The single and mixed solute retention studies demonstrate the ability of the membranes to efficiently retain dye molecules from aqueous solutions as well as an unprecedented separation of small organic molecules (1 – 2 nm) from each other.



## **Chapter 7    Potential of Integral Asymmetric Isoporous Membrane towards Enzymatic Membrane Reactors**

Molecular characterization of polymers used in this chapter.

Polymer	PS [wt%]	P4VP [wt%]	$M_n$ [kg mol <sup>-1</sup> ]	$M_w$ [kg mol <sup>-1</sup> ]	Dispersity indices
PS <sup>a)</sup>	100	0	--	113	2.3
P4VP <sup>b)</sup>	0	100	--	~60	--
PS <sub>76</sub> - <i>b</i> -P4VP <sub>24</sub> <sup>246 c)</sup>	76	24	238	246	1.04
PS <sub>81</sub> - <i>b</i> -P4VP <sub>19</sub> <sup>154K</sup>	82	18	143	154	1.08

<sup>a)</sup> PS was purchased from BASF and the sample information was obtained from BASF. <sup>b)</sup> P4VP was purchased from Sigma-Aldrich who supplied the sample information. <sup>c)</sup> PS<sub>76</sub>-*b*-P4VP<sub>24</sub><sup>246</sup> was synthesized by Ivonne Ternes.

## 7.1 Introduction

Except various potential applications of SNIPS membranes in the separation technology, SNIPS membranes also have intrinsic advantages to act as the support of enzymatic membrane reactors where enzymes are immobilized for enhanced enzyme/process stability and a repetitive use.<sup>188</sup> For example, the integral asymmetric structure not only supplies the abundant surface area for the enzyme immobilization, also maintains the high permeance of the products for the reduction of the often encountered product inhibition.<sup>189</sup> The isoporous selective layer endows the excellent contact between the substrates and immobilized enzyme, which is a prerequisite for the enzymatic reaction. These characteristics are crucial to improve the productivity and minimize the energy consumption for enzymatic membrane reactors.

Based on these points, a collaborative study was done with the group of Prof. Ulrich Schwaneberg (DWI – Leibniz-Institut für Interaktive Materialien e.V. and Lehrstuhl für Biotechnologie, RWTH Aachen University) which is working on the engineering of proteins, enzymes and peptides for the development of biohybrid materials with tailor-made properties and functionalities. According to their previous studies materials binding peptides (also known as anchor peptides (APs)) can act as adhesion promoters to achieve the desired surface functionalization, *e.g.*, the AP cecropin A (Cec) can bind to polyisobutylene-polyethylene glycol-polyisobutylene (PIB-PEG-PIB) triblock copolymer,<sup>190</sup> the AP liquid chromatography peak I (LCI) serves as an adhesion promoter to polypropylene (PP),<sup>191-193</sup> the AP Tachystatin A2 (TA2) is able to bind to PS and polyester-polyurethane.<sup>192, 194</sup> Meanwhile, Cec, LCI and TA2 were investigated to immobilize enzymes on different materials, *e.g.* gold, stainless steel, PS, PP and silicon-based materials.<sup>188</sup> Phytases caught major attention due to their ability to initiate stepwise removal of inorganic phosphate from phytate and also a huge market value of approximately US \$350 million per year, therefore *Yersinia mollaretii* phytase (YmPh) was

chosen as a target enzyme.<sup>195-197</sup> In order to achieve the directed immobilization of YmPh, different fusion constructs of YmPh with Cec, LCI and TA2 were employed, *i.e.*, Cec-YmPh, TA2-YmPh, LCI-YmPh, YmPh-Cec, YmPh-TA2, YmPh-LCI. As we know, however, there is no study on AP binding for PS-*b*-P4VP block copolymer and also any porous membrane to date. The hydrophilicity, charge, BCP microphase separation, and pore size (in case of porous membrane) of the support may likely play a role in the binding ability of the APs on the support. Herein dense films of PS homopolymer (homo-PS), P4VP homopolymer (homo-P4VP) and the corresponding quaternized homo-P4VP with different quaternization degrees (homo-QP4VP) were used for the first preliminary study. Furthermore, two series of membranes derived from PS-*b*-P4VP with different pore sizes and different degrees of quaternization were studied to select the suitable porous membrane for the immobilization of YmPh-AP fusion proteins. The stability of the immobilized enzyme was also roughly evaluated.<sup>1</sup>

Table 7.1. Molecular characterization of the polymers used for the sample preparation

Polymer	PS [wt%]	P4VP [wt%]	M <sub>n</sub> [kg mol <sup>-1</sup> ]	M <sub>w</sub> [kg mol <sup>-1</sup> ]	Dispersity indices
PS <sup>a)</sup>	100	0	--	113	2.3
P4VP <sup>b)</sup>	0	100	--	~60	--
PS <sub>76</sub> - <i>b</i> -P4VP <sub>24</sub> <sup>246 c)</sup>	76	24	238	246	1.04
PS <sub>81</sub> - <i>b</i> -P4VP <sub>19</sub> <sup>154K</sup>	82	18	143	154	1.08

<sup>a)</sup> PS was purchased from BASF and the sample information was obtained from BASF. <sup>b)</sup> P4VP was purchased from Sigma-Aldrich who supplied the sample information. <sup>c)</sup> PS<sub>76</sub>-*b*-P4VP<sub>24</sub><sup>246</sup> was synthesized by Ivonne Ternes.

<sup>1</sup> Note that the author of this thesis is responsible for the preparation of all the dense films and SNIPS membranes and the corresponding morphological investigation before and after the immobilization of enzyme protein. The fusion proteins of enzyme-AP are prepared and the corresponding characterizations are performed by the group of Prof. Ulrich Schwaneberg.

---

---

## 7.2 Preliminary Study of Anchor Peptides Binding on Homo-PS and Homo-P4VP Dense Films

The dense films of homo-PS and homo-P4VP were prepared by dip-coating on the non-woven support (the molecular characteristics are shown in Table 7.1). Homo-P4VP dense films were quaternized by MeI for different reaction times, *i.e.*, 3 h, 14 h and 26 h. Among the series of homo-P4VP dense films, homo-QP4VP with 14 h MeI quaternization showed a promising stronger AP binding than the other samples (these preliminary results are not shown in the thesis). This phenomenon gives us the hint that the charge density of P4VP and the correlated hydrophilicity may have an effect on the AP binding. The binding results of different YmPh-AP fusion constructs on the representative dense film samples are provided in Chapter 10 Appendix, Figure 10.22. It implies that compared to the corresponding reference of the wild type YmPh (YmPh WT), Cec-YmPh shows a stronger binding to homo-QP4VP with 14 h MeI quaternization, and TA2-YmPh displays a stronger binding to homo-PS which is consistent with the previous report for PS support.<sup>192</sup>

## 7.3 Preparation of PS-*b*-P4VP Membranes with Different Pore Sizes and Degrees of Quaternization

Based on the above results, PS-*b*-P4VP membranes with different pore sizes were prepared from two batches of PS-*b*-P4VP differing in composition and molecular weight (Table 7.1). Afterwards, two series of isoporous membranes with various degrees of quaternization were prepared using MeI vapour, namely M0B, M22B, M40B, M76B and M0S, M16S, M39S, M69S (the letters M, B and S stand for MeI, bigger pore size and smaller pore size, while the numbers stand for the degree of quaternization roughly evaluated by ATR-FTIR, respectively). The success of quaternization is confirmed by FTIR (Figure 7.1). The SEM images of the

membrane top surfaces demonstrate that all the quaternized membranes possess the intact isoporous structure and slightly smaller pore size in the dry state compared to the pristine membranes (*i.e.*, M0B and M0S, Figure 7.2).

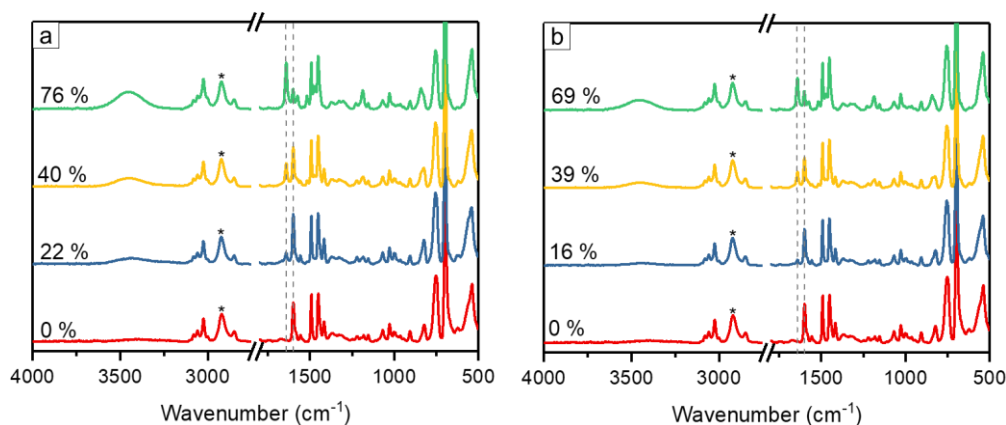


Figure 7.1. ATR-FTIR spectra of two series of membranes with different degrees of quaternization modified by MeI: (a) the series of the membranes with bigger pore size. (b) the series of the membranes with smaller pore size. The relative intensities were normalized using the characteristic CH<sub>2</sub> stretching vibrations (\*) of the unreactive backbone around 2924 cm<sup>-1</sup>.

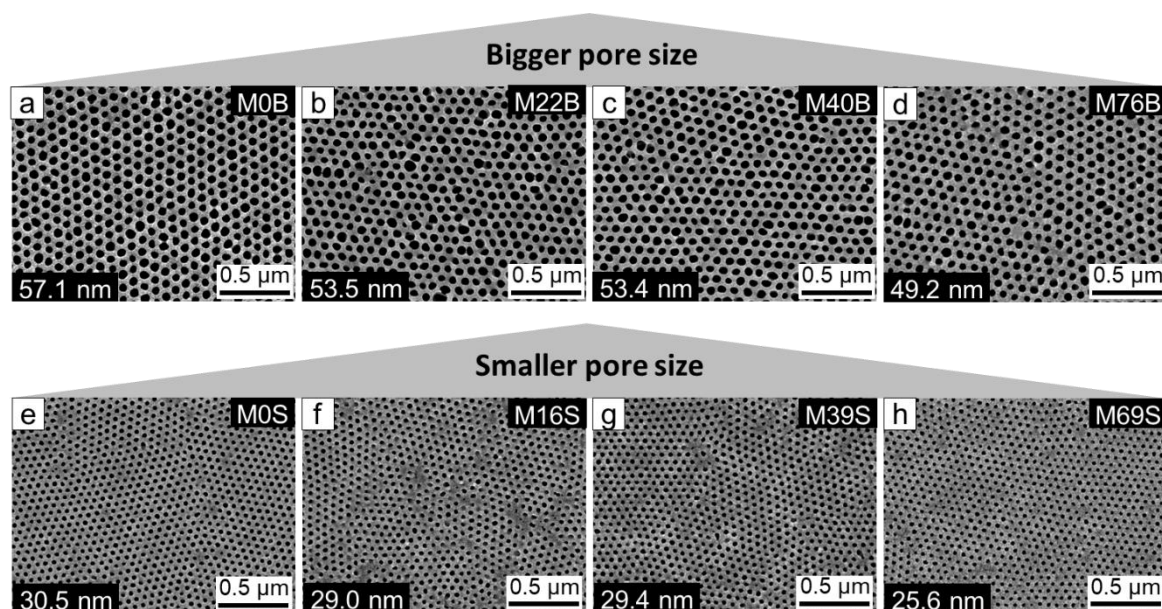


Figure 7.2. SEM images of the top surfaces of two series of membranes with different degrees of quaternization: (a-d) M0B, M22B, M40B and M76B, (e-h) M0S, M16S, M39S and M69S.

## 7.4 Immobilization of YmPh-AP Fusion Proteins on Various PS-*b*-P4VP Membranes

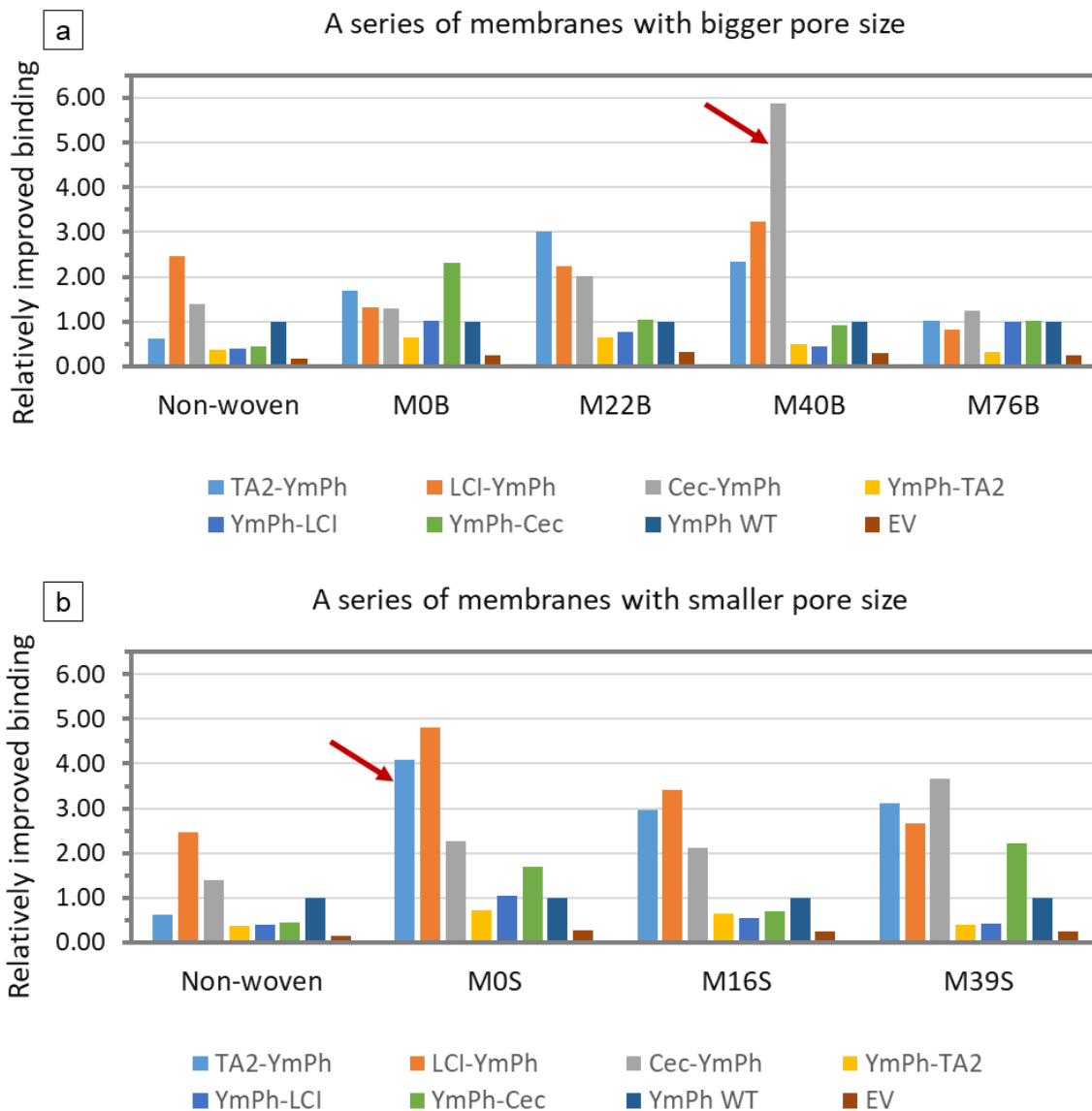


Figure 7.3. Comparison of relative improvement of YmPh-AP binding calculated relative to wild type YmPh (YmPh WT). (a) the series of membranes with bigger pore size. (b) the series of the membrane with smaller pore size. Note: The fusion proteins of enzyme-AP are prepared and the corresponding characterizations are performed by the group of Prof. Ulrich Schwaneberg.

The corresponding binding of different YmPh-AP fusion proteins for the different membranes are depicted in Chapter 10 Appendix, Figure 10.24 and Figure 7.3. Briefly, TA2-YmPh and Cec-YmPh bind stronger to most of the membranes than the others, in agreement with the results of the homopolymer dense films. In terms of TA2-YmPh, M0S shows the highest improved binding, *i.e.*, 4.1-fold compared to YmPh WT, which is much higher than that of M0B (1.7-fold). When M0B is quaternized to some extent, *e.g.*, M22B, the improved binding is increased to 3.0-fold, presumably due to decreased pore size from the swelling of quaternized P4VP. This result implies the membrane pore size may affect the binding of TA2-YmPh. In the case of Cec-YmPh, the strongest improved binding is obtained by M40B (5.9-fold), interestingly much higher than M39S with similar quaternization degree. It may suggest that the effective pore size of M40B and M39S in the hydrated state are likely different, leading to the different improved binding. Additionally, other membranes (*i.e.*, M0B, M22B, M76B, M0S and M16S) do not show significantly improved binding as M40B, implying that there is an optimal degree of quaternization for P4VP. It again means the charge density or hydrophilicity of P4VP may have an impact on the Cec-YmPh binding. Overall, TA2-YmPh selectively binds to the PS matrix of M0S, while Cec-YmPh selectively binds to the quaternized P4VP pore-forming block of M40B.

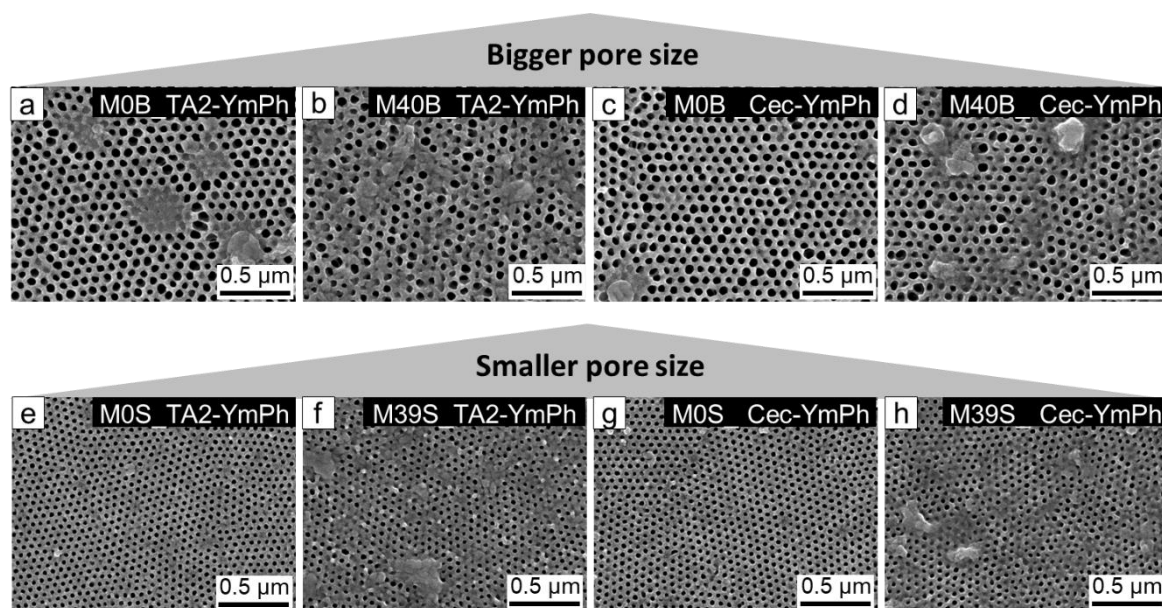


Figure 7.4. SEM images of the top surfaces of the representative membranes with the immobilization of YmPh-AP fusion constructs: (a) M0B\_TA2-YmPh, (b) M40B\_TA2-YmPh, (c) M0B\_Cec-YmPh, (d) M40B\_Cec-YmPh, (e) M0S\_TA2-YmPh, (f) M39S\_TA2-YmPh, (g) M0S\_Cec-YmPh, (h) M39S\_Cec-YmPh.

Figure 7.4 depicts the top surface structure of the representative membranes after the immobilization of TA2-YmPh and Cec-YmPh. There are visible immobilized fusion proteins on all the membrane top surfaces, which mostly form aggregates, presumably due to the denaturation of proteins. Interestingly, more immobilized fusion proteins are detected on the top surfaces of quaternized membranes (M40B and M39S) compared to the pristine membranes (M0B and M0S).

Additionally, a rough estimation of the stability of immobilized TA2-YmPh and Cec-YmPh suggests that the activity of YmPh can be still determined after storage at 4 °C or 25 °C for 3 days, with a higher activity after storage at 4 °C, as shown in Chapter 10 Appendix, Figure 10.26.

## 7.5 Conclusion

In this chapter, two series of PS-*b*-P4VP membranes with different pore sizes and degrees of quaternization as well as different fusion constructs of YmPh-AP were assessed for the directed YmPh immobilization. The results suggest that TA2-YmPh selectively binds to the PS matrix of M0S, while Cec-YmPh selectively binds to the quaternized P4VP pore-forming block of M40B. This may open the way to selectively bind different functional enzymes or other molecules in a spatially well-controlled way on the membrane, also offering the possibility of reaction cascades occurring at the membrane surface with the final product crossing through the membrane. Overall, the PS-*b*-P4VP pristine membrane and quaternized membrane with positively charged nanochannels are indeed promising to prepare the enzymatic membrane reactor.

## **Chapter 8    Summary**

## 8.1 Summary

The work presented in this thesis was focusing on the fabrication of isoporous membranes with charged nanochannels and tailored pore sizes, which are promising candidates as next generation membranes and may hold a huge potential in the applications of water treatment, purification/fractionation of organic matters as well as catalytic membrane reactors. For this purpose, several diblock copolymers and triblock copolymers were investigated to fabricate isoporous membranes. The different types of charged isoporous membranes were thoroughly explored to satisfy various membrane applications.

A polystyrene-*block*-poly(4-vinylpyridine) (PS-*b*-P4VP) diblock copolymer was employed to prepare positively charged membranes. For the introduction of positive charges, compared to the protonation of 4-vinylpyridine units, the quaternization is not limited to acidic condition. However, the quaternization was a challenge for a kinetically trapped non-equilibrium isoporous structure, which was addressed by a facile scalable heterogeneous gas-solid reaction. The isoporous structure was retained as well as the quaternization was homogeneous overall the membrane. The influence of the size of the alkyl group of the quaternization agents and the degree of quaternization on the membrane morphology and performance was thoroughly investigated. The effective pore size of the membrane in a hydrated state was successfully tuned in a wide range from ultrafiltration toward nanofiltration. The excellent performance of the membranes to separate the cationic molecule methylene blue (MB<sup>+</sup>, ~1 nm) from aqueous solutions demonstrated their potential for nanofiltration. However, we only employed MB<sup>+</sup> as a model molecule to estimate the separation performance. To extend their potential for practical applications, it is necessary to figure out the substance which can be effectively separated by a membrane with a given pore size.

---

---

For a negatively charged membrane, a tailor-made polystyrene-*block*-poly(4-(2-hydroxyethyl-thio)-2-methyl butene-*random*-4-(2-hydroxyethyl-thio)-3-methyl butene-*random*-isoprene) (PS-*b*-P(HTMB-*r*-I)) diblock terpolymer composed of a hydrophobic major block and an amphiphilic minor block was used. Four PS-*b*-P(HTMB-*r*-I) diblock terpolymers with different content of hydroxyl (–OH) groups were investigated. Increasing content of –OH groups can enable the formation of the isoporous structure, as the –OH content must be above a certain threshold to bring about the formation of an isoporous top layer via the evaporation induced self-assembly together with the non-solvent induced phase separation (SNIPS). The often encountered issue of the membrane dense bottom interface was addressed by introducing sol-based titanium dioxide nanoparticles (TiO<sub>2</sub> NPs) instead of conventional porogens (e.g. poly(ethylene glycol)), which did not serve well. The ultimate organic-inorganic hybrid nanocomposite isoporous membrane with TiO<sub>2</sub> NPs was obtained in a wide processing window. Based on the success of the gas-solid reaction for preparation of quaternized PS-*b*-P4VP diblock copolymer membranes, the negatively charged moiety was also introduced via a gas-solid reaction. The negatively charged polyelectrolyte swelled to a moderate extent in a hydrated state which was less than the high extent of swelling observed for the quaternized PS-*b*-P4VP diblock copolymer membranes, due to the molecular-scale compositional heterogeneity of the amphiphilic pore-forming block P(HTMB-*r*-I). As a result, the membrane with well-defined soft nanochannels exhibited not only a significantly high water permeance in the nanofiltration regime but also the potential for a good separation of 1 – 2 nm small anionic molecules from each other. Due to the combined effect of the electrostatic repulsion, physical and energy barrier of hydration layer and the addition of TiO<sub>2</sub>, the negatively charged membrane also showed an excellent antifouling performance. Despite high water permeance and excellent antifouling properties of the prepared membrane, the separation selectivity of the

target molecules needs to be further improved in order to minimize the energy consumption of the separation.

On the basis of the success of PS-*b*-P4VP and PS-*b*-P(HTMB-*r*-I) diblock copolymer membranes, a tailor-made triblock quaterpolymer poly(4-(2-hydroxyethyl-thio)-2-methyl butene-*random*-4-(2-hydroxyethyl-thio)-3-methyl butene-*random*-isoprene)-*block*-polystyrene-*block*-poly(4-vinylpyridine) (P(HTMB-*r*-I)-*b*-PS-*b*-P4VP) appeared promising for the fabrication of charge-mosaic membranes. However, regardless of the solvent composition and evaporation rate, the two end blocks can form mixed microdomains by hydrogen-bonding of –OH and 4VP moieties in the target polymer. Therefore, a charge-mosaic membrane with distinctly separated nanochannels was not obtained. Instead another attractive isoporous membrane with different functional groups on the interior of the pore walls was obtained (multifunctional isoporous membrane). These highly accessible functional groups within the pore walls were readily transformed into positively or negatively charged moieties along the pore walls by straightforward gas-solid interface post-functionalizations. The pores of the post-functionalized membranes acted as target-specific functional soft nanochannels due to swelling of the polyelectrolyte blocks in a hydrated state. Five model molecules with different charge signs and sizes were used to assess the separation performance by single and mixed solute retention measurements. The positively charged membranes allowed the free passage of neutral solutes (riboflavin, RB0) while highly rejected the similar sized cationic ones (MB<sup>+</sup>) from their mixture with a selectivity of 28.3. The negatively charged membranes efficiently separated the mixed anionic organic solutes (1-2 nm Orange II (OR<sup>-</sup>) and naphthol green B (NGB3<sup>-</sup>)) with a selectivity of 44.6 based on the charge- and size-exclusion. Such high selectivity has never been reported before. The prepared positively/negatively charged membranes showed an unprecedented separation selectivity of small organic molecules (1 – 2 nm) as well as the ability to efficiently retain dye molecules from aqueous solutions.

---

---

Besides their potential for separating ionic molecules from aqueous solutions, another aim of this thesis was to explore the potential of SNIPS membranes as enzymatic membrane reactors using the PS-*b*-P4VP system. Various membrane pore sizes, degrees of quaternization as well as different fusion protein constructs of *Yersinia mollaretii* phytase with anchor peptide (YmPh-AP) were studied for the directed enzyme (YmPh) immobilization. It demonstrated that the fusion protein construct of YmPh with Tachystatin A2 (TA2-YmPh) selectively bound to the PS matrix of the pristine PS-*b*-P4VP membrane with the pore size of 30.5 nm, while the fusion protein constructs of YmPh with cecropin A (Cec-YmPh) selectively bound to the quaternized P4VP pore-forming block of the PS-*b*-P4VP membrane with the degree of quaternization of 40%. The effectively directed enzyme immobilization onto the membrane points to the potential of PS-*b*-P4VP membranes as host structures for enzymatic membrane reactors. Although we took a first key step, future investigations of the efficiency of catalytic reactions during the substrate flowing through the membrane still need to prove the concept.

Overall, the fabrication of positively or negatively charged isoporous membranes and multifunctional isoporous membranes was achieved and some of their corresponding potential applications were investigated. However, regarding the ambitious goal of charge-mosaic isoporous membranes, a rational designed triblock terpolymer is still the key point. This work may give some guidance for possible future research in this direction. The concept of manipulating the functionality of the membrane by a bottom-up molecular design of a block copolymer provides a strong platform to fabricate next generation membranes for solving on-demand separation problems.

## 8.2 Zusammenfassung

Diese Arbeit konzentriert sich auf die Herstellung isoporöser Membranen mit geladenen Nanokanälen und maßgeschneiderten Porengrößen, die vielversprechende Kandidaten für Membranen der nächsten Generation sind und ein enormes Potenzial für Anwendungen in der Wasseraufbereitung, Reinigung/Fraktionierung organischer Stoffe sowie in katalytischen Membranreaktoren besitzen. Zu diesem Zweck wurden mehrere Diblockcopolymere und Triblockcopolymere zur Herstellung isoporöser Membranen untersucht. Die verschiedenen Typen geladener isoporöser Membranen wurden gründlich charakterisiert, um verschiedenen Membrananwendungen gerecht zu werden.

Ein Polystyrol-*block*-poly(4-vinylpyridin)- Diblockcopolymer (PS-*b*-P4VP) wurde zur Herstellung positiv geladener Membranen verwendet. Für die Einbringung von positiven Ladungen ist die Quaternisierung im Vergleich zur Protonierung von 4-Vinylpyridin-Einheiten nicht auf den sauren Zustand beschränkt. Die Quaternisierung war jedoch eine Herausforderung für eine kinetisch eingefrorene, nicht im Gleichgewicht befindliche isoporöse Struktur, welche mithilfe einer leicht skalierbaren heterogenen Gas-Festkörper-Reaktion angegangen wurde. Die isoporöse Struktur blieb erhalten, und die Quaternisierung war in der Membran insgesamt homogen. Der Einfluss der Größe der Alkylgruppe der Quaternisierungsmittel und des Quaternisierungsgrades auf die Morphologie und Leistung der Membran wurde gründlich untersucht. Die effektive Porengröße der Membran in einem hydratisierten Zustand wurde in einem weiten Bereich von der Ultrafiltration bis zur Nanofiltration erfolgreich eingestellt. Die ausgezeichnete Leistung der Membranen zur Abtrennung des kationischen Moleküls Methylenblau (MB<sup>+</sup>, ~1 nm) aus wässrigen Lösungen zeigte ihr Potenzial für die Nanofiltration. Wir verwendeten MB<sup>+</sup> jedoch nur als Modellmolekül zur Abschätzung der Trennleistung. Um ihr Potenzial für praktische

---

---

Anwendungen zu erweitern, ist es notwendig, eine Substanz zu bestimmen, die durch eine Membran mit bestimmter Porengröße effektiv getrennt werden kann.

Für eine negativ geladene Membran wurde ein maßgeschneidertes Polystyrol-*block*-poly(4-(2-hydroxyethylthio)-2-methylbuten-*random*-isopren)- Diblockterpolymer (PS-*b*-P(HTMB-*r*-I)) verwendet, das aus einem hydrophoben Hauptblock und einem amphiphilen Nebenblock besteht. Es wurden vier PS-*b*-P(HTMB-*r*-I) Diblockterpolymere mit unterschiedlichem Gehalt an Hydroxygruppen (OH-Gruppen) untersucht. Ein zunehmender Gehalt an OH-Gruppen kann die Bildung der isoporösen Struktur ermöglichen, da der OH-Gehalt über einem bestimmten Schwellenwert liegen muss, um die Bildung einer isoporösen Deckschicht durch verdampfungsinduzierte Selbstorganisation in Kombination mit Nicht-Lösungsmittel-induzierter Phasenseparation (engl. evaporation induced self-assembly together with non-solvent induced phase separation, SNIPS) zu bewirken. Das oft auftretende Problem einer dichten unteren Grenzfläche der Membran wurde durch die Einführung von sol-basierten Titandioxid-Nanopartikeln (TiO<sub>2</sub> NPs) anstelle von herkömmlichen Porogenen (z.B. Poly(ethylenglycol), PEG) gelöst, welche nicht gut funktionierten. Die endgültige organisch-anorganische isoporöse Hybrid-Nanokomposit-Membran mit TiO<sub>2</sub> NPs konnte in einem breiten Verarbeitungsfenster erhalten werden. Basierend auf dem Erfolg der Gas-Festkörper-Reaktion zur Herstellung von quaternisierten PS-*b*-P4VP Diblockcopolymermembranen wurde der negativ geladene Anteil ebenfalls über eine Gas-Festkörper-Reaktion eingebracht. Der negativ geladene Polyelektrolyt quoll in einem hydratisierten Zustand mäßig auf. Die geringere Quellung im Vergleich zu den stark quellenden quaternisierten PS-*b*-P4VP Diblockcopolymermembranen war auf die heterogene Zusammensetzung des amphiphilen porenbildenden Blocks P(HTMB-*r*-I) auf molekularer Skala zurückzuführen. Infolgedessen wies die Membran mit wohldefinierten weichen Nanokanälen nicht nur eine signifikant hohe Wasserpermeanz im Nanofiltrationsregime auf, sondern auch das Potenzial für eine gute

Trennung von 1 - 2 nm kleinen anionischen Molekülen voneinander. Aufgrund der kombinierten Wirkung der elektrostatischen Abstoßung, der physikalischen und energetischen Barriere der Hydratationsschicht und der Zugabe von TiO<sub>2</sub> zeigte die negativ geladene Membran auch ein ausgezeichnetes Antifouling. Trotz hoher Wasserpermeanz und ausgezeichneter Antifouling-Eigenschaften der präparierten Membran muss die Trennselektivität der Zielmoleküle weiter verbessert werden, um den Energieverbrauch der Trennung zu minimieren.

Auf der Grundlage des Erfolgs von Diblockcopolymermembranen auf der Basis von PS-*b*-P4VP und PS-*b*-P(HTMB-*r*-I) erschien ein maßgeschneidertes Triblockquaterpolymer Poly(4-(2-hydroxyethylthio)-2-methylbuten-*random*-isopren)-*block*-polystyrol-*block*-poly(4-vinylpyridin) (P(HTMB-*r*-I)-*b*-PS-*b*-P4VP) als vielversprechend für die Herstellung von Ladungsmosaikmembranen. Unabhängig von der Lösungsmittelzusammensetzung und Verdampfungsrate können die beiden Endblöcke jedoch gemischte Mikrodomänen durch Wasserstoffbrückenbindungen von OH- und 4VP-Anteilen im Zielpolymer bilden. Daher wurde keine Ladungsmosaikmembran mit deutlich getrennten Nanokanälen erreicht. Stattdessen wurde eine weitere attraktive isoporöse Membran mit verschiedenen funktionellen Gruppen auf der Innenseite der Porenwände erhalten (multifunktionelle isoporöse Membran). Diese leicht zugänglichen funktionellen Gruppen innerhalb der Porenwände konnten durch einfache Gas-Festkörper-Grenzflächen-Nachfunktionalisierungen leicht in positiv oder negativ geladene Moleküle entlang der Porenwände umgewandelt werden. Die Poren der postfunktionalisierten Membranen wirkten als zielspezifische funktionelle weiche Nanokanäle aufgrund der Quellung der Polyelektrolytblöcke in einem hydratisierten Zustand. Fünf Modellmoleküle mit unterschiedlichen Ladungsvorzeichen und -größen wurden zur Beurteilung der Trennleistung durch Einzel- und Mischretentionsmessungen von gelösten Stoffen verwendet. Die positiv geladenen Membranen erlaubten den freien Durchgang von

---

---

neutralen gelösten Stoffen (Riboflavin, RB<sup>0</sup>), während die ähnlich großen kationischen Moleküle (MB<sup>+</sup>) mit einer Selektivität von 28,3 aus der Mischung stark abgestoßen wurden. Die negativ geladenen Membranen trennten die gemischten anionischen organischen gelösten Stoffe (1-2 nm Orange II (OR<sup>-</sup>) und Naphtholgrün B (NGB<sup>3-</sup>)) effizient mit einer Selektivität von 44,6 basierend auf der Ladungs- und Größenausschluß. Über eine derart hohe Selektivität wurde noch nie zuvor berichtet. Die präparierten positiv/negativ geladenen Membranen zeigten eine noch nie dagewesene Trennselektivität kleiner organischer Moleküle (1 - 2 nm) sowie die Fähigkeit, Farbstoffmoleküle aus wässrigen Lösungen effizient zurückzuhalten.

Neben ihrem Potenzial zur Trennung ionischer Moleküle aus wässrigen Lösungen war ein weiteres Ziel dieser Arbeit die Untersuchung des Potenzials von SNIPS-Membranen als enzymatische Membranreaktoren unter Verwendung des PS-*b*-P4VP-Systems. Verschiedene Membranporengrößen, Quaternisierungsgrade sowie unterschiedliche Fusionsproteinkonstrukte von *Yersinia mollaretii* Phytase mit Ankerpeptiden (YmPh-AP) wurden für die gerichtete Enzymimmobilisierung (YmPh) untersucht. Es zeigte sich, dass das Fusionsproteinkonstrukt aus YmPh mit Tachystin A2 (TA2-YmPh) selektiv an die PS-Matrix der ursprünglichen PS-*b*-P4VP-Membran mit der Porengröße von 30,5 nm gebunden war, während das Fusionsproteinkonstrukt aus YmPh mit Cecropin A (Cec-YmPh) selektiv an den quaternisierten P4VP-porenbildenden Block der PS-*b*-P4VP-Membran mit dem Quaternisierungsgrad von 40% gebunden war. Die effektiv gerichtete Enzymimmobilisierung auf der Membran deutet auf das Potenzial von PS-*b*-P4VP-Membranen als Wirtsstrukturen für enzymatische Membranreaktoren hin. Obwohl wir einen ersten wichtigen Schritt gemacht haben, werden zukünftige Untersuchungen die Effizienz katalytischer Reaktionen bei denen das Substrat durch die Membran fließt am wichtigsten seinzeigen müssen.

Alles in allem wurde die Herstellung positiv oder negativ geladener isoporöser Membranen und multifunktionaler isoporöser Membranen erreicht, und einige ihrer potenziellen Anwendungen wurden untersucht. Im Hinblick auf das ehrgeizige Ziel einer isoporösen Membran mit Ladungs mosaik ist ein passend konzipiertes Triblockterpolymer jedoch nach wie vor entscheidend. Diese Arbeit könnte eine Basis für zukünftige Arbeiten in jene Richtung sein. Das Konzept der Manipulation der Membranfunktionalität durch ein Bottom-up-Molekulardesign eines Blockcopolymers bietet ein starkes Fundament für die Herstellung von Membranen der nächsten Generation zur Lösung von bedarfsorientierten Trennproblemen.

## **Chapter 9    References**

1. World Health Organization: Drinking-Water., Available at <https://www.who.int/news-room/fact-sheets/detail/drinking-water>.
2. M. A. Shannon, P. W. Bohn, M. Elimelech, J. G. Georgiadis, B. J. Marinas and A. M. Mayes, *Nature*, 2008, **452**, 301-310.
3. Water purification., Available at [https://en.wikipedia.org/wiki/Water\\_purification#cite\\_note-1](https://en.wikipedia.org/wiki/Water_purification#cite_note-1).
4. C. G. Daughton and T. A. Ternes, *Environ. Health Perspect.*, 1999, **107**, 907-938.
5. K. E. Murray, S. M. Thomas and A. A. Bodour, *Environ. Pollut.*, 2010, **158**, 3462-3471.
6. R. P. Schwarzenbach, B. I. Escher, K. Fenner, T. B. Hofstetter, C. A. Johnson, U. Von Gunten and B. Wehrli, *Science*, 2006, **313**, 1072-1077.
7. S. D. Richardson and T. A. Ternes, *Anal. Chem.*, 2014, **86**, 2813-2848.
8. A. Alsaiee, B. J. Smith, L. Xiao, Y. Ling, D. E. Helbling and W. R. Dichtel, *Nature*, 2016, **529**, 190-194.
9. M.-C. Shih, *Desalination*, 2005, **172**, 85-97.
10. R. Van Reis and A. Zydney, *Curr. Opin. Biotechnol.*, 2001, **12**, 208-211.
11. R. van Reis and A. Zydney, *J. Membr. Sci.*, 2007, **297**, 16-50.
12. X. Qiu, H. Yu, M. Karunakaran, N. Pradeep, S. P. Nunes and K.-V. Peinemann, *ACS nano*, 2013, **7**, 768-776.
13. S. U. Hong and M. L. Bruening, *J. Membr. Sci.*, 2006, **280**, 1-5.
14. Y. Shim and S. Chellam, *Biotechnol. Bioeng.*, 2007, **98**, 451-461.
15. K. Y. Wang and T.-S. Chung, *J. Membr. Sci.*, 2005, **247**, 37-50.
16. H. Woo, J. Elbe and C. Amundson, *J. Food Sci.*, 2006, **45**, 875-879.
17. A. Kalbasi and L. Cisneros-Zevallos, *J. Agric. Food. Chem.*, 2007, **55**, 7036-7042.
18. M. Ulbricht, *Polymer*, 2006, **47**, 2217-2262.
19. V. Abetz, *Macromol. Rapid Commun.*, 2015, **36**, 10-22.
20. Nuclepore Track-Etched Membrane., Available at [https://www.gelifesciences.com/en/us/search#q=track%20etched&t=coveo5819fbca&f:@content\\_type=\[Product%20Pages](https://www.gelifesciences.com/en/us/search#q=track%20etched&t=coveo5819fbca&f:@content_type=[Product%20Pages).
21. Unique-Mem® Track-Etched Membranes., Available at <https://www.oxyphen.com/index.php?id=8&L=1>.
22. K. Han, W. Xu, A. Ruiz, P. Ruchhoeft and S. Chellam, *J. Membr. Sci.*, 2005, **249**, 193-206.
23. L. Vogelaar, J. N. Barsema, C. J. M. van Rijn, W. Nijdam and M. Wessling, *Adv. Mater.*, 2003, **15**, 1385-1389.
24. L. Vogelaar, R. G. Lammertink, J. N. Barsema, W. Nijdam, L. A. Bolhuis-Versteeg, C. J. van Rijn and M. Wessling, *Small*, 2005, **1**, 645-655.
25. X. Yan, G. Liu, M. Dickey and C. G. Willson, *Polymer*, 2004, **45**, 8469-8474.
26. F. S. Bates, M. A. Hillmyer, T. P. Lodge, C. M. Bates, K. T. Delaney and G. H. Fredrickson, *Science*, 2012, **336**, 434.
27. J. C. Brendel and F. H. Schacher, *Chem Asian J*, 2018, **13**, 230-239.
28. P. van Rijn, M. Tutus, C. Kathrein, L. Zhu, M. Wessling, U. Schwaneberg and A. Boker, *Chem. Soc. Rev.*, 2013, **42**, 6578-6592.
29. J. K. Kim, S. Y. Yang, Y. Lee and Y. Kim, *Prog. Polym. Sci.*, 2010, **35**, 1325-1349.
30. E. A. Jackson and M. A. Hillmyer, *ACS Nano*, 2010, **4**, 3548-3553.
31. M. Radjabian and V. Abetz, *Prog. Polym. Sci.*, 2020, DOI: <https://doi.org/10.1016/j.progpolymsci.2020.101219>, 101219.
32. W. A. Phillip, J. Rzayev, M. A. Hillmyer and E. L. Cussler, *J. Membr. Sci.*, 2006, **286**, 144-152.
33. W. A. Phillip, B. O'Neill, M. Rodwogin, M. A. Hillmyer and E. L. Cussler, *ACS Appl. Mater. Interfaces*, 2010, **2**, 847-853.
34. C. G. Gamys, J. M. Schumers, C. Mugemana, C. A. Fustin and J. F. Gohy, *Macromol. Rapid Commun.*, 2013, **34**, 962-982.

35. S. Y. Yang, I. Ryu, H. Y. Kim, J. K. Kim, S. K. Jang and T. P. Russell, *Adv. Mater.*, 2006, **18**, 709-712.
36. C. G. Gamys, A. Vlad, O. Bertrand and J.-F. Gohy, *Macromol. Chem. Phys.*, 2012, **213**, 2075-2080.
37. K. V. Peinemann, V. Abetz and P. F. Simon, *Nat. Mater.*, 2007, **6**, 992-996.
38. S. Schöttner, H.-J. Schaffrath and M. Gallei, *Macromolecules*, 2016, **49**, 7286-7295.
39. J. Wang, M. M. Rahman, C. Abetz, S. Rangou, Z. Zhang and V. Abetz, *Macromol. Rapid Commun.*, 2018, **39**, 1800435.
40. A. Jung, V. Filiz, S. Rangou, K. Buhr, P. Merten, J. Hahn, J. Clodt, C. Abetz and V. Abetz, *Macromol. Rapid Commun.*, 2013, **34**, 610-615.
41. W. A. Phillip, R. M. Dorin, J. Werner, E. M. Hoek, U. Wiesner and M. Elimelech, *Nano Lett.*, 2011, **11**, 2892-2900.
42. R. A. Mulvenna, J. L. Weidman, B. Jing, J. A. Pople, Y. Zhu, B. W. Boudouris and W. A. Phillip, *J. Membr. Sci.*, 2014, **470**, 246-256.
43. Q. Zhang, Y. Gu, Y. M. Li, P. A. Beaucage, T. Kao and U. Wiesner, *Chem. Mater.*, 2016, **28**, 3870-3876.
44. A. Jung, S. Rangou, C. Abetz, V. Filiz and V. Abetz, *Macromol. Mater. Eng.*, 2012, **297**, 790-798.
45. J. Hahn, V. Filiz, S. Rangou, J. Clodt, A. Jung, K. Buhr, C. Abetz and V. Abetz, *J. Polym. Sci., Part B: Polym. Phys.*, 2013, **51**, 281-290.
46. J. Hahn, V. Filiz, S. Rangou, B. Lademann, K. Buhr, J. I. Clodt, A. Jung, C. Abetz and V. Abetz, *Macromol. Mater. Eng.*, 2013, **298**, 1315-1321.
47. S. Saleem, S. Rangou, C. Abetz, B. Lademann, V. Filiz and V. Abetz, *Polymers*, 2017, **9**, 216.
48. C. Höhme, J. Hahn, B. Lademann, A. Meyer, B. Bajer, C. Abetz, V. Filiz and V. Abetz, *Eur. Polym. J.*, 2016, **85**, 72-81.
49. J. I. Clodt, S. Rangou, A. Schröder, K. Buhr, J. Hahn, A. Jung, V. Filiz and V. Abetz, *Macromol. Rapid Commun.*, 2013, **34**, 190-194.
50. S. Saleem, S. Rangou, C. Abetz, V. Filiz and V. Abetz, *Polymers*, 2019, **12**, 41.
51. R. M. Dorin, W. A. Phillip, H. Sai, J. Werner, M. Elimelech and U. Wiesner, *Polymer*, 2014, **55**, 347-353.
52. S. Rangou, K. Buhr, V. Filiz, J. I. Clodt, B. Lademann, J. Hahn, A. Jung and V. Abetz, *J. Membr. Sci.*, 2014, **451**, 266-275.
53. M. Radjabian and V. Abetz, *Adv. Mater.*, 2015, **27**, 352-355.
54. H. Yu, X. Qiu, S. P. Nunes and K. V. Peinemann, *Angew. Chem. Int. Ed. Engl.*, 2014, **53**, 10072-10076.
55. J. I. Clodt, V. Filiz, S. Rangou, K. Buhr, C. Abetz, D. Höche, J. Hahn, A. Jung and V. Abetz, *Adv. Funct. Mater.*, 2013, **23**, 731-738.
56. D. Keskin, J. I. Clodt, J. Hahn, V. Abetz and V. Filiz, *Langmuir*, 2014, **30**, 8907-8914.
57. S. P. Nunes, M. Karunakaran, N. Pradeep, A. R. Behzad, B. Hooghan, R. Sougrat, H. He and K.-V. Peinemann, *Langmuir*, 2011, **27**, 10184-10190.
58. Y. Gu and U. Wiesner, *Macromolecules*, 2015, **48**, 6153-6159.
59. Y. Zhang, R. A. Mulvenna, S. Qu, B. W. Boudouris and W. A. Phillip, *ACS Macro Letters*, 2017, **6**, 726-732.
60. G. G. Du Sart, R. Rachmawati, V. Voet, G. A. van Ekenstein, E. Polushkin, G. Ten Brinke and K. Loos, *Macromolecules*, 2008, **41**, 6393-6399.
61. R. Bieringer, PhD thesis, Universität Bayreuth, 1999.
62. V. Abetz, A. Boschetti-de-Fierro and J.-F. Gohy, in *Controlled and Living Polymerizations*, eds. A. H. E. Müller and K. Matyjaszewski, WILEY-VCH Verlag GmbH & Co. KGaA, Weinheim, 2009, p. 473.
63. N. Hadjichristidis, M. Pitsikalis and H. Iatrou, in *Block Copolymers I*, 2005, DOI: 10.1007/12\_005, ch. Chapter 5, pp. 1-124.

64. H. Schmalz, V. Abetz, R. Lange and M. Soliman, *Macromolecules*, 2001, **34**, 795-800.
65. M. A. Hillmyer, in *Block Copolymers II*, ed. V. Abetz, Springer Berlin Heidelberg, Berlin, Heidelberg, 2005, DOI: 10.1007/12\_002, pp. 137-181.
66. Y. Kakizawa and K. Kataoka, *Adv. Drug Deliv. Rev.*, 2002, **54**, 203-222.
67. M. Tambasco, J. E. G. Lipson and J. S. Higgins, *Macromolecules*, 2006, **39**, 4860-4868.
68. P. J. Flory, *Principles of Polymer Chemistry*, Cornell University, 1953.
69. F. S. Bates and G. H. Fredrickson, *Annu. Rev. Phys. Chem.*, 1990, **41**, 525-557.
70. F. S. Bates and G. H. Fredrickson, *Physics Today*, 1999, **52**, 32-38.
71. V. Abetz and A. Boschetti-de-Fierro, in *Polymer Science: A Comprehensive Reference*, 2012, DOI: 10.1016/b978-0-444-53349-4.00192-8, pp. 3-44.
72. M. W. Matsen and F. S. Bates, *J. Chem. Phys.*, 1997, **106**, 2436-2448.
73. V. Abetz, *Encyclopedia of polymer science technology*, 2002, **1**, 482.
74. L. Leibler, *Macromolecules*, 1980, **13**, 1602-1617.
75. I. Y. Yerukhimovich, *Polymer Science U.S.S.R.*, 1982, **24**, 2223-2232.
76. J. Melenkevitz and M. Muthukumar, *Macromolecules*, 1991, **24**, 4199-4205.
77. K. Almdal, J. H. Rosedale, F. S. Bates, G. D. Wignall and G. H. Fredrickson, *Phys. Rev. Lett.*, 1990, **65**, 1112-1115.
78. A. N. Semenov, *Zh. Eksp. Teor. Fiz.*, 1985, **88**, 1242-1256.
79. Y. Mogi, M. Nomura, H. Kotsuji, K. Ohnishi, Y. Matsushita and I. Noda, *Macromolecules*, 1994, **27**, 6755-6760.
80. Y. Matsushita, J. Suzuki and M. Seki, *Physica B: Condensed Matter*, 1998, **248**, 238-242.
81. R. Stadler, C. Auschra, J. Beckmann, U. Krappe, I. Voight-Martin and L. Leibler, *Macromolecules*, 1995, **28**, 3080-3097.
82. R. S. Susanne Brinkmann, and Edwin L. Thomas, *Macromolecules*, 1998, **31**, 6566-6572.
83. R. W. Baker, in *Membrane Technology and Applications*, John Wiley & Sons, Ltd, England, 2nd edition edn., 2004, ch. 1, p. 1.
84. M. Mulder, in *Basic Principles of Membrane Technology*, Springer Netherlands, Dordrecht, 1996, ch. 1, p. 1.
85. S. Loeb and S. Sourirajan, in *Saline Water Conversion—II*, AMERICAN CHEMICAL SOCIETY, 1963, vol. 38, ch. 9, pp. 117-132.
86. M. Mulder, in *Basic Principles of Membrane Technology*, Springer Netherlands, Dordrecht, 1996, ch. 3, p. 71.
87. R. W. Baker, in *Membrane Technology and Applications*, John Wiley & Sons, Ltd, England, 2004, ch. 3, p. 89.
88. J. G. Wijmans and C. A. Smolders, in *Synthetic Membranes Science, Engineering and Applications*, eds. P. M. Bungay, H. K. Lonsdale and M. N. d. Pinho, Springer Netherlands, Dordrecht, 1986, p. 39.
89. H. Strathmann, K. Kock, P. Amar and R. Baker, *Desalination*, 1975, **16**, 179-203.
90. S. P. Nunes and K.-V. Peinemann, in *Membrane Technology in the Chemical Industry*, eds. Suzana Pereira Nunes and K.-V. Peinemann, Wiley-VCH, Weinheim, Germany, 2006, p. 9.
91. H. Strathmann, P. Scheible and R. Baker, *J. Appl. Polym. Sci.*, 1971, **15**, 811-828.
92. W. A. Phillip, M. A. Hillmyer and E. L. Cussler, *Macromolecules*, 2010, **43**, 7763-7770.
93. N. Noor, Doctor, University of Hamburg, 2018.
94. J. Wang, M. M. Rahman, C. Abetz and V. Abetz, *J. Membr. Sci.*, 2020, 118074.
95. C. Stegelmeier, V. Filiz, V. Abetz, J. Perlich, A. Fery, P. Ruckdeschel, S. Rosenfeldt and S. Förster, *Macromolecules*, 2014, **47**, 5566-5577.
96. D. S. Marques, U. Vainio, N. M. Chaparro, V. M. Calo, A. R. Behzad, J. W. Pitera, K.-V. Peinemann and S. P. Nunes, *Soft Matter*, 2013, **9**, 5557.
97. D. S. Marques, R. M. Dorin, U. Wiesner, D.-M. Smilgies, A. R. Behzad, U. Vainio, K.-V. Peinemann and S. P. Nunes, *Polymer*, 2014, **55**, 1327-1332.

98. R. M. Dorin, D. S. Marques, H. Sai, U. Vainio, W. A. Phillip, K.-V. Peinemann, S. P. Nunes and U. Wiesner, *ACS Macro Letters*, 2012, **1**, 614-617.
99. Y. Gu, R. M. Dorin, K. W. Tan, D.-M. Smilgies and U. Wiesner, *Macromolecules*, 2016, **49**, 4195-4201.
100. M. Radjabian, C. Abetz, B. Fischer, A. Meyer and V. Abetz, *ACS Appl. Mater. Interfaces*, 2017, **9**, 31224-31234.
101. K. Sankhala, D. C. F. Wieland, J. Koll, M. Radjabian, C. Abetz and V. Abetz, *Nanoscale*, 2019, **11**, 7634-7647.
102. S. P. Nunes, R. Sougrat, B. Hooghan, D. H. Anjum, A. R. Behzad, L. Zhao, N. Pradeep, I. Pinnau, U. Vainio and K.-V. Peinemann, *Macromolecules*, 2010, **43**, 8079-8085.
103. S. P. Nunes, A. R. Behzad, B. Hooghan, R. Sougrat, M. Karunakaran, N. Pradeep, U. Vainio and K.-V. Peinemann, *ACS Nano*, 2011, **5**, 3516-3522.
104. P. Madhavan, K. V. Peinemann and S. P. Nunes, *ACS Appl. Mater. Interfaces*, 2013, **5**, 7152-7159.
105. L. Oss-Ronen, J. Schmidt, V. Abetz, A. Radulescu, Y. Cohen and Y. Talmon, *Macromolecules*, 2012, **45**, 9631-9642.
106. M. Mulder, in *Basic Principles of Membrane Technology*, Springer Netherlands, Dordrecht, 1996, ch. 5, p. 210.
107. J. R. Werber, C. O. Osuji and M. Elimelech, *Nat. Rev. Mater*, 2016, **1**.
108. R. W. Baker, in *Membrane Technology and Applications*, John Wiley & Sons, Ltd, England, 2004, ch. 2, p. 15.
109. H. B. Park, J. Kamcev, L. M. Robeson, M. Elimelech and B. D. Freeman, *Science*, 2017, **356**.
110. S. Bandini and D. Vezzani, *Chem. Eng. Sci.*, 2003, **58**, 3303-3326.
111. W. R. Bowen, A. W. Mohammad and N. Hilal, *J. Membr. Sci.*, 1997, **126**, 91-105.
112. W.-J. Lau and A. F. Ismail, *Desalination*, 2009, **245**, 321-348.
113. B. S. Lalia, V. Kochkodan, R. Hashaikeh and N. Hilal, *Desalination*, 2013, **326**, 77-95.
114. Leos Zeman and M. Wales, in *Synthetic Membranes Volume II. Hyper- and Ultrafiltration Uses*, ed. A. F. Turbak, American Chemical Society, Washington, DC, 1981, ch. 23, p. 411.
115. A. Mehta and A. L. Zydney, *J. Membr. Sci.*, 2005, **249**, 245-249.
116. A. W. Mohammad, Y. H. Teow, W. L. Ang, Y. T. Chung, D. L. Oatley-Radcliffe and N. Hilal, *Desalination*, 2015, **356**, 226-254.
117. L. Dresner, *Desalination*, 1972, **10**, 27-46.
118. P. Georgopoulos, S. Rangou, T. Gil Haenelt, C. Abetz, A. Meyer, V. Filiz, U. A. Handge and V. Abetz, *Colloid. Polym. Sci.*, 2014, **292**, 1877-1891.
119. P. Georgopoulos, V. Filiz, U. A. Handge and V. Abetz, *Macromol. Chem. Phys.*, 2016, **217**, 1293-1304.
120. Y. Gu, R. M. Dorin and U. Wiesner, *Nano Lett.*, 2013, **13**, 5323-5328.
121. P. Docampo, M. Stefik, S. Guldin, R. Gunning, N. A. Yufa, N. Cai, P. Wang, U. Steiner, U. Wiesner and H. J. Snaith, *Adv. Energy Mater.*, 2012, **2**, 676-682.
122. B. P. Tripathi, N. C. Dubey, S. Choudhury, F. Simon and M. Stamm, *J. Mater. Chem. B*, 2013, **1**, 3397.
123. Y. Miyaki, H. Nagamatsu, M. Iwata, K. Ohkoshi, K. Se and T. Fujimoto, *Macromolecules*, 1984, **17**, 2231-2236.
124. H. Lee and K. Char, *ACS Appl. Mater. Interfaces*, 2009, **1**, 913-920.
125. D. M. Stachera and R. F. Childs, *J. Membr. Sci.*, 2001, **187**, 213-225.
126. M. H. Park, C. Subramani, S. Rana and V. M. Rotello, *Adv. Mater.*, 2012, **24**, 5862-5866.
127. E. N. Savariar, K. Krishnamoorthy and S. Thayumanavan, *Nat. Nanotechnol.*, 2008, **3**, 112-117.
128. E. N. Savariar, M. M. Sochat, A. Klaukherd and S. Thayumanavan, *Angew. Chem. Int. Ed. Engl.*, 2009, **48**, 110-114.

129. S. B. Lee, D. T. Mitchell, L. Trofin, T. K. Nevanen, H. Soederlund and C. R. Martin, *Science*, 2002, **296**, 2198-2200.
130. S. B. Lee and C. R. Martin, *Anal. Chem.*, 2001, **73**, 768-775.
131. L. Velleman, J. G. Shapter and D. Losic, *J. Membr. Sci.*, 2009, **328**, 121-126.
132. A. Asatekin and K. K. Gleason, *Nano Lett.*, 2011, **11**, 677-686.
133. A. Asatekin and A. M. Mayes, *Sep. Sci. Technol.*, 2009, **44**, 3330-3345.
134. P. Tyagi, A. Deratani, D. Bouyer, D. Cot, V. Gence, M. Barboiu, T. N. Phan, D. Bertin, D. Gigmes and D. Quemener, *Angew. Chem. Int. Ed. Engl.*, 2012, **51**, 7166-7170.
135. X.-L. Wang, T. Tsuru, S.-i. Nakao and S. Kimura, *J. Membr. Sci.*, 1997, **135**, 19-32.
136. L. Antonov, G. Gergov, V. Petrov, M. Kubista and J. Nygren, *Talanta*, 1999, **49**, 99-106.
137. K. Fujita, K. Taniguchi and H. Ohno, *Talanta*, 2005, **65**, 1066-1070.
138. T. Hinoue, Y. Yokoyama and T. Ozeki, *Japan analyst*, 1994, **43**, 443-448.
139. Y. Su, Y. Liu, T. Liu and X. Wang, *J. Appl. Polym. Sci.*, 2018, DOI: 10.1002/app.47137, 47137.
140. J. I. Clodt, B. Bajer, K. Buhr, J. Hahn, V. Filiz and V. Abetz, *J. Membr. Sci.*, 2015, **495**, 334-340.
141. X. Feng, K. Kawabata, G. Kaufman, M. Elimelech and C. O. Osuji, *ACS Nano*, 2017, **11**, 3911-3921.
142. J. d. S. Macedo, N. B. da Costa Júnior, L. E. Almeida, E. F. d. S. Vieira, A. R. Cestari, I. d. F. Gimenez, N. L. Villarreal Carreño and L. S. Barreto, *J. Colloid Interface Sci.*, 2006, **298**, 515-522.
143. L. Tinghui, T. Matsuura and S. Sourirajan, *Ind. Eng. Chem. Prod. Res. Dev.*, 1983, **22**, 77-85.
144. J. Justynska, Z. Hordyjewicz and H. Schlaad, *Polymer*, 2005, **46**, 12057-12064.
145. Z. Zhang, M. M. Rahman, C. Abetz, A. L. Höhme, E. Sperling and V. Abetz, *Adv. Mater.*, 2020, **32**, 1907014.
146. M. Radjabian, C. Abetz, B. Fischer, A. Meyer and V. Abetz, *ACS Appl. Mater. Interfaces*, 2017, **9**, 31224-31234.
147. Y. Ma, F. Shi, J. Ma, M. Wu, J. Zhang and C. Gao, *Desalination*, 2011, **272**, 51-58.
148. B. Chakrabarty, A. K. Ghoshal and M. K. Purkait, *J. Membr. Sci.*, 2008, **309**, 209-221.
149. N. Noor, J. Koll, N. Scharnagl, C. Abetz and V. Abetz, *Membranes (Basel)*, 2018, **8**, 54.
150. H. Matsuyama, T. Maki, M. Teramoto and K. Kobayashi, *Sep. Sci. Technol.*, 2003, **38**, 3449-3458.
151. M. Son, H. Kim, J. Jung, S. Jo and H. Choi, *Chemosphere*, 2017, **179**, 194-201.
152. K. Sankhala, J. Koll and V. Abetz, *Membranes (Basel)*, 2020, **10**.
153. Z. Zhang, M. M. Rahman, C. Abetz, B. Bajer, J. Wang and V. Abetz, *Macromol. Rapid Commun.*, 2019, **40**, 1800729.
154. Y. Liao, T. P. Farrell, G. R. Guillen, M. Li, J. A. T. Temple, X.-G. Li, E. M. V. Hoek and R. B. Kaner, *Mater. Horiz.*, 2014, **1**, 58-64.
155. M. E. Amy E. Childress, *J. Membr. Sci.*, 1996, **119**, 253-268.
156. G. M. Geise, B. D. Freeman and D. R. Paul, *Polymer*, 2010, **51**, 5815-5822.
157. S. Temmel, W. Kern and T. Luxbacher, *Prog. Colloid Polym. Sci.*, 2006, **132**, 54-61.
158. S. H. Baxamusa and K. K. Gleason, *Adv. Funct. Mater.*, 2009, **19**, 3489-3496.
159. X. Zhao, Y. Su, J. Cao, Y. Li, R. Zhang, Y. Liu and Z. Jiang, *J. Mater. Chem. A*, 2015, **3**, 7287-7295.
160. M.-L. Luo, J.-Q. Zhao, W. Tang and C.-S. Pu, *Appl. Surf. Sci.*, 2005, **249**, 76-84.
161. R.-X. Zhang, L. Braeken, T.-Y. Liu, P. Luis, X.-L. Wang and B. Van der Bruggen, *Applied Sciences*, 2017, **7**, 81.
162. Z. Zhao, H. Ni, Z. Han, T. Jiang, Y. Xu, X. Lu and P. Ye, *ACS Appl. Mater. Interfaces*, 2013, **5**, 7808-7818.
163. C. A. Amadei, R. Yang, M. Chiesa, K. K. Gleason and S. Santos, *ACS Appl. Mater. Interfaces*, 2014, **6**, 4705-4712.
164. C. Liu, C. Wang, Y. Guo, J. Zhang, Y. Cao, H. Liu, Z. Hu and C. Zhang, *J. Mater. Chem. A*, 2019, **7**, 6695-6707.

165. L. Shen, C. Cheng, X. Yu, Y. Yang, X. Wang, M. Zhu and B. S. Hsiao, *J. Mater. Chem. A*, 2016, **4**, 15575-15588.
166. G. Jiang, S. Zhang, Y. Zhu, S. Gao, H. Jin, L. Luo, F. Zhang and J. Jin, *J. Mater. Chem. A*, 2018, **6**, 2927-2934.
167. L. C. Cesteros, J. R. Isasi and I. Katime, *Macromolecules*, 1993, **26**, 7256-7262.
168. L. C. Cesteros, J. R. Isasi and I. Katime, *Macromolecules*, 1994, **27**, 7887-7892.
169. L. C. Cesteros, J. R. Isasi and I. Katime, *J. Polym. Sci. B Polym. Phys.*, 1994, **32**, 223-230.
170. P. Hiekkataipale, T. I. Löbbling, M. Poutanen, A. Priimagi, V. Abetz, O. Ikkala and A. H. Gröschel, *Polymer*, 2016, **107**, 456-465.
171. S. Valkama, A. Nykänen, H. Kosonen, R. Ramani, F. Tuomisto, P. Engelhardt, G. ten Brinke, O. Ikkala and J. Ruokolainen, *Adv. Funct. Mater.*, 2007, **17**, 183-190.
172. H. Kosonen, S. Valkama, A. Nykänen, M. Toivanen, G. ten Brinke, J. Ruokolainen and O. Ikkala, *Adv. Mater.*, 2006, **18**, 201-205.
173. T. Ruotsalainen, J. Turku, P. Heikkilä, J. Ruokolainen, A. Nykänen, T. Laitinen, M. Torkkeli, R. Serimaa, G. ten Brinke, A. Harlin and O. Ikkala, *Adv. Mater.*, 2005, **17**, 1048-1052.
174. S. Valkama, T. Ruotsalainen, A. Nykänen, A. Laiho, H. Kosonen, G. t. Brinke, O. Ikkala and J. Ruokolainen, *Macromolecules*, 2006, **39**, 9327-9336.
175. R. Mäki-Ontto, K. d. Moel, W. d. Odorico, J. Ruokolainen, M. Stamm, G. t. Brinke and O. Ikkala, *Adv. Mater.*, 2001, **13**, 117-121.
176. K. Jung, PhD thesis, Johannes Gutenberg-Universität Mainz, 1996.
177. J. Ruokolainen, G. t. Brinke and O. Ikkala, *Adv. Mater.*, 1999, **11**, 777-780.
178. M. Gallei, S. Rangou, V. Filiz, K. Buhr, S. Bolmer, C. Abetz and V. Abetz, *Macromol. Chem. Phys.*, 2013, **214**, 1037-1046.
179. R. Yang and K. K. Gleason, *Langmuir*, 2012, **28**, 12266-12274.
180. I. Sadeghi, J. Kronenberg and A. Asatekin, *ACS Nano*, 2018, **12**, 95-108.
181. P. Bengani-Lutz, E. Converse, P. Cebe and A. Asatekin, *ACS Appl. Mater. Interfaces*, 2017, **9**, 20859-20872.
182. S. Qu, T. Dilenschneider and W. A. Phillip, *ACS Appl. Mater. Interfaces*, 2015, **7**, 19746-19754.
183. K. Boussu, J. De Baerdemaeker, C. Dauwe, M. Weber, K. G. Lynn, D. Depla, S. Aldea, I. F. Vankelecom, C. Vandecasteele and B. Van der Bruggen, *Chemphyschem*, 2007, **8**, 370-379.
184. K. Boussu, C. Vandecasteele and B. Van der Bruggen, *J. Membr. Sci.*, 2008, **310**, 51-65.
185. S. Datta, A. T. Conlisk, D. M. Kanani, A. L. Zydney, W. H. Fissell and S. Roy, *J. Colloid Interface Sci.*, 2010, **348**, 85-95.
186. S. Déon, P. Fievet and C. Osman Doubad, *J. Membr. Sci.*, 2012, **423-424**, 413-421.
187. A. Zilman, S. Di Talia, T. Jovanovic-Talisman, B. T. Chait, M. P. Rout and M. O. Magnasco, *PLoS Comput Biol*, 2010, **6**, e1000804.
188. S. Dedisch, A. Wiens, M. D. Davari, D. Soder, C. Rodriguez-Emmenegger, F. Jakob and U. Schwaneberg, *Biotechnol. Bioeng.*, 2020, **117**, 49-61.
189. N. Büscher, G. V. Sayoga, K. Rübsam, F. Jakob, U. Schwaneberg, S. Kara and A. Liese, *Org. Process Res. Dev.*, 2019, **23**, 1852-1859.
190. M. Noor, T. Dworeck, A. Schenk, P. Shinde, M. Fioroni and U. Schwaneberg, *J. Biotechnol.*, 2012, **157**, 31-37.
191. L. Apitius, K. Rubsam, C. Jakesch, F. Jakob and U. Schwaneberg, *Biotechnol. Bioeng.*, 2019, **116**, 1856-1867.
192. K. Rübsam, L. Weber, F. Jakob and U. Schwaneberg, *Biotechnol. Bioeng.*, 2018, **115**, 321-330.
193. K. Rübsam, B. Stomps, A. Böker, F. Jakob and U. Schwaneberg, *Polymer*, 2017, **116**, 124-132.
194. S. Islam, L. Apitius, F. Jakob and U. Schwaneberg, *Environment international*, 2019, **123**, 428-435.
195. A. V. Shivange and U. Schwaneberg, in *Directed Enzyme Evolution: Advances and Applications*, 2017, DOI: 10.1007/978-3-319-50413-1\_6, ch. Chapter 6, pp. 145-172.

196. G. Korfer, C. Novoa, J. Kern, E. Balla, C. Grutering, M. D. Davari, R. Martinez, L. Vojcic and U. Schwaneberg, *Appl. Microbiol. Biotechnol.*, 2018, **102**, 9607-9620.
197. A. V. Shivange, A. Serwe, A. Dennig, D. Roccatano, S. Haefner and U. Schwaneberg, *Appl. Microbiol. Biotechnol.*, 2011, **95**, 405-418.
198. S. Li, F. Huo, Q. Li, C. Gao, Y. Su and W. Zhang, *Polym. Chem.*, 2014, **5**, 3910-3918.
199. V. S. D. Voet, D. Hermida-Merino, G. ten Brinke and K. Loos, *RSC Advances*, 2013, **3**, 7938.
200. C. Xu, X. Fu, M. Fryd, S. Xu, B. B. Wayland, K. I. Winey and R. J. Composto, *Nano Lett.*, 2006, **6**, 282-287.
201. C. L. Feng, G. J. Vancso and H. Schönherr, *Langmuir*, 2005, **21**, 2356-2363.
202. S. Ludwigs, K. Schmidt and G. Krausch, *Macromolecules*, 2005, **38**, 2376-2382.
203. K.-i. Yamamoto, M. Hiwatari, F. Kohori, K. Sakai, M. Fukuda and T. Hiyoshi, *Journal of Artificial Organs*, 2005, **8**, 198-205.

## **Chapter 10 Appendix**

## 10.1 Exploratory Investigation Aiming for Charge-mosaic Isoporous Membranes

### 10.1.1 Synthesis of PS-*b*-PtBMA Diblock Copolymers

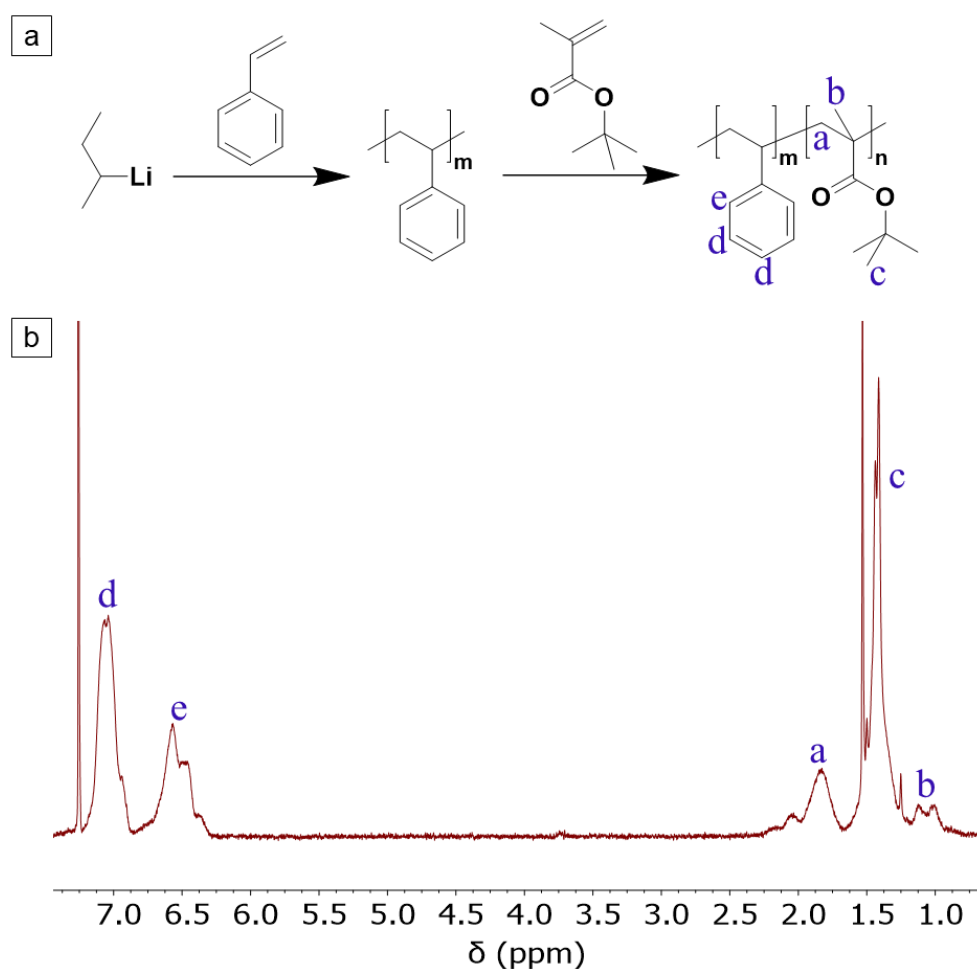


Figure 10.1. (a) Synthesis of PS-*b*-PtBMA diblock copolymer by living anionic polymerization. (b) <sup>1</sup>H NMR spectrum of the prepared PS-*b*-PtBMA.

PS-*b*-PtBMA diblock copolymers were prepared by living anionic polymerization as shown in Figure 10.1a.<sup>2</sup> The success of the polymerization was confirmed by <sup>1</sup>H NMR (Figure 10.1b). As the molecular weight and block composition of the BCP play an important role in the

<sup>2</sup> Diblock copolymer PS-*b*-PtBMA was synthesized by my colleague Brigitte Lademann, not my own.

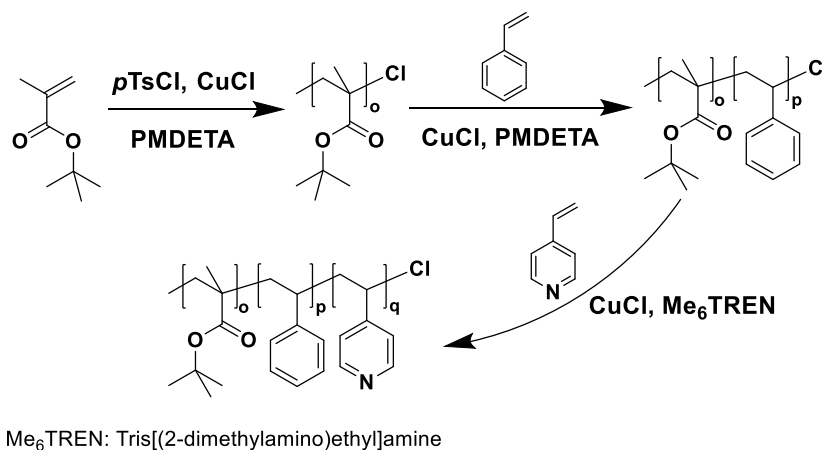
fabrication of SNIPS membranes, two batches of PS-*b*-PtBMA were prepared with different molecular weights and block compositions, i.e. PS<sub>85</sub>-*b*-PtBMA<sub>15</sub><sup>100</sup> and PS<sub>80</sub>-*b*-PtBMA<sub>20</sub><sup>153</sup> (Subscripts represent the weight fractions in % of the corresponding blocks, while superscripts denote the molecular weight with the unit of kg mol<sup>-1</sup>). The detailed molecular characteristics of PS-*b*-PtBMA are shown in Table 10.1.

Table 10.1. Molecular characterization of the polymers used for the sample preparation (Synthesis was performed by Brigitte Lademann)

	PS [wt%] <sup>a)</sup>	PtBMA [wt%] <sup>a)</sup>	M <sub>n</sub> [kg mol <sup>-1</sup> ] <sup>b)</sup>	M <sub>w</sub> [kg mol <sup>-1</sup> ] <sup>b)</sup>	Dispersity indices
PS <sub>85</sub> - <i>b</i> -PtBMA <sub>15</sub> <sup>100</sup>	85	15	97	100	1.03
PS <sub>80</sub> - <i>b</i> -PtBMA <sub>20</sub> <sup>153</sup>	80	20	147	153	1.04

<sup>a)</sup> The composition of polymers was determined from <sup>1</sup>HNMR. <sup>b)</sup> The molecular weight of polymers and dispersity index were determined by GPC.

### 10.1.2 Synthesis of PtBMA-*b*-PS-*b*-P4VP Triblock Terpolymers



Scheme 10.1. Synthesis route of PtBMA-*b*-PS-*b*-P4VP triblock terpolymers by ATRP.

Synthesis of PtBMA-*b*-PS-*b*-P4VP triblock terpolymer is difficult by living anionic polymerization, as the polyanions of PtBMA and P4VP both cannot initiate styrene

polymerization. Therefore ATRP was employed to prepare *PtBMA-b-PS-b-P4VP* where *PtBMA* was the first block followed by PS and P4VP, respectively, as depicted in Scheme 10.1. A typical procedure to prepare macroinitiator *PtBMA* is reported by Sart *et al.*<sup>60</sup> Specially, CuX (0.4mmol) was added into a Schlenk flask which was evacuated and backfilled with N<sub>2</sub> for three times. Monomer *tBMA* (84 mmol), ligand PMDETA (0.4 mmol) and solvent toluene (10 ml) were added into another Schlenk flask and degassed by three freeze-pump-thaw cycles. The mixture was transferred into a flask with CuX and then degassed once more. The mixture was stirred for 30 min to form a blue coloured complex. The solvent toluene (3 ml) and initiator *pTsCl* (0.4 mmol) were degassed in separated Schlenk flasks. The degassed toluene was transferred into the flask with *pTsCl* and the mixture was degassed by three freeze-pump-thaw cycles. The bluish complex solution was added to the initiator *pTsCl* solution. The reaction flask was put into a thermostated oil bath at 60 °C and the polymerization was carried out for 16 h. Afterwards, the mixture was dissolved in THF and passed through a basic Al<sub>2</sub>O<sub>3</sub> column to remove the copper species. The polymer solution was concentrated and precipitated into methanol/H<sub>2</sub>O (75/25 v/v). This procedure was repeated several times and the polymer was then dried under vacuum. The copolymerizations of *PtBMA-b-PS* and *PtBMA-b-PS-b-P4VP* can be performed using the same setup as the homopolymerization of *PtBMA*.

The macroinitiator *PtBMA* was prepared successfully, as confirmed by <sup>1</sup>HNMR spectrum with characteristic signals of the newly formed methylene groups (-CH<sub>2</sub>C- at  $\delta = 1.81$  ppm) and methyl groups (-CCH<sub>3</sub> at  $\delta = 1.03\sim 1.11$  ppm; -C(CH<sub>3</sub>)<sub>3</sub> at  $\delta = 1.41\sim 1.44$  ppm), as shown in Figure 10.2.<sup>198, 199</sup> In order to obtain the different end-functionalized *PtBMA-X*, different catalysts (i.e. CuCl and CuBr) and initiators (i.e. MBrP and *pTsCl*) were employed. Compared to the MBrP/CuX/PMDETA system, the *pTsCl*/CuCl/PMDETA system results in well-defined polymers with higher molecular weight and low dispersity index (Table 10.2). Afterwards, *PtBMA-b-PS* diblock copolymer was synthesized using the macroinitiator *PtBMA*-

X/CuCl/PMDETA system at 100 °C. But there was no polymerization of styrene in the solution polymerization. Under bulk polymerization, the styrene was polymerized by thermal self-initiation instead of polymerization on the macroinitiator *Pt*BMA. Therefore, the synthesis of the *Pt*BMA-*b*-PS-*b*-P4VP triblock terpolymer by ATRP was not successful.

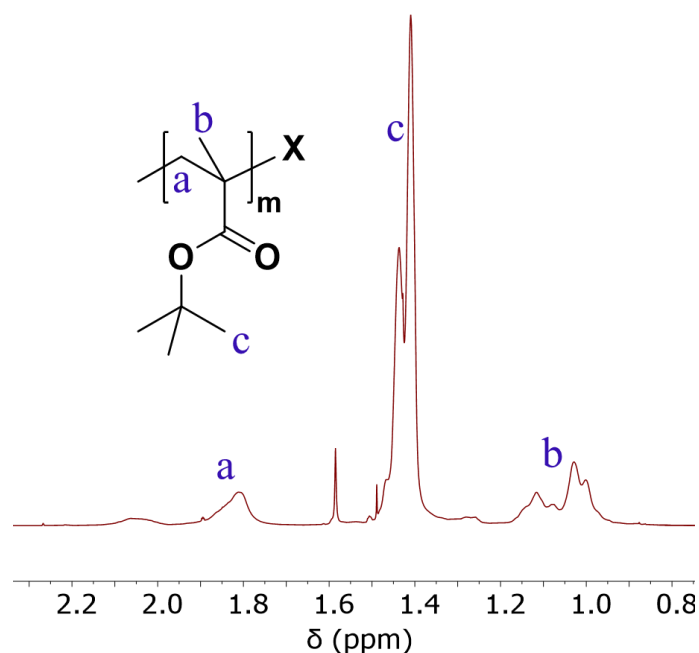


Figure 10.2. <sup>1</sup>H NMR spectrum of macroinitiator *Pt*BMA prepared by ATRP.

Table 10.2. Molecular characteristics of the macroinitiator *Pt*BMA prepared using different initiator and catalyst systems.

Monomer	Initiator	Catalyst	Ligand	$M_n$ (kg mol <sup>-1</sup> )	$M_w$ (kg mol <sup>-1</sup> )	Dispersity Index
	MBrP	CuCl		11.4	13.2	1.16
<i>t</i> BMA	MBrP	CuBr	PMDETA	10.6	14.2	1.34
	<i>p</i> TsCl	CuCl		16.6	18.1	1.09

The molecular weight of polymers was determined by GPC.

### 10.1.3 Fabrication of Isoporous Membrane via SNIPS from PS-*b*-*Pt*BMA Diblock Copolymers

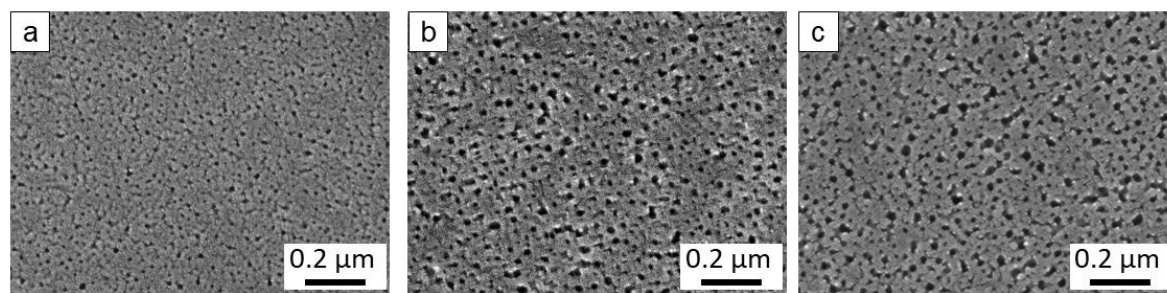


Figure 10.3. SEM images of representative membranes cast from (a)  $\text{PS}_{85}\text{-}b\text{-PtBMA}_{15}^{100}$  with 39 wt%, THF/DMF 1/1, the evaporation time is 5 s. (b)  $\text{PS}_{80}\text{-}b\text{-PtBMA}_{20}^{154}$  with 33 wt%, THF/DMF 1/1, the evaporation time is 3 s. (c)  $\text{PS}_{80}\text{-}b\text{-PtBMA}_{20}^{154}$  with 33 wt%, THF/DMF 1/1 with 0.05 wt%  $\text{CuCl}_2$  as the casting solution, the evaporation time is 5 s.

Diblock copolymers  $\text{PS}_{85}\text{-}b\text{-PtBMA}_{15}^{100}$  and  $\text{PS}_{80}\text{-}b\text{-PtBMA}_{20}^{154}$  were employed to cast membranes via SNIPS. Different solvent mixtures in the binary solvent system THF/DMF or ternary solvent system THF/DMF/DOX were used, e.g., the solvent mixtures of THF/DMF 2/3, THF/DMF 1/1, THF/DMF 3/2, and THF/DMF/DOX 1/1/1. The concentration of polymer solution and solvent evaporation time were also tuned. The surface morphology of the most representative membranes derived from  $\text{PS}_{85}\text{-}b\text{-PtBMA}_{15}^{100}$  and  $\text{PS}_{80}\text{-}b\text{-PtBMA}_{20}^{154}$  are shown in Figure 10.3a and b, respectively. Compared to  $\text{PS}_{85}\text{-}b\text{-PtBMA}_{15}^{100}$  membrane, the membrane of  $\text{PS}_{80}\text{-}b\text{-PtBMA}_{20}^{154}$  exhibited a more porous structure with a bigger pore size, presumably due to its larger pore-forming block *PtBMA*. In both cases, the best membrane structure was obtained by the solvent mixture of THF/DMF 1/1. Furthermore, in order to facilitate the formation of an isoporous structure, the additive was introduced into the casting solution of  $\text{PS}_{80}\text{-}b\text{-PtBMA}_{20}^{154}$ , i.e.  $\text{CuCl}_2$ . No improvement was observed with the addition of  $\text{CuCl}_2$  (Figure 10.3c) in comparison with the pristine membrane (Figure 10.3b). One possible reason could be the lack of molecular specific interactions between *PtBMA* and  $\text{CuCl}_2$ , which can promote BCP self-assembly during the SNIPS procedure. The isoporous membrane from *PS-b-PtBMA* was not obtained via SNIPS.

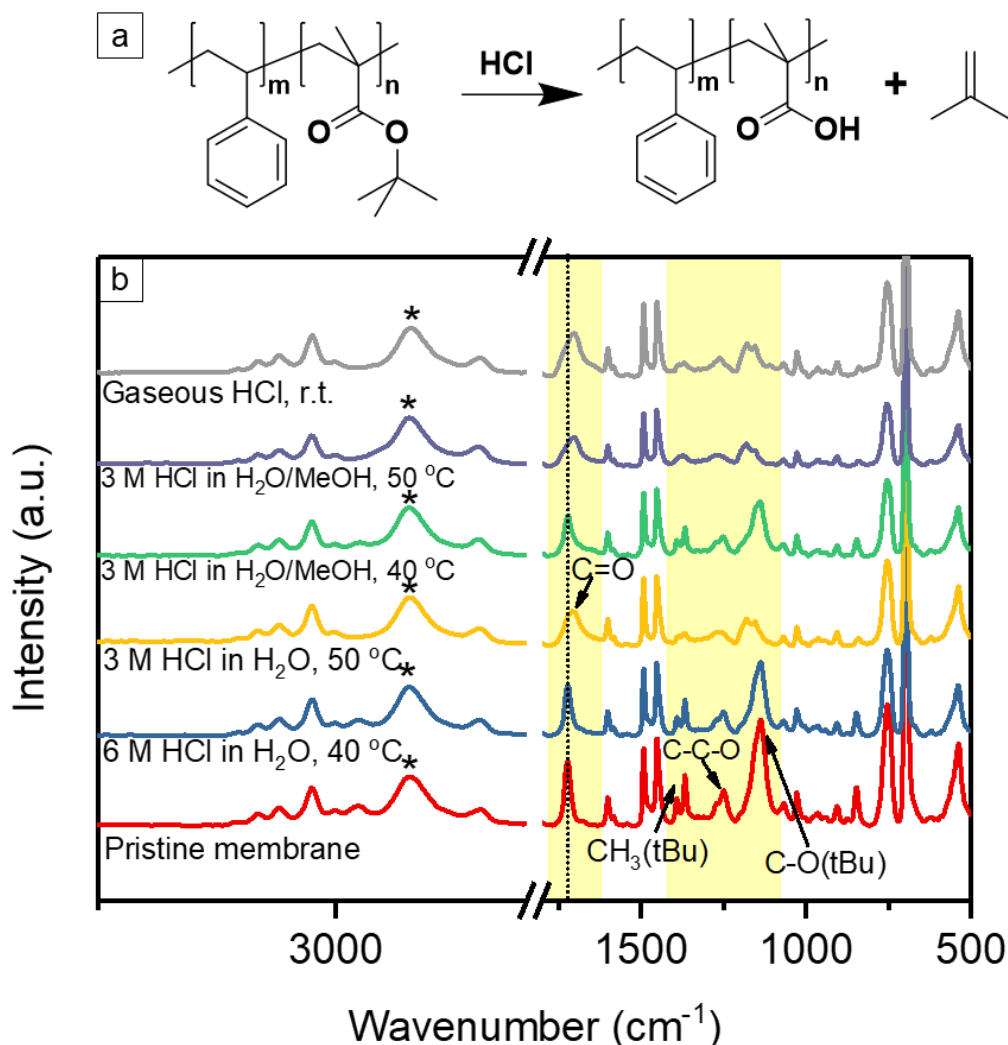
10.1.4 Hydrolysis of the PS-*b*-PtBMA Diblock Copolymer Membrane

Figure 10.4. (a) Acid-catalyzed hydrolysis of PS-*b*-PtBMA membrane to PS-*b*-PMAA membrane. (b) FTIR spectra of the pristine membrane and modified membranes using different hydrolysis conditions. The relative intensities were normalized using the characteristic  $\text{CH}_2$  stretching vibrations (\*) of the unreactive backbone around  $2924 \text{ cm}^{-1}$ . All the reactions were performed for 7 days.

The porous PS-*b*-PtBMA membrane was subjected to acid-catalyzed hydrolysis with HCl under heterogeneous condition to obtain the PS-*b*-PMAA membrane (Figure 10.4a). The hydrolysis condition was optimized by changing the HCl concentration in nonsolvent of  $\text{H}_2\text{O}$

or H<sub>2</sub>O/methanol (MeOH) and reaction temperature, or by using gaseous HCl. Specifically, the membrane was placed in the excess amount of 3 M or 6 M HCl in H<sub>2</sub>O or H<sub>2</sub>O/methanol solution (i.e, molar ratio [HCl]<sub>0</sub>/[*t*BMA]<sub>0</sub> = 2000:1) at 40 or 50 °C, or in the HCl vapour produced by concentrated aqueous HCl (37 wt%) at room temperature (r.t.). After the predetermined reaction time, the membrane was dried at 60 °C under vacuum for several days.

In FTIR spectra of the hydrolyzed membrane, the most characteristic peaks of *tert*-butyl groups (*t*Bu) at ca. 1391 cm<sup>-1</sup> and 1367 cm<sup>-1</sup> disappear while the stretching vibration of C=O at ca. 1722 cm<sup>-1</sup> broadens and shifts to ca. 1702 cm<sup>-1</sup>, assigned to the formation of carboxylic groups (Figure 10.4b).<sup>200-202</sup> Therefore, the hydrolysis reaction was successful under the conditions of 3 M HCl in H<sub>2</sub>O at 50 °C for 7 days, 3 M HCl in H<sub>2</sub>O/MeOH at 50 °C for 7 days, or gaseous HCl at room temperature for 7 days, respectively. We can also see that the reaction temperature (i.e. 40 and 50 °C) affects the hydrolysis significantly while the nonsolvent system (i.e. H<sub>2</sub>O or H<sub>2</sub>O/MeOH) shows no obvious influence.

On the basis of the success of hydrolysis, another key point is to persist the porous structure of the membrane. From SEM images, only the hydrolyzed membrane with gaseous HCl retains the kinetically trapped porous morphology of the pristine membrane (Figure 10.5). Therefore the optimal hydrolysis condition without destroying the membrane structure is gaseous HCl at room temperature.

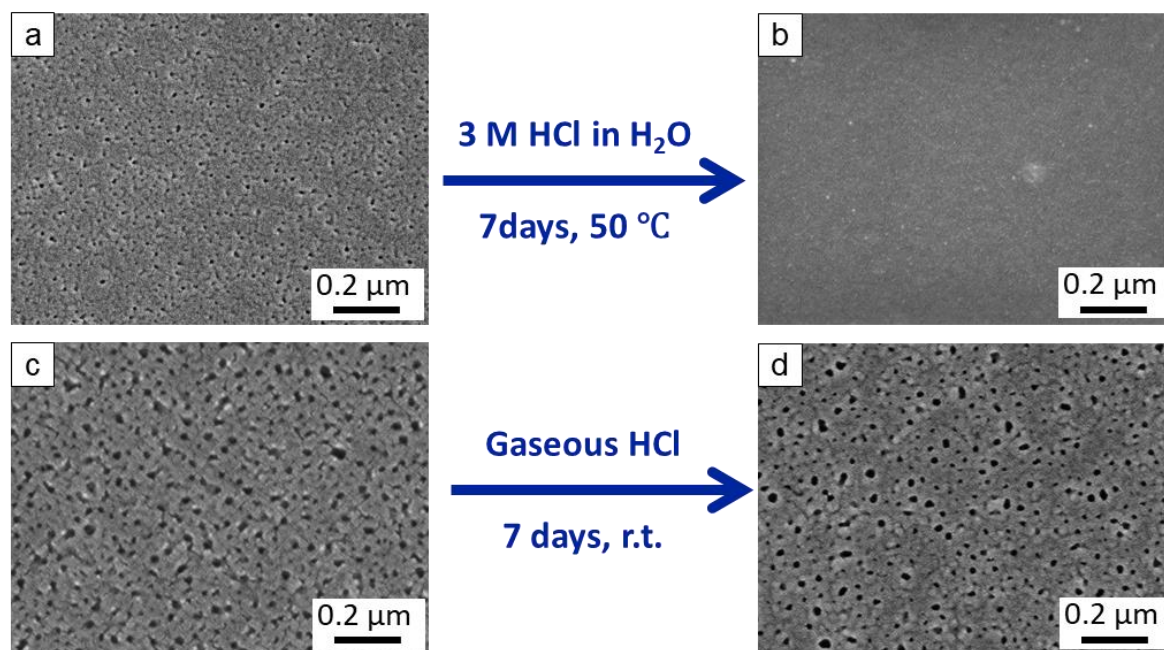


Figure 10.5. SEM images of the membranes: Exemplary  $\text{PS}_{85}\text{-}b\text{-PtBMA}_{15}^{100\text{k}}$  membrane (a) before and (b) after hydrolysis. Exemplary  $\text{PS}_{80}\text{-}b\text{-PtBMA}_{20}^{150\text{k}}$  membrane (c) before and (d) after hydrolysis.

### 10.1.5 Synthesis of PDMAi-*b*-PS-*b*-PtBMA Triblock Terpolymer

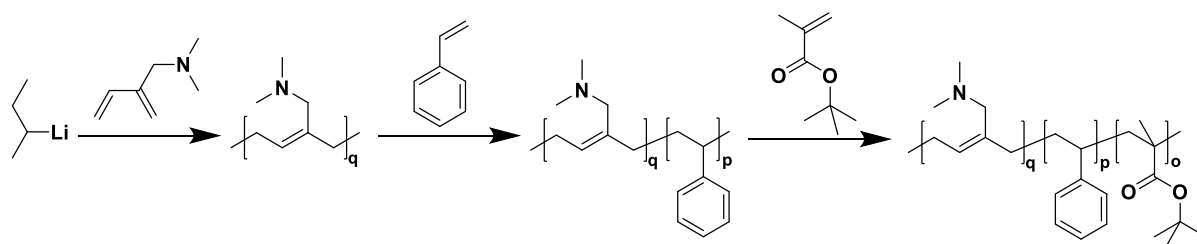


Figure 10.6. Scheme of synthesis route of the triblock terpolymer PDMAi-*b*-PS-*b*-PtBMA by living anionic polymerization.

The triblock terpolymer PDMAi-*b*-PS-*b*-PtBMA was synthesized via sequential living anionic polymerization by Dr. Ruth Bieringer during her PhD study<sup>61</sup>, as shown in Figure 10.6. In this work, the employed PDMAi-*b*-PS-*b*-PtBMA has a molecular weight ( $M_w$ ) of  $40 \text{ kg mol}^{-1}$ , a

dispersity index of 1.5, and a block composition of 17 wt% PDMAi, 57 wt% PS and 26 wt% PtBMA.

### 10.1.6 Membrane Fabrication of PDMAi-*b*-PS-*b*-PtBMA Triblock Terpolymer

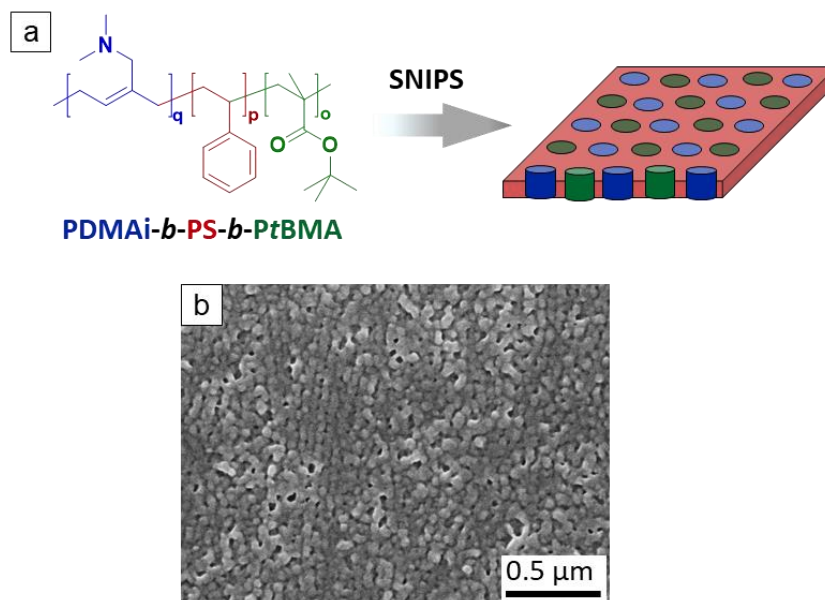


Figure 10.7. (a) Schematic representation of the desired membrane derived from PDMAi<sub>17</sub>-*b*-PS<sub>57</sub>-*b*-PtBMA<sub>26</sub><sup>40</sup>. (b) SEM images of a representative membrane cast from PDMAi<sub>17</sub>-*b*-PS<sub>57</sub>-*b*-PtBMA<sub>26</sub><sup>40k</sup> with 26 wt% polymer in THF/DMF 1/1, the evaporation time is 5 s.

From the thorough morphological investigation of Dr. Ruth Bieringer on PDMAi-*b*-PS-*b*-PtBMA it follows that all three blocks show a strong microphase segregation with each other, leading to three-phase morphologies with three discrete microdomains.<sup>61</sup> Therefore, PDMAi<sub>17</sub>-*b*-PS<sub>57</sub>-*b*-PtBMA<sub>26</sub><sup>40</sup> with a major mid-block of PS and two minor end-blocks of PDMAi and PtBMA provided the possibility to form the desired membrane with two discrete pore channels in the PS matrix, as shown in Figure 10.7a. PDMAi<sub>17</sub>-*b*-PS<sub>57</sub>-*b*-PtBMA<sub>26</sub><sup>40</sup> was cast using THF/DMF 1/1 solvent, as this was the optimal solvent mixture for the PS-*b*-PtBMA system.

The representative membrane shows a porous structure with few irregular pores, as shown in Figure 10.7b.

### 10.1.7 Post-functionalization of PDMAi-*b*-PS-*b*-PtBMA Triblock Terpolymer

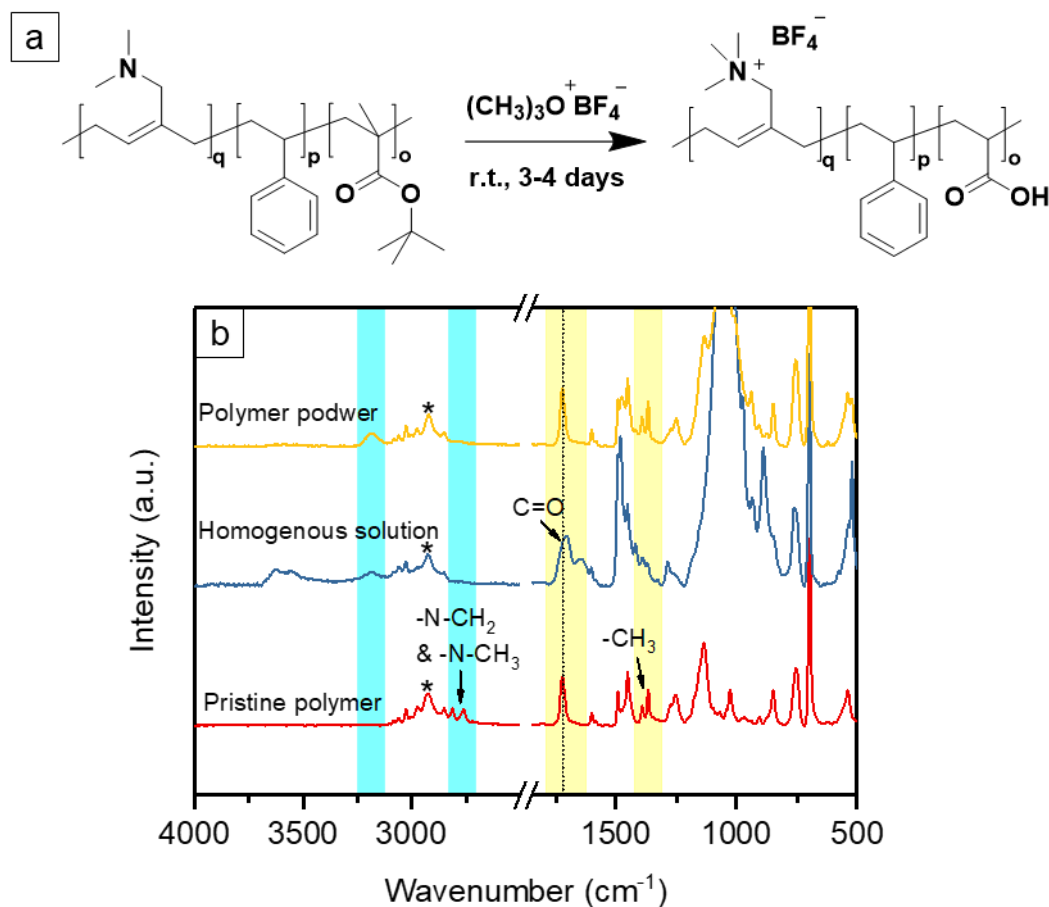


Figure 10.8. (a) Post-functionalization of PDMAi-*b*-PS-*b*-PtBMA by trimethyloxonium tetrafluoroborate ( $(\text{CH}_3)_3\text{O}(\text{BF}_4)$ ). (b) FTIR spectra of the pristine polymer and the modified polymers in the homogeneous or heterogeneous conditions. The relative intensities were normalized using the characteristic  $\text{CH}_2$  stretches (\*) of the unreactive backbone around  $2926 \text{ cm}^{-1}$ .

In order to obtain the distinct charged channels, we explored to transform two end blocks PDMAi and PtBMA into positively and negatively charged moieties in a one-step reaction by

using trimethyloxonium tetrafluoroborate ((CH<sub>3</sub>)<sub>3</sub>O(BF<sub>4</sub>)), respectively (Figure 10.8a). Such one-step reaction was first performed in the homogeneous condition using dichloromethane as the solvent. Specifically, 0.1 g polymer was dissolved in 5 ml dichloromethane, and a certain amount of trimethyloxonium tetrafluoroborate (i.e molar ratio [(CH<sub>3</sub>)<sub>3</sub>O(BF<sub>4</sub>)]<sub>0</sub>/[-N(CH<sub>3</sub>)<sub>2</sub>]<sub>0</sub> = 1.5:1) was added into the mixture. The mixture was stirred for 3-4 days at room temperature. Afterwards, the polymer solution was precipitated into *n*-hexane and washed with H<sub>2</sub>O. The product was dried at 60 °C under vacuum for several days.

After post-functionalization in homogeneous solution, the characteristic peaks of *t*Bu groups (ca. 1391 cm<sup>-1</sup> and 1367 cm<sup>-1</sup>), N-CH<sub>2</sub> and N-CH<sub>3</sub> (ca. 2810 cm<sup>-1</sup> and 2760 cm<sup>-1</sup>) disappear while the stretching vibration of C=O at ca. 1722 cm<sup>-1</sup> broadens and shifts to ca. 1703 cm<sup>-1</sup>, attributed to quaternization of PDMAi and the formation of carboxylic groups (Figure 10.8b, blue curve). However, the post-functionalization of the membranes has to be performed under heterogeneous condition. Thus, the reaction with a similar condition (e.g. the same amount of reagent) was carried out in the heterogeneous condition, where the polymer powder was dispersed in the nonsolvent of methanol. In the FTIR spectrum, the intact signal of *t*Bu groups demonstrates that hydrolysis of *Pt*BMA did not occur while the disappearance of peaks from N-CH<sub>2</sub> and N-CH<sub>3</sub> confirms the success of quaternization of the PDMAi under such heterogeneous condition (Figure 10.8b, yellow curve).<sup>200-202</sup> Therefore the so-called “one-step” reaction with (CH<sub>3</sub>)<sub>3</sub>O(BF<sub>4</sub>) can only introduce the positively charged moieties rather than the positively/negatively charged moieties together in the heterogeneous condition. However, the hydrolysis of *Pt*BMA can be achieved with gaseous HCl without the disturbance of membrane structure. PDMAi block can be protonated with HCl due to tertiary amine groups. Therefore, it is possible to bring about the positively/negatively charged moieties into membrane via first quaternization of PDMAi with (CH<sub>3</sub>)<sub>3</sub>O(BF<sub>4</sub>) and subsequent hydrolysis of *Pt*BMA with gaseous HCl.

## 10.2 PS-*b*-P4VP Isoporous Membranes with Tunable Positively Charged Nanochannels

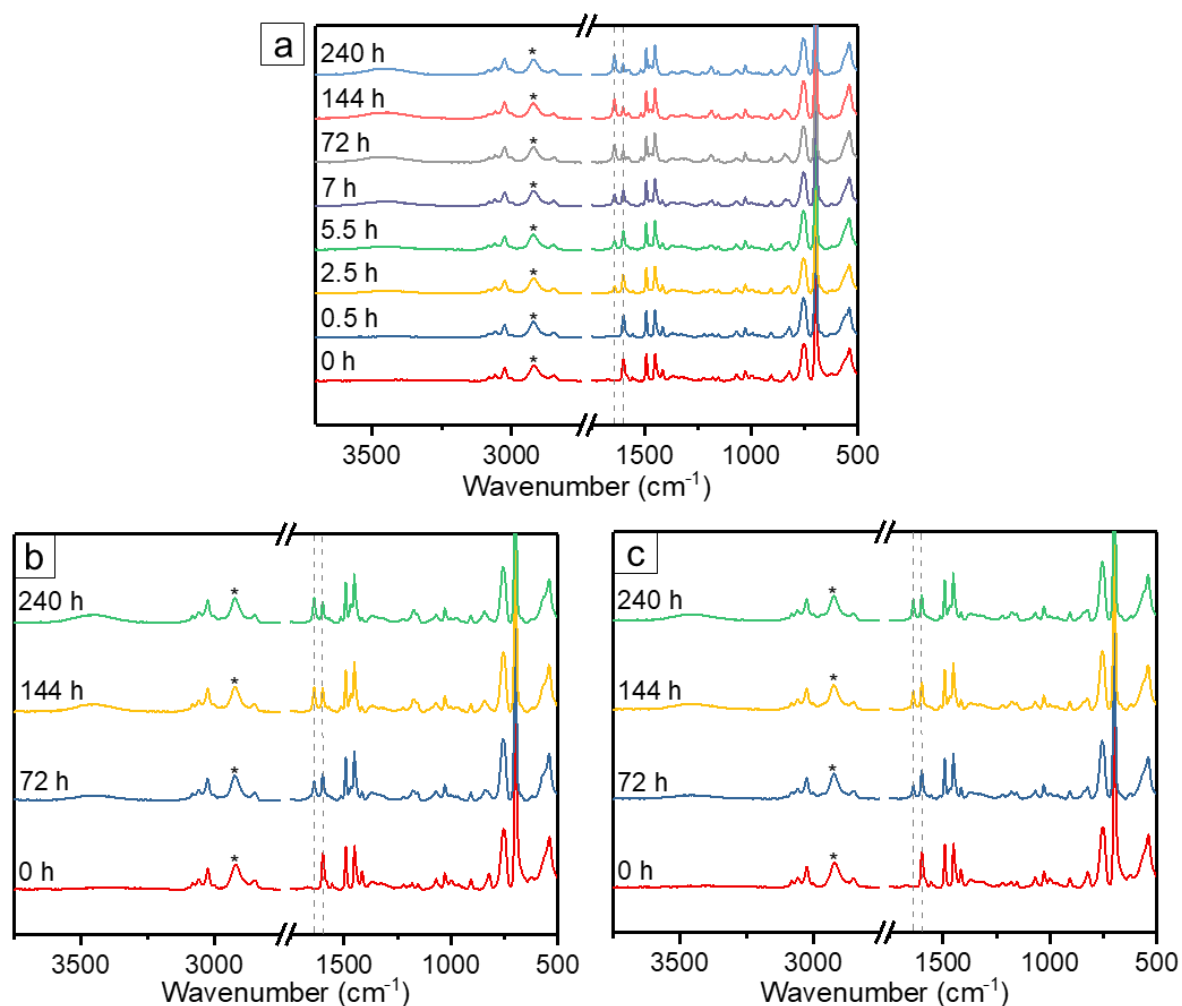


Figure 10.9. ATR-FTIR spectra: (a) the membranes quaternized with MeI as a function of time, (b) the membranes quaternized with EtI as a function of time, (c) the membranes quaternized with 1-PrI as a function of time. The relative intensities were normalized using the characteristic CH<sub>2</sub> stretching vibrations (\*) of the unreactive backbone around 2924 cm<sup>-1</sup>.

The pristine PS-*b*-P4VP membrane and a series of quaternized membranes were also analyzed by ATR-FTIR, as shown in Figure 10.9. The vibration peak from unquaternized 4-vinyl pyridine (4VP) groups decreases while the corresponding vibration peak from quaternized 4VP groups increases as a function of time, in agreement with the results of <sup>1</sup>H NMR.

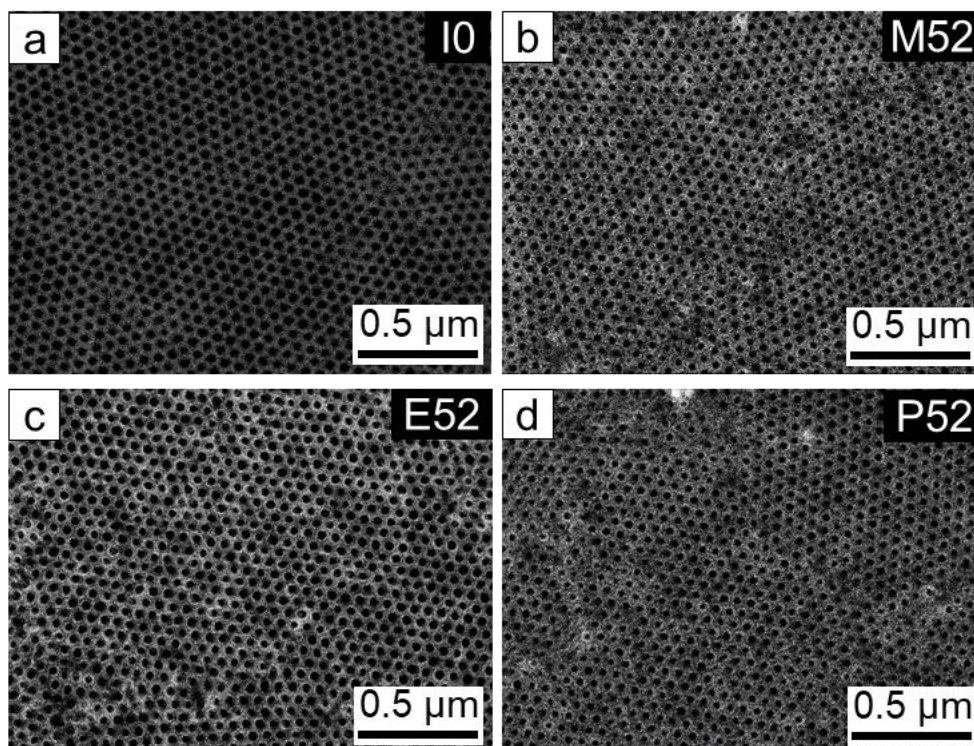


Figure 10.10. Back scattered electron (BSE) images of the top surface of membrane: (a) IO, (b) M52, (c) E52, (d) P52.

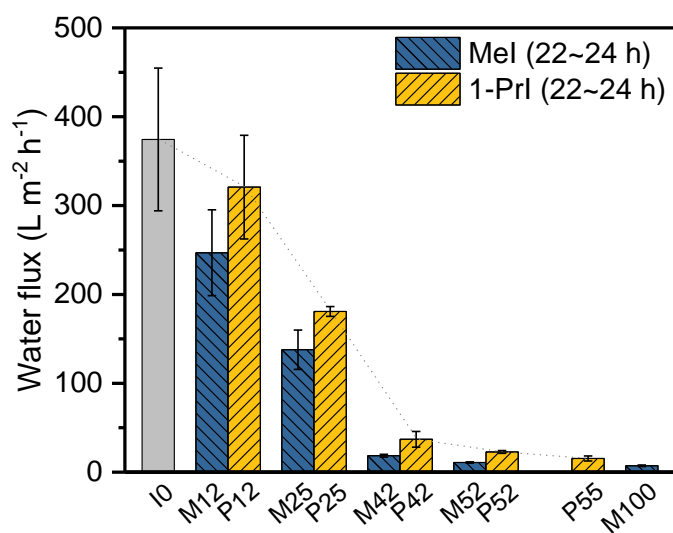


Figure 10.11. Water flux (average values of 22~24 h measurement) of the membranes having the series of different degrees of quaternization with MeI and 1-PrI, respectively.

Table 10.3. Comparison of the calculated lateral dimensions of five model organic molecules using MM2 force field energy minimization model and the reported Stokes diameters.

	MB+ (nm)	RB0 (nm)	OR- (nm)	NG3- (nm)	RG6- (nm)
Calculated sizes	1.1	1.0	1.3	1.8	1.9
Stokes diameters	0.886 <sup>143</sup>	0.912 <sup>203 a)</sup>	0.898 <sup>143</sup>	1.438 <sup>143</sup>	-- b)

<sup>a)</sup>The value was measured at 37 °C. <sup>b)</sup>No available reported data.

The calculation of the lateral dimensions of model organic molecules involved in this research was performed by using MM2 force field energy minimization model (in vacuum), while the retention measurements were carried out in the corresponding solute aqueous solutions. Therefore, we compared the calculated lateral dimensions of small molecules with the reported Stokes radius of the molecules. As shown in Table 10.3, the calculated values show a slight deviation compared to reported values. Based on the reported Stokes diameters, MB+, RB0 and OR- also exhibit a similar size.

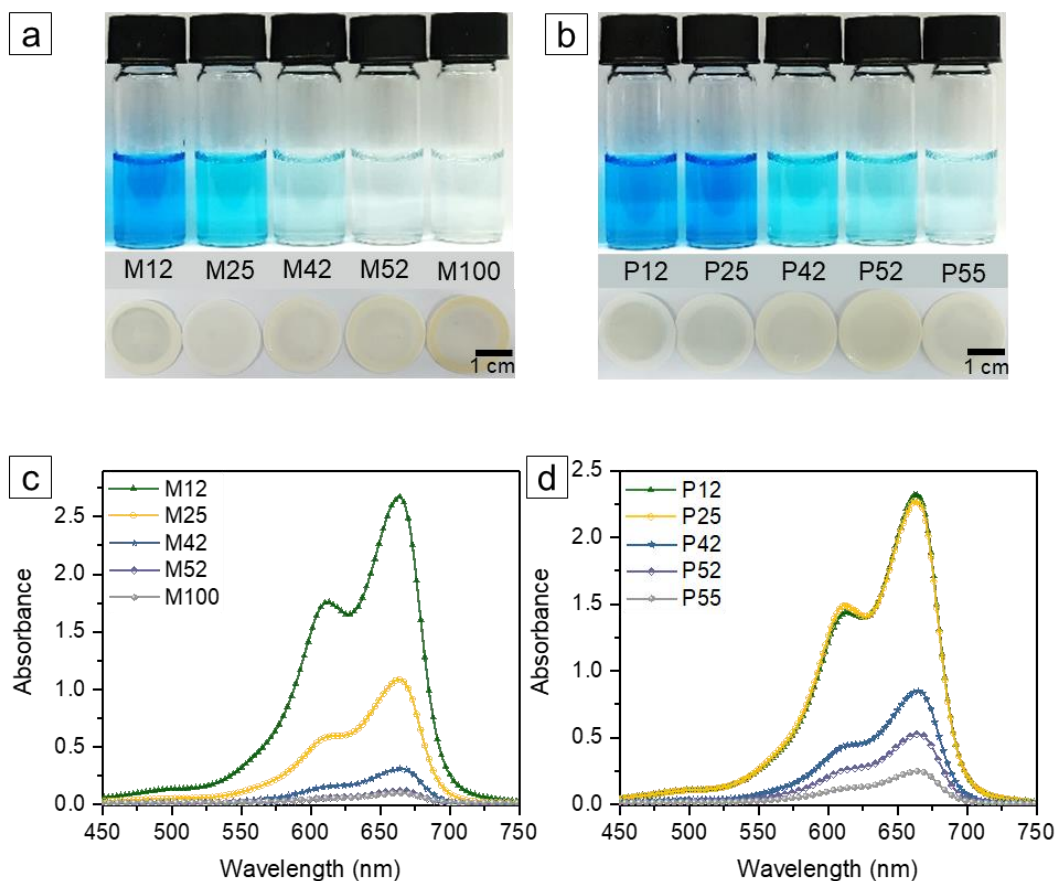


Figure 10.12. (a, b) The photography of the permeate solutions of the membranes having the series of different degrees of quaternization with MeI and 1-PrI, respectively, and the corresponding prepared membranes after MB rejection measurements with feed solution of 10 mg L<sup>-1</sup>. (c, d) UV-vis absorbance of the corresponding permeate solutions.

### 10.3 High-Performance Asymmetric Isoporous Nanocomposite Membranes with Chemically-Tailored Amphiphilic Negatively Charged Nanochannels

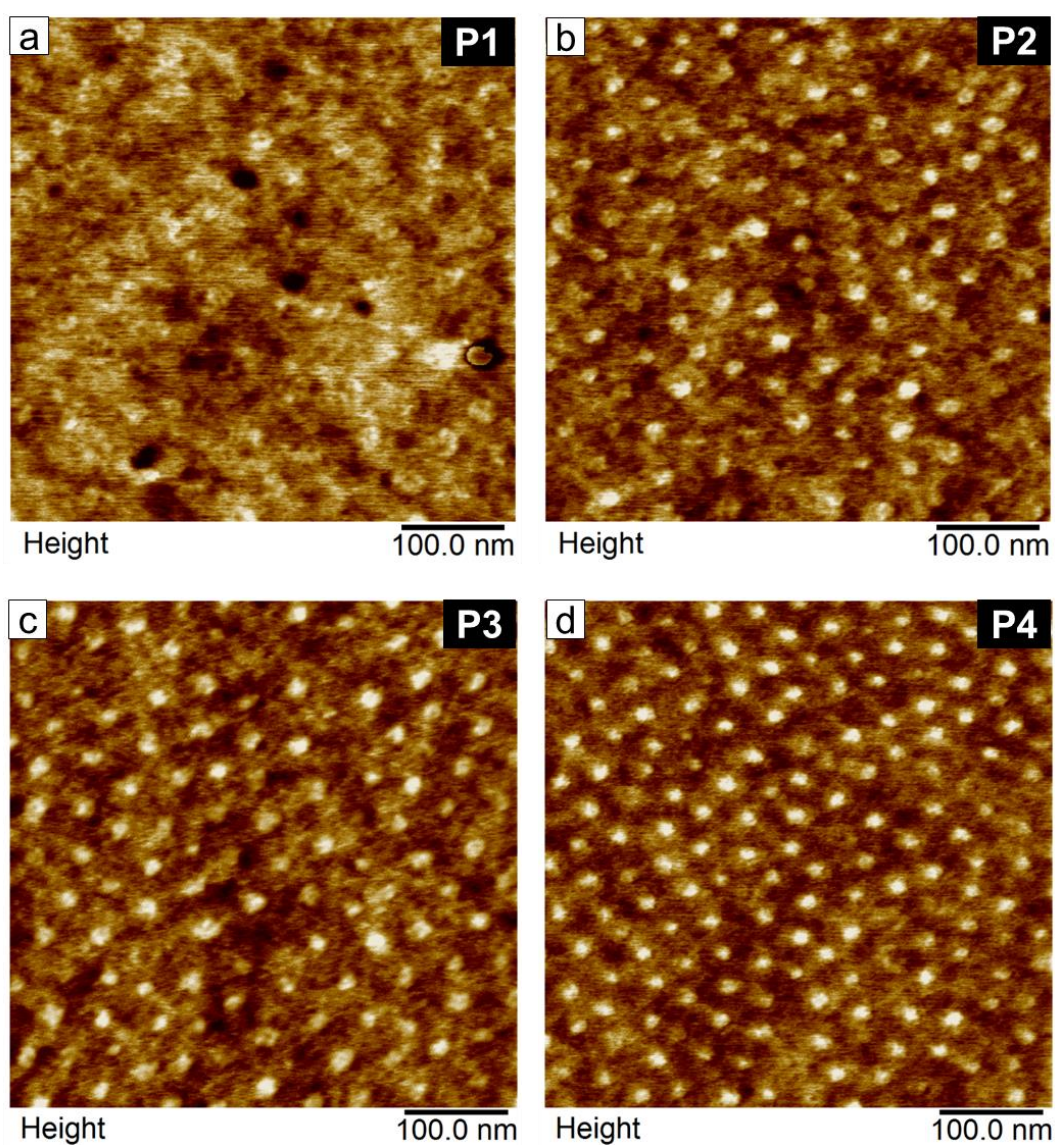


Figure 10.13. AFM height maps of the thin films of the polymers prepared by spin-coating procedure from CHCl<sub>3</sub> solutions: (a) P1, (b) P2, (c) P3 and (d) P4.

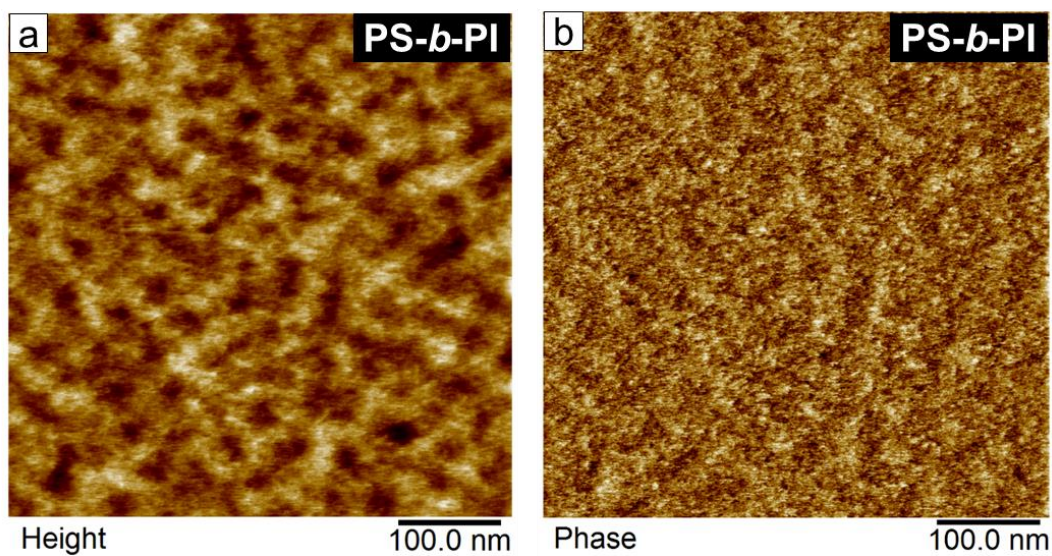


Figure 10.14. AFM maps of the thin films of PS-*b*-PI prepared by spin-coating procedure from CHCl<sub>3</sub> solutions: (a) height, (b) phase.

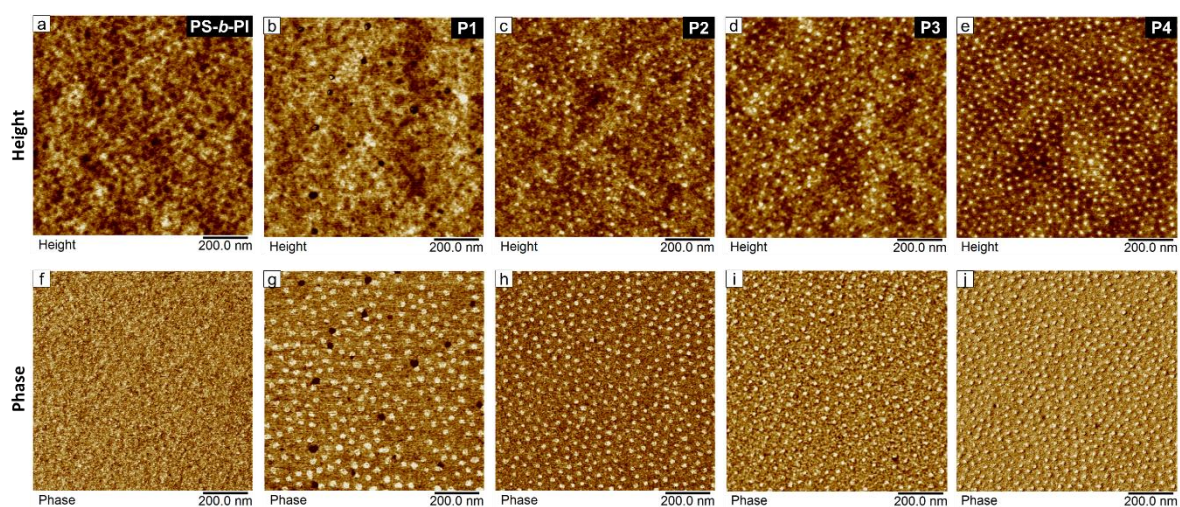


Figure 10.15. AFM height and phase maps with lower magnification (scale 1  $\mu\text{m}$ ) of the thin films of the polymers prepared by spin-coating procedure from CHCl<sub>3</sub> solutions: (a, f) PS-*b*-PI, (b, g) P1, (c, h) P2, (d, i) P3 and (e, j) P4.

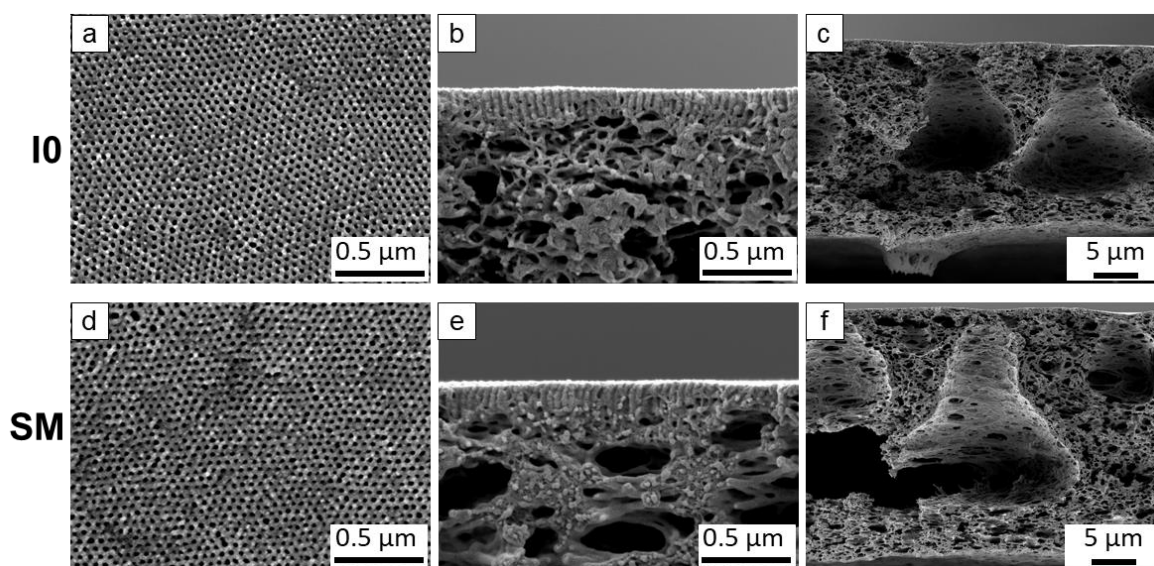


Figure 10.16. Comparison of membrane morphology determined by SEM of (a-c) the pristine membrane I0 and (d-f) the sulfonated membrane SM. Both were cast from 18 wt% solution with 8 wt% TiO<sub>2</sub> in THF/DMF/DOX 2/1/1, the evaporation time  $t = 15$  s.

Table 10.4. Performance comparison of the pristine membrane I0 and the sulfonated membrane SM, including water permeance, retention and adsorption of OR- and RG6-.

Membrane	Water permeance (L m <sup>-2</sup> h <sup>-1</sup> bar <sup>-1</sup> )	Retention ( $R$ , %)		Selectivity ( $\psi_{OR-/RG6-}$ )	Adsorption ( $\mu\text{g cm}^{-2}$ )	
		OR-	RG6-		OR-	RG6-
I0	159 ± 25	59 ± 6	64 ± 6	1.3	0	0
SM	74 ± 11	69 ± 2	94 ± 6	5.2	0	0

## 10.4 Chemically-Tailored Multifunctional Asymmetric Isoporous Triblock Quaterpolymer Membranes for Selective Transport

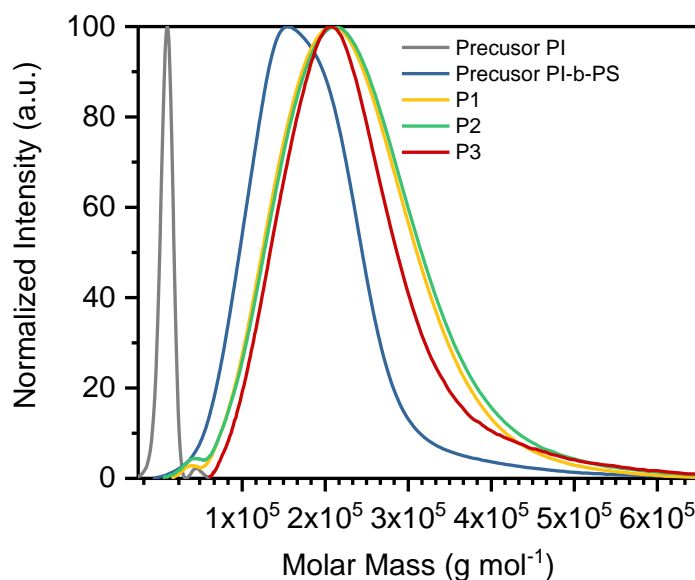


Figure 10.17. Molar mass distribution obtained by GPC for the precursor PI, the precursor PI-*b*-PS in THF, and triblock terpolymers P1, P2, P3 in DMAC/LiCl.

Figure 10.17 shows the GPC data for the precursors PI and PI-*b*-PS prepared by living anionic polymerization. The precursors PI and PI-*b*-PS possessed the narrow polydispersities, 1.02 and 1.22, respectively. The triblock terpolymer PI-*b*-PS-*b*-P4VP was not soluble in the polar solvents, *e.g.* DMF and DMAC, because of the hydrophobic PI-*b*-PS segment. Using THF or CHCl<sub>3</sub> as the solvent for GPC, the signal of P4VP block cannot be monitored. In this case, we cannot obtain the molecular characteristics of the prepared PI-*b*-PS-*b*-P4VP. After thiol-ene click chemistry, the PI block was converted into hydroxylated P(HTMB-*r*-I), soluble in the polar solvent, *i.e.* DMAc. Figure 10.17 displays the GPC data of the triblock terpolymers P1, P2, P3 with different degree of hydroxylation. All the dispersity indices are smaller than 1.25. Overall, the results prove the good control over the living anionic polymerization as well as the thiol-ene click reaction.

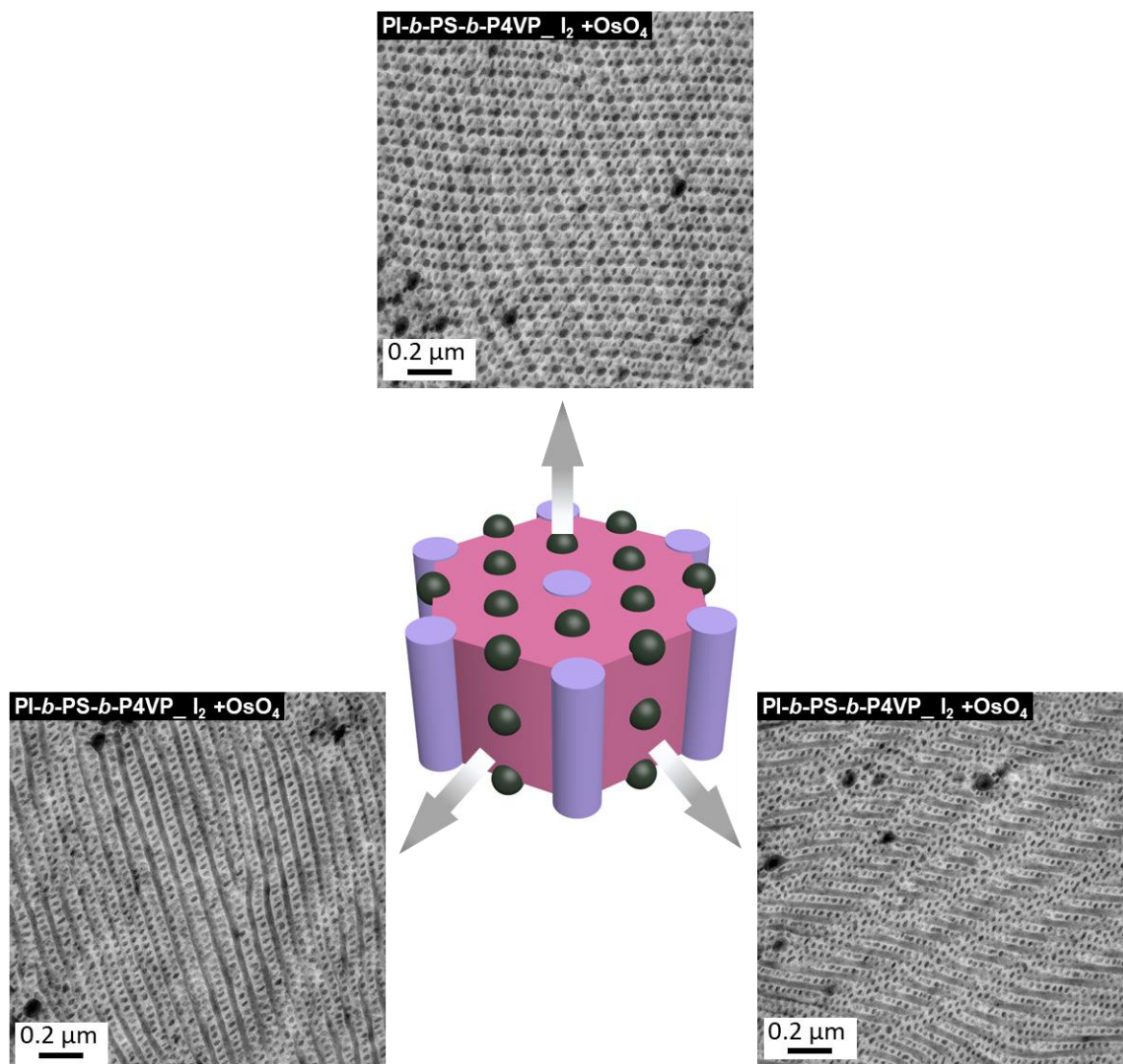


Figure 10.18. TEM images of PI-*b*-PS-*b*-P4VP films double stained with I<sub>2</sub> and OsO<sub>4</sub>. Films were cast from polymer solution in CHCl<sub>3</sub>/DMF (95/5 v/v). All the images demonstrate the cylinder-sphere three-phase morphology of P4VP cylinder and PI sphere in the PS matrix.

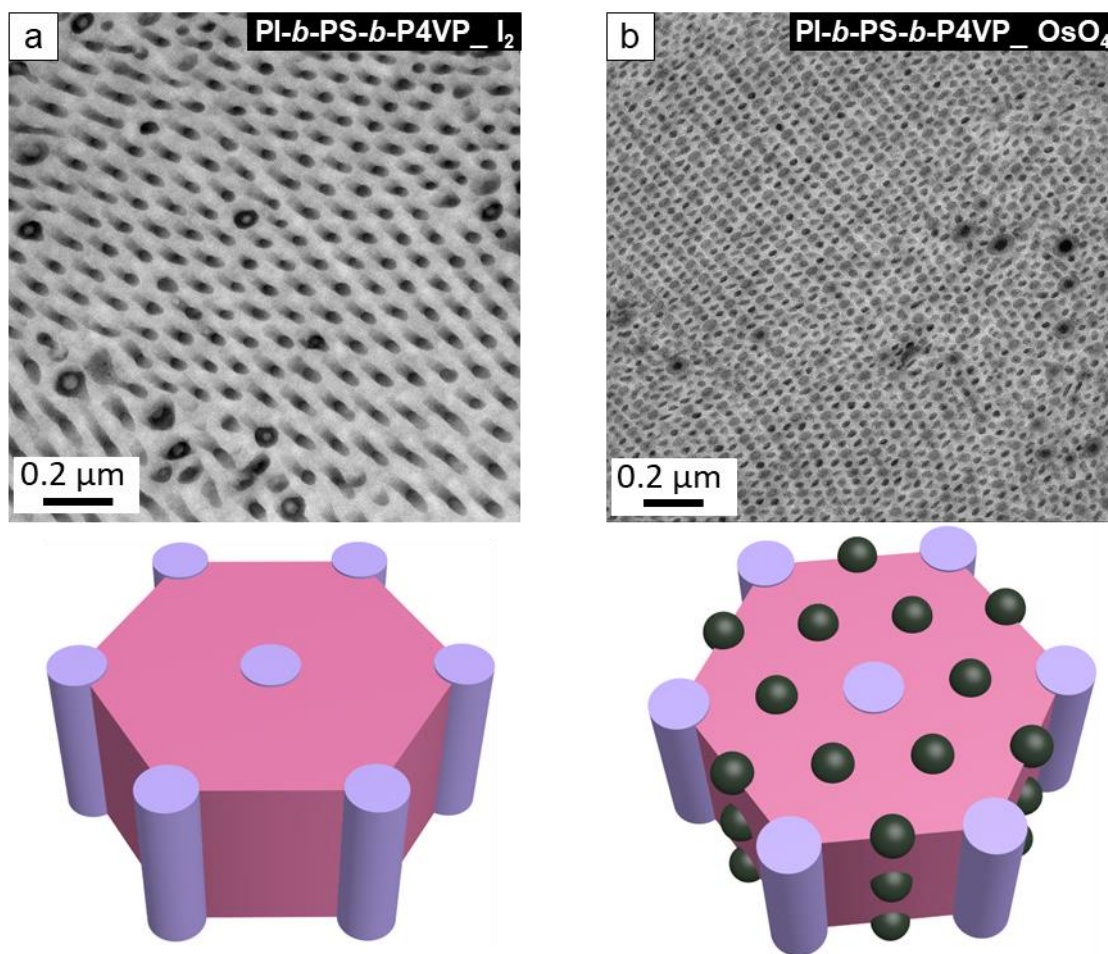


Figure 10.19. TEM images of PI-*b*-PS-*b*-P4VP films: (a) stained with I<sub>2</sub> (only selective for P4VP (dark domain)), (b) stained with OsO<sub>4</sub> (strong selective for PI (dark domain) and weak selective P4VP (gray domain)). Films were cast from polymer solutions in CHCl<sub>3</sub>/DMF (95/5 v/v). All the images also demonstrate the cylinder-sphere three-phase morphology of P4VP cylinder and PI sphere in the PS matrix.

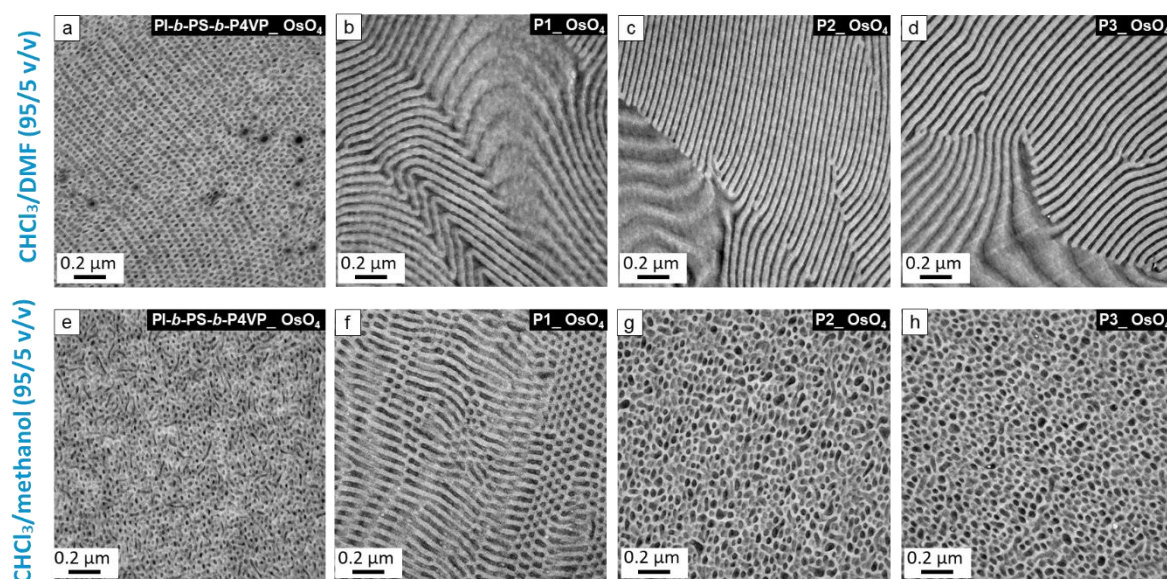


Figure 10.20. TEM images of (a, e) PI-*b*-PS-*b*-P4VP, (b, f) P1, (c, g) P2, (d, h) P3 films stained with OsO<sub>4</sub>, which is selective for both P4VP and P(HTMB-*r*-I). Films were cast from polymer solutions in CHCl<sub>3</sub>/methanol (95/5 v/v) and CHCl<sub>3</sub>/DMF (95/5 v/v), respectively.

As OsO<sub>4</sub> can stain both PI and P4VP blocks in the PI-*b*-PS-*b*-P4VP film (Figure 10.18, Figure 10.19b), Figure 10.20 depicts that the OsO<sub>4</sub> stained films exhibit the similar results as these of films double stained with I<sub>2</sub> and OsO<sub>4</sub> (Figure 6.4).

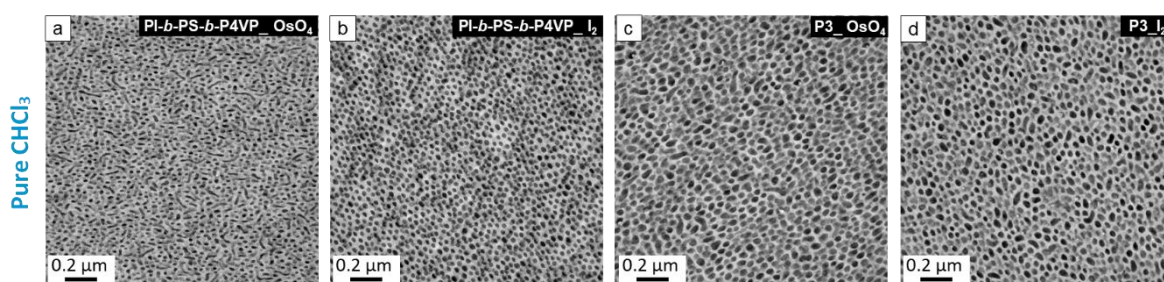


Figure 10.21. TEM images of films cast from PI-*b*-PS-*b*-P4VP and P3 solutions in pure CHCl<sub>3</sub>: (a) PI-*b*-PS-*b*-P4VP film stained with OsO<sub>4</sub> (strong selective for PI (dark domain) and weak selective P4VP (gray domain)), (b) PI-*b*-PS-*b*-P4VP film stained with I<sub>2</sub> (only selective for P4VP (dark domain)), (c) P3 film stained with OsO<sub>4</sub> (strong selective for PI (dark domain) and

weak selective P4VP (gray domain)), (d) P3 film stained with I<sub>2</sub> (only selective for P4VP (dark domain)).

Table 10.5. The concentrations of feed ( $C_f$ ), permeate ( $C_p$ ), retentate ( $C_r$ ) and the calculated retention ( $R_0$ ) employed in single-solute retention measurements.

Membrane type	Solute	Replica no.	Permeate solution <sup>a)</sup>				Average retention ( $R_0$ ,%)
			$C_f$ (mg L <sup>-1</sup> )	$C_p$ (mg L <sup>-1</sup> )	$C_r$ (mg L <sup>-1</sup> )	$R_0$ (%)	
IO	MB+	1	31.59	32.55	32.49	0	0
		2	32.58	32.82	32.49	0	
		3	32.25	32.19	32.22	0	
MM		1	30.72	1.465	33.67	95.45	95.3 ± 0.1
		2	32.16	1.536	33.21	95.30	
		3	33.15	1.638	35.52	95.23	
IO	RB0	1	35.7	36.94	37.94	0	0
		2	34.84	35.22	35.65	0	
		3	35.09	35.5	35.66	0	
MM		1	36.63	36.77	36.71	0	0
		2	36.05	36.53	36.82	0	
		3	34.65	34.90	35.14	0	
IO	OR-	1	34.87	34.35	34.82	1.42	2.0 ± 0.6
		2	34.85	34.04	34.98	2.51	
		3	35.27	34.47	35.23	2.23	
MM		1	34.63	34.55	35.95	2.10	2.83 ± 1.1
		2	35.5	34.54	35.18	2.26	
		3	35.01	33.75	35.40	4.13	
IO	OR-	1	34.87	34.35	34.82	1.42	2.0 ± 0.6
		2	34.85	34.04	34.98	2.51	
		3	35.27	34.47	35.23	2.23	
PM		1	33.80	21.37	35.47	38.30	29.3 ± 9.1
		2	34.48	22.11	34.41	35.81	
		3	34.77	26.70	34.37	22.76	
	4	34.42	27.38	34.3	20.31		
IO	NG3-	1	84.24	83.28	85.20	1.70	1.4 ± 0.2
		2	85.11	83.62	84.15	1.19	

		3	83.28	82.58	84.15	1.36	
PM		1	82.05	3.31	83.89	96.01	95.2 ± 1.2
		2	82.75	3.48	84.85	95.85	
		3	83.89	5.23	87.73	93.90	
IO	RG6-	1	135.9	79.04	176.4	49.38	55.0 ± 12.8
		2	139.0	51.11	199.1	69.77	
		3	135.5	77.25	150.6	46.00	
PM	RG6-	1	136.7	1.682	139.5	98.78	98.9 ± 0.6
		2	139.8	0.544	142.4	99.61	
		3	139.7	2.391	140.0	98.29	

a) In the case of pristine membrane IO, the second permeate was used to do the calculation. For positively charged membrane MM and negatively charged membrane PM, the third permeate was used.

Table 10.6. The concentrations of feed ( $C_f$ ), permeate ( $C_p$ ), retentate ( $C_r$ ) and the calculated retention ( $R_0$ ) employed in mixed-solute retention measurements.

Membrane type	Solute	Replica no.	Permeate solution <sup>a)</sup>								Average retention ( $R_0$ , %)	
			$C_f$ (mg L <sup>-1</sup> )		$C_p$ (mg L <sup>-1</sup> )		$C_r$ (mg L <sup>-1</sup> )		$R_0$ (%)		MB+	RB0
IO	MB+/RB0	1	14.51	18.6	14.48	19.69	14.15	20.47	0	0	0	0
		2	14.31	21.38	14.11	22.28	13.69	22.76	0	0		
		3	14.27	21.89	14.18	22.70	14.02	23.50	0	0		
MM	MB+/RB0	1	14.65	19.66	0.3	16.68	15.47	19.93	98.01	15.74	97.0 ± 0.9	15.0 ± 0.6
		2	14.59	18.97	0.535	16.34	15.54	19.45	96.45	14.94		
		3	14.57	18.87	0.522	16.35	15.52	19.35	96.53	14.44		
IO	OR-/NG3-	1	17.22	41.16	16.97	39.93	17.32	41.86	1.74	3.81	2.2 ± 0.3	4.5 ± 0.6
		2	17.30	41.51	16.70	39.23	16.95	40.81	2.48	4.69		
		3	17.22	41.24	16.68	39.06	16.91	40.89	2.26	4.88		
PM	OR-/NG3-	1	17.29	41.68	11.91	1.311	17.7	44.64	31.92	96.96	33.1 ± 10.1	98.5 ± 1.5
		2	17.15	42.90	9.46	0.696	16.53	45.82	43.82	98.43		
		3	17.56	40.72	13.44	0	17.64	44.94	23.64	100		

a) In the case of pristine membrane I0, the second permeate was used to do the calculation. For positively charged membrane MM and negatively charged membrane PM, the third permeate was used.

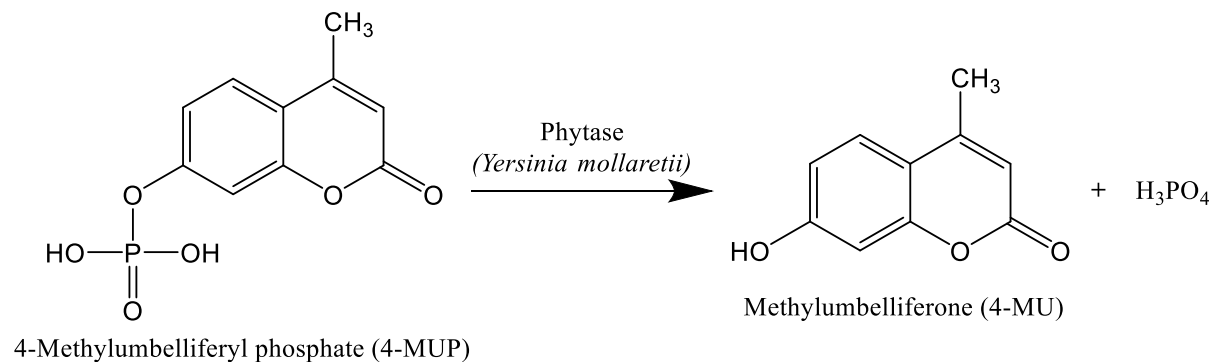
Table 10.7. Performance comparison among various membranes for charge- and charge/size-based separation of small molecules.

Membrane type	Small molecules	Molecular weight (g mol <sup>-1</sup> )	Molecular charge	Selectivity_diffusion <sup>a)</sup>	Selectivity_filtration		Water flux (L m <sup>-2</sup> h <sup>-1</sup> bar <sup>-1</sup> )	Reference
					Single solutes	Mixed solutes		
NP-Den hybrid membrane	Rhodamine 6G	479.02	+	11	--	--	--	126
	Calcein	622.53	-4					
Self-assembled polyelectrolyte deposited PCTE	Rhodamine 6G	479.02	+	3.5	--	--	--	127
	Calcein	622.53	-4					
Cationic dendrimer deposited PCTE	Calcein	622.53	-4	10	--	--	--	128
	Rhodamine 6G	479.02	+					
Amphiphilic random copolymer membrane	Riboflavin	376.36	0	263	8.4 <sup>b)</sup>	19.2 <sup>b)</sup>	4.2	180
	Acid blue 45	474.33	-2					
MM	Riboflavin	376.36	0	--	21.3	28.3	11.0	
	Methylene blue	319.85	+					
PM	Orange II	350.32	-	--	14.7	44.6	9.5	This study
	Naphthol green B	878.45	-3					
	Orange II	350.32	-	--	64.3	--		
	Reactive green 19	1418.93	-6					

a) The selectivity based on the diffusion test were determined using a single solute system. b)

The selectivities are calculated using the reported retention values.

## 10.5 Potential of Integral Aysmmetric Isoporous Membrane towards Enzymatic Membrane Reactors



Scheme 10.2. Schematic illustration of the phytase hydrolytic reaction using 4-methylumbelliferyl phosphate (4-MUP) as the substrate. The product methylumbelliferone (4-MU) are fluorescent which can be measured with excitation at 360 nm and emission at 465 nm.

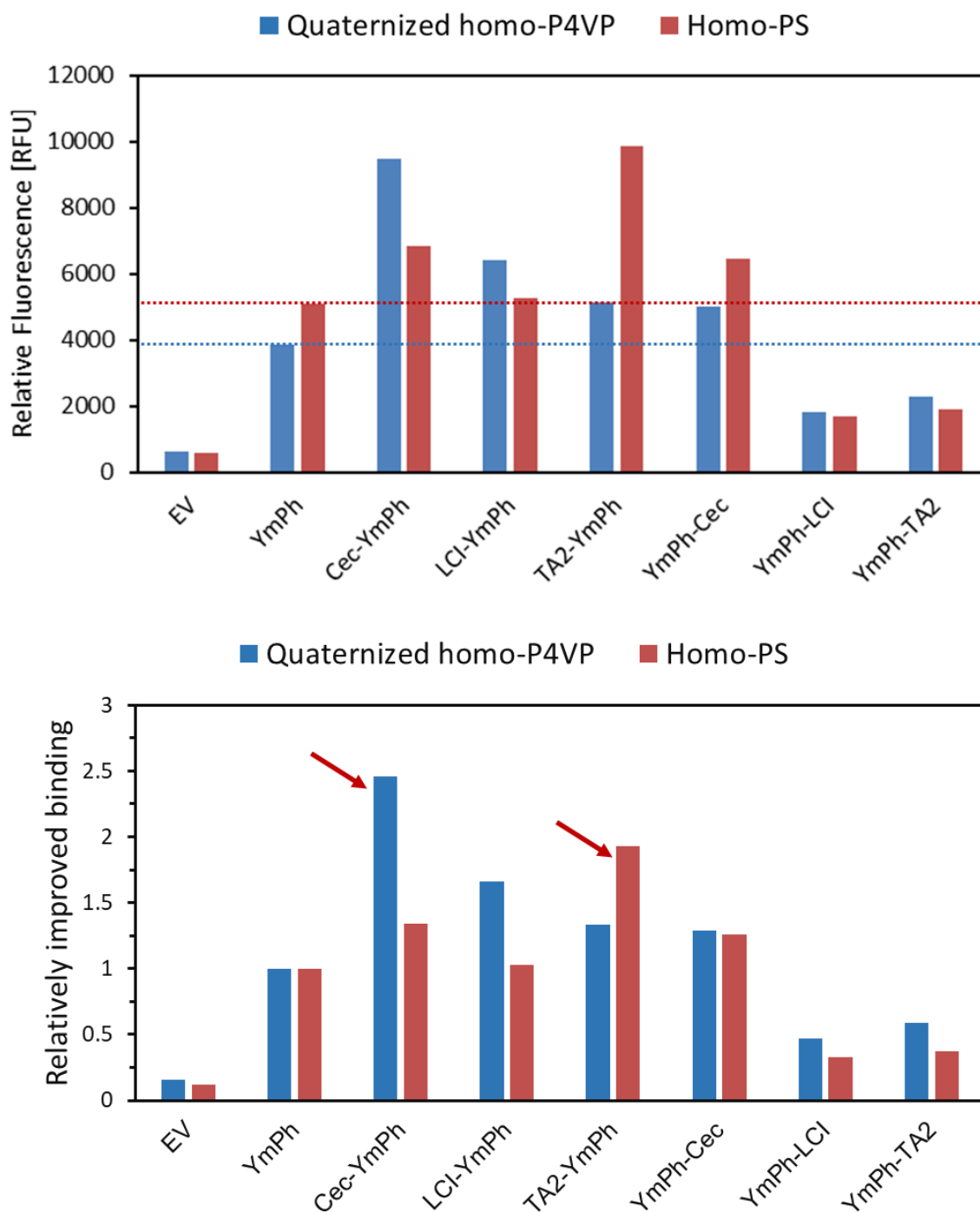


Figure 10.22. (a) Comparison of the fluorescence intensity of the product 4-MU from enzymatic reaction with different immobilized YmPh-AP fusion constructs on the dense films of homo-PS and homo-QP4VP with 14 h MeI quaternization. (b) Relative improvement of YmPh-AP binding calculated relative to the wild type YmPh (YmPh WT).

The binding of YmPh-AP fusion constructs was evaluated by measuring the fluorescence of the hydrolysed product 4-MU. All the experiments were carried out at the same conditions, e.g., 50  $\mu$ l enzyme containing cell free extracts, support polymer samples with 6 mm diameters, 50  $\mu$ l 0.5 mM 4-MUP solution (250 mM sodium acetate, pH 5.5, 1 mM calcium chloride, 0.01 % Tween-20). The detection of fluorescence was test after 10 min enzymatic reaction. Basically, a stronger fluorescence intensity implied a higher binding of the YmPh-AP fusion proteins.

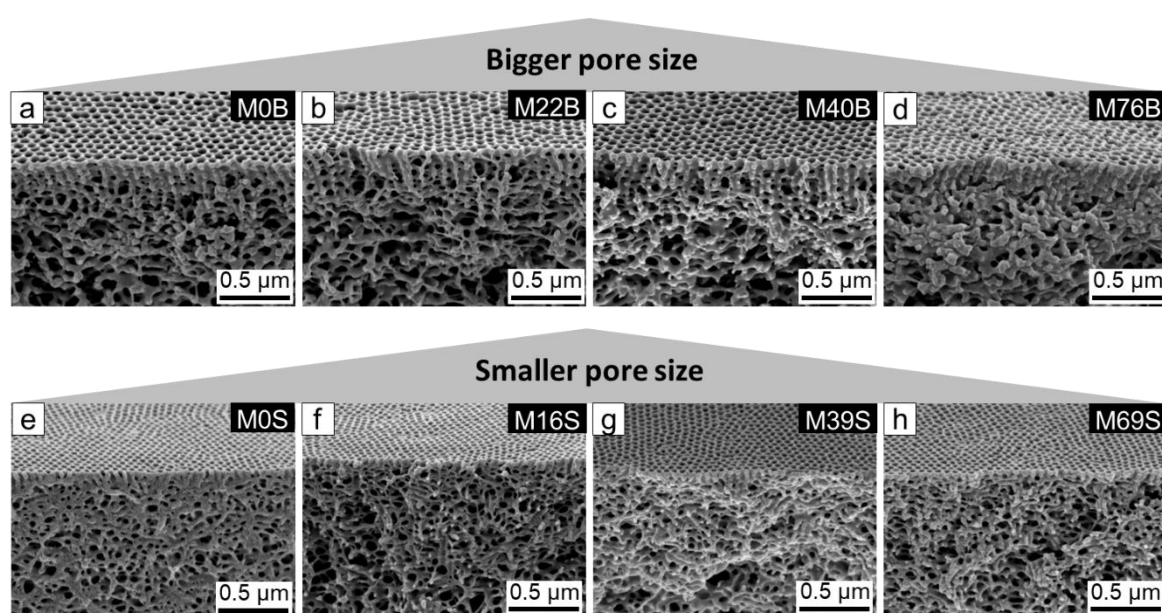


Figure 10.23. SEM images of the cross sections of two series of membranes with different degree of quaternization: (a-d) M0B, M22B, M40B and M76B, (e-h) M0S, M16S, M39S and M69S.

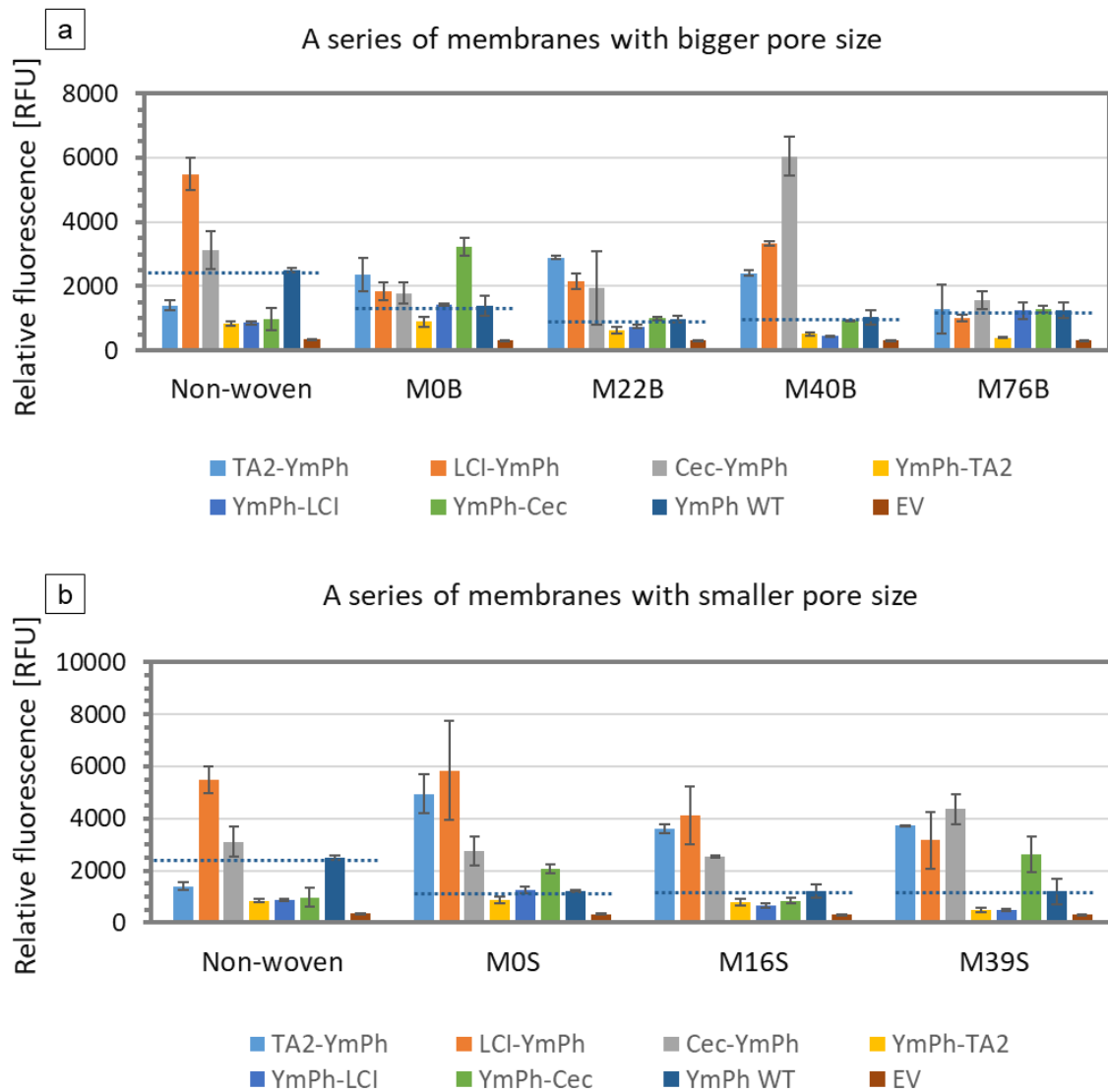


Figure 10.24. Comparison of the fluorescence intensity of the product 4-MU from enzymatic reaction with different immobilized YmPh-AP fusion constructs on two series of PS-*b*-P4VP derived membranes: (a) bigger pore size, (b) smaller pore size.

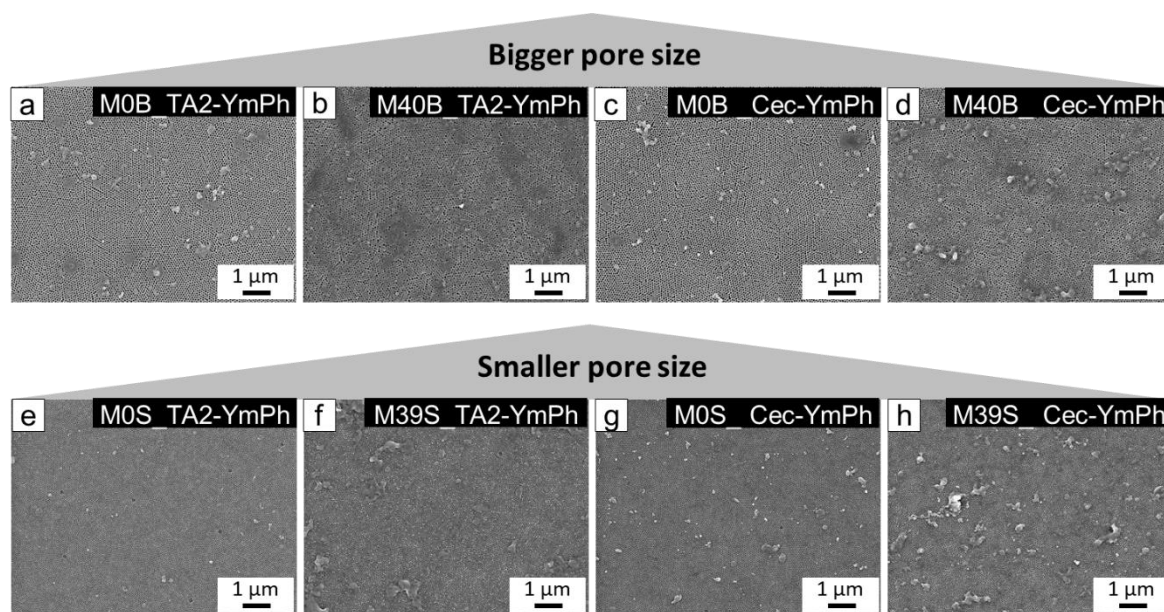


Figure 10.25. SEM images of the top surfaces of the representative membranes with the immobilized YmPh-AP fusion proteins: (a) M0B\_TA2-YmPh, (b) M40B\_TA2-YmPh, (c) M0B\_Cec-YmPh, (d) M40B\_Cec-YmPh, (e) M0S\_TA2-YmPh, (f) M39S\_TA2-YmPh, (g) M0S\_Cec-YmPh, (h) M39S\_Cec-YmPh.

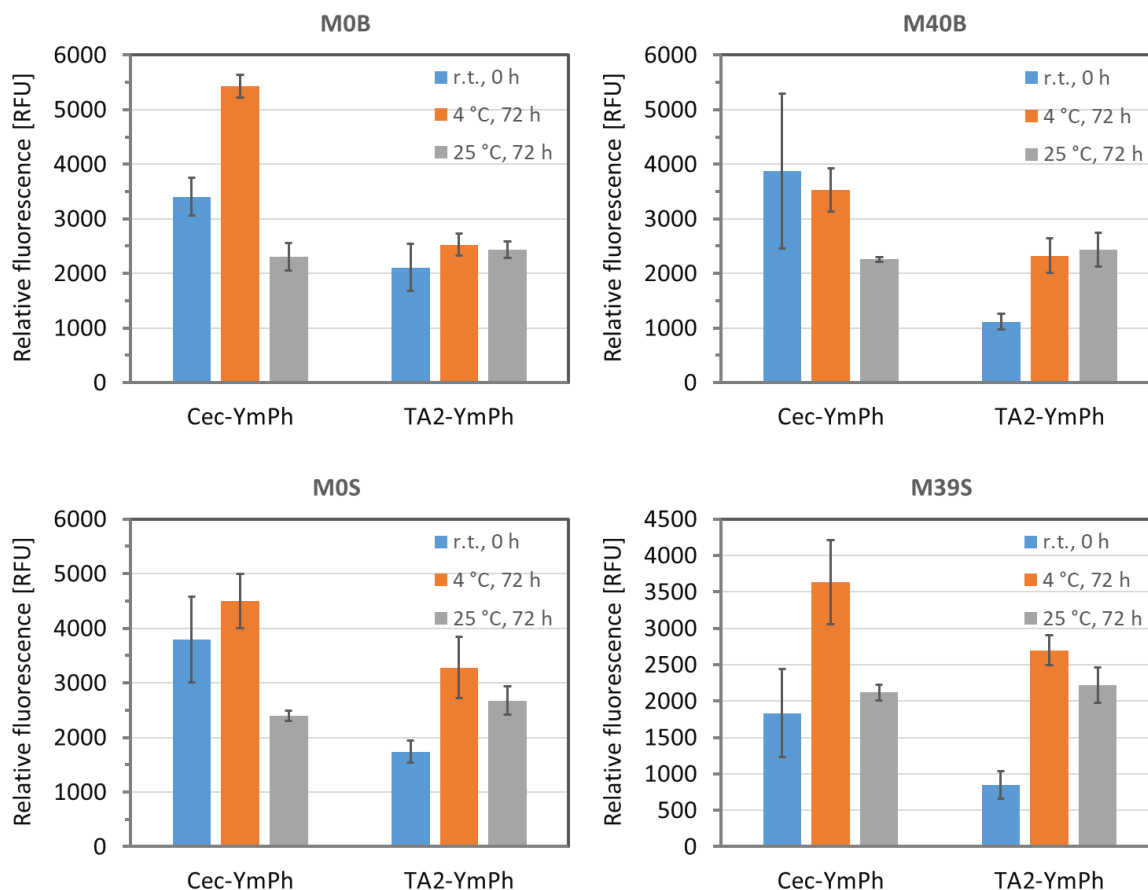


Figure 10.26. Stability of the immobilized TA2-YmPh and Cec-YmPh on the representative membranes was roughly evaluated by comparison of the conversion of substrates 4-MUP before and after storage at 4 °C or 25 °C for 3 days, respectively: (a) M0B, (b) M40B, (c) M0S and (d) M39S.

## 10.6 Toxicity of Chemicals

Table 10.8. List of chemicals with GHS symbol, H- and P-data.

Substance	GHS symbol	Hazard Statement	Precautionary statement
Tetrahydrofuran	GHS02, GHS07, GHS12	H225, H319, H335, H351, EUH019	P210, P240, P305 + P351 + P338, P308 + P313, P403 + 233
1,4-dioxane	GHS02, GHS07, GHS08	H225, H319, H335, H351, EUH019, EUH066	P210, P233, P240, P281, P304 + P340, P308 + P313, P403 + P235
<i>N,N</i> -dimethylformamide	GHS02, GHS07, GHS08	H360D, H226, H312+ H332, H319	P201, P210, P302+ P352, P305 + P351 + P338, P308 + P313

Isoporous Block Copolymer Membranes with Charged Nanochannels

Chloroform	GHS02, GHS07, GHS09	H302, H332, H315, H319, H351, H361d H336, H373	P261, P281, P305+P351+P338
Diethyl ether	GHS02, GHS07	H224, H302, H336	P210, P261
Dimethylacetamide	GHS07, GHS08	H312+H332-H319, H360D	P201-P280, P305 + P351 + P338, P308 + P313
Methanol	GHS02, GHS06, GHS08	H225, H301, H311, H331, H370	P210, P233, P240, P241, P242, P243, P260, P264, P270, P271, P280, P301+330+331, P310, P302+352, P312, P303+361+353, P304+340, P311, P305+351+338, P307+311, P337+313, P361, P363, P370+378, P403+233
Dichloromethane	GHS07, GHS08	H315-H319-H335-H336-H351-H373	P261-P281-P305 + P351 + P338
N-pentane	GHS02, GHS07, GHS08, GHS09	H225, H304, H336, H411	P210, P261, P273, P301+310, P331
2-Mercaptoethanol	GHS05, GHS06, GHS09	H301, H310, H315, H317, H318, H330, H410	P260, P273, P280, P284, P301+310, P302+350
Calcium hydride	GHS02	H260	P223-P231 + P232, P370 + P378-P422
Ethylaluminium dichloride	GHS02, GHS05, GHS07, GHS08, GHS09	H225, H250, H261, H304, H314, H336, H361f, H373, H411, EUH014	P210, P231 + P232, P280, P301 + P310, P302 + P334, P303 + P361 + P353, P304 + P340 + P310, P305 + P351 + P338, P331, P422
Sec-butyl lithium	GHS02, GHS05, GHS07, GHS08, GHS09	H225, H250, H260, H304, H314, H336, H410	P210, P222, P223, P231 + P232, P370 + P378, P422
Styrene	GHS02, GHS07	H226-H315-H319 H332	P305 + P351 + P338
4-Vinyl pyridine	GHS02, GHS05, GHS06	H226-H301-H314 H317	P280-P301 + P310 P305 + P351 + P338, P310
<i>Tert</i> -butyl methacrylate	GHS02, GHS07	H319-H226-H315	P210, P233, P240, P241, P242, P243, P261, P264, P271, P280, P302+P352, P303+P361+P353, P304+P340, P305+P351+P338, P312, P321, P332+P313, P337+P313, P362, P370+P378, P403+P233, P403+P235, P405, P501
Isoprene	GHS02, GHS08	H224, H341, H350, H412	P202, P210, P280,

			P303+P361+P353, P308+P313, P273
Di-n-butylmagnesium	GHS02,GHS05, GHS07,GHS08, GHS09	H224-H250-H260-H302- H304-H314-H336-H361f- H373-H412-H225-H410	P210-P231+P232-P280- P305+P351+P338-P370+P378-- P422
n-Butyl lithium	GHS02,GHS05, GHS07,GHS08, GHS09	H225-H250-H261-H304- H314-H336-H361f-H373- H411-H260-H361d- H410-H252-H318-H332- H401-H361	P210-P222-P231+P232-P261-P273- P422-P223-P370+P378-P280- P301+P310-P302+P334- P303+P361+P353- P304+P340+P310- P305+P351+P338-P331-P201- P301+P310a-P405-P422a-P501a- P262
<i>p</i> -Toluene sulfonyl chloride	GHS05	H314-H315-H318	P260h-P301+P330+P331- P303+P361+P353-P405-P501a- P280-P305+P351+P338
Methyl 2-bromopropionate	GHS07,GHS02, GHS05	H318-H226-H314-H335	P210, P233, P240, P241, P242, P243, P260, P261, P264, P271, P280, P301+P330+P331, P303+P361+P353, P304+P340, P305+P351+P338, P310, P312, P321, P363, P370+P378, P403+P233, P403+P235, P405, P501
<i>N,N,N',N'',N'''</i> -pentamethyldiethylenetriamine	GHS05, GHS06, GHS07	H302, H311, H314	P280, P305+351+338, P310
Copper(I) chloride	GHS07, GHS09	H302, H400, H410	P264, P270, P273, P301+P312, P330, P391, P501
Copper(I) bromide	GHS07	H315-H319-H335	P261-P305 + P351 + P338
Aluminum oxide	GHS07, GHS08	H335, H370, H372	P260, P261, P264, P270, P271, P304+P340, P307+P311, P312, P314, P321, P403+P233, P405, P501
2,2-Dimethoxy-2-phenylacetophenone	GHS07, GHS08, GHS09	H302, H373, H400, H410, H412	P260, P264, P270, P273, P301+P312, P314, P330, P391, P501
Methyl iodide	GHS06, GHS08	H301, H312, H315, H331, H335, H351	P261, P280, P301+P310, P311
Ethyl iodide	GHS07, GHS08	H302, H315, H317, H319, H334, H335	P261, P280, P305+P351+P338, P342+P311
1-Propyl iodide	GHS03, GHS07	H226, H302, H315,	P261, P305+P351+P338

Isoporous Block Copolymer Membranes with Charged Nanochannels

		H319, H332, H335	
1,3-Propane sultone	GHS07, GHS08	H302, H312, H350	P201, P202, P264, P270, P280, P281, P301+P312, P302+P352, P308+P313, P312, P322, P330, P363, P405, P501
Trimethyloxonium tetrafluoroborate	GHS05	H314	P260, P264, P280, P301+P330+P331, P303+P361+P353, P304+P340, P305+P351+P338, P310, P321, P363, P405, P501
Methylene blue	GHS05, GHS07	H302, H318	P264, P270, P280, P301+P312, P305+P351+P338, P310, P330, P501
Riboflavin	-	-	-
Orange II	GHS07	H372-H412	P260-P264-P270-P273-P314-P501
Naphthol green B	-	-	-
Reactive green 19	GHS07	H319	P305+P351+P338
Titanium(IV) isopropoxide	GHS02, GHS05, GHS07	H226, H318, H319, H336	P210, P233, P240, P241, P242, P243, P261, P264, P271, P280, P303+P361+P353, P304+P340, P305+P351+P338, P310, P312, P337+P313, P370+P378, P403+P233, P403+P235, P405, P501
poly(ethylene glycol)	-	-	-
Magnesium acetate	-	-	-
Hydrochloric acid	GHS05, GHS07	H314, H335	P261, P280, P305+P351+P338, P310
Sodium hydroxide	GHS05	H314	P280, P305+P351+P338, P310

## **Chapter 11 Acknowledgement**

I express my best and heartiest gratitude to Prof. Dr. Volker Abetz for his meticulous supervision and eternal support during my PhD study. It is a great honour for me to enter the world of “Block Copolymer Membranes” under his guidance. I benefited greatly from his long standing experience and was truly influenced by his passion and persistence in science. These have helped me to perceive the questions in a different perspective and bigger picture, and also shaped me all round to be a scientist. The scientific discussions with him were always fruitful and inspiring, and in most cases opened up new dimensions in my work. Every moment of the discussions with him was wonderful and delightful, which comforted and motivated me in front of the challenging work. Without his valuable ideas and industrious input and efforts, it is not possible to achieve the ultimate success of my research goals. I am also very much thankful further to him for external collaborative study to exploit another new potential of my work, which made my PhD work more exciting.

I am truly grateful to Dr. Md. Mushfequr Rahman for his tremendous care and continuous support and inputs in all activities throughout my PhD study. The daily scientific discussions with him were always positive and highly motivating. He always showed lots of passion and patience in teaching and hands-on assistance in the lab even very minute things which were definitely an enormous help in my work. I show my heartfelt gratitude to Clarissa Abetz for her persistent efforts in the whole morphological investigation throughout my work. I really appreciate her kindness and lots of valuable discussion and ideas about the analysis of the complicated morphologies. Her diligence and hard work have resulted in the discovery of very amazing morphologies. It is my great pleasure to work with experienced and knowledgeable person like her.

My sincere thanks go also to Anke-Lisa Höhme, Dr. Evgeni Sperling and Dr. Erik Schneider for their tiresome efforts in conducting the SEM, TEM and AFM measurements. I am truly

thankful to Barbara Bajer for her relentless efforts in the solute adsorption and retention measurements. I would like to thank Brigitte Lademann for her technical support in the living anionic polymerization, and also Dr. Sofia Rangou and Ivonne Ternes for their synthesis of some PS-*b*-P4VP polymers. Many thanks to Silvio Neumann, Ivonne Ternes, Dr. Thomas Emmeler and Maren Brinkmann for their efforts in conducting all the NMR, TGA, DSC and GPC measurements, respectively.

I am thankful to Jiali Wang, Dr. Maryam Radjabian, Dr. Prokopios Georgopoulos, Kristian Buhr, Joachim Koll, Berthold Wendland, Carsten Scholles, Jan Wind from HZG, and Maryam Bozorg, Elaine Rahmstorf, Dr. Steffen Eggers, Dr. Birgit Fischer, Martin Kehden, Stephan Hinrichs, Felix Lauterbach for their support and help in my work. A special thanks goes to Prof. Dr. Ulrich Schwaneberg, Dr. Felix Jakob, Dr. Lina Apitius and Dr. Tayebah Mirzaeigarakani for their kind support in the collaborative study.

I would like to thank Dr. Christian Höhme, Dr. Kirti Sankhala, Dr. Nazia Noor, Thomas Buhr, Sarah Saleem, Silke Dargel, Elvin Aliyev, Katharina Nieswandt, Dr. Christian Otto, Nils Müller-Wendt, Dr. Karabi Halder, David Meis and all other my former and present coworkers at HZG. It is these people who have made my PhD life at HZG very amazing and wonderful.

For financial support, I do appreciate the funding from Holmholtz Association throughout my PhD period.

Last but not least, I cannot thank my parents and family members enough whose eternal love, support and encouragement has always being an internal force for my work and life.



## **Curriculum Vitae**

**Lebenslauf entfällt aus datenschutzrechtlichen Gründen.**



## **Declaration of Oath**

I hereby declare that this thesis on “Isoporous Block Copolymer Membranes with Charged Nanochannels” accommodates the original work of my PhD. Several parts of this dissertation had been published in different peer-reviewed international journals and therefore the similarities with those published works exist. All the sources used in this thesis are acknowledged. This dissertation is written by me and has never been submitted in the present form or similar to any other University or board of examiners.

Zhenzhen Zhang

Date: \_\_\_\_\_

Signature: \_\_\_\_\_